INFORMATION TO USERS

This manuscript has been reproduced from the microfilm master. UMI films the text directly from the original or copy submitted. Thus, some thesis and dissertation copies are in typewriter face, while others may be from any type of computer printer.

The quality of this reproduction is dependent upon the quality of the copy submitted. Broken or indistinct print, colored or poor quality illustrations and photographs, print bleedthrough, substandard margins, and improper alignment can adversely affect reproduction.

In the unlikely event that the author did not send UMI a complete manuscript and there are missing pages, these will be noted. Also, if unauthorized copyright material had to be removed, a note will indicate the deletion.

Oversize materials (e.g., maps, drawings, charts) are reproduced by sectioning the original, beginning at the upper left-hand corner and continuing from left to right in equal sections with small overlaps.

Photographs included in the original manuscript have been reproduced xerographically in this copy. Higher quality 6" x 9" black and white photographic prints are available for any photographs or illustrations appearing in this copy for an additional charge. Contact UMI directly to order.

ProQuest Information and Learning
300 North Zeeb Road, Ann Arbor, MI 48106-1346 USA
800-521-0600

UMI®

Net Primary Productivity of Aquatic Vegetation of the Amazon Floodplain: a Multi-SAR Satellite Approach

by

Maycira Costa

Bachelor of Oceanography, University of Rio Grande, Brazil, 1988
Master of Remote Sensing, National Institute for Space Research, Brazil, 1992

A Dissertation Submitted in Partial Fulfillment of the Requirements for the Degree of

DOCTOR OF PHILOSOPHY

In the Department of Geography

We accept this dissertation as conforming to the required standard

Dr. O. Niemann, Supervisor (Department of Geography)

Dr. M. Flaherty, Departmental Member (Department of Geography)

Dr. M. Wulder, Departmental Member (Department of Geography)

Dr. H. Barclay, Outside Member (Department of Biology)

Dr. F. Ahern, Additional Member (Canada Center for Remote Sensing)

Dr. M. T. Piedade, External Examiner (Instituto Nacional de Pesquisas da Amazônia)

University of Victoria

Superviser: Dr. Olaf Niemann

ABSTRACT

Field measures were combined with synthetic aperture radar (SAR) images to evaluate the use of radar for estimating temporal biomass and mapping of aquatic vegetation in the lower Amazon. A SAR-based methodology was developed for quantification of the annual net primary productivity (NPP) of aquatic vegetation. The predictable monomodal flooding cycle of the floodplain is the primary control of the growth pattern of the aquatic vegetation. The total biomass increased steadily from November to August following the hydrological cycle. However, the above water biophysical properties of the canopy remained constant all year around, except in November. By November, when the water level started to rise, new leaves and nodes were formed; the backscattering values were on average -12 and -14dB for RADARSAT and JERS-1, respectively. By April, a full canopy was developed, remaining constant due to the high turn over rate of leaves. By August, the water level quickly receded, the senescent stage began, the plant water content decreased, and the stems bent, changing from an almost vertical orientation. From April onwards the backscattering coefficientes were on average -7 and -9.5 dB, respectively.

The spatial variability of the canopy biophysical properties was detectable with radar data. Significant correlation existed between backscattering coefficients and above water dry biomass, height, and percentage of canopy cover. The logarithmic relationship between backscattering coefficients and biomass suggested that (1) at low biomass, high transmissivity of the microwave radiation through the vegetation canopy occurred and the backscattering was a result of quasi-specular reflection of both C and L bands and a minor contribution of canopy volume scattering from C band; (2) at intermediate levels of biomass, moderate changes in backscattering values occurred and the backscattering saturation point was reached at 470, 660, and 620 gm^{-2}, for C band, L band, and the index, respectively; and (3) at high biomass, the transmissivity of C and L band radiation was equally attenuated and backscattering approached similar values for both. The derived index ($\sigma^{o}_{index} = \frac{\sigma^{o}_{C} + \sigma^{o}_{L}}{2}$) combines the capabilities of both C and L bands providing an empirical model for estimating above water biomass ($B_{a,} = 4.022 + 0.175 \times \sigma^{o}_{index\,,}$) with the highest R^2 (0.67), the lowest root mean square error (34%), and an intermediate saturation point.

The despeckled composite SAR images (C and L bands from the same season) were classified using a region-based approach. Complementary information of the satellites yielded classification accuracy higher than 95% for vegetated areas of the floodplain. The seasonal thematic classification yielded an estimate of the length of inundation of different regions of the floodplain. Regions under flooded conditions of at least 300 days yr^{-1} were colonized predominantly by the aquatic vegetation, *Hymenachne amplexicaulis*; the tree-like aquatic plant, *Montrichartia arborescens*; and some shrub-like trees. Secondary colonizers such as *Cecropia sp.*, *Pseudobombax munguba*, and *Astrycaryum jauari*, which are tall well-developed flooded forest, colonized regions with inundation periods of approximately 150 days yr^{-1}. Climax forest colonized regions with inundation periods of approximately 60 days yr^{-1}.

The combination of the mapped area of seasonal aquatic vegetation with the SAR derived-biomass estimation allowed the calculation of the seasonal total biomass. By November, the new generation of aquatic vegetation started to develop; total biomass in the area was $0.1x10^{12}$ g. The steady growth of vegetation yielded a total biomass of $1.5x10^{12}$ g in an area of 395 km^2 in May. From May onwards, with the water receding, some plants detached from the sediment and were carried towards the Amazon River. Consequently, by August, both area and total biomass decreased to $281km^2$ and $5x10^{11}g$, respectively. Any estimate of total biomass had a margin of error of at least 18%. After correction for seasonal biomass loss, the estimated annual NPP was $6350gm^{-2}$ or $4.1x10^{12}g$ for the entire area. Despite the smaller dimensions and the C3 photosynthetic pathway of the dominant *H. amplexicaulis*, its estimated productivity was comparable to the values reported for the most productive aquatic vegetation of the Amazon floodplain, and other aquatic plants colonizing wetlands worldwide. The estimated NPP of the aquatic vegetation yielded a total carbon uptake of $1.9x10^{12}$ g C yr^{-1}. Calculations based on the estimated area of each habitat of the floodplain, and the productivity data suggested in the literature, resulted in a net carbon productivity from flooded forest, phytoplankton, and periphyton of $0.35x10^{12}gC$ yr^{-1}, $0.22x10^{12}$ g C yr^{-1}, $0.07x10^{12}$ g C yr^{-1}, respectively. The total combined autochthonous annual net productivity of the study area was $2.5x10^{12}$ g C, of which 75% was from C3 aquatic plants. This study represents the first attempt to develop a method to use SAR and field data for estimating spatial and temporal variations in biomass of aquatic vegetation from a natural floodplain.

Examiners:

Dr. O. Niemann, Supervisor (Department of Geography)

Dr. M. Flaherty, Departmental Member (Department of Geography)

Dr. M. Wulder, Departmental Member (Department of Geography)

Dr. H. Barclay, Outside Member (Department of Biology)

Dr. F. Ahern, Additional Member (Canada Center for Remote Sensing)

Dr. M. T. Piedade, External Examiner (Instituto Nacional de Pesquisas da Amazônia)

TABLE OF CONTENTS

CHAPTERS

LIST OF TABLES

LIST OF FIGURES

ACKNOWLEDGEMENTS

The following are gratefully acknowledged for their support and contribution to this thesis:

My supervisor, Dr. Olaf Niemann at University the University of Victoria (UVic), and my co-supervisor, Dr. Frank Ahern at the Canada Center of Remote Sensing, for support and encouragement.

The Coordenadoria de Aperfeiçoamento de Pessoal Nível Superior (CAPES) for the graduate scholarship (BEX1116/96-7).

The University of Victoria, National Institute for Space Research (INPE, Brazil), and Canada Center for Remote Sensing for the learning experience and logistic support.

The Canadian International Development Agency (CIDA) and Fundação de Amparo a Pesquisa do Estado de São Paulo (FAPESP, Brazil) for funding this research

The Canadian Space Agency (CSA) and the Japanese Space Agency (NASDA) for supplying the satellite images.

Dr. John Melack at the University of California in Santa Barbara for financial contribution for field work.

My committee members, Dr. Flaherty at the University of Victoria, Dr. Wulder, Dr. Barclay at the Pacific Forest Center, and Dr. Piedade at the Amazon Research Institute (INPA, Brazil) for reviews.

The Pacific Forest Center for the carbon analysis; Ole Heggen at UVic for the help with the drawings of the thesis document.

My colleague and friend, Dr. Evlyn Novo for being a model of perseverance.

My colleague and friend José Eduardo Mantovani at INPE and colleagues from the Centro de Energia Nuclear e Agricultura (CENA, Brazil) for assistance with field work.

My friends: Silvana, Milton, Marisa, Luciano, Regina, Marília, Lúbia, Sandra, and Sérgio for being my friends. My colleague Eduardo Loos for his friendly help.

My parents, Ruti and Uarandy for the opportunity to be here. My sister, Maíra, and my brother, Júnior, for the laughs

My parents-in-law, Fred and Margo for their support.

And final special thanks to my husband, Kevin Telmer for continuous support and love.

DEDICATION

To my grandmother, Nazaré Mota Pereira,
who led the women work force of my family

1. INTRODUCTION

1.1. Overview

Wetlands are important environments due to their unique role in the transformation of biogeochemical material and as wildlife habitats for innumerous species. The organic carbon productivity of these environments is the largest on earth, on average 1300 g C m^{-2} yr^{-1} (Schlesinger, 1997). Wetland environments contribute approximately 32% of the total methane annually emitted to the atmosphere (Bartlett and Harriss, 1993). The action of humans in transforming these ecosystems into agriculture fields and other uses is likely contributing to the carbon imbalance in the atmosphere (Schlesinger, 1997). Given the global importance of wetland ecosystems, it is surprising that at the present not even the global extent of wetlands is well known (Matthews et al., 2000, Melack et al., 2000). Estimates of global distribution of wetlands vary from 5.3×10^{12} m^2 (Matthews and Fung, 1987) to 8.6×10^{12} m^2 (Mitsch and Gosselink, 1993), 6% of the land surface of the world. These numbers are based on crude estimates worldwide. This is especially true for one of the largest and most productive wetlands in the world, the Amazon floodplain.

The area occupied by the Amazon floodplain is still unknown. Estimates suggest an area of at least 300,000 km^2 (Junk, 1993). The annual production of organic carbon in the Amazon floodplain is reported as 1.17×10^{14}g yr^{-1}, of which 62% originates from the productivity of herbaceous plants (Melack and Forsberg, 2000). From the total produced organic carbon, a rough estimate of 70% is exported to the riverine system (Melack and Forsberg, 2000). Researchers acknowledge that there is an urgent need for a better understanding of the regional biogeochemistry of the Amazon floodplain. To achieve this understanding on a regional scale, methods for assessing the productivity and seasonal mapping of the ecosystems within the floodplain are required. Satellites can assist in providing this information (Matthews et al., 2000, Melack et al., 2000, Junk, 2000).

1.1.1. Carbon and the biosphere

Carbon reservoirs on the Earth are constantly in a state of flux, a balancing act between the atmosphere, the hydrosphere, the biosphere, and the lithosphere. The carbon reservoir in the atmosphere plays a major role in the increase of the temperature of the earth's surface ("greenhouse effect") due to its ability to absorb infrared radiation (Schlesinger, 1997). Recently, the acknowledgement that anthropogenic emissions of CO_2 are likely causing additional increases in atmospheric temperature beyond those that occur naturally has put the carbon cycle in the forefront of research efforts. Recognizing that humans can potentially alter global climate, and knowing that we have already altered global atmospheric chemistry, has created an urgent need to understand and quantify the carbon cycle of the Earth (Schlesinger, 1997). Accordingly, it is important to understand the carbon cycle in order to minimize future impacts, and make rational decisions on how to implement and enforce worldwide systems for management of carbon.

Because carbon is the fundamental building block of life, its movements from one system to another can reveal much about the structure and function of ecosystems (Field et al., 1995), and for the purposes of this study, vice versa. This model holds true from the very small inter-plant scale to the global scale. Unfortunately, ecosystems and their carbon fluxes vary greatly across the planet and through time (seasonally), making extrapolation from local to global scale very difficult. Often, important details are lost through generalization. The high spatial and temporal resolution and large volumes of data produced by satellites, along with the new data processing technologies are, however, currently able to produce quantitative data on a seasonal scale, on a regional, and perhaps on a global scale (Sellers et al., 1995).

The seasonal effect has a great influence on the annual oscillations of atmospheric CO_2. These atmospheric oscillations are primarily due to the seasonal exchange of CO_2 with the terrestrial biosphere in the Northern Hemisphere (Schlesinger, 1997). The biosphere consumes atmospheric carbon through photosynthesis and releases it by respiration and litter decomposition. Approximately one-half of the gross carbon uptake by photosynthesis is used by plants to build up plant tissue, while the remainder is used in the plant's own respiration.

The rate of atmospheric carbon uptake by the biosphere minus autotrophic respiration is termed net primary production (NPP) (Schlesinger, 1997). The NPP is one of the most modeled ecological parameters in the quest for global and regional scale carbon budgets because of its representation of exchanges between atmosphere and biosphere (Potter et al., 1993; Field et al., 1995; Sellers et al, 1997). The NPP is used as an input paramater for (i) characterizing the fixation and release of biospheric carbon on a global scale (Potter et al., 1993; Field et al., 1995), and (ii) understanding the carbon budget on a regional scale (Sellers et al., 1997; Piedade et al., 1991; Bergan et al., 1998).

The assessment of how changes in both CO_2 and climate affect the NPP is another area of research. According to simulation models, an increase of atmospheric CO_2 from the contemporary levels to 625 ppmv, together with the associated climate responses, will likely cause an increase of 20 to 26% in the global NPP (Melillo et al., 1993). However, the response of vegetation to an increase in atmospheric CO_2 is complex and still unknown because there are few studies that integrate atmospheric changes, soil, water, nutrient availability, and plant physiology (Schlesinger, 1997).

Present estimates of global NPP range from 45×10^{15} g C yr^{-1} to 65×10^{15} g C yr^{-1} (Ruimy et al., 1994; Schlesinger, 1997), showing a general declining gradient from forest to grasslands, and very low values in deserts and ice (Figure 1.1). The data in Figure 1.1 suggests that the mean NPP of wetlands is the highest among the land ecosystems: 1300 g C m^{-2} yr^{-1}, which emphasizes the importance of wetlands in a global context. Furthermore, the above mentioned figure illustrates the high carbon productivity of the Amazon floodplain's aquatic vegetation, more than twice the average NPP of wetlands worldwide.

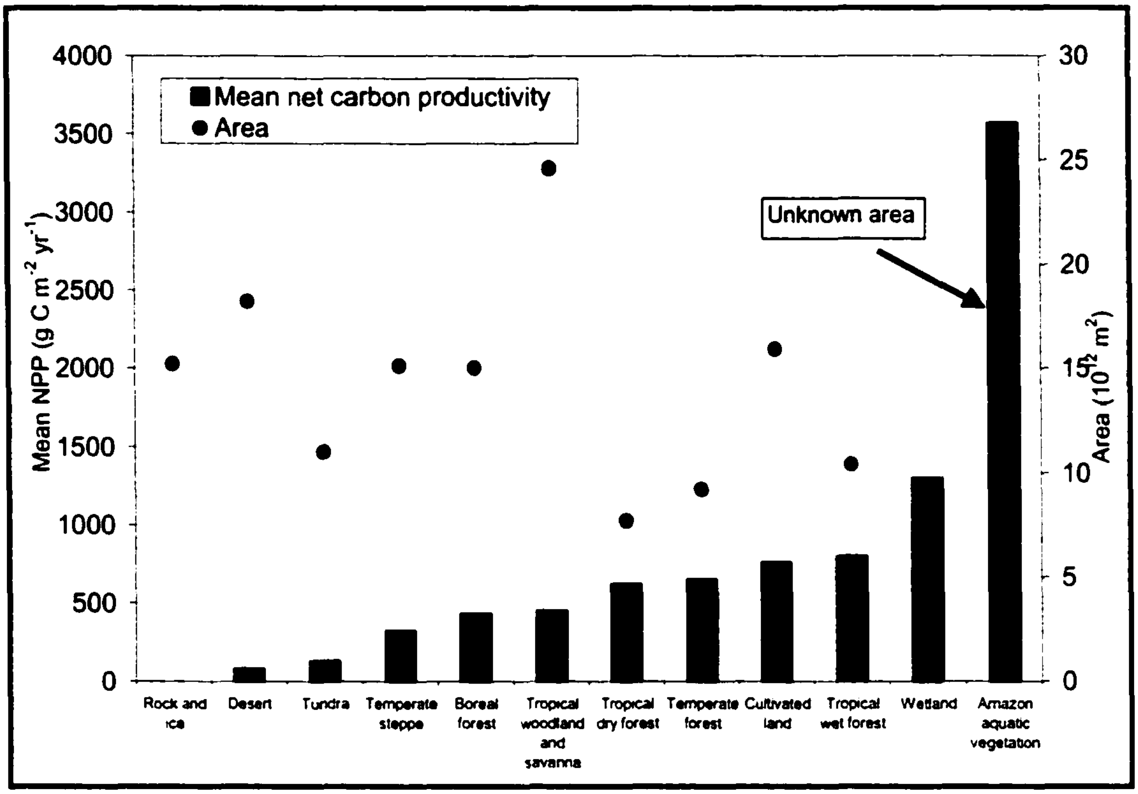

Figure 1.1. Net primary productivity (g C m^{-2} yr^{-1}) and area (x 10^{12} m^{2}) estimates for different ecosystems. Modified from Schlesinger (1997). NPP of aquatic vegetation of the Amazon is from Piedade et al., 1991.

Net primary productivity is not a simple parameter to estimate. Field methods must be adapted to the type of vegetation being studied. For instance, the most traditional methods for estimating NPP of forest and shrubland rely on the measurement of the growth of different tissues and the development of mathematical relationships between plant growth and plant size (Whittaker and Marks, 1975). Harvest techniques based on quadrat or grids are very common for estimating the NPP of grasslands (Singh et al., 1975) and aquatic vegetation (Dowing and Anderson, 1985). Another technique, based on gas-exchange, measures the photosynthetic rate at a leaf level; nonetheless, this technique is difficult to apply at a community level (Whittaker and Marks, 1975). A more recent technique, termed eddy-correlation, is based on the difference between the concentration of atmospheric CO_2 and the concentration of CO_2 at the level of the plant canopy. This difference is related to the net carbon uptake by vegetation, and can be used to estimate the NPP of whole ecosystems. All these techniques require intensive field work and frequently fail to produce estimates for large areas. For understanding global and regional processes, estimates of the NPP in a large scale are necessary. Remote sensing techniques associated with intense field survey are under development so that large scale and seasonal NPP can be assessed (Schlesinger, 1997).

1.2. Objectives and Structure of the Thesis

The purpose of this research is to evaluate the use of synthetic aperture radar (SAR) satellites for seasonal estimation of the biomass and the area occupied by aquatic vegetation in the Amazon floodplain. The objectives of this project are:

1. Investigate seasonal changes in the biophysical properties of aquatic vegetation of the lower Amazon floodplain based on field data.
2. Understand and process satellite SAR data.
3. Evaluate seasonal changes of radar signatures of different cover types according to structural changes and the main scattering processes occurring between microwave radiation and ground cover.
4. Develop a statistical model to estimate seasonal biomass of aquatic vegetation using satellite SAR and field data.

5. Evaluate SAR data to map the seasonal extension of aquatic vegetation in the Amazon floodplain using a region based classification approach.
6. Estimate the NPP/ carbon uptake of aquatic vegetation based on SAR and field data.

1.2.1. Thesis framework

The main goal of this research is to evaluate the use of SAR satellites for estimating net primary productivity of grass-like aquatic vegetation of the lower Amazon floodplain through statistical models that combine field and satellite data. Three factors form the basis for this research: (1) growth and decline of aquatic vegetation of the Amazon floodplain follows the monomodal hydrological cycle of the floodplain. Accordingly, the primary productivity of the areas colonized by these plants is high and has a seasonal variability. Most of the available data in the literature are concerned with the central Amazon. Currently, no research evaluating new methods for estimating the productivity and the area occupied by these plants in a larger temporal and spatial scale has been presented. (2) SAR satellites have yielded estimates of biomass of flooded rice plants; however, these systems have not been used to estimate biomass of natural grass-like aquatic vegetation. (3) There is an urgent need for better understanding the Amazon floodplain at a regional scale.

Initially, a general understanding of the seasonal variability of the biophysical properties of the aquatic vegetation was required. Second, the above water biomass was estimated on a seasonal base so that total biomass could be incorporated into the NPP model. The above water biomass was estimated through empirical relationships between the radar backscattering (RADARSAT and JERS-1) and the measured above-water biomass. The total biomass of a given period was estimated as a function of the above and below water biomass of the period. Finally, the area occupied by the aquatic vegetation was determined through a region-based classification of the SAR images. Consequently, the NPP for each period was estimated on a pixel basis only for the areas occupied by aquatic vegetation. The total NPP was the summation of the NPP of each period and the total carbon content was a percentage of the total NPP.

1.2.2. Structure of this document

The thesis contains eight Chapters. Chapter 1 introduces a general overview of the importance of the proposed study, characterizes the main features of the Amazon floodplain, presents background information about global and regional NPP, and reviews the use of remote sensing for studies of NPP and wetlands. Chapter 2 presents the methods of acquisition of the biophysical properties of the aquatic vegetation during five periods of the hydrological cycle of the lower Amazon floodplain. RADARSAT and JERS-1 (Japanese Earth Resources Satellite) satellites acquired synthetic aperture radar (SAR) images (11 images) concomitant with the field campaigns. The general characteristics of the satellite images are also presented in this chapter.

Chapter 3 presents the analysis of the measured biophysical properties of the aquatic vegetation and the characterization of the main habitats of the study area. Chapter 4 describes the methodology for processing and analyzing the SAR data, aimed to estimate the biomass of emergent aquatic vegetation and the spatial-temporal extent of the different habitats of the floodplain. In Chapter 5, backscattering coefficients are extracted from the SAR data and evaluated according to the dominant ground cover of the study area, namely upland forest, pastureland, savanna, water, flooded forest, and aquatic vegetation. A detailed analysis of backscattering coefficients and biophysical properties of aquatic vegetation is also presented.

Chapter 6 evaluates the capability of using SAR satellites for mapping the spatial-temporal extent of the different habitats of the floodplain. Chapter 7 describes the association of the biomass and the seasonal extent of the aquatic vegetation derived from SAR and field data to provide an estimate of NPP and carbon uptake of emergent aquatic vegetation throughout the hydrological cycle. Finally, in Chapter 8 the study's conclusions are presented.

1.3. The Floodplains of the Amazon Basin

1.3.1. Origin and geomorphology

The evolution of the Amazon Basin is generally categorized by two major geological events: (i) successive marine transgressions and regressions during the Mesozoic Era formed a channel between the Brazilian and Guiana Precambrian shields; (ii) later, during the Tertiary Era, this channel lost the connection to the Pacific Ocean due to the Andean orogeny. The formation of the Andes was perpendicular to the prevailing wind direction and to the main Amazon channel, resulting in higher precipitation in the equatorial region, blockage of drainage towards the Pacific Ocean, and the formation of a large freshwater lake. During the last glacial period, the Pleistocene epoch, water storage in the polar ice caps resulted in a decrease in sea level, and consequently a deep and wide valley was eroded in the central Amazon region. Following this, during the Holocene epoch, the sea level rose about 100 meters, damming rivers in their valleys and consequently increasing the sedimentation processes (Schobbenhaus and Campos, 1984; Iron et al., 1997). In some areas the sedimentation was not complete and large lakes were formed. The alluvial sedimentation process produced the *várzeas*, areas flooded annually by water originating in the Andes (white water rivers). Later, the rainforest and the black and clear water rivers developed. Because the black water rivers have a low concentration of suspended matter, their associated floodplain, called *igapós*, filled more slowly with sediment than the *várzeas* zones. Other important geological features for the formation of the floodplains are the four structural arches that lie transverse to the main Amazon channel (Caputo, 1991). A relationship has been observed between these arches and erosion/deposition processes along the Amazon channel due to the water-surface gradient across the arches (Mertes et al., 1996).

The above-mentioned geological events associated with the hydrology and hydraulics of the Amazon River have strongly influenced the geomorphologic diversity of its floodplain. In general, the upstream segment of the Amazon River in Brazil tends to be highly sinuous and relatively narrow (width of 2200m), promoting an increased water-surface gradient. The increased gradient promotes high rates of erosion on the floodplain. The recycling time of the alluvial plain in this area is approximately 1000 years;

therefore, lakes and islands are small and not very numerous. Changes in the profiles of the Amazon main channel and associated islands are more pronounced in this sector than the downstream sector. Furthermore, the floodplain associated with the Amazon main channel is wider than those of the other segments, and the floodplain's channels are narrower. The migration dynamics of this sector of the Amazon River leaves behind numerous curved scroll bars and oxbow lakes. The downstream segment of the Amazon River tends to be straighter and wider (width of 4500 m); the lakes and islands of its associated floodplain are numerous and larger than the upstream sector. The recycling time of the alluvial plain is in the order of 2000 to 4000 years, suggesting a more stable environment. Annual rates of vertical deposition of sediment on the Amazon floodplain can be in the order of centimeters to a meter. The depositional process builds levees and the wide floodplain construction is controlled by overbank deposition of fine material (Mertes et al., 1996).

A combination of high water levels and low topography leads to the seasonal flooding of a large area of the Amazon Basin. Remarkably, the vertical drop along the entire plain is only 120m. For instance, two thousand kilometers upstream of the mouth, the river level is only sixty meters above sea level. In the lowland basin the water levels of the main channel fluctuate an average of 7 to 13 m annually, causing water to penetrate 20 to 100 km inland forming an enormous floodplain ecosystem thousands of kilometers long (Goulding et al., 1995). The area occupied by the Amazon floodplain is still controversial (Junk, 2000). Some estimates suggest an area of at least 3000,000 km^2 of the Amazon Basin (Junk, 1993), or 92,400 Km^2 for the floodplain along the Amazon River in Brazil, and 62,000 Km^2 for the floodplain of the major tributaries of the Amazon

River in Brazil (Sippel et al., 1992). The different methods used to calculate the floodplain area, however, make it difficult to compare the numbers suggested by the different authors.

Generally, rough estimates suggest that a range between 30% (Junk, 1985) to 42% (Melack and Forsberg, 2000) of the Amazon floodplain is occupied by flooded forest. Of the remaining percentage, during high water stage, 15% of the floodplain is composed of open lake water (Sippel et al., 1992) – areas where phytoplankton communities are well developed. Aquatic vegetation or herbaceous vegetation occupies 43% of the floodplain associated with the main channel (Melack and Forsberg, 2000). These numbers change during the dry season with terrestrial herbaceous plants generally occupying what is lost by the aquatic vegetation (Junk, 1985). Other estimates, calculated through Landsat/TM classification, show that aquatic vegetation could occupy up to 26% of the lower Amazon floodplain (Novo et al., 1997). Generally, the area occupied by the Amazon floodplain, and the fraction of aquatic vegetation within it, are still largely unknown.

1.3.2. Hydrology and climate

The Amazon River is 6580 km long and together with its approximately one thousand tributaries drains an area of 6.5 x 10^6 km^2 of South America (Soares, 1991). The maximum and minimum discharge of the Amazon River, as measured at Óbidos (most eastern gauging station), are reported as 203,000 m^3s^{-1}, post high water, and 91,700 m^3s^{-1}, post low water, respectively (Richey et al., 1986), which represents roughly 20% of the global riverine water supplied to the oceans.

The Amazon basin is one of the wettest regions in the world. Total annual precipitation can be as much as 4000 mm yr^{-1}, with average values ranging from 2000 to 2400 mm yr^{-1}. More than half of this precipitation comes from locally evapotranspirated water; moisture from the Atlantic Ocean accounts for the remainder (Molion, 1991). The rainfall regime is related to the position of the Intertropical Convergence Zone and the Equatorial Continental and Atlantic air masses, such that the maximum and minimum precipitation occurs in alternating seasons in the northern and southern regions of the basin; as a result, the Amazon River has permanently inflow of water. The rainy pattern of the Amazon generally allows the prediction of the monomodal flood pattern of the Amazon River. This predictable monomodal flood cycle is crucial for the survival of the biota of the Amazon floodplain (Junk, 1997).

The water level throughout the basin follows the precipitation patterns along, but the flow of the main river experiences a sustained flood period, often out of synchrony with the local precipitation conditions (Junk, 1984). The wet and dry seasons are in February and June for the south, June and November for the north, and March and August for the central Amazon (Junk, 1984). For the central Amazon, the maximum and minimum water levels are 26-29m in June and 16-19m above sea level in November, respectively (Iron et al., 1997). A bit earlier, in May, the water level rises in the lower Amazon due to the flood of the Tapajós River and other tributaries; the water level varies between 5 to 7m and the lower waters occur in November-December (Soares, 1991).

1.3.3. River waters and soil characteristics

The three main types of Amazon waters have distinct characteristics which depend on the origin of the water, the type of soil and vegetation that are drained, and the chemical and biological reactions occurring in the waters (Konkauser et al., 1994). The 'white water rivers' originate in the Andes. Due to high relief, high precipitation, and particular geological materials, the Andean region is characterized by high erosion rates, which result in the transporting of high concentrations of unweathered minerals, metal-rich clays, and dissolved metals. The transport and sedimentation of minerals by the white water rivers produces the fertile soils of the *várzea* (Konhauser et al., 1994). These waters are rich in nutrients, tend to have a neutral or basic pH, and are high in alkalinity (Frosberg et al., 1988). The Amazon River is a typical 'white water river'.

The headwaters of the 'black water rivers' are in the Amazon lowlands. The drainage basins of these rivers are associated with highly weathered lateritic and podsolitic soils (Kling, 1967). These are sandy nutrient poor soils that do not decompose large quantities of secondary plant compounds. Furthermore, rainwater quickly percolates through these soils. These characteristics result in waters rich in humic and fulvic acids, which are carried off before decomposition is complete. Therefore, the 'black waters' tend to be acidic, low in nutrients, and have low alkalinity (Frosberg et al., 1988). Rio Negro is a typical example of a 'black water river'.

The headwaters of the 'clear water rivers' are found in the stable Brazilian and Guiana shields. These Precambrian shields are not undergoing strong physical erosion like that occurring in the Andes (Goulding, 1993), and are associated with clay latozol soils. Clay soils retain the organic matter for a sufficient time to complete mineralization of the organic matter. The 'clear water rivers' have low concentrations of suspended solids, tend to have an unstable acidic pH, are nutrient poor (Walker, 1990), and have low alkalinity (Frosberg et al., 1988). The Tapajós River is a typical example of a 'clear water river'. These three water types represent chemical end-members, but in fact many of the Amazon's large rivers are a mixture of the three water types (Walker, 1990).

The composition of the floodplain soils is a mix of river sediment originating from the Andes (minerals and volcanic rock), from the intensely weathered lowlands (silt and clay), and from organic particulates. Hence, the chemical composition of the floodplain soils is related to the river sediment composition. The sediment load decreases downstream along the Amazon River, unless there is a major input of sediment from a tributary (Richey et al., 1986). The Amazon River transports daily an average of 3×10^6 to 5×10^6 g m^{-2} of sediment to the floodplain. Approximately 80% of the load is deposited on the floodplain, and the other 20% is worked back to the main stream (Mertes, 1994). The deposited sediment is weathered and also mixed with tributary waters. In general, there are spatial changes in the sediment composition. As the sediment is transported downriver, mixed and reworked on the floodplain, the major elements, such as Al, Fe, Ca, Mg, and Na decreases, SiO_2 increases, and organic composition becomes less degradable (Martinelli et al., 1993). However, no major chemical differences in the floodplain sediment are detected on a temporal basis. This is related to the aquatic vegetation storing of nutrients during elevated water levels, equilibrating the inflow gains, and returning the nutrients (after decomposition) to the sediment/water during low water, equilibrating the lack of inflow (Victoria et al., 1989).

The current hydrological cycle and the erosion/deposition of alluvial sediment result in a continuous change in the geomorphology of the area. Islands, channels, lakes, and floodplains are formed and reworked annually in accordance with the hydrological cycle (Mertes et al., 1996). Very specific biological adaptations are required for the local fauna and flora to survive in these environments (Junk and Piedade, 1997).

1.3.4. Plant communities

The most important plant communities of the Amazonian floodplains are algae, aquatic and terrestrial herbaceous plants, and the floodplain forest. These communities have adapted to survive in an environment that changes by year, decade, and century, as a result of the "flood pulse" of these ecosystems. Consequently, there are major temporal changes in the plant community through time and between types of floodplain due to geomorphologic and sedimentation processes, climatic conditions, water level variation and, other related factors such as chemistry of water and soil (Junk and Piedade, 1997).

The water level guides the flood gradient and therefore the differentiation between plant communities. At the *igapós*, the high-level community is inundated for approximately 90 days and the low-level community for more than 150 days yr^{-1}. At the *várzea* the number of days that the plant is inundated directs the succession processes, varying from grass communities (300 flood days), shrubs (270 flood days), low biomass trees (around 250 days), and tall-high biomass climax forest (230 to 150 flood days) (Worbes, 1997; Junk and Piedade, 1997).

Not only the hydrological cycle influences the species distribution of the *várzea* and *igapó*, but also the soil chemistry. *Várzea* soils, flooded by white water-rivers, are rich in nutrients; hence, high annual biomass and nutrient content in the biomass of the vegetation are observed. The average annual total net primary productivity of the forest is 32 t of dry weight ha^{-1} (Worbes et al., 1997). On the other hand, *igapó* soils, flooded by black water-rivers, are poor in nutrients; accordingly, low biomass and nutrient content in the biomass of the vegetation is observed. The estimated total NPP is not available for the *igapós*; however, litter production, which is assumed to be 65% of the total NPP, is estimated at 10.3 t of dry weight ha^{-1} y^{-1} (Worbes et al., 1997).

The high productivity is a strategy adopted by the vegetation so it can survive in the adverse flood conditions of the *várzea*. Other strategies, adopted mainly by the floodplain forest of the *várzea*, at high water stage, are defoliation at the end of the submersion phase, cambial dormancy, development of aerenchyma tissues in the roots, development of lenticells, adventicious roots, anaerobic pathways, and seeding at the end of the aquatic phase (Worbes, 1997).

The herbaceous community of the Amazonian floodplain shows large differences when colonizing areas of *várzea* and *igapó*. Differences as well occur depending on the duration of the flooded period, water level, geomorphologic processes, and human impact within each habitat. The *igapó* regions do not efficiently sustain terrestrial and aquatic herbaceous plant growth and diversity due to the low nutrient levels of the black/clear waters, sandy soil and drought stress. Conversely, the *várzea* shows both high diversity (388 species) and productivity of herbaceous plants (Piedade et al., 1991; Junk and

Piedade, 1994; Junk and Piedade, 1993; Camarão and Marques, 1995; Luciano, 1997). Although the diversity of herbaceous plants is very high, the abundance is low for most of the species. Approximately 4% of the total number of species are considered to be highly abundant. Of these species, *Pistia stratiotes, Scirpus cubensis, Eichhornia crassipes*, and *Salvinia auriculata* are classified as aquatic macrophytes; *Echinochloa polystachya, Hymenachne amplexicaulis, Leersia hexandra, Oryza perennis, Paspalum repens*, and *Montrichardia arborescens* are classified as aquatic with a terrestrial phase; *Cynodon dactylon* and *Paspalum fasciculatum* are terrestrial with some adaptation for surviving in flood conditions; *and Alternanthera pilosa, A. brasiliana, Paspalum conjugatum, Ludwigia densiflora,* and *Sorghum arundinaceum* are exclusively terrestrial (Junk and Piedade, 1993).

The zonation of these species is dependent on environmental conditions such as habitat stability, light availability, length of the hydroperiod, and rainfall during the terrestrial phase. The main habitats for colonization are as follows: sediment bars along the main river channel, stable river banks, low-lying alluvial deposits, lake beds, inundation forest, sheltered bays, floating islands, permanent moist depressions, and anthropogenic disturbed areas. For instance, *E. polystachya* and *P. repens* form monospecific stands in the alluvial deposits in the main channel of the rivers where strong currents, waves, high load of suspended sediments, and erosion/deposition processes happen. On the other hand, *H. amplexicaulis and Oryza* spp. form large monoespecific stands in low-lying lake beds where the conditions are not as stressful and the sediment load is low (Junk and Piedade, 1997). The preferred habitat is a result of distinct adaptations to the environmental conditions.

Some perennial grasses for example, *P. fasciculatum*, are terrestrial plants highly adapted to flood conditions (Junk and Piedade, 1993), at which time their stems assume the function of rhizomes (Junk and Piedade, 1997). Other species, such as *M. arborescens*, an aquatic plant with terrestrial phase, develop better in areas where soils retain moisture even during the dry season. The low availability of light underwater in the *várzea* prevents the development of submerged photosynthetic organs. Therefore, in general, plants are free-floating or rooted in the sediment but with leaves above the water (Junk and Piedade, 1997). The high productivity of most of the aquatic plants of the *várzea* is also an adaptation (maintaining emergent leaves) to the low light condition of the water (Piedade et al., 1991). The rooted plants are subject to anoxic conditions at the level of the roots during elevated water levels. The anoxic environment promotes the development of plant adaptations, such as formation of aerenchyma, pneumatophores, and adventitious roots. Other important adaptations to the water level variations are the development of resistant seeds or spores, dormancy, and vegetative reproduction (Junk and Piedade , 1993). For some rooted species, such as *E. polystachya*, the vegetative reproduction happens when the sediment surface is exposed and new shoots form at the nodes of the old stems. The old stems decompose and the new shoots develop in new plants. There is almost no overlap between generations (Piedade et al., 1991).

Another important factor that guides the distribution of the herbaceous plants is human interference. The conversion of flooded forest into pasture allows large colonization of monoespecific stands of aquatic plants. Furthermore, the use of the *várzea* as a natural feeding area for cattle and buffalo might influence the species diversity and abundance in some areas. For instance, 25 million of hectares of flooded area of the

Amazon is used as pasture, and most of this area is in the lower Amazon where there are approximately 780 thousand buffalo and cattle (Camarão et al., 1998). It can be hypothesized that some of the differences between the species and the productivity of herbaceous plants from the central and lower Amazon are associated with human interference in these natural habitats (Luciano, 1997). *E. polystachya*, a highly productive herbaceous plant, is very abundant in the central Amazon (Piedade et al., 1991), whereas *H. amplexicaules* and *P. repens*, which are less productive herbaceous plants, form large monospecific stands in the lower Amazon (Luciano, 1997; Camarão et al., 1998), where the environment is more disturbed by humans. As of yet, there is no research focusing on the relationship between herbaceous plant distribution/abundance and human impact in different areas along the Amazon floodplain.

1.4. Review of Previous Work

1.4.1. The net primary productivity of wetlands

Wetlands are generically defined as transitional areas where the water table is either near or above the soil surface; these areas can be either permanently or periodically saturated, showing both terrestrial and aquatic phases indicated by hydric soils, hydrophytic vegetation, and various kinds of biological activities which are adapted to the transitional environment (Mitsch and Gosselink, 1993). The definition of wetlands is very controversial and varies for each country (Whigham et al., 1993). One of the difficulties resides in defining the border between the aquatic and terrestrial ecosystems so that it satisfies scientists and managers. Riparian ecosystems are also incorporated in the definition of wetlands. Riparian ecosystems are ecotones between aquatic and upland ecosystems where the water table is high (Mitsch and Gosselink, 1993).

Only some wetlands around the world, such as in Canada, the U.S. and Australia, have been studied in great detail. In other areas of the world, information is rudimentary or concentrated in individual studies (Whigham et al., 1993). Even the global extent of wetlands is not well known. Estimates of global distribution of wetlands vary from 5.3 x 10^{12} m^2 (Matthews and Fung, 1987) to 8.6 x 10^{12} m^2 (6% of the land surface of the world), of which 56% are in tropical and subtropical regions (Mitsch and Gosselink, 1993). Wetlands are considered the most productive environment on earth - 2600 g of dry weight m^{-2} yr^{-1} as an average value (Table 1.1) (Schlesinger, 1997). Net primary productivity of wetlands varies largely from a range of 100 g m^{-2} yr^{-1} to 9900 g m^{-2} yr^{-1} (Table 1.1).

Table 1.1. Annual Net Primary Productivity (g of dry weight m^{-2} yr^{-1}) of different wetland types[a]

Ecosystem	Net Primary Productivity
Tidal salt marsh	1000 – 8000
Tidal freshwater marsh	1000 – 3000
Mangrove	1000 – 5400
Freshwater marshes	900 – 6000
Northern peatlands	100 – 1000
Southern deep-water swamps	387 – 1780[b]
Reparian forested wetlands	668 – 1374[b]
Floodplain-herbaceous plants	9900[c]

[a] Data compiled from Mitsch and Gosselink (1993)
[b] Above ground biomass
[c] Piedade et al. (1991)

The high productivity of many wetlands associated with the anaerobic conditions of the soil and the water column favor the accumulation of very rich organic soil in various stages of decomposition (peatlands). Peatlands are therefore an important atmospheric carbon sink. However, since the industrial revolution, large areas of the peatlands of Europe and North America (Glooschenko et al., 1993; Wilen and Tiner, 1993) have been converted to agriculture fields, releasing 32 – 39 x 10^{12} g yr^{-1} of carbon due to peat combustion.

The other important greenhouse gas with a high rate of production in wetland environments is methane. In wetlands, the produced methane can be either consumed by bacteria or lost to the atmosphere through ebullition or conduction by vegetation. The methane lost by natural wetland habitats to the atmosphere is estimated as 160 x 10^{12} g yr^{-1}, defining these regions as the dominant natural source of methane to the atmosphere. The increase of the rice cultivation area around the world adds another 60 x 10^{12} g of CH_4 emitted annually. Together, natural wetlands and rice fields, contribute approximately 33% of the total methane annually emitted to the atmosphere (Schlesinger, 1997). Thus, combining peat combustion (Mitsch and Gosselink, 1993) with the increase in rice cultivation areas and the natural CH_4 emission from wetlands (Anselmann and Crutzen, 1989), it is suggested that wetlands are shifting from being a net sink to a net source of carbon to the atmosphere (Schlesinger, 1997).

1.4.2. Primary productivity and carbon in the Amazon

The primary Amazon forest historically occupied 4 x 10^6 km^2 of the total area classified as the Brazilian Amazon basin (5 x 10^6 km^2). The best estimate for average biomass of this forest is 31.1 x 10^3 g m^{-2} (Fearnside et al., 1993), which places it amongst the highest in the world. The total living biomass of the Brazilian Amazon basin is estimated as 60 x 10^{15} g C (Fearnside et al., 1993), approximately equal to the global annual NPP.

By 1998, approximately 13% of the Brazilian Amazon had been deforested, i.e., 515.3 x 10^3 km^2 (Fearnside and Ferraz, 1995; INPE, 1999; Houghton et al., 2000). (Deforestation refers to the clearing of the primary forest, and does not include clearing of secondary forest and savannas.) Deforestation of this carbon rich landscape releases large amounts of CO_2 to the atmosphere. The regrowth of vegetation re-captures some of the released carbon (approximately 50%); however the net result of deforestation is CO_2 evasion to the atmosphere (Fearnside et al., 1993). The conversion of forest to pasture, the most common use of the forest land in the Amazon, results in the immediate emission of a larger portion of carbon to the atmosphere, but continues to be a net emitter of CO_2 for approximately 10 years after the initial burn (Barbosa and Fearnside, 1996). Conversion of the land also releases approximately 1.6 x 10^3 g C m^{-2} from the top 1 m of soil and changes the soil from a sink to a source of CH_4 to the atmosphere (Nepstad et al., 1994). Nonetheless, estimates of the annual fluxes of carbon in the Amazon are still uncertain due to the difficulties in estimating the total biomass of the forest (Brown et al., 1995; Houghton et al., 2000). Recent estimates (Houghton et al., 2000), suggest that on average the Brazilian Amazon may vary annually between a sink and a source of 0.2 x 10^{15} g yr^{-1} of carbon to the atmosphere. It is likely that the floodplain plays an equally vital role in Amazonian carbon dynamics (Melack and Forsberg, 2000).

The carbon balance of the floodplain is a result of exchanges between atmosphere, vegetation, water, and soil. The floodplain vegetation sequesters carbon primarily from the atmospheric layer immediately above the river, which is significantly influenced by the riverine degassing. As outflow, plant respiration and riverine degassing are net emitters of CO_2 to the atmosphere. Part of the organic carbon is exported to the Amazon River (Martinelli et al., 1994). The annual organic carbon production of the Amazon floodplain is approximately 1.17 x 10^{14} g yr^{-1} (Melack and Forsberg, 2000), which is approximately 3% of the estimated global annual NPP of wetlands (Schlesinger, 1997) or approximately 41% of the annual estimated exchange of carbon between the upland Amazonian forest and the atmosphere (Houghton et al., 2000).

Of the annual produced organic carbon in the floodplain, 62% is from herbaceous plants (aquatic, semi-aquatic and terrestrial), 27% from the flooded forest, 7% from phytoplankton and periphyton, and 3.6% from allochthonous material. Of the total annual produced carbon, 2.5% is permanently buried in the floodplain sediment, and 21% is emitted to the atmosphere. Of the remaining carbon, more than 70%, is exported as dissolved organic carbon (mainly from decomposed material) to the river (Melack and Forsberg, 2000). Therefore, the combined highly productive herbaceous plants and flooded forest can be depicted as important sequesters of CO_2 from the atmosphere to the

Amazon waters. The carbon budget shows that the Amazon floodplain is an important source of carbon for the riverine systems.

The annual productivity of the herbaceous plants of the Amazon floodplain has one of the highest values ever recorded for natural vegetation. *Echinocloa polystachya*, a widely spread C4 semi-aquatic plant of the Amazon floodplain, shows values of maximum biomass of 8000 g m^{-2} and NPP as high as 9900 g m^{-2} y^{-1} (Piedade et al., 1991), which is only comparable to the NPP of tidal saltwater marshes (Mitsch and Gosselink, 1993). The high productivity of this species is related to the high efficiency of conversion of intercepted solar energy into biomass of 2.3 g of dry matter/MJ, and a canopy light interception efficiency of 0.946 (Piedade et al., 1991). The high levels of efficiencies are essential to the survival of the plant since they have to keep pace with the steady rise in water level. Using a conservative estimate of the area occupied by *E. polystachya* within the central Amazon, the annual consumption of carbon from the atmosphere would be approximately 0.714 x 10^{14} g of C yr^{-1} (Piedade et al., 1991; 1994) - roughly 61% of the total annual organic carbon production of the Amazon floodplain reported by Melack and Forsberg, 2000. If these estimates are valid, *E. polystachya*, a single species, is extremely important in the biogeochemical processes of the Amazon floodplain.

Other monoespecific stands of the central Amazon show lower values of maximum biomass and NPP for the growing period (approximately 5 months), for example, *P. repens* (2200 g m^{-2} and 3300 g m^{-2}), *O. perennis* (1700g m^{-2} and 2700 g m^{-2}) *and P. fasciculatum* (5700g m^{-2} and 7000 g m^{-2}). Mixed population, for instance, *H.*

amplexicaules and *O. Perennnis*, shows maximum biomass and NPP of 1600g m^{-2} and 4800g m^{-2}, respectively (Junk and Piedade, 1993). Mixed population of the lower Amazon shows lower value of maximum biomass (1200g m^{-2}) when compared with the population of the central Amazon. The lower values of biomass might be a result of the lower water level variation for this region (Luciano, 1997). The reported rates of NPP of aquatic vegetation of the Amazon floodplain are either higher or comparable to the annual productivity of some emergent grasses of inland freshwater marshes around the world (1000 – 6000 g m^{-2}) (Mitsch and Gosselink, 1993).

Part of the carbon fixed by the aquatic plants is eventually converted to methane due to the anaerobic conditions of the floodplain waters and sediments. Of the main methane producing ecosystems in the floodplain, emissions from macrophytes (215 g m^{-2} yr^{-1}) are higher than the emissions reported for open water/lakes, flooded forest, and soil in the central Amazon, with rates of 44, 40, and 4.5 g m^{-2} yr^{-1} respectively (Bartellet et al., 1990). The rate of produced methane by the aquatic vegetation of the Amazon is among the highest for natural ecosystems in the world, proportional to some tidal freshwater marsh (160 g m^{-2} yr^{-1}) (Mitsch and Gosselink, 1993).

Most of the organic carbon produced in the floodplain is exported to the river as dissolved organic carbon (Melack and Forsberg, 2000). Generally, the decomposition rate of Amazonian aquatic plants is very high; in two weeks about 50% of the exposed dry weight is dissolved in the water (Haward-Williams and Junk, 1979). The Amazonian research community acknowledges that a better understanding of the regional carbon cycle of the Amazon floodplain will only be possible when the biogeochemical processes became understood on a regional scale. For achieving this understanding on a regional basis, methods for seasonal assessment of the primary production and mapping of the ecosystems within the floodplain are required, and satellites can assist in providing this information in the required spatial-temporal resolution (Matthews et al., 2000, Melack et al., 2000, Junk, 2000).

1.4.3. Remote sensing and NPP

The NPP, expressed as g m^{-2} yr^{-1}, is generically defined as gross primary productivity minus plant respiration. Field methods for estimating NPP are based on (i) measurement of produced organic matter minus the loss of tissues, (ii) measurement of gas exchanges between the photosynthetic tissues and the atmosphere, and (iii) eddy-correlation techniques (Field et al., 1995; Schlesinger, 1997). Field techniques are applied mostly for local scale studies; regional and global estimates of NPP require different approaches due to the extent and variability of the ecosystems.

On a regional or a global scale, NPP is based on (i) statistical models, which typically calculate NPP as a function of climatic variables (Field et al., 1995); (ii) parametric models, which relate NPP to efficiency concepts and interception of solar radiation (Ruimy et al., 1994; Field et al., 1995); and (iii) process models, which take into account photosynthetic efficiency, soil attributes, climate data (Potter et al., 1993). To overcome problems such as biome variability and seasonality, the only possible method of estimating the NPP of the biosphere, with sufficient temporal and spatial resolution, is by using models that combine satellite data with ecological parameters. The desired temporal and spatial resolutions of information of vegetation related parameters for regional and global studies are monthly and 1 by 1 km, respectively (Sellers et al., 1995).

Optical data such as AVHRR (Advanced Very High Resolution Radiometer) imagery is widely used in parametric models to calculate NPP (Field et al., 1985; Ruimy et al., 1994; Liu et al., 1997). Generally, these models provide NPP estimates by combining the fraction of photosynthetically active radiation absorbed by green vegetation (FPAR) with the efficiency by which radiation is converted into plant biomass increments. FPAR is derived from the satellite normalized difference vegetation index (NDVI). Nonetheless, this approach has limitations for some ecosystems due to the NDVI-saturation effect at low biomass levels of forest. Process models (Potter et al., 1993), likewise, use NDVI as input data, therefore, the effect of biomass saturation becomes a problem. Other models for calculating carbon fluxes, combine the area of the ecosystems which are estimated from optical-satellite data with biomass data estimated from field data and allometric equations for biomass changes (Houghton et al., 2000). A new approach is the use of radar satellites for estimating vegetation parameters (Dobson et al., 1996).

Radar satellites are a promising source of data for estimating NPP of vegetated areas (Kasischke, et al., 1997). SAR (Synthetic Aperture Radar) data has proven useful for estimating the aboveground biomass of trees (Imhoff, 1995; Dobson et al., 1995; Bergan et al., 1998), grasslands, and agricultural crops (Ferrazzoli et al., 1997; Le Toan et al., 1997). However, an inherent biomass saturation level limits single- SAR data for both forest (Imhoff, 1995) and agriculture (Ferrazzoli et al., 1997; Le Toan et al., 1997). The limited biomass saturation level for SAR is dependent on the wavelength of the radiation (Imhoff, 1995; Dobson et al., 1995). For example, trees show a biomass saturation level of approximately 2000 g m^{-2}, 4000 g m^{-2} and 10000 g m^{-2} at C, L, and P band, respectively (Imhoff, 1995). The multiple-wavelength SAR approach provides estimates of a higher biomass level than a single-SAR data (Kasischke, et al., 1997). Bergen et al., (1998), demonstrated that the shuttle SAR images (X, C, and L band) provides a very close agreement of biomass (within 14%) with data produced by intensive field measurements of the NPP of northern forests. The saturation level of non-woody vegetation will be discussed subsequently.

Neither optical nor SAR based methodologies have been widely applied for calculating biomass and the NPP of flooded biomes. Furthermore, neither permanent nor seasonal wetlands are presently included in most global estimates of NPP and carbon budget. The lack of data concerning the wetlands (Townshend et al., 1991) and the low spatial resolution of global estimates (1° x 1 ° of grid size) may be reasons for this oversight. As previously discussed, the global area occupied by wetlands and their associated NPP are of significance: 8.6 x 10^{12} km^2 (Mitsch and Gosselink, 1993) and 2600 g of dry matter m^{-2} yr^{-1} (Schlesinger, 1997), respectively. A considerable portion of this important but neglected aspect of the global carbon budget occurs in the Amazon River basin.

Optical satellites have been used to study wetlands, including the Amazon floodplain (Sippel et al., 1992; Mertes et al., 1995; Novo et al., 1997), and others around the world (Bartlett et al., 1990; Augusteijn and Warrender, 1998). Landsat-5 satellite was used to investigate the geomorphology of the Amazon floodplain and the exchange of sediment between the floodplain and the rivers (Mertes et al., 1995). However, most of the research in regard to the Amazon floodplain and satellites is focused on mapping the flooded areas (Sippel et al., 1992; Novo et al., 1997). Due to the seasonality of this region, flooding during the rain season – high cloud cover, the use of optical systems is limited. For instance, Novo et al., (1997) had to acquire Landsat/TM images for 10 years to built a cloud-free mosaic of the Amazon floodplain. For the particular area of the Amazon floodplain that is the subject of this research, a survey of the last four years of acquisition of Landsat/TM images (total 38 images) showed that only 3% of the images were partially cloud-free; the others had almost 100% cloud cover. Moreover, optical systems are not very useful for detecting flooding in forested areas, and due to the nature of optical systems, the images have strong radiometric variability. Perhaps with the launch of the new generation of hyperspectral satellites more research will be conducted in this field and optical wavelengths will be more efficiently exploited. Airborne hyperspectral data has been useful for detailed visual mapping of small-scale wetlands (Jollineau and Howarth, 2000). Currently, understanding the capabilities of using microwave wavelengths for studying different aspects of wetlands is a new frontier (Melack et al., 2000).

1.4.3.1. SAR and wetlands

Microwave images, such as those provided by SAR systems, are a key source of information for the study of wetlands due to radar's all-weather functionality and their independence from the Sun as an illumination source. SAR systems acquire images of different wavelengths, polarization, and incidence angles. As a result, different interactions or scattering mechanisms between the radiation and the target are expected. For land and water application, the most commonly used wavelengths of SAR systems are in a range from 100 to 1 cm of the electromagnetic spectrum (Table 1.2). A radar antenna can transmit and receive microwave radiation in horizontal and horizontal polarization (HH), respectively, or in vertical and vertical polarization (VV), respectively. These are called like-polarized systems. Furthermore, the antenna can transmit in horizontal and receive in vertical polarization (HV), or vice-versa (VH). These are called cross-polarized systems. In addition to these options, there are the fully polarimetric systems, which can provide information for all components of the returned signal.

The angle of the incident microwave radiation varies from very steep (20° off nadir) to very shallow (60° off nadir) (Ulaby et al., 1981). Currently, only airborne systems or systems in the space shuttle can acquire data in multiple wavelength, polarization, and incidence angles. Satellites only operate in a particular wavelength and polarization; however, data acquired at different angles of incidence have been collected by RADARSAT 1. The next generation of SAR satellites, such as RADARSAT 2 and ENVISAT, will acquire data at several polarization and incidence angles.

Table 1.2. Radar band designations for land and water applications

Band designation	Wavelength (cm)	Frequency (GHz)
P	30-100	0.225-0.3990
L	15-30	0.390-1.550
S	7.5-15	1.550-4.20
C	3.75-7.5	4.20-5.75
X	2.4-3.75	5.75-10.90

Radar systems have been used successfully in the last decade in studying tropical wetlands (Richards et al., 1987; Pope et al., 1994; Hess et al., 1995; Wang et al., 1995; Pope et al., 1997; Kasischke and Bourgeau-Chavez, 1997; Costa et al., 1998) and irrigated rice fields (Le Toan et al., 1997; Ribbes and Le Toan, 1999). These authors have worked in various wetlands of the world using different systems, such as airborne SAR and satellite SAR. In the results reported by the above-mentioned authors, both commonalties and differences have been found. The differences reflect that wetlands around the world have distinct characteristics in terms of vegetation type and timing of flooding. The water table level is a crucial factor in the characterization of the backscattering coefficient (Dobson et al., 1996). The geometry and organization of the vegetation are also important factors for characterizing the radar signal (Holmes, 1992).

SAR based methods have rarely been applied to map and estimate the biomass of above-water of grass-like aquatic plants. The few existing studies have focused on mapping and estimating the biomass of wetland rice paddies (Kurosu et al., 1995; Le Toan et al., 1997; Ribbes and Le Toan, 1999). Other studies have focussed on the characterization of the structure of the plants and the interaction with microwave radiation (Pope et al., 1997), and on modeling spectral scattering in response to biomass and structural features of the plants (Dodson et al., 1996). The structural features of the aquatic plants are important in defining the amount of backscattered radiation. For instance, dense, tall (1.5 m), vertically-oriented herbaceous plants of marshes show double-bounce mechanism with L (HH and VV) and even C-HH at low incidence angles (Pope et al., 1997). Double-bounce mechanisms are caused by the interaction of the radiation with the stem/trunk, followed by a change in direction towards the surface (water) and a strong bounce back towards the radar antenna (dihedral corner reflector behavior). An equal amount of energy is also reflected from the water to the plant and then to the antenna (Ulaby et al., 1988). The characteristics of both the plants and the sensor are important to explain double-bounce interaction. The combination of the long wavelength (L band- 25 cm), the polarization (HH), and the incidence angle ($\theta < 25°$) allows higher penetration of the radiation through the canopy. The wavelength plays an important role in defining the scattering mechanism. At the long wavelength of L band, the leaves of the plants are quasi-transparent, hence the radiation interacts mostly with the stem and the underlying water. Furthermore, at HH polarization the radiation penetrates deeply into vertically oriented structures favoring the interaction with the stem/water surface (double-bounce). For the same configuration of radiation/target, but with VV polarization, the interaction is mostly with the upper canopy (Ulaby et al., 1986). Double-bounce mechanisms are enhanced for radiation at lower incidence angles when compared with higher incidence angles (higher than 55°) (Ford and Cassey, 1998; Hess et al., 1990). At lower incidence angle the pathway of the incidence wave through the canopy is minimal; therefore, the radiation is less attenuated by the canopy.

For less dense herbaceous plants of the flooded wetlands (Pope et al., 1997) the backscattering values are not as high as those observed for high density stands due to the increase in the forward scattering off water patches, a scattering mechanism known as specular reflection. For herbaceous plants (different densities), at either C-VV or cross-polarized and low incidence angles ($\theta<25°$) radiation, double-bounce effects were not observed, only those related to canopy volume-scattering (Pope et al., 1997; Kasischke and Bourgeau-Chavez, 1997; Hess et al., 1995). Volume-scattering mechanisms are characterized by the interaction of the radiation within the canopy of the vegetation, i.e. with the leaves and stems. The radiation is scattered by the elements in all directions within the volume. The resultant backscattered radiation towards the antenna is not as strong as it is for double-bounce mechanism (Ulaby et al., 1982).

Simulations of backscattering from grass-like flooded vegetation (*juncus*) for two different sensors, ERS-1 (C band) and JERS-1 (L band), showed that the signal was much smaller in the L band when compared with the C band, i.e. the blade-like vegetation of flooded wetlands were mostly transparent at L band. For C band, VV-polarization data, the increase in backscattering was approximately proportional to the modeled biomass until a saturation level of 2000 gm^{-2} of dry biomass was reached (Dodson et al., 1996). Measured backscattering values from flooded rice plants showed a lower saturation level of dry biomass. At C-VV (ERS-1) the saturation point is 400 gm^{-2} at –8dB (Le Toan et al., 1997); at C-HH (RADARSAT S1), the saturation point is 200 gm^{-2} at approximately –8dB (Ribbes and Le Toan, 1999). According to the authors, these different saturation levels are currently not well understood.

Overall, the total backscattering from wetland herbaceous plants is dependent on the interaction of the microwave energy with both the canopy and the canopy-ground. Not only the characteristics of the canopy, such as density, distribution, orientation, shape of the foliage, dielectric constant, height and components of the canopy, but also the characteristics of the sensor (polarization, incidence angle and wavelength) are important in determining the amount of radiation backscattered towards the radar antenna.

In the case of wetlands with woody vegetation, the situation changes due to the presence of trunks and higher density of the canopies as compared to non-woody vegetation. Both modeled and measured backscattering coefficients are consistent with the interpretation that L band, HH polarization and lower incidence angles ($\theta<30°$) data produced canopy-volume scattering and double-bounce interactions (Richards et al., 1987; Wang et al., 1995; Hess et al., 1995). The contribution of canopy-volume scattering to the total backscattering is higher when the incidence angle of the radiation is high and the polarization is VV. At P band, independent of the polarization and incidence angle, the backscattered radiation increases for flooded forest when compared to non-flooded forest. This happens because the foliage and branches of trees are largely transparent at this wavelength (100 cm), hence double bounce (trunk/water) is predominant (Hess et al., 1990). At C band, independent of the polarization and the incidence angle, canopy-volume scattering is predominant (Richards et al., 1987). Flood detection beneath trees is only possible with C-band, HH polarization and low incidence angle, when trees lose their leaves, which, in the case of some species, is during flood period in the Amazon floodplain (Wang et al., 1995).

2. FIELD STUDIES AND SATELLITE DATA

2.1. General Description of the Study Site

The study area (Figure 2.1), 2°00'S/54 ° 32'W to 2°30'S/54 °00'W, is a sedimentary basin located in the northeast of the Brazilian Amazon Basin, at the border separating the central and lower Amazon Basin. This floodplain system was established during the Holocene as part of the alluvial sedimentation process. The litology of the alluvial floodplain is predominantly silt and clay materials. The predominant vegetation is graminaceous, pioneers shrub and forest. The northern part of this floodplain is located in a small rural setting where part of the flooded forest has been converted to pasture land. To the north of the floodplain limit, part of the low Amazon plateau is observed. Its average elevation is 100 meters, but some mountains are up to 300 meters high. In this region, the sediment is composed mostly of silt stones, sand stones, and conglomerates. The predominate vegetation is savanna ("cerrado"), secondary vegetation, pasture, and dense forest (RADAMBRASIL, 1976). The southern portion of the floodplain, during the high water period, is connected to the Amazon's main channel.

This floodplain area is geomorphologically more stable than the upstream reaches of the Amazon River, being characterized by a flat region covered by large shallow lakes (Mertes et al., 1996). These characteristics favour the colonization and high productivity of aquatic and semi-aquatic vegetation (Junk 1985).

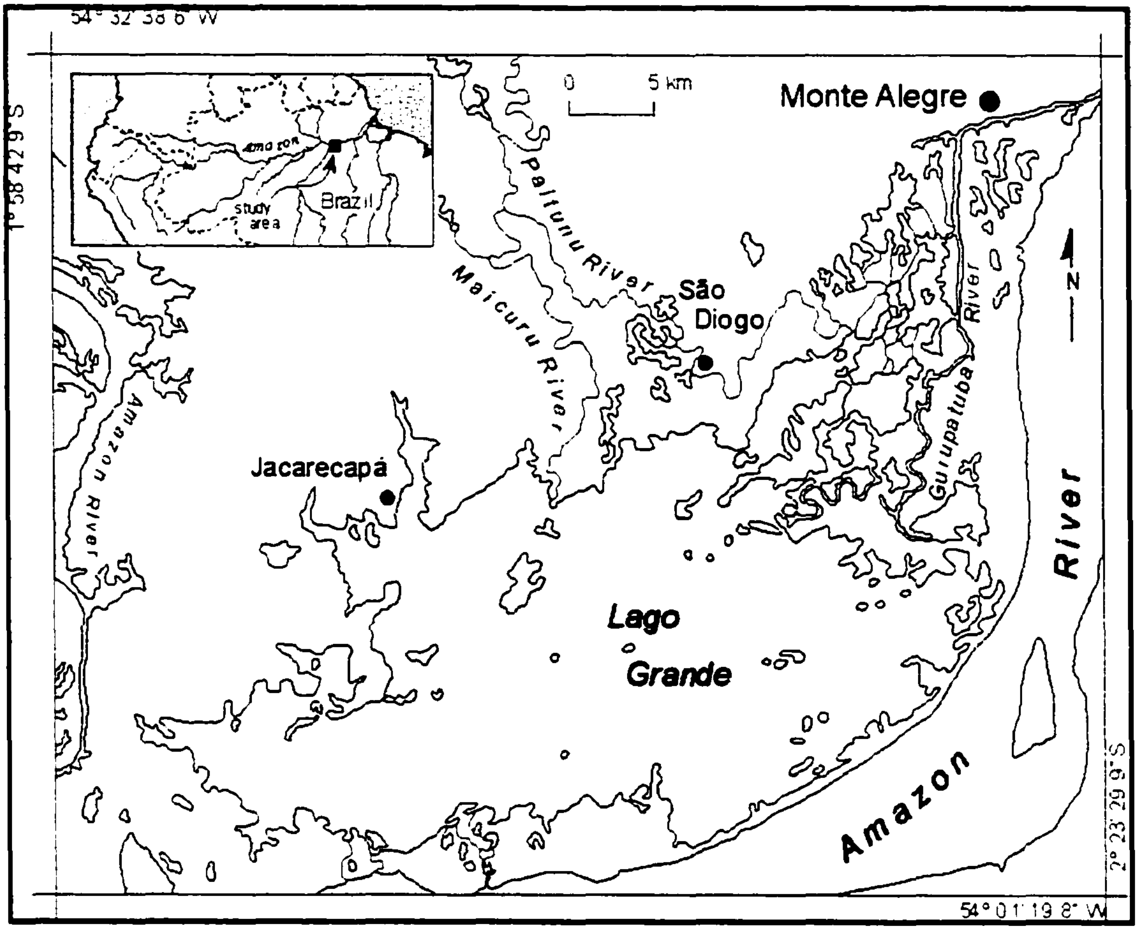

Figure 2.1. Study area.

The main climatic patterns of the area are: (i) a wet season during which the Equatorial Continental air mass dominates over the Intertropical Convergence air mass causing strong rains; the rainy season prevails from February to May, and precipitation is up to 400 mm per month; the relative humidity is close to 90%; cloud cover is between 7.1 and 9.0 (on a scale of 0 to 10); the air temperature is on average 25°; and (ii) a dry season during which the Equatorial Continental and Intertropical Convergence air masses are not as dominant; the dry season prevails from August to November, and precipitation is lower than 80 mm per month; the relative humidity is approximately 80%; the month with the least cloud cover is September; and the air temperature is on average close to 30° (RADAMBRASIL, 1976).

The largest lake of the area, Lago Grande de Monte Alegre (Figure 2.1), is approximately 60 km long and 40 km wide during the high water season in May and June when the water level variation can reach a height of 7 meters. The lake receives water from the Maicurú River, other small rivers, and from the Amazon River through narrow channels. The Amazon is the major source of water to this lake. The Amazon River, before it reaches the lake, receives water from the Tapajós River. The diverse characteristics of the origin, drainage basins, and water regimes of these rivers result in the different temporal contribution of water and spatial differences of the water chemistry of the study area.

The average depth of the shallow areas during high water stage (close to the margins of the lake and riparian zone) is 3 meters; the central part of the lake reaches 7 meters in depth and the depth of the narrow channels can reach 15 meters. At low water stage, part of the lake dries and other areas are extremely shallow; a person can wade through most parts of the lake. The characteristics of the study area change dramatically from the high water (aquatic phase) to the low water (terrestrial phase) season due to the water level variations. At high water stage, different distribution of aquatic plants (herbaceous plants) is observed. The major concentration of aquatic vegetation is located in areas where there is a dominant contribution of the nutrient-rich white-waters of the Amazon, as already observed by Junk and Piedade (1993) in other areas of the Amazon floodplain. Dominant among the aquatic plants is the family Poaceae with the following species, *Hymenachne amplexicaulis (*rabo-de rato*), Paspalum fasciculatum (*muri*), E. polystachya (*canarana*), Paspalun repens* (premenbeca), *Orzya* spp. (arroz selvagem), and *Panicunum chloroticeu (*arroz*)*, as well as the family Aracea with the species *Montrichardia arborescens* (aninga). The inundated forest is colonized by several different species of trees such as *Astrocaryum jauari* (jauari), *Pseudobombax munguba* (munguba), and *Cecropia* spp. (imbauba). Part of the forested region (in the northwest) is not a typical Amazon rainforest. Scattered trees (cerrado) and a soil covered by graminaceas or bare soil is characteristic of this landscape. Transitional areas between "cerrado" and forest are also present, as well as pastureland.

In the study area, as in many areas of the Amazon with rural populations, forestland and flooded-forest are gradually being deforested and converted into pasture for herbivores, particularly cattle and buffalo. The deforestation has a number of adverse consequences, most notable are the increased siltation to the lake water and colonization by aquatic vegetation in the deforested areas. In addition, the fruits and seeds of some species of flooded trees are important sources of food for certain fish (Goulding et al., 1995). Therefore, deforestation of the flooded forest will reduce the food supply for the fish population, and possibly modify the balance of carbon in the area due to the increase of colonization by aquatic vegetation.

The geographic location of the study area has several advantages for performing the proposed study, namely (i) its location on the lower Amazon floodplain, a large extent dense covering of aquatic vegetation occur; (ii) it comprises a large diversity of habitats such as white and black water rivers, lakes, flooded-forest, non-flooded forest, levees, aquatic-vegetation and agriculture areas, describing the most common habitats along the Amazon floodplain, and (iii) relatively easy access for field data collection. The results derived from this area can provide insight in regard to the use of the same methodology for other areas of the Amazon floodplain.

2.2. Field Methodology

The total biomass of aquatic plants is the key information for estimating the NPP. Net primary productivity of aquatic plants has been estimated by the following field methods: (i) measuring peak biomass; (ii) multi-temporal harvest; (iii) disappearance methods; (iv) gas exchange (la Cruz, 1978); and non-destructive technique that takes into account the density of stems and the biomass or height of the stems (Giroux and Benard, 1987; Piedade et al., 1991). NPP was estimated according to a multi-temporal harvest technique that is employed by researchers in the Amazon (Junk, 1970; Piedade et al., 1991; Junk and Piedade, 1993) following the equation:

$$NPP = \sum [(B_{t+1} - B_t) + (L_{t+1} \times B_{t+1})] \qquad \text{Equation 2.1}$$

where B_t and B_{t+1} are the total biomass at the beginning and the end of the measured interval, and L_{t+1} is the percentage of litter or loss produced during the interval. The total biomass is the summation of above and below water biomass.

Herbivorous animals, such as mammals, birds, fish, and aquatic invertebrates play a minor role as primary consumers of aquatic plants of the Amazon floodplain (Furch and Junk, 1997; Junk and Robertson, 1997). Most of the plant material produced in the floodplain decomposes very quickly; 50 % of submerged dead leaves decompose in less than a month (Howard-Williams and Junk, 1976; Furch and Junk, 1997). Loss data are very difficult to measure due to the fast decomposition of the organic material. Hence, based on the detailed studies performed by Junk and Howard-Williams (1984), losses are assumed to be between 10 and 25% of the available biomass, 25% being more realistic (Junk and Piedade, 1993). Losses are mostly due to the high turnover rates of leaves (average longevity of leaves is 34 days for *E. polystachya*), so the plants can keep alive-photosynthetic organs above the water (Piedade et al., 1991).

The requirements for Equation 2.1 are total biomass and produced litter for the period of study. Litter or loss was assumed to be 25% of B_{t+1}, the total weight of the period (Piedade, 1991; Junk and Piedade, 1993). The total biomass of a given period was estimated as a function of the above-water biomass of the period and the below-water biomass (as function of depth). The above-water biomass component of the model was estimated through the empirical relation between radar backscattering coefficient (RADARSAT and JERS-1) and measured above-water biomass. The NPP for each period was estimated on a pixel basis according to the estimated total biomass, loss, and area covered only by aquatic vegetation derived from the image classification. The total NPP was the summation of the NPP of each period. Carbon content was determined based on the data collected in the field. The carbon uptake (fixed carbon) was considered as percentage of the total NPP.

2.2.1. Sampling strategy

Field campaigns were carried out five times, as follows: high water stage (May 1996 - campaign 1), falling water (August 1996– campaign 2), low water stand (November 1996 – campaign 3), rising water (April 1997- campaign 4), and, again, high water stage (June 1999 – campaign 5). The last field campaign in June 1999 was not part of the original research plan, however, after performing the analysis of some of the previous data it was decided to conduct a second campaign during the high water season in order to complement the data set. The number of sites sampled during each field campaign was as follow: May 1996 - 22 sites; August 1996 – 17 sites; November 1996 – 8 sites; April 1997 – 23 sites, and June 1999– 38 sites.

For conducting studies of productivity of aquatic vegetation it would have been best to collect data starting at the beginning of the growing period (November), following the growing season, and finishing at the end of the growing season (August). For logistical reasons the sequence of the field campaigns did not follow the growing cycle of the plants. The schedule of the field campaigns had to be adapted to the schedule of acquisition of Radarsat and JERS-1 data. Nonetheless, the analysis of the data set is based on the assumption that the data set (field and satellite data) was acquired following the growth cycle of the vegetation, i.e. in the following sequence, November, April, May, July, and August thus, fulfilling one growth cycle. This is a reasonable assumption due to the fact that the water pattern was similar for the three years of data acquisition (item 2.2.4), and that the water level is the most important variable on the growth pattern of the aquatic vegetation (Junk and Piedade, 1997).

Different strategies are suggested for spatial sampling of aquatic plants biomass, for instance, (i) sampling at constant intervals along a transect line perpendicular (Hudon, 1997) or parallel (Piedade et al., 1991) to the shoreline; (ii) stratified random sampling (van der Valk and Davis, 1978); (iii) systematically located sampling stations (Giroux and Bedard, 1987), and (iv) sampling in the center of the stand (Brock et al., 1983). The options are numerous, and the selection of the adopted method was a compromise between a representation of the stands and the logistical conditions in the field.

For this study, the sample sites were selected based on a stratified random design, and, for all the campaigns, the samples were collected in approximately the same regions. The number and location of the samples were determined based on the distribution of the plants, accessibility to the areas, and available time in the field. The sites were located as far as possible from the boundary between the stands and open water. These boundaries are subjected to intense wind and current stress and may not be representative of the characteristics of a whole stand. The process of collecting samples close to the center of the stands was very arduous and some times not possible. The stands of aquatic plants are extremely dense, making it difficult to move the 3 meters long boat within the stand. The alternative, and sometimes a very dangerous strategy, was to walk on the top of the plants (average depth was 3 m at high water season) and push the boat for hundred of meters towards the center of the stand. Figure 2.2 shows the sampled regions for the 5 field campaigns.

During the field campaigns four major strategies were conducted with the objectives of understanding the behavior of the radar backscattering values, estimating above-water biomass, and mapping the aquatic plants areas, namely (i) measurements of the aquatic vegetation biophysical parameters; (ii) visual observations synchronized with hand-held photography of the area around the sampling sites and the different environments of the study area; (iii) acquisition of aerial photographs of the study area; and (iv) acquisition of ancillary data. The following sections present details of each strategy performed during the field campaigns.

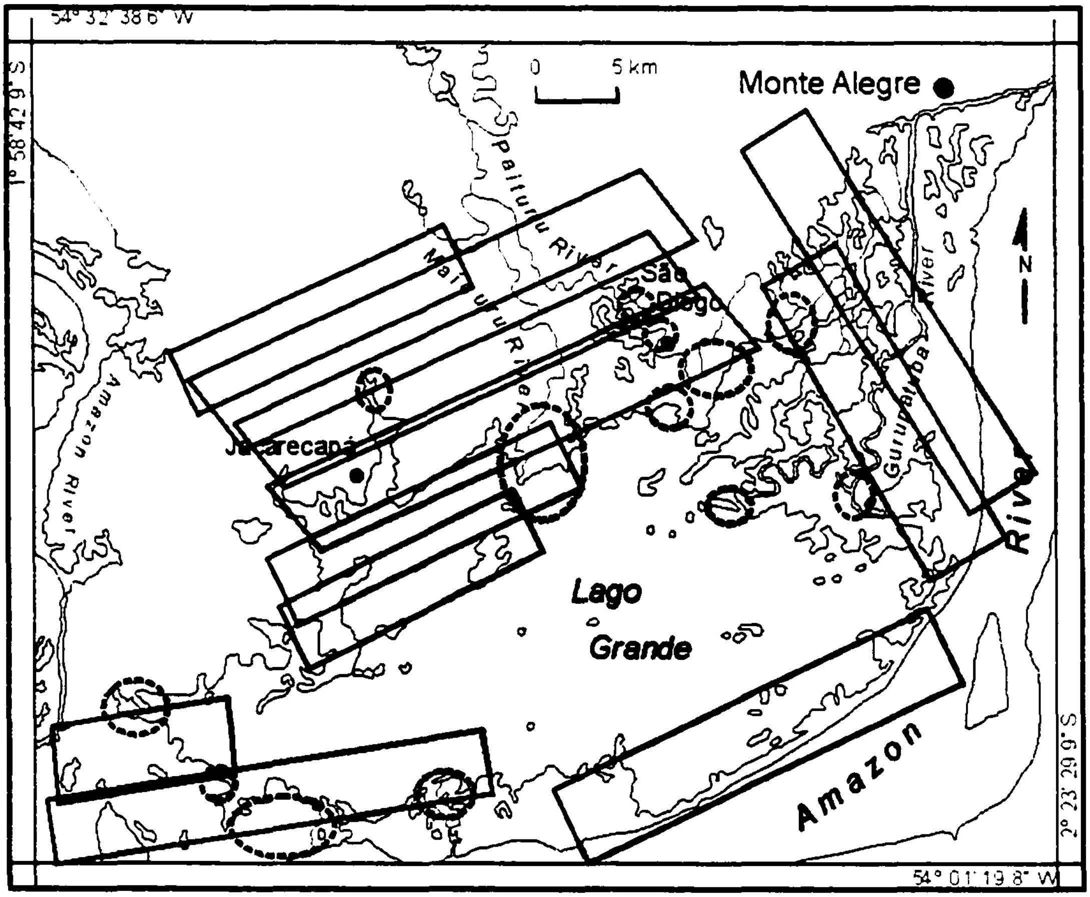

Figure 2.2. Sampled regions are highlighted with circular dashed line; rectangles represent aerial photograph cover.

2.2.2. Aquatic vegetation measurements

In Chapter 1 it was emphasized that the backscattering signal from vegetation is strongly dependent on both the properties of the vegetation, such as the size, shape, orientation, biomass, and dielectric constant of the scatters, the characteristics of the underlying surface (soil, or water), and the characteristics of the sensor, such as wavelength, polarization, and incidence angle of the microwave radiation (Ulaby et al., 1982). With this understanding, homogeneous areas representative of the distribution of the aquatic plants were characterized by observation and measurements of the following parameters: (i) the percentage of canopy closure, phenological stage, plant height, average plant inclination, leaf length, width and inclination, number of leaves, diameter of the stem, and percentage of dominant species, (ii) above and below-water biomass (fresh weight and dry weight), and (iii) carbon content of the aquatic vegetation. All the parameters were determined in the field, except for the dry biomass, the canopy cover, and the carbon content data, which were determined in the laboratory.

2.2.2.1. Biophysical properties and canopy cover

The biophysical properties such as plant height, leaf length and width were measured with a tape measure; the diameter of stem was measured with a paquimeter; the inclination of the stem and leaves was measured with an inclinometer. The phenological stage was determined based on the presence of flowers and general stage of development of the plants. The percentage of dominant species was determined through visual observation of an area of approximately 100 meters surrounding the sampling site (section 2.2.4).

The canopy cover of the aquatic vegetation was determined through photographs taken using a 35mm camera at a nadir-viewing angle over an area of 0.25 m^2. The photographs were scanned, and the canopy cover of aquatic plants per area was digitally estimated using the software Gap Light Analyzer (GAP) (Frazer and Canham, 1999). GAP offers the option of visualizing the digital numbers corresponding to aquatic plants and water, hence a threshold was established for automatically classifying water and plants. Thresholds representing vegetation were established, and subsequently binary images were created by assigning value 0 to water and 255 to vegetation. The system automatically calculated the percentage of digital values corresponding to aquatic vegetation. Figure 2.3 illustrates the original and binary files. The entire data set is presented in Appendix I.

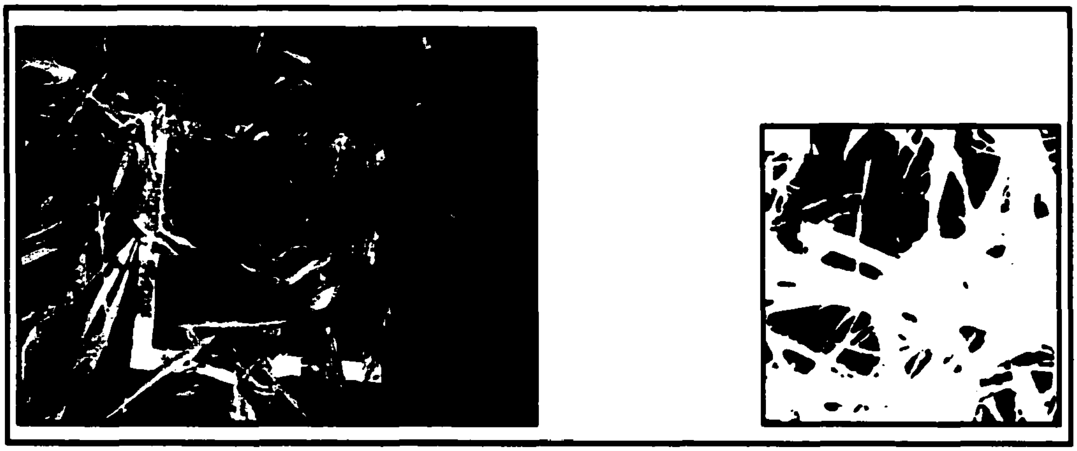

a. Original nadir photograph of a sample site

b. Binary file (GAP)

Figure 2.3. Area with a canopy cover of 73% determined through GAP.

2.2.2.2. Biomass

2.2.2.2.1. Above water biomass

The fresh biomass was measured by the destructive method using a square quadrat of 0.25 m^2. According to Dowing and Anderson (1985), 0.25m^2 is the most common size of sampler for sampling macrophytes, yielding good estimates of the mean biomass. The quadrat was placed randomly at either side of the boat. Above water plant matter was cut with grass-clippers and then placed in meshed nylon bags and weighted (fresh biomass). The samples were air dried, and then transported to the laboratory, where they were ovendried at 80°C to constant weight (approximately 48 h).

The number of replicate samples at each site was problematic for the first three campaigns (May, August, and November) due to logistical constrains. For April and June, two and three replicates were collected at each site, respectively. According to Dowing and Anderson (1985), three replicates yields a level of precision of 20% of the true mean biomass when using a 0.25 m^2 sample unit and the average biomass is approximately 450 g of dry weight m^{-2}.

A comparison of the mean above water biomass of two independent sets of field data was conducted to find if the lack of replicate samples of some field campaigns would cause errors in the estimates. A test was run between the mean values of biomass obtained in May (no replicates) and June (three replicates), both during high water period. The statistical test showed that there was no significant difference ($p<0.05$) between the two means. Therefore, biomass values obtained in May without replicates were similar to the values obtained in June with three replicates, which minimizes the errors that could occur due to the lack of replicate samples for some field campaigns. This result was expected since both data sets were collected during the high water stage.

2.2.2.2.2. Below water biomass

Traditional field methods used for sampling below water biomass of macrophytes are either scuba diving or, in the case of shallow water, by hand (Dowing and Anderson, 1985; Hudon, 1997). In the Amazonian waters neither method can be used because of the low under water visibility (total solids suspended in the water is higher than 40 mg l^{-1}) and the depth of the areas (average 3 meters). Piedade et al. (1992 and 1993), pulled out entire individual stems and used them as the basic sampling unit for estimating below-water biomass of Amazonian aquatic vegetation. Other authors (Bernard and Gorham, 1978; Lieffers, 1983; Giroux and Bédard, 1987) have used the same technique to monitor seasonal growth of emergent macrophytes in other regions of the world.

To estimate below water biomass, it would have been best to sample all the stems within a quadrat rather than a few entire stems. For reasons such as restricted time in the field and the difficulties of collecting entire stems, one rooted stem from two replicate quadrats were collected. The samples were washed with a sieve, placed in meshed nylon bags, air dried, transported to the laboratory and ovendried to constant weight at 80°C for approximately 48h. Additionally, the number of stems in $0.25m^2$, the stem length (below water), and the number of nodes per 0.5 meter of the stem were recorded. This information combined with the sampled above water biomass provided an estimate for the total biomass of the plants.

The below water data was only measured in the field campaign of June. For this campaign, equations of regression of dry biomass and volume of a submerged stem were calculated for each species; mean submerged biomass of the stems within each quadrat was estimated by taking into account the density within the quadrat and the biomass of a submerged stem. The following steps show the procedures to estimate the total biomass of submerged stems within a quadrat for the most common species in the study area. The procedures were developed with the data collected in June and data available in the literature of aquatic vegetation from the Amazon floodplain (Junk, 1970; Piedade et al., 1992; Piedade et al., 1993; Junk and Piedade, 1993; Junk and Piedade, 1997), and subsequently used to estimate below-water biomass of stems for the other months. The procedures vary according to the statistics of the most common species measured in June and the life history of the species (Junk, 1970; Bernard and Gorham, 1978).

Hymenachene amplexicaulis

(i) Calculated submerged length of the stem

Regression of below water length of an entire stem, L_{si}, and depth for each sample site, d_i, was calculated. The relation between the length of the stems of rooted emergent aquatic vegetation and the water level (depth) for the Amazon floodplain has already been suggested by Piedade et al., (1993) and Luciano, (1997). Total length of the stems was calculated as a function of d_i, the local depth, according to a linear equation (Equation 2.2). The data collected in June was used to produce this linear relationship (Figure 2.4), which showed a R^2 of 0.96 ($p<0.05$).

$$L_{si} = a + b\, d_I \qquad \text{Equation 2.2}$$

a and *b* are the coefficients of the regression equation. For June, L_{si} and d_i were measured. For April and May, d_i was measured and L_{si} was estimated according to the above regression equation. For August, when the water level is declining, there was no relation between the length of the stem and the local depth. Some authors suggested that during the first two months after the water starts to decline, the plants (*E. polystachya*) are still growing (Piedade et al., 1992, 1993; Junk and Piedade, 1997). Hence, the average growth rates of the previous month were used to estimate growth for August.

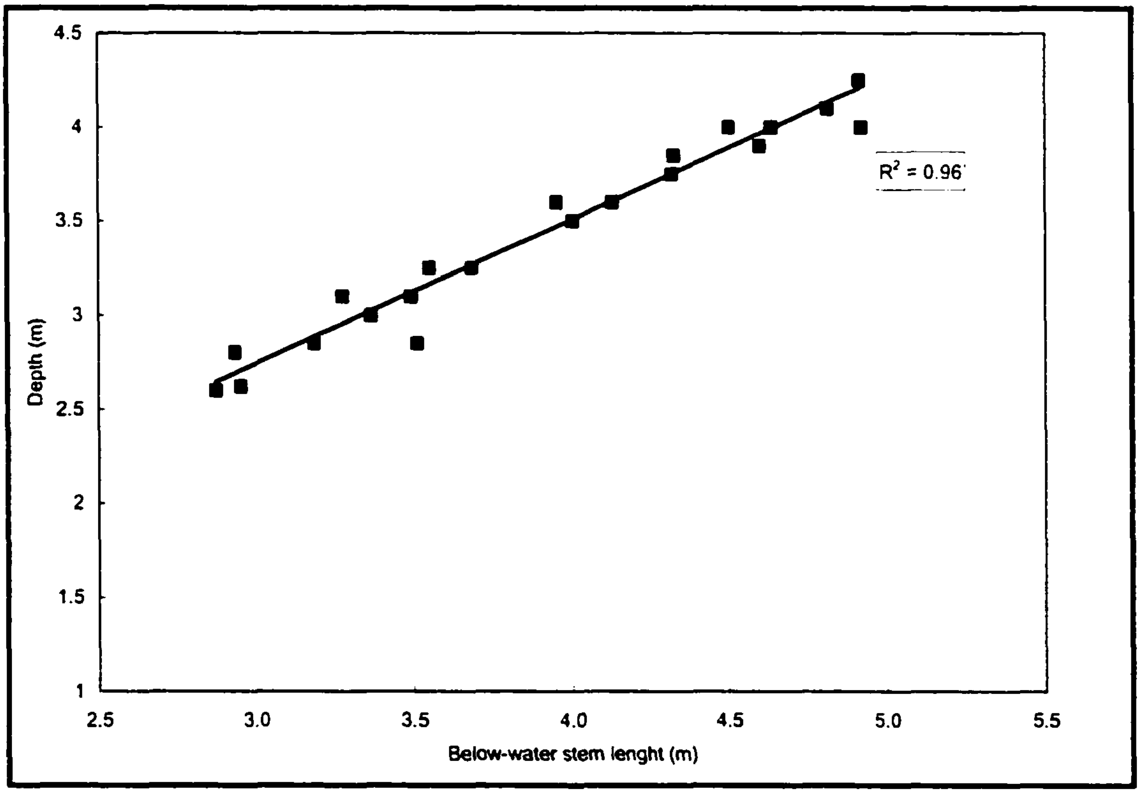

Figure 2.4. Linear relationship between the length of the stems (below-water) and local depth from the data set collected in June.

(ii) Calculated below-water biomass of the stem

Regression of below-water biomass of the stems (b_{si}) and volume of the stems (v_{si}) was calculated. Regressions of shoot biomass versus shoot length are more commonly used for estimating total shoot biomass of emergent aquatic vegetation (Bernard and Gorham, 1978; Lieffers, 1983, Giroux and Bédard, 1987), which includes leaves, flowers, and stems. For estimating below-water biomass of the stem it is reasonable to use the relationship between volume of the stem and biomass. The stems of the Amazonian aquatic vegetation are approximately cylindrically shaped, thus the volume of the submerged stem, v_{si}, was calculated as following (volume of a cylinder):

$$v_{si} = \pi \, r_i^2 \, L_{si} \qquad \text{Equation 2.3}$$

where π is the ratio of the circumference of a circle to its diameter (approximately 3.14), r_i is the radius of the stem, and L_{si} is the length of the below-water stem. The radius of the stems were measured in each field campaign; the length of the stems was either measured in the field (June) or estimated through the local depth (item i) for April and May. A linear regression between the below water biomass of the stems, b_{si}, and the volume of the stems, v_{si}, measured in June was calculated according to the following equation:

$$b_{si} = a + b \, v_{si} \qquad \text{Equation 2.4}$$

where a and b are the coefficients of the regression equation. The regression showed a R^2 equal to 0.86 ($p<0.05$). Three random subsamples of the total samples were selected and the reliability of the model was evaluated.

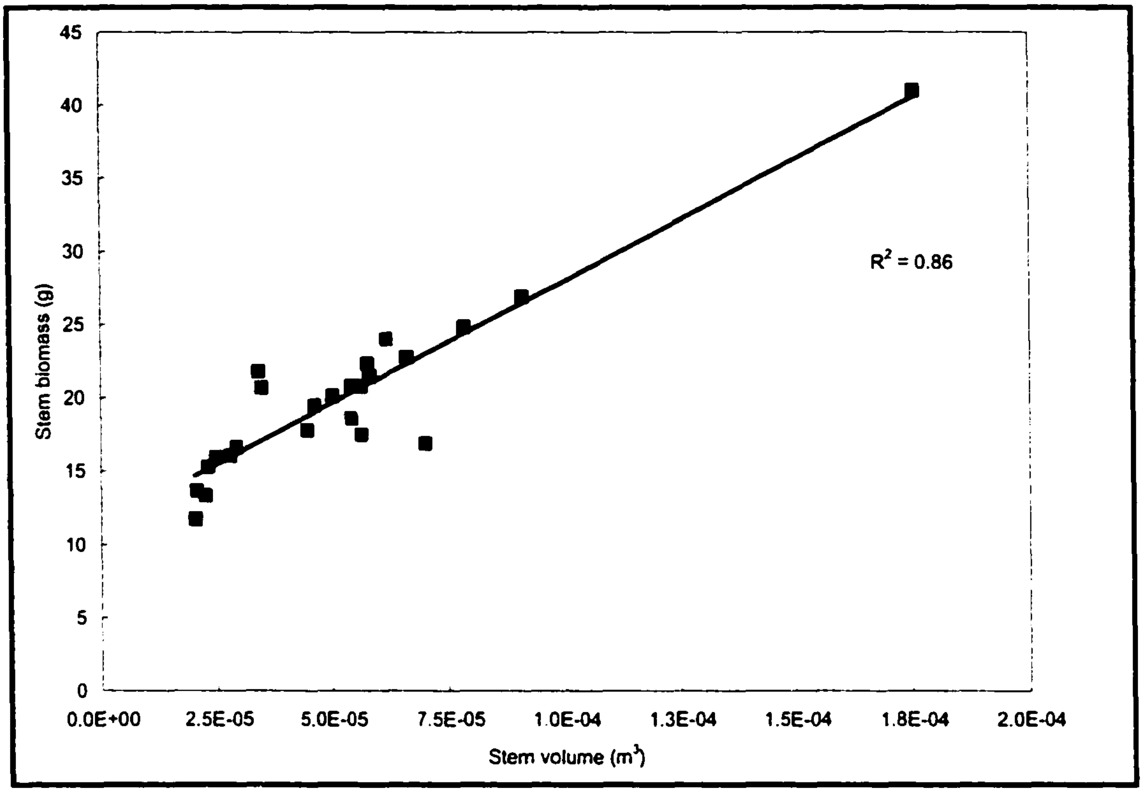

Figure 2.5. Linear relationship between the volume of the stems (below-water) and the biomass of the stems from the data set collected in June.

(iii) Calculated total below-water biomass of the stems within a quadrat

The total below-water biomass of the stems within the quadrat, B_{si}, was calculated as follows:

$$B_{si} = n_{si} \times b_{si} \qquad \text{Equation 2.5}$$

where n_{si} is the number of stems within a quadrat; n_{si}. The number of stems within a quadrat was calculated based on the data set of June and subsequently used as a mean stem density for the other months. The use of a mean stem density was based on the assumption that (1) there was no significant difference between months for the mean stem density of the aquatic plants (Piedade et al., 1993), (2) there was no significant difference ($p<0.05$) of the mean canopy cover between months, i.e. approximately the same number of plants exist within the quadrat and, (3) a more subjective inference, but still valid, field observations suggested that the plant density was approximately constant all year around, except for the low water season when the new stems were added to the population.

The variance of the estimated B_{si} was calculated using the double sampling technique (Cochran, 1963). This technique is used when a parameter is estimated by the regression of two other parameters with a high coefficient of correlation. This technique has been used successfully to estimate biomass of grassland (Francis et al., 1979), intertidal rockweeds (Pielou, 1981), and freshwater emergent aquatic vegetation (Lieffers, 1983, Giroux and Bédard, 1987). Finally, the interval of confidence of B_{si} was estimated (Coloquhoum, 1971; Pielou, 1981).

For August (falling water), because of the impossibility of estimating the total length of the stem (item i), the corrected below-water biomass was estimated by applying the average growth rate of the pervious months (1.105) to the biomass of June. This growth rate compared favorably with those observed by Piedade et al, 1992 and 1993 for *E. polystachya.*

Echinochloa polystachya

(i) Calculated submerged length of the stem

In general, for this species, regression equations between stem length and depth could not be calculated because either the number of samples was not adequate or at a given depth the stem lengths were approximately the same. Therefore, it was assumed that the relative length of the stem was a proportion of the depth. It is understood that this was a rough assumption. However, it was the only feasible option due to the limitations of the data set.

(ii) Calculated below-water biomass of the stem and total below-water biomass within a quadrat

The same approach of item (ii) and (iii) of *H. amplexicaulis* was adopted to calculate the below-water biomass of a stem and the total below-water biomass of the stems within a quadrat. This approach was possible due to the cylindrical shape of the stems of this species. For August (falling water), because of the impossibility of estimating the total length of the stem based on depth, the corrected below-water biomass was estimated by applying the average rate of growth of this species (1.22) to the biomass of June. This growth rate compared favorably with those observed by Piedade et al., 1992 and 1993 for *E. polystachya*. Table presents the final equations for estimating below water biomass of *E. polystachya*.

Paspalum repens

P. repens is probably one of the most difficult species for estimating below water biomass due to the nature of its development within the course of the year. As the water rises the new stem starts to grow and soon detaches from the bottom. On each node an aerial shoot and a bunch of submerged roots are formed. Junk, (1970) described details of the growth cycle of this species and also the relation between age of the population and the number of shoots per stem length. The general characteristics for a population of *P.*

rapens developing in a *várzea*-lake with a continuous connection to the main river are as follows: (1) as the population gets older the stem length increases and the number of shoots per stem length decreases, i.e. the stem length between shoots is longer; and (2) for the high water season, the number of shoots per m^2 are on average 60 shoots and it changes according to the growth stage. These differences show the complexity of *P. repens* populations, making it difficult to estimate total biomass of this species. A combination of the observations reported by Junk (1970) and the collected field data in June was used to estimate a rough number for below-water biomass of *P. rapens*. Three major assumptions were considered so that the collected data could be used in conjunction with the data of Junk (1970).

1. The study area is characterized as a *várzea*-lake with high fluctuations in water level and with continuous connection to the main river (Junk, 1970);
2. *P. rapens* in the study area has the same growth pattern as that reported by Junk (1970) for similar biotope and high water season. For the reasons of simplification, the mean number of shoots per 10 meters of stem length estimated by Junk, (1970) was used for estimating the total length of the stem per m^2; and
3. the last point is more an observation than an assumption. The measured average below-water dry biomass of one meter of stem ($4.6gm^{-2}$) was very similar to the average value ($4.5gm^{-2}$) measured by Junk (1970) for well developed populations during high water season.

Based on these assumptions and the data set measured in June, the below water biomass of the stems was calculated.

(i) Calculated the length m^{-2} of below-water stem

The stem length per m^2 (L_{si}) was estimated as follows:

$$L_{si} = (n_{si} \times 10) / n_s \qquad \text{Equation 2.6}$$

where n_{si} is the measured number of shoots m^{-2}, and n_s is the mean number of shoots per 10 meters of stem length for populations of *P. repens* measured by Junk (1970).

(ii) Calculated the below-water biomass of the stems m^{-2}

The below-water biomass of the stems (B_{si}) was estimated as follow:

$$B_{si} = L_{si} \times b_{spi} \qquad \text{Equation 2.7}$$

where b_{spi} is the dry biomass of 1 meter of below-water stem of *P. repens*. For June, b_{spi} was measured. For April, May, and August, b_{spi} was estimated through the regression equation between volume and biomass of 1 meter of below-water stem measured in June (R^2=0.99), significant to 95% level. Table 2.1 summarizes the equations developed for each species. These equations were developed through the data collected in June and subsequently used for estimating the below water biomass of the other field campaigns. The final total below water biomass is presented in Appendix I.

Table 2.1. Equations for estimating below water biomass

Species	Stem length	Stem biomass	Total stem biomass
H. amplexicaulis	$L_{si}=(1.2606 x d_i) - 0.4226$ $R^2=0.96$ (n=25)	$b_{si}=(166848 \text{ x } v_{si})+11.292$ $R^2=0.86$ (n=25)	$B_{si}=n_{si} x b_{si}$
P. repens	$L_{spi}=(n_{si} x 10)/n_s$	$b_{spi}=(267287 \text{ x } v_{spi})+0.8616$ $R^2=0.99$ (n=4)	$B_{si}=L_{si} x b_{spi}$
E. polystachya	$L_{si}=1.42 x d_i$	$b_{si}=(35536 \text{ x } v_{si})+59.073$ $R^2=0.86$ (n=3)	$B_{si}=n_{si} x b_{si}$

L_{si} is the total length of a submerged stem at site *i*, d_i is the depth at site *i*, b_{si} is the below-water biomass of a submerged stem, v_{si} is the volume of a submerged stem, n_{si} is the total number of submerged stems per m^2, and B_{si} is the total below-water biomass of the stems per m^2. For *P. rapens*, L_{spi} is the total length in meters per m^2, n_s is the estimated value of number of shoots per 10 meters of stem length measures by Junk, (1970), b_{spi} is the below water biomass of 1 meter of submerged stem of *P. rapens*, and v_{spi} is the volume of 1 meter of submerged stem of *P. rapens*.

2.2.2.3. Carbon content of the aquatic vegetation

Samples of the most frequently observed plants in the area were collected for carbon content determination. In the laboratory, the plants were dried at 50°C until constant weight and then ground in a mill (#42 mesh). The samples were analyzed at the Chemical Services Laboratory of the Pacific Forest Center, BC, Canada, using the LECO CR-12 carbon analyzer (accuracy of ±1 % of the carbon content). 0.2g of each sample were then combusted in oxygen at 1350°C, the CO_2 gas was measured by an infrared detector and the percentage of carbon calculated. The results are presented in Appendix II.

2.2.3. Visual observations and aerial photos

The stand height and the dominant species of an area of approximately 100m around the sampled point were visually determined (Figure 2.6). The geographic coordinates of each sample site were recorded with a Global Positioning System (GPS), and photographs north, south, east and west of the point were taken. This information was important for evaluating the homogeneity of the sample sites in relation to the resolution of the satellites. A photographic survey (hand-held 35mm camera) of the common flooded-trees, land-trees, floating-aquatic plants, rooted-aquatic plants, and pasture/agriculture areas was performed. These data were very useful in identifying the sampled areas on the SAR images and to help on the interpretation of the aerial photographs.

Aerial photos were acquired at 1:20,000 and 1:15,000 scale at high and rising water seasons, respectively, of selected areas of the floodplain (Figure 2.2). The interpretation of the aerial photos was intuitive because of the photo interpreter's familiarity with the study area. This data set was used as a reference for the identification of training areas during the classification procedure and the identification of the location of the sample sites.

Site	GPS coordinates	Data	Time
#2	2°22'10.7"	09.06.1999	11:30
Piapo	54°25'15.9"		

Wind: Yes	Temperature: 30°
Waves: No	Rain: No

	Species	Phenology	Height (m)
North	water	water	
East	*H. amplexicaulis*	flowering	1.5
South	*H. amplexicaulis*	flowering	1.5
West	*H.amplexicaulis*	flowering	1.5

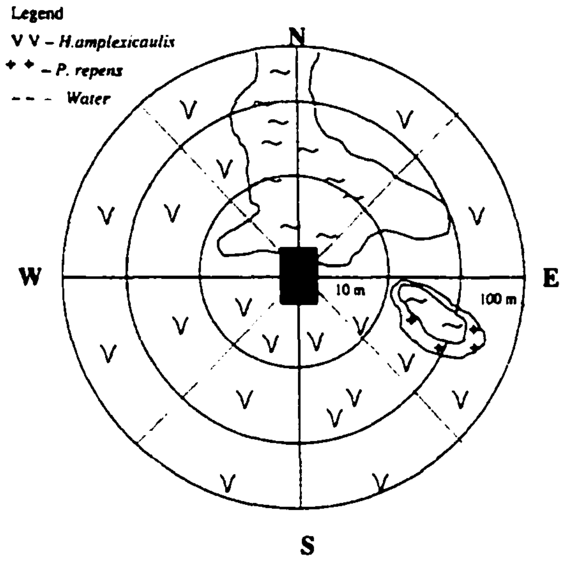

Figure2.6. Visual observation diagram

2.2.4. Water level and precipitation data

River levels and precipitation for the period of study were obtained from the Brazilian Institute of Hydrology (ANEEL), and the Brazilian Institute of Hydrography and Navigation (DHN). The data were collected at Óbidos (Amazon River), located 200 km Northwest of the study site, and at Santarém (Tapajós River), located 20 km Southwest of the study site. The water levels of both the Amazon (Figure 2.7) and the Tapajós Rivers (Figure 2.8) influence the inundation patterns of the study site. Both rivers show similar patterns of water variation. A predictable monomodal cycle in which higher and lower water levels occurred in May/June and October/November, respectively. The predictability of the water cycle of the Amazon River and its tributaries is well known (Irion et al., 1997). The amplitude of the water variation was similar at the Amazon River and the Tapajós River. For both rivers, the peak of high water occurred after the peak of precipitation and the maximum flood was approximately 7.5 m.

The curves of water level fluctuations of the Amazon River show not only a monomodal pattern but also similar amplitude of water variation along the hydrological cycle of the three years of study. Some dissimilarity is observed during low water stand. The lack of water level data of the Tapajós River constrains similar observation for the whole year; however, for the restricted available data, the amplitude of the curves was very similar. A 50 year survey of the hydrography of the Amazon River showed the same results, a monomodal cycle and similar amplitude of water level through the year (Soares, 1991).

The monomodal cycle and the similar amplitude of the curves of the three years in which data were acquired are important characteristics for allowing the assumption that the field campaigns followed one full growth cycle of the aquatic vegetation, starting in November and finishing in August (section 2.2.1).

The weather data (Table 2.2) were collected at the airport in Santarém (20 km southeast of the study area) for the day of SAR image acquisition. The weather conditions of the area proved to be uniform prior to, and during image acquisition, except for some higher levels of precipitation on the 16.05.96 and 20.03.97. It is important to emphasize that for these two days the precipitation occurred as heavy showers, as shown in the airport records. For this area, generally, most of the heavy showers occur during the evening and RADARSAT and JERS-1 acquire images in early morning. Furthermore, either no rain or light rain fell during the three days prior to the image acquisitions, for any acquisition day. Nonetheless, we can assume that the weather conditions on these two days were similar to the other acquisitions. The analysis of the GOES images acquired on the morning of the acquisition of the radar images showed that generally there was constant cloud cover in the area (Appendix III). Based on these data, it was concluded that the weather conditions did not interfere with the quality of the satellite images.

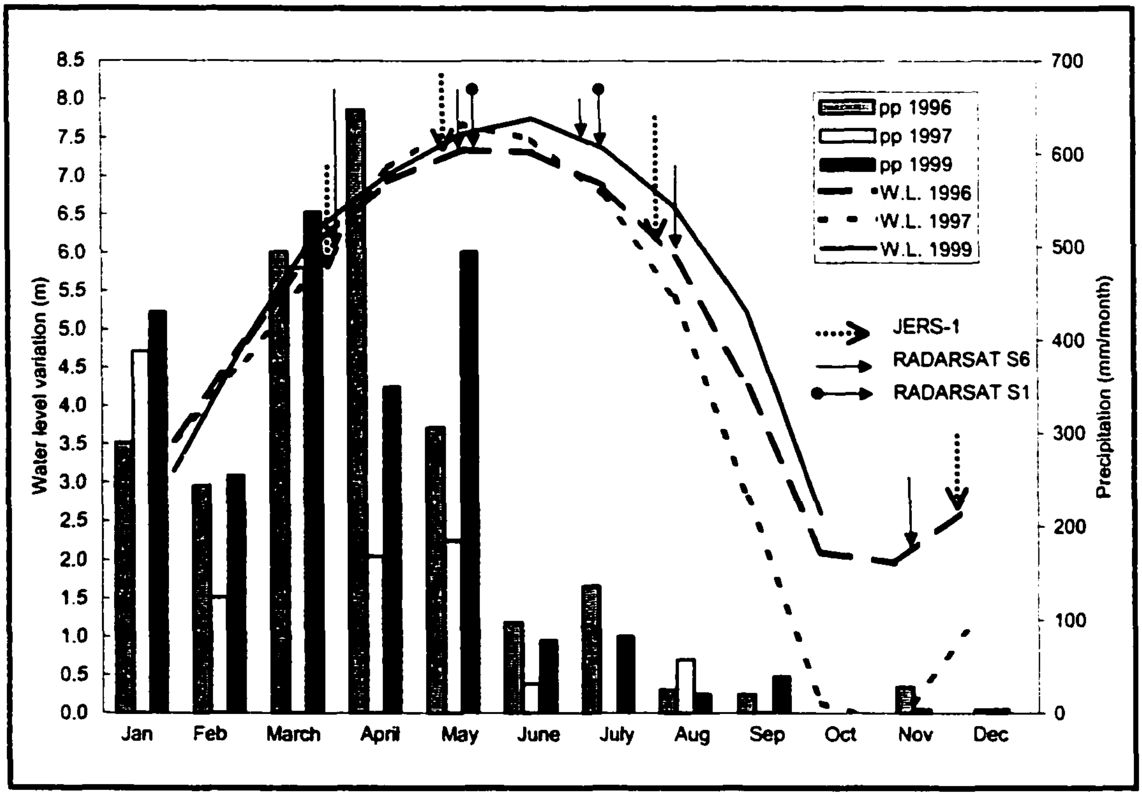

Figure 2.7. Water level fluctuations and precipitation data of the Amazon River. Arrows represent the acquisition date of JERS-1, RADARSAT S6, and RADARSAT S1 images. pp represents precipitation and WL water level fluctuation

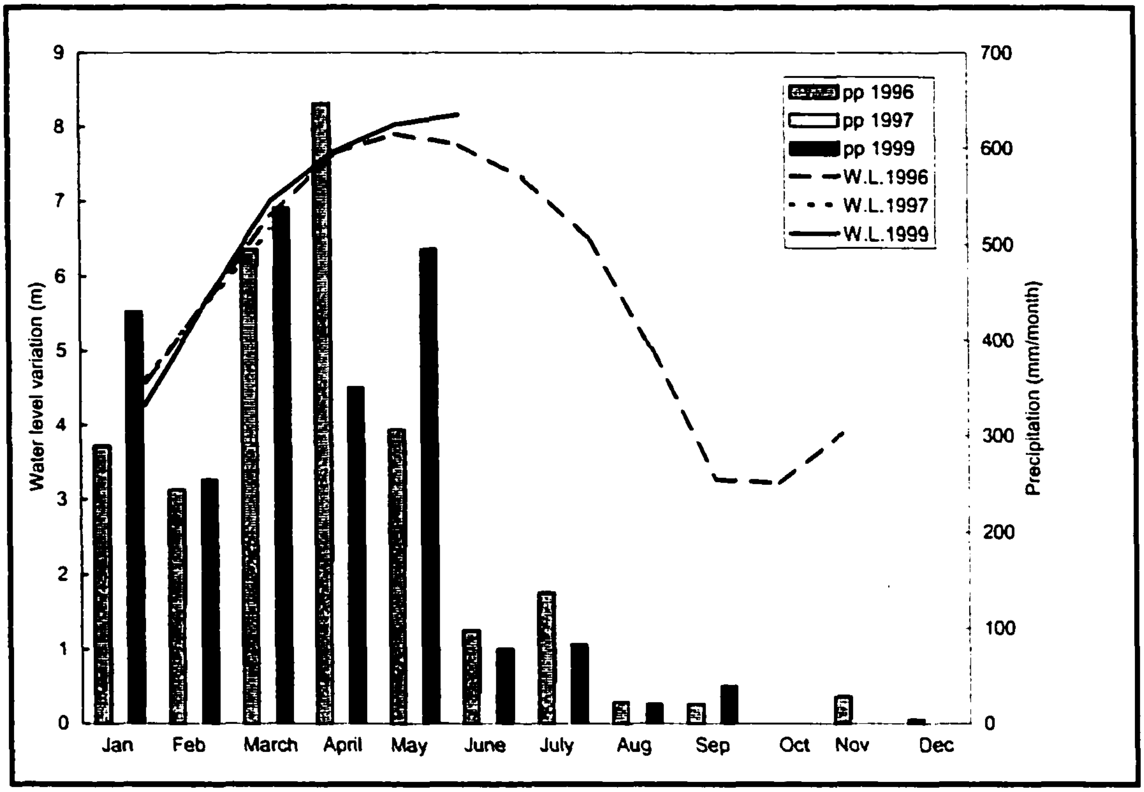

Figure 2.8. Water level and precipitation data of the Tapajós River. Acquisition of satellite images was the same as of previous figure.

Table 2.2. Detail of the weather conditions for the date of acquisition of the SAR images.

Date	Temperature (°C)	Relative humidity (%)	Precipitation (mm)	Duration of heavy showers (h)
16.05.96	26.1	87	40.8	3:18
27.05.96	27.5	79	3.7	0
30.05.96	26.8	82	7.4	0
07.08.96	28.5	64	0	0
12.08.96	28.4	71	0	0
11.11.96	29.9	67	0	0
22.12.96	29.5	72	0.3	0
20.03.97	26.1	88	50.2	5:40
05.04.97	26.9	84	3.2	0:35
05.06.99	27.5	80.1	0	0
08.06.99	26.6	84.5	1.0	0

2.3. Satellite Data

2.3.1. SAR characteristics

Radar sensors have been used for the last 34 years for terrain analysis. At the end of the 1970's SAR was aboard of a satellite platform for the first time. After this period several satellites, and shuttle missions started to operate with SAR systems, for instance, the Earth Resources Satellites 1 and 2 (ERS-1 and ERS-2), the Japanese Earth Resources Satellite (JERS-1), Almaz-1, SIR-C/XSAR shuttle mission, and RADARSAT-1. In years to come new systems will be launched, such as RADARSAT-2, RADAR-1, Cosmo/SkyMed series, ALOS series, ENVISAT, and IRS-3 (Glakin, 1998). RADARSAT-1 and JERS-1 acquired the satellite images examined in this project. The following are the general description of these two satellites.

RADARSAT

RADARSAT is a Canadian satellite launched in November 1995. The satellite has a near-polar, sun-synchronous orbit of 798 km of altitude. It crosses the equator at dawn (descending orbit) and dusk (ascending orbit), and has a repeat cycle of 24 days. It is equipped with a right-looking pointable Synthetic Aperture Antenna (15 x 15 m) that acquires data in 5.3 GHz (C-band, 5.6cm of wavelength), and the transmission and reception are both at horizontal polarization (HH). The pointability characteristic of the antenna allows RADARSAT to acquire images at different incidence angles and swaths (different image modes); other SAR satellites acquire images in only one mode, i.e. a specific incidence angle and swath. Table 2.3 presents the general characteristics of the different image modes of RADARSAT (RADARSAT Illuminated, 1995).

Table 2.3. General characteristics of RADARSAT data.

Image mode	Incidence angle (°)	Resolution (m)	Pixel spacing (m)	Image size
Fine mode(5 beams)	37-48	~ 8 x 8	6.25 x 6.25	50 x 50
Standard mode(7 beams)	20-49	~ 24 x 27	12.5 x 12.5	100 x 100
Wide mode(3 beams)	20-45	~ 28 x 27	12.5 x 12.5	150 x 150
ScanSAR narrow(2 beams)	20-46	~ 56 x 65	25 x 25	300 x 300
ScanSAR wide(2 beams)	20-49	~ 98 x 107	50 x 50	500 x 500
Extended mode(6 beams)	49-59	~ 19 x 27	12.5 x 12.5	75 x 75
Extended mode(1 beam)	10-23	36 x 27	12.5 x 12.5	170 x 170

Incidence angle is for near range and far range, respectively; resolution, pixel spacing, and image size are for range x azimuth; all the information is for ground range path image mode (SGF). Path images are corrected for systematic errors related to satellite movement, SAR instrument and processor, and data reception.

RADARSAT is a fully calibrated system, i.e. the images are radiometrically and geometrically calibrated. The radiometric calibration refers to both, (i) the electrical stability of the radar sensor, so that the repeatability of the reflectivity measurements is preserved, and (ii) the stability of the electrical signal when compared with a known radar reflectivity, such as transponders, corner reflectors, and the Amazon rainforest. These are referred to the relative radiometric accuracy and the absolute radiometric accuracy, respectively. At present RADARSAT has an overall accuracy (relative and absolute accuracy) of less than 1dB (Hawkins and Srivastava, 1999), which is within the minimum accuracy requirement for monitoring some aspects of the Earth's surface. The SAR overall calibration requirements for vegetation mapping and monitoring is within 1dB; other geophysical parameters have different calibration requirements (Freeman, 1992).

The geometric accuracy also has two components; (i) relative accuracy (errors within the image), and (ii) absolute accuracy (errors referenced to a coordinate system).

The overall geometric accuracy for standard image modes is approximately 50 m, assuming a flat terrain with no elevation differences (Srivastava et al., 1997).

JERS-1

The Japanese SAR satellite, JERS-1 (Japanese Earth Resources satellite), was launched in 1992 and operated until 1999. JERS-1 had a near-polar, sun-synchronous orbit of 568 km of altitude. It crossed the equator at approximately 10:30 am (descending orbit), local time, and had a repeat cycle of 44 days. It was equipped with a right looking Synthetic Aperture Antenna (12 x 2.4 m) that acquired data at 1.25 GHz (L-band, 23.5 cm of wavelength), and the transmission and reception were both at horizontal polarization (HH). The images were acquired in a nominal incidence angle of 35° at the swath center and over an 80 km swath width. JERS-1 was a fully calibrated system; the overall radiometric accuracy was between 1 and 1.8 dB over the satellite mission life, and the overall geometric accuracy was approximately 100m (Shimada, 1996), which was less accurate than the accuracy reported for RADARSAT. A test of the multi-temporal, and within image radiometric stability of the acquired JERS-1 images determined that the data were suitable for vegetation monitoring and mapping, which coincides with the findings of others (Luckman et al., 1997; Rosenqvist, 1999).

2.3.2. Acquisition of SAR data

RADARSAT and JERS-1 images were acquired over the study area at different periods in 1996, 1997, and 1999. The different satellite data were selected to evaluate characteristics such as wavelength and incidence angle of acquisition for estimating biomass and mapping of aquatic vegetation. The date of acquisition was timed to coincide with the field campaigns. JERS-1 data could not be acquired in June 1999 because the operation life of the satellite ended before that period. The RADARSAT data were acquired and calibrated by the Canada Center of Remote Sensing (CCRS) at the Gatineau receiving station in Canada. The images have the following characteristics: single beam detected products, ground range, 16 bit unsigned, and geocoded standard resolution. JERS-1 data were acquired and calibrated by the Japanese Space Agency (NASDA), and have the following characteristics: ground range, 16 bit unsigned, and geocoded image products with correction to the ellipsoid of the Earth. The major characteristics of the data set are outlined in Table 2.4.

Table 2.4. Characteristics of the satellite data

Satellite	Date of acquisition (D.M.Y)	Incidence angle (degrees)	Coverage (km)	Swath mode	Band/Polarization	pixel spacing (m)	resolution (m)	number of looks
RADARSAT	27.05.96	41-46	100x100	S6descending	C/HH	12.5 x 12.5	26x27	1x4
	30.05.96	20-27	100x100	S1descending	C/HH			
	07.08.96	41-46	100x100	S6descending	C/HH			
	11.11.96	41-46	100x100	S6descending	C/HH			
	05.04.97	41-46	100x100	S6descending	C/HH			
	05.06.99	20-27	100x100	S1descending	C/HH			
	08.06.99	41-46	100x100	S6descending	C/HH			
JERS-1	16.05.96	~35	75x75	descending	L/HH	12.5 x 12.5	26x27	3
	12.08.96							
	22.12.96							
	20.03.97							

3. AQUATIC VEGETATION

Since most published research is performed in the central Amazon region, aquatic vegetation communities from this region are well described. The species diversity of the central Amazon has been the subject of study for at least 10 years. *E. polystachya* is the dominant species (Piedade et al., 1991, 1997); however, studies of lower Amazon describe productivity and species diversity of aquatic vegetation that are different from the central Amazon (Luciano, 1997; Camarão et al., 1998). The main factors that contribute to these differences are (1) the human use of the land, (2) the water level variation, and (3) the geomorphology of the area. The conversion of flooded forest into pasture, as is the case in some areas of the lower Amazon, allows the colonization of large monoespecific stands of aquatic vegetation, for instance, *H. amplexicaulis*. Areas where large and quick variability of the water level occurs and depositional and erosional processes are intense, for example, the islands along the central Amazon region, require fast growing species, such as *E. polystachya*, or free-floating species, such as *P. repens*. Differences in the amount of area covered by aquatic vegetation and flooded forest along the Amazon floodplains are observed. LANDSAT data revealed that the upper Amazon is dominated by flooded forest, the central Amazon has an even mix of flooded forest and aquatic vegetation, and in the lower Amazon (downstream) aquatic vegetation dominates (Novo et al., 1997). Quantification of these areas on a seasonal/regional basis has only been possible in the last years with the advent of stable airborne SAR (Hess et al., 1995) and satellite SAR systems (Costa et al., 1998).

Measuring the productivity/diversity and quantifying of the area covered by aquatic vegetation and flooded forest are not easy tasks; however, it is a requirement for understanding the biogeochemistry of the Amazon region. It is now recognized that to understand the Amazon on a regional and seasonal scale researches must incorporate large quantities of field and remote sensing data (Junk, 2000, Melack, 2000). The main aspects of the seasonal characteristics of the aquatic vegetation are the focus of this chapter, including (1) species distribution and canopy characteristics, and (2) biomass and productivity. These are not only requirements for understanding the seasonal characteristics of the aquatic vegetation, but also for interpreting the satellite data, which is the focus of chapter 4.

3.1. General Characterization of the Areas Colonized by the Aquatic Vegetation

At high water stand, the areas colonized by the aquatic vegetation generally showed a stable minimum stratification in the water column due to the thermal density differences (1°C) of the top and bottom of the water column. The average temperature of the surface water was 29°C for most of the year, except at the beginning of the rising water period when the temperature is higher. The bottom temperature was on average 28°C. Simultaneously, a stratification existed with low dissolved oxygen below the euphotic zone, where the oxygen production by phytoplankton is restricted by low light conditions and the oxygen consumed by organic decomposition is elevated (Junk, 1984). The oxygen levels were on average 2.5 mg l^{-1} and 1.5 mg l^{-1} at the surface and bottom, respectively. These levels were much lower in areas where dense stands of aquatic vegetation prevented any water circulation (1 mg l^{-1} and 0.1 mg l^{-1} at surface and bottom, respectively). The same anoxic environment is observed in other lakes of the Amazon floodplain (Furch and Junk, 1997). At the beginning of the rising water period, the oxygen level was on average 10 mg l^{-1} and the temperature 33°C, a fully-mixed water column was observed due to the low depth and wind mixing effect. The water pH was approximately neutral (pH~6.5) all year, except in areas where the inflow from the *igarápes* was large (pH~5). *Igarápes* are the floodplain areas where the water is rich in humic acids. Emergent aquatic vegetation was not found in the *igarápes*.

Lago Grande shows water characteristics similar to other Amazon floodplain lakes (Melack and Fisher, 1990; Furch and Junk, 1997). Table 3.1 presents the yearly general physio-chemical characteristics of the water column of the areas colonized by aquatic vegetation. The general characteristics of these areas were temperatures close to 30°, anoxia all year around except for November, and neutral pH (which is typical of the Amazon River).

Table 3.1. General physio-chemical characteristics of the water column

	November	April	May	June	August
Temperature-surface	33	29	29	30	29
Temperature-bottom	33	28	28.5	28.5	28
Oxygen - surface	10	3	2	3	4
Oxygen-bottom	10	1.6	1	2	2
pH	6.8	6	6.4	6	6.6

Temperature in °C and oxygen in mg l^{-1}.

3.2. Aquatic Vegetation Distribution

The most common species of aquatic vegetation found in the study area were identified according to the collection organized by Luciano (1997) for the lower Amazon region. The seasonally flooded area contains a wide variety of aquatic vegetation. Dominant among this vegetation was the family Poaceae represented by the following herbaceous plants: *H. amplexicaules, P. repens, E. polystachya,* and a few occurrences of *P. fasciculatum, Orzya* spp., and *Panicunum chloroticeu*. In addition, the family Malvacea with the species *Hibiscus furcatus* and the family Aracea with the species *M. arborescens* (*aninga*) were also present. *H. amplexicaulis, E. polystachya,* and *P. repens* were dominant in 53%, 26%, and 6%, respectively, of the total sampled sites. The other 15% of the sampled sites were dominated by *H. furcatus, P. fasciculatum*, and mixed vegetation. Among the grass-like aquatic vegetation, *H. amplexicaulis, E. polystachya,* and *P. repens* were dominant in 65%, 28%, and 7% of the sampled sites, respectively.

In terms of aquatic vegetation zonation, the plants were distributed according to their preferred habitat and adaptations to the flood conditions, as it is common for inland freshwater wetlands (Mitsch and Gosselink, 1993). The prevailing distribution of the plants was as follows. Emergent rooted species, such as *H. amplexicaules* and *E. polystachya* colonize most of the wide littoral margin of the lake, where the mean depth is approximately 3.5±0.5 m (mean±1SD) during the highest water level stage and dries up in October, when the water level is at its lowest. These are aquatic species with a terrestrial phase and a large distribution along the Amazon floodplain, most specifically in *várzea* lakes and areas of intensive sedimentation (Junk and Piedade, 1993). These species degenerate when the sediment becomes exposed (low water), and new plants start to grow as the water level rises. In the study area, *H. amplexicaules* was the predominant species, forming large monospecific stands. *E. polystachya* also forms monospecific stands in areas closer to the Amazon River, a preferential habitat for this species because the inflow of nutrient-rich waters is higher (Junk and Piedade, 1993). In the study area, *E. polystachya* was not as dominant as it is in islands along the central area of the Amazon River (Piedade et al., 1991).

P. repens, also an emergent aquatic plant, colonizes a similar depth range (3.8±1.7m) during high water periods, and totally dies during the dry season. This species has developed a different adaptation; it can change from rooted to free-floating when the water is deeper (Junk and Piedade, 1993), allowing its presence in the outer fringe of the vegetation populations, between the rooted species and the open waters of the lake where depths reach 6 meters. Strong currents and wind can carry away marginal stands of *P. repens*. It was very common to see floating mats of *P. repens* either driven by the prevailing wind (direction Northeast) on the Lake, or following the currents to the Amazon River through the Gurupatuba River (field observation and comments from local people).

P. fasciculatum, a rooted-emergent semi-aquatic plant, typically occupies the shallow (0.5m depth) flooded edge of fluvial corridors. It dominates areas of higher elevation and intensive sedimentation (Junk and Piedade, 1993), surviving all year round. *Hibiscus bifurcatus (manhorana)* is a broad-leaved terrestrial plant that survives long periods of inundation (Junk and Piedade, 1993). It was most common in areas of human use and at a mean depth of 3.5 m. *M. arborescens*, a tall (3m of above-water height) tree-like semi-aquatic plant, formed large monospecific elongated or round stands in areas that keep some soil moisture even during the low water periods. This species survives all year around and it is the last in the succession process before the swamp forest is established (Junk and Piedade, 1997). In the Southwest region of the study area the succession process is clearly present, and alternating corridors of *M. arborescens* and swamp forest are observed.

Figure 3.1 and Figure 3.2 show a schematic representation of the zonation of the most common aquatic vegetation in two distinct environments of the study area: (i) a fluvial lake, which is a more protected area where the depth gradient is less step, and (ii) a fluvial channel, where higher currents, sedimentation processes, and the direct influence of water from the Amazon River are observed. Observe that *H. amplexicaulis* is always present in more protected areas within the lake, whereas *E. polystachya* and *P.fasciculatum* occur in areas where the influence of the water of the Amazon River is increased. *P. repens* formed narrow stands at the outer fringe of the aquatic vegetation at deeper water levels. Ground photographs of some of the species found in the study area are presented in Figure 3.3; note the high density of *H. amplexicaulis* stand.

Between open water and emergent species, floating-leafed species might grow. Typical floating-leafed species were *Salvinia* spp. and *Eichhornia* spp.; however, their presence was not as dominant as the Poacea. *Salvinia* sp. some times occurred under the canopy of Poacea and *H. furcatus*. Submerged species were not found in the area due to the low availability of light underwater, shown by the lower Secchi depth of most areas of the lake (on average 0.7 m during high water). In some areas within the *igarápes*, where the suspended sediment was low, a few species of submerged aquatic plants were found, but not in abundance.

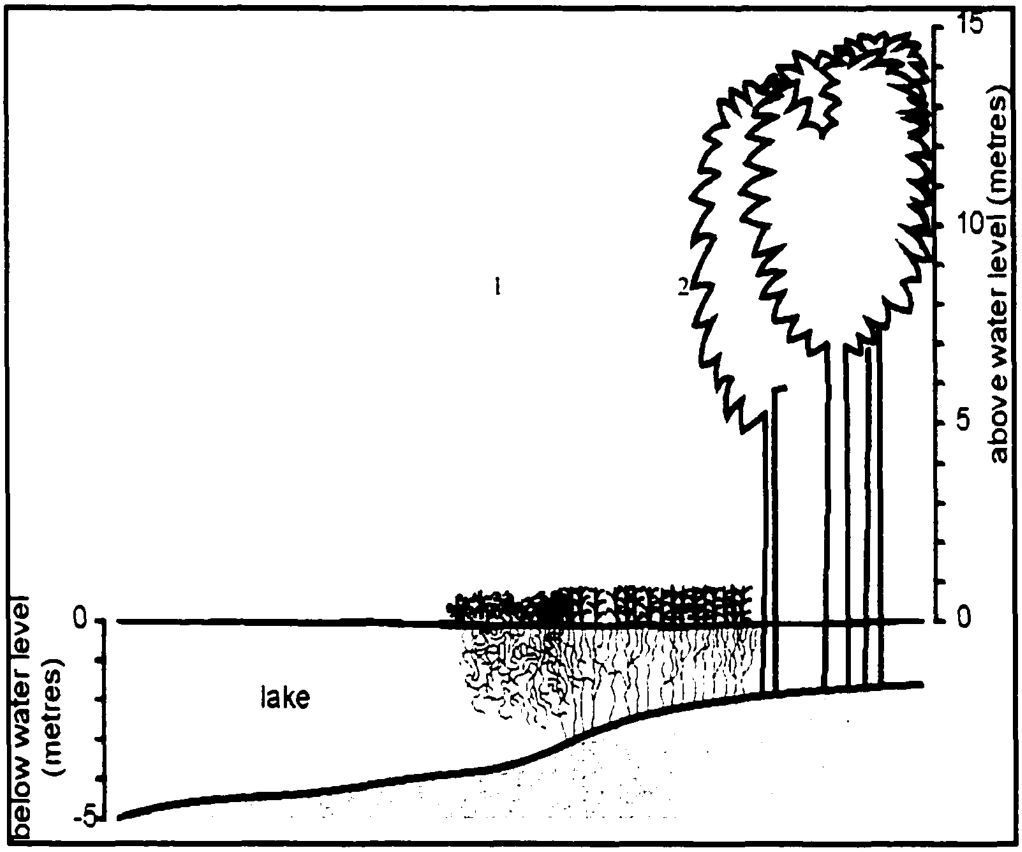

Figure 3.1. Schematic representation of the distribution of aquatic vegetation in the study area – fluvial lake. 1- *P. repens*; 2- *H. amplexicaulis*.

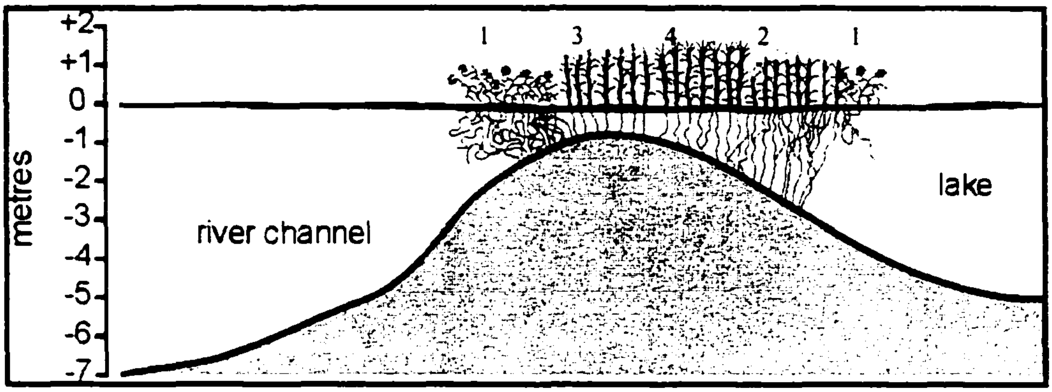

Figure 3.2. Schematic representation of the distribution of aquatic vegetation in the study area-fluvial channel. 1- *P. repens*; 2- *H. amplexicaulis*; 3- *P. fasciculatum*; 4- *E. polystachya*.

(a). *E. polystachya* (b) *H. amplexicaulis*

Figure 3.3. Ground photographs of some typical stand of aquatic vegetation found in the study area

3.3. Biophysical Properties of the Aquatic Vegetation

The following results and analysis focus on the dominant species in the study area namely, *H. amplexicaulis*, *P. repens*, and *E. polystachya*. The characteristics of the architecture of these species are exhibited in Table 3.2 Note in Table 3.2 that at the low water period, for the three species, the values are either not available or they are the same for each parameter. The identification of the species during low water stand was not possible. The vegetation exhibited uniform growth (0.2 m height above water) as the water rose (0.3 m depth), yielding the same characteristics. Therefore, it was assumed that, regardless of the species, the grass-like aquatic vegetation presented the same biophysical properties.

A comparison among the three species showed that *E. polystachya*, the least abundant species, had the most developed above-water canopy; *H. amplexicaulis*, the most abundant species, and *P. repens* showed similar size in their above water structures, leaves and stems. At high water, the mean number of plants m^{-2} were 111 (26), 27 (6), and 84(58) of *H. amplexicaulis*, *E. polystachya*, and *P.repens*, respectively (values between brackets correspond to standard deviation of the mean). The high density and low diversity of species are typical characteristics of aquatic vegetation of the Amazon floodplain (Junk and Piedade, 1993).

The above water structure of the stems and leaves of *H. amplexicaulis*, in general, were not different from April onwards (Table 3.2). By April, when the plants were flowering, they had a fully developed canopy. The stem of the plants grew continuously (Figure 3.4), reaching a maximum below-water length of 4m, and new leaves developed at a very high rate following the rising water, so that a canopy of photosynthetic organs of approximately 0.8m height and five 23cm long-green leaves were kept constantly above the water. Figure 3.4 illustrates the constant length of the above water stem and the continuous growth of the plant represented by the increased length of the submerged stem following the water level.

Remnants of the most recent submerged leaves of *H. amplexicaulis* could be observed in the water; these remnants were always in a very advanced stage of decomposition, as observed in other regions of the Amazon. The high rate of decomposition of Amazonian aquatic vegetation was well documented by Howard-Willians and Junk (1976), and more recently by Furch and Junk (1997). According to the authors, more than 50% of the organic material (leaves) of the aquatic vegetation is lost in one month of submergence. One of the reasons for the fast decomposition is the high temperature of the water; it can reach 40°C in the central of the stands. Due to the rapid decomposition of the submerged leaves, the plants are required to grow new leaves very quickly, keeping the new photosynthetic organs above the water. Piedade et al., (1991) reported the same adaptation for *E. polystachya*, a highly productive C4 plant that colonizes large areas adjacent to the islands of the central Amazon. Similar decomposition rates are reported for fresh water marsh in North America (Mitsh and Grosslink, 1993) and for *E. polystachya* in the South of Brazil (Pompêo and Henry, 1998).

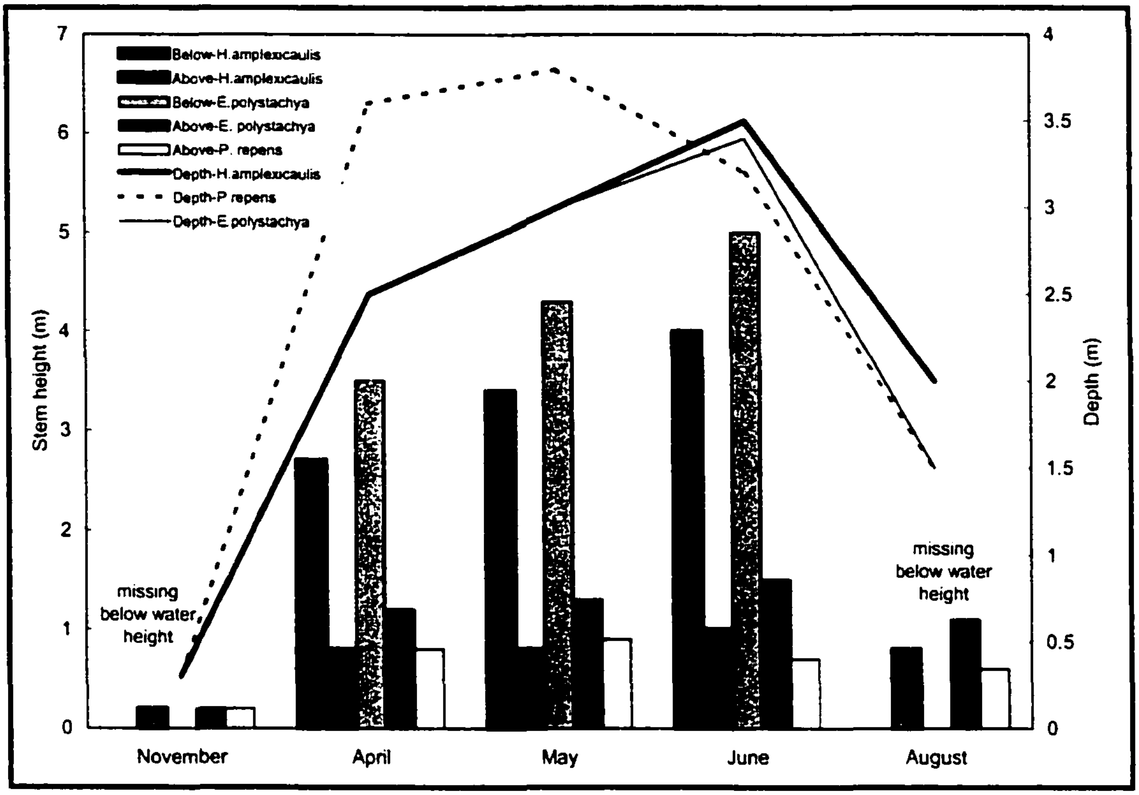

Figure 3.2. Above and below water mean stem length of *H. amplexicaulis*, *P. repens*, and *E. polystachya* recorded along the hydrological cycle.

H. amplexicaulis showed the most dramatic change of stem inclination, canopy cover (Figure 3.5), and water content (Figure 3.6) of the above water canopy during the high and falling water periods. By August, when the water level started to fall rapidly, the plants reached the senescent stage (yellow in color), the water content decreased (65%), and the stems bent (30° off nadir), changing from an almost vertical orientation (15° off nadir) observed at high water. At this point, the senescent plants of the large stands bent with no preferential orientation, making it difficult to see the water surface (canopy cover is approximately 90%- Figure 3.5). Except during the low water period, the leaves of this species kept approximately the same width and length during the life cycle. Likewise, the inclination of the leaves in relation to the stem was approximately constant, showing a mean angle of 40° with the stem and changing to a quasi-horizontal position towards the tip of the blade. This configuration of the five leaves with the stem results in a vertical span of approximately 40 cm occupied by the canopy structures. Given the high average density (111 plants m^{-2}), the vertical span, and the size of the canopy elements, it is easy to visualize the compactness of the stands (average canopy cover of 82%). When the water dropped (October), the plants became exposed to the sediment and degenerate. As the water rose (beginning of November), a new generation of plants started to grow by vegetative propagation. This life cycle is well described by Piedade et al. (1991 and 1992), for *E. polystachya.* According to the field observations, the same pattern of life cycle applies to other Poecea, such as *H. amplexicaulis* and *P.repens*, but not for *P. fasciculatum*, which is a terrestrial plant that survives periods of submergence (Junk and Piedade, 1993), and is well developed all year around.

Table 3.2. General biophysical characteristics of the aquatic vegetation

a. H. amplexicaulis

Characteristics	November	April	May	June	August
Water stage	Low	Rising	High	High	Falling
Depth (m)	0.3(0.2)	2.5(0.1)	3(1.3)	3.5(0.5)	2(0.3)
Stem					
Length above (m)	0.2(0.1)	0.8(0.1)	0.8(0.1)	1(0.2)	0.8(0.2)
Length below (m)	na	2.7	3.4	4.0	na
Diameter (cm)	na	0.5(0.1)	0.5(0.006)	0.3(0.009)	0.4(0.1)
Inclination (degrees)	na	29(6)	15(5)	~15	30(11)
Leaves					
Number	na	na	5(1)	5(1)	na
Length (cm)	na	22.5(0.2)	27(14)	22(8)	19(5)
Width (cm)	na	na	2(0.8)	2(0.9)	2(0.6)
Inclination (degrees)	na	84(3)	36(13)	~45	39(8)
Canopy cover(%)	78(7)	78(19)	75(15)	88(7)	89(7)
Water content (%)	81(2)	84(3)	80(4)	73(3)	65(6)
Phenology	establishment	flowering	flowering	flowering	senescence

b. *E. polystachya*

Characteristics	November	April	May	June	August
Water stage	Low	Rising	High	High	Falling
Depth (m)	0.3(0.2)	2.5	3	3.6(0.2)	1.5
Stem					
Length above (m)	0.2(0.1)	1.2	1.3	1.5(0.006)	1.1
Length below (m)	na	3.5	4.3	5(0.9)	na
Diameter (cm)	na	1	1.7	1.7(0.3)	1.8
Inclination (degrees)	na	15	20	~20	10
Leaves					
Number	na	na	8	7(1)	na
Length (cm)	na	61	46	87(6)	41
Width (cm)	na	3	3	3.5(0.5)	3
Inclination (degrees)	na	40	30	~30	20
Canopy cover(%)	78(7)	89	97	92(2)	76
Water content (%)	81(2)	83	84	84(2)	84
Phenology	establishment	flowering	flowering	no flowers	flowering/ senescence

c. *P.repens*					
Characteristics	November	April	May	June	August
Water stage	Low	Rising	High	High	Falling
Depth (m)	0.3(0.2)	2.6(0.5)	3.8(1.7)	3.0(0.5)	1.5(0)
Stem					
Length above (m)	0.2(0.1)	0.8(0.2)	0.9(0.2)	0.7(0.2)	0.6(0.1)
Length below (m)	na	na	na	na	na
Diameter (cm)	na	0.8(0.2)	0.5(0.01)	0.4(0.2)	0.45(0.007)
Inclination (degrees)	na	na	20(10)	na	38(11)
Leaves					
Number	na	na	7(1)	6(0.5)	na
Length (cm)	na	37(22)	24(7)	24(12)	15(2)
Width (cm)	na	2(1)	1.5(0.1)	1.5(0.7)	1(0.007)
Inclination (degrees)	na	20	45(16)	na	28(25)
Canopy cover(%)	78(7)	79(16)	89(8)	96(2)	87(11)
Water content (%)	81(2)	87(3)	80(3)	70(3)	76(2)
Phenology	establishment	flowering	flowering	flowering/ senescence	senescence

na means that the data is not available; values represent mean and one standard deviation of the mean in brackets.

Similar to *H. amplexicaulis*, the characteristics of the above water structures of *E. polystachya* (Table 3.2b) were kept constant during rising, high, and falling water stand. This species were, as a whole, larger than *H. amplexicaulis* and *P. repens*. The above water height was greater than 1 meter from April onwards. By June, the length of the submerged stem reached a value of 5 meters at areas where the local depth was approximately 3.5 m (Figure 3.4). The diameter of the stems was approximately 1.7 cm at high water stage, and the leaves reached a length higher than 0.5 m. During the same period, *E. polystachya* presented a density of approximately 27 plants m^{-2}; i.e. four times lower than the density of *H. amplexicaulis*. Furthermore, *E. polystachya* showed a larger number and size of leaves when compared with *H. amplexicaulis* and *P. repens*. For *E. polystachya,* leaves form a 30° angle with the stem, and change to a quasi-horizontal inclination towards the tip of the blade. The spatial organization of both leaves and stem results in a vertical span of approximately 40 cm. Although the density of this species is relatively low compared with the other species, the spatial organization and size of the above water canopy elements form very compact stands (canopy cover higher than 90% at high water stage). Field observations showed that by the end of the growth cycle (August) this species started to lose its flowering organs; however, the plants preserved their almost vertical orientation (10 degrees) and little dryness was observed when compared with *H. amplexicaulis*. (Figure 3.6).

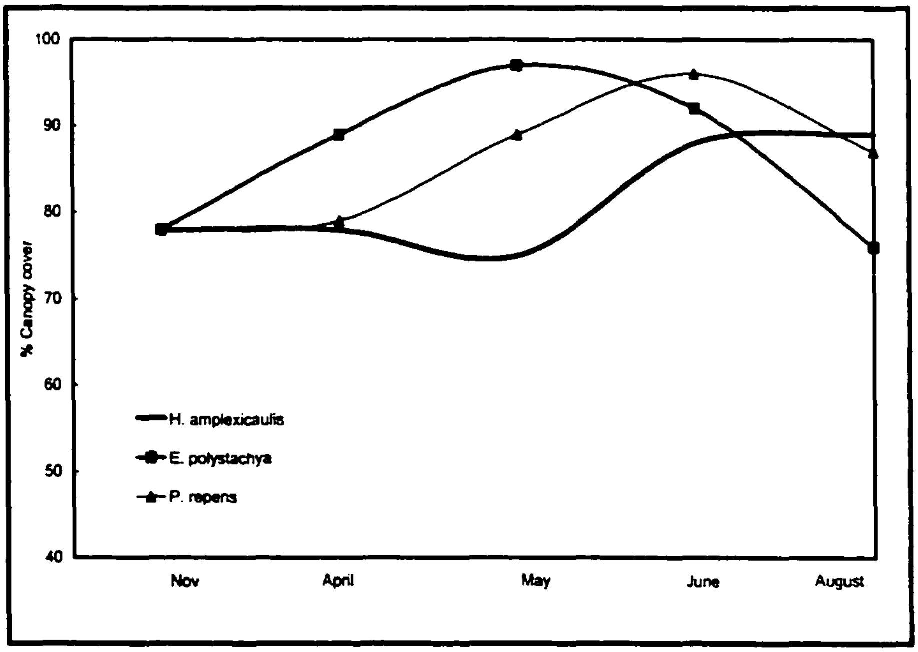

Figure 3.5. Canopy cover of the three most common species throughout the water cycle.

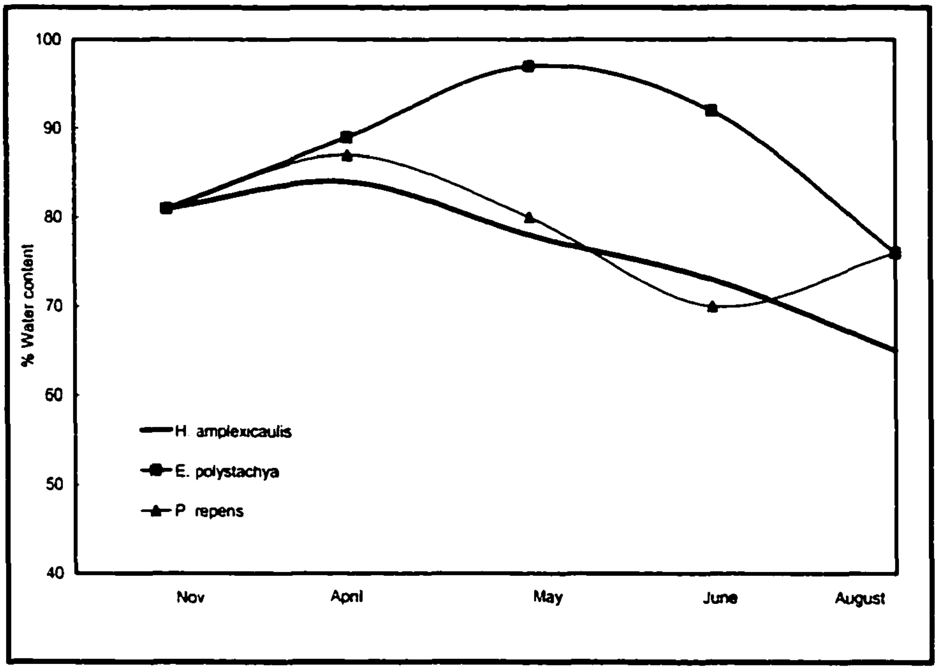

Figure 3.6. Water content of the three most common species throughout the water cycle.

P. repens is a smaller grass compared to *E. polystachya*; its structures are similar in size to *H. amplexicaulis*. However, *P. repens* has a very complex history in regard to canopy changes during its life cycle (Junk, 1970). By April, the young plants were creeping and in full blossom, the stems were thick (1 cm) and the leaves long (37 cm). By May and June, the plants reached maturity; the thin shoots were almost vertically oriented (20 degrees off vertical). The leaves were a little smaller (24 cm) than during the previous phase and formed a 45 degrees angle with the stem, and changed to a quasi-horizontal inclination from the central to the tip of the blade. During this period, the spatial configuration of the above water structures results in a vertical span of approximately 30 cm. Similar to the other species, the high density of the plants and the spatial configuration of their structures favour the formation of compact stands. By August, the plants started to dry (senescent stage) and the stems bent to 38° off vertical; the leaves became more vertically oriented (28° off vertical) and shorter (15cm) than in the previous phases. These observations coincide with the description of *P. repens* life cycle documented by Junk (1970).

In summary, the water level is a primary influence in the life cycle of the most common aquatic vegetation in the study area. In November, when the water started to rise, the plants grew steadily so that their photosynthetic organs were kept above the water. The above water canopy was mostly constant and formed very compact stands from April onwards. After August, the plants completed their life cycle and started disappearing (senescence). Subsequently, the soil became dry, and as the rainy season advanced a new generation of plants grew in November.

3.4 Below and Above Water Biomass of the Aquatic Vegetation

Table 2.1 presented the equations used for estimating the below-water biomass per species for April, May, June, and August. The equations were developed from data collected in June for estimating below-water stem length and below-water biomass of one stem for all *H. amplexicaulis*, *E. polystachya*, and *P.repens*. The equations, developed for estimating submerged stem length and biomass of *H. amplexicaulis,* were significant to the 95% confidence level. The reliability of the models developed for *H. amplexicaulis* were evaluated by selecting three random sets of samples and calculating the regression line for the remaining original data set. In general, more than 85% of the random samples fit within the 95% confidence bands of the best-fit line of the regressions. From this, the models were considered reliable and the biomass of the stems (b_{si}) of April and May were estimated based on these regression equations.

The variance of the biomass of one stem, b_{si}, was estimated by double sampling (regression equations), $V(b_{si})$, as given by (Cochran, 1963):

$$V(bi) = \frac{S_b^2 (1 - r^2)}{n_2} + \frac{r^2 S_b^2}{nsi} \qquad \text{Equation 3.1}$$

where S_b^2 is the variance of the stem biomass of the regression sample; r is the correlation coefficient of the regression; n_2 is the size of the sample used in the regression equation; and n_{si} is the number of stems within the quadrat. The variance of all stems within a quadrat, $V(B_{si})$, is given by (Coloquhoum, 1971)

$$V(Bsi) = n_{si}^2\, V(bi), \qquad \text{Equation 3.2}$$

and the 95% confidence interval for the estimated total biomass of stems within a quadrat is (Pielou, 1981):

$$Bsi \pm t_{0.025\ ,v}\, S(Bsi) \qquad \text{Equation 3.3}$$

with $t_{0.025}$ equal to 2.06 (24 degrees of freedom), and $S(B_{si})$ is the standard deviation of the estimated total biomass of stems within a quadrat. Table 3.3 presents the 95% confidence interval of B_{si} for *H. amplexicaulis*. The maximum estimated variability at 95% confidence interval is approximately 300 gm^{-2}, which is on average 14% of the estimated total below water biomass of the stems. Note that in Table 3.3 there is no confidence interval for November and August. For November, the below water biomass of the stems was assumed the same as the above water biomass (Piedade et al., 1991). For

August, the below water biomass of the stems was estimated based on the average growth rate of the previous months (1.105).

Table 3.3. Mean and the 95% confidence interval for below water biomass of *H. amplexicaulis* (gm^{-2})

Month	Mean below-water biomass of stems	Lower limit	Higher limit
November	91*	-	-
April	1872	1719	2025
May	2097	1944	2250
June	2231	2078	2383
August	2729	-	-

*the standard deviation of the mean is 93 gm^{-2}

For the other species, the small sample size did not allow either a reliability test of the models or an estimate of the variance of the biomass of the below-water stem to be performed; therefore, the estimates were considered caution estimates. However, the estimated values of below-water biomass of *E. polystachya* and *P. repens* (Table 3.4) are very similar to the values measured by Junk (1970) and Piedade et al., (1992, 1993). For *P. repens* of the central Amazon, during high water periods, Junk (1970) estimated a mean value of 320gm^{-2} of dry matter of below-water stem. However, recent estimates of total biomass of dense stands are considerably higher (Junk and Piedade, 1997). For *E. polystachya*, Piedade et al., (1991, 1993), reported a mean value of below water stem biomass of no more than 5000gm^{-2} and stem length of 9 meters during the period of highest water level in the central Amazon.

Table 3.4 presents the mean estimated below water, above water, and total biomass per species for November, April, May, June, and August. The below water biomass comprises the below water biomass of the stems and the biomass of the roots. Biomass of the subterranean roots is assumed to be 5% total biomass (Piedade et al., 1991; Junk and Piedade, 1997). For November (low water period), the below water biomass was assumed the same as the above water biomass (Piedade et al., 1992, 1993). At this period, the areas colonized by aquatic vegetation had either a mean depth of 0.3 ± 0.2 m (mean ± 1 standard deviation of the mean) or moist exposed soils where the aquatic vegetation was starting to develop. Appendix I presents the entire data set.

Table 3.4. Mean values of above water, below water, and total biomass of aquatic vegetation.

Month	*H. amplexicaulis*			*E. polystachya*		
	Above	Below	Total	Above	Below	Total
November	91(93)	100(103)	191(197)	91(93)	100(37)	191(70)
April	270(72)a	1985(257)a	2255(314)a	491	1959	2500
May	347(256)ab	2226(517)ab	2573(448)ab	1102	2713	3815
June	556(226)b	2378(653)b	2934(674)b	956(79)	2892(664)	3848(728)
August	590(200)b	2885(52)	3489(210)	418	4253	4671

Month	*P. repens*		
	Above	Below	Total
November	91(93)	151(156)a	241(250)
April	256(80)a	284(150)ab	539(213)
May	445(144)b	352(67)bc	797(192)a
June	403(115)abc	408(141)bcd	811(229)ab
August	307(5)abc	492(103)bcd	799(108)ab

The values are in gm^{-2} of mean dry biomass; values between brackets are one standard deviation (SD) of the mean; mean values without SD are due to the inadequate number of samples; for each column, means followed by the same letter are significantly equivalent at 95% confidence level according to the Welch test for independent populations (Snedecor and Cochran, 1980). Values of submerged biomass for August are adjusted for the decrease in the water level.

In general, for all the species, from November onwards the total biomass augmented steadily until August (Figure 3.7); the mean difference test showed that the significant differences ($p<0.05$) were mainly between the beginning and the end of the growth period, as shown by the letters in Table 3.4. In fact, these differences can be mostly attributed to the steady increase in the below water biomass from November to August (Figure 3.7).

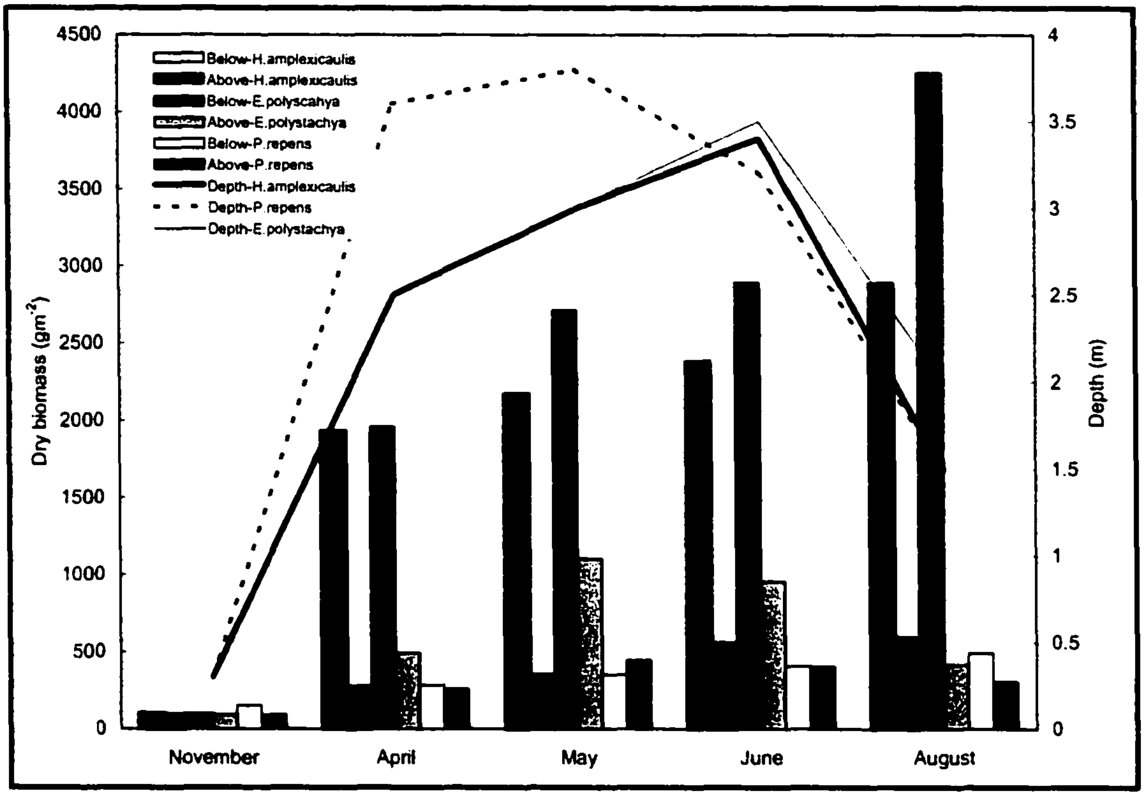

Figure 3.7. The bars indicate above and below water dry biomasses during each month and the lines indicate the seasonal local depths.

For the studied species, though the water level changed with time, the above water biomass remained constant ($p<0.05$) for May, June and August. After August, the data set did not allow further interpretations of the growth pattern of the plants. Nonetheless, it can be speculated that, in general, the growth decreased after August, mainly because the water level declined rapidly (declining rate is higher than 2 m per month). Piedade et al., (1992, 1993) and Luciano (1997) reported the same growth pattern for monospecific stands of *E. polystachya* and multi-specific stands of aquatic vegetation, respectively. The authors described how the plant kept growing after the peak of the high water for approximately two months; afterward the senescent and decomposition phase extended until the rainy season started, and once again new growth commenced.

From April until August, for *H. amplexicaulis, E. polystachya,* and *P.repens*, the above water biomass (i.e. above water stems and leaves) contributed on average with 16%, 21%, and 47%, respectively, of the their total biomass (Table 3.5). The distinct canopy structure (Table 3.2) and life history of each species explained these different contributions. For instance, *H. amplexicaulis* and *E.polystachya* are rooted species. Consequently, as the water level rose, an increasing percentage of the growing stems became submerged; for both species, approximately 80% of the total length of the stem was submerged during maximum water level (Figure 3.4). Similar results were reported by Piedade et al., (1991).

The contribution of the above water biomass of *H. amplexicaulis* and *E. polystachya* to the total biomass was slightly different. At high water stage, the total dry weight of the above water large leaves of *E. polystachya* was on average 450gm^{-2} (each leaf weights on average 2.10±0.6g), i.e. 44% of the total above water biomass. The smaller leaves of *H. amplexicaulis* weighed on average 188gm^{-2} (each leaf weighs on average 0.34±0.2g), i.e. 42% of the above water biomass. *P. repens*, showed the larger proportion of above water biomass (47%) of the total biomass. This might be related to the life history of this species, during which the stems detached from the substrata (bottom) as the water rose; therefore, the need for a fast growth of the below water stems was minimized. Junk (1970) reported similar values.

Table 3.5. Percentage of above water biomass to the total biomass

	H. amplexicaulis	E. polystachya	P. repens
November	48	48	37
April	12	20	47
May	14	29	56
June	19	25	50
August	17	9	38

The maximum values of total biomass of *H. amplexicaulis* and *E. polystachya* were similar to the maximum values reported for the same species of the central Amazon (Piedade et al., 1991; Junk and Piedade, 1993; Junk and Piedade, 1997). The differences are a function of the characteristics of the environment in which they occur. For instance, *E. polystachya* of the central Amazon develop a below water stem of approximately 9 m due to very deep water. As a result, the total biomass is relatively higher (Piedade et al., 1991) than the one observed in this study. Furthermore, *H. amplexicaulis* colonize protected areas of the lake, which allows for full development and formation of large monospecific stands (Camargo and Esteves, 1994). Table 3.6 shows biomass values of some species of emergent aquatic vegetation in Brazil and other regions of the world. Most of the estimates of total maximum biomass fall in the range of 1000 to 2500 gm^{-2}. The only few species that showed values higher than this range are in the Amazon floodplain (annual species) and tidal freshwater marshes (perennial species). The extremely high values of the Amazon aquatic plants are due to the morphology of the species and the fast growth, a survival requirement to keep pace with the rising water. In view of the general growth pattern of the different species under analysis, for each species second order polynomial regressions were applied between total biomass and water level. The regressions resulted in significant correlation ($p<0.05$); the R^2 are 0.97, 0.99, and 0.91, for *H. amplexicaulis, E. polystachya,* and *P. repens*, respectively. These results indicated that the growth patterns followed the water periodicity, once more suggesting that growth is an adaptation for surviving in the flooding conditions of the Amazon floodplain (Piedade et al., 1991, 1993; Junk and Piedade 1997).

Table 3.6. Maximum values of dry biomass (gm^{-2}) of different species of aquatic vegetation. ER (emergent rooted), EF (emergent floating).

Species	Ecological type	Locality	Maximun biomass	Author
Scirpus cubensis	ER	São Paulo, Brazil	1202	Nogueira (1989)*
Eichhornia azurea	EF	São Paulo, Brazil	684	Camargo and Esteves, (1994)
E. polystachya	ER	Central Amazon, Brazil	8000	Piedade et al., 1991
P. fasciculatum	ER	Central Amazon, Brazil	5760	Junk and Piedade, 1993
P. repens	EF	Central Amazon, Brazil	2200	Junk and Piedade, 1993
H. amplexicaulis	ER	Central Amazon, Brazil	2270	Junk and Piedade, 1997
P. repens	EF	Central Amazon, Brazil	666	Junk, 1970
Mixed of emergent rooted	ER	Quebec, Canada	1379	Hudon, 1997
E. polystachya	ER	Lower Amazon, Brazil	2280	Luciano, 1997
Typha angustifolia	ER	Czechoslovak	8000	Kvet and Husak, 1978**
Typha sp.	ER	-	1215	Odum et al., 1984**
H. amplexicaulis	ER	Lower Amazon, Brazil	3490	This study
E. polystachya	ER	Lower Amazon Brazil	4670	This study
P. repens	EF	Lower amazon, Brazil	800	This study

* cited by Camargo and Esteves, (1994); ** cited by Mitsch and Gosselink, (1993)

To summarize, the data set showed that the above water dry biomass of grass-like aquatic plants was similar (April/May, May/June, and August) year round, with the exception of the low water season (November). The total biomass showed differences between low and rising water (November and April), high water (May and June) and falling water periods (August). These differences were a function of the below water biomass. The architecture of the canopy also showed a similar pattern. When the water level started to fall (August), the plants reached the senescent stage, the plant water content decreased, and the stems bent, changing from an almost vertical orientation observed at high water. When the water level dropped (October), the plants became exposed to the sediment and started to decompose. A new generation of plants started to grow as the water rose (November); the new material (leaves and nodes) formed as rapidly as the water rose, keeping the photosynthetic organs (leaves) above the water. Therefore, the above water structure per species, summarized by some of the parameters in Table 3.2 and Table 3.4 (leaves and stems characteristics), showed that the canopy of the plants was homogeneous during the water cycle, with the exception of low water stage. The annual homogeneous pattern of the above water structure of the aquatic vegetation is an important information in understanding the backscattering values measured by RADARSAT and JERS-1.

4. RADAR BACKSCATTERING

4.1. Laboratory Analysis

4.1.1. Radiometric correction

In order to derive an image with numbers that are estimates of scene reflectivity radiometric correction must be performed to minimize both the radiometric calibration problems and the dynamic range requirements. Following the radiometric calibration, RADARSAT and JERS-1 were converted to normalized backscattering coefficients (σ^0 in intensity). The average of σ^0 is calculated by averaging the individual pixel intensities (σ^0 estimate), expressed in linear units rather than dB. This provides an un-biased estimate of the mean backscatter, while reducing the standard error of the mean (Oliver and Quegan, 1998). For convenience (most of the data published in the literature is in dB, Freeman, 1992), and also to have a better probability distribution of the data, σ^0 is expressed in terms of dB (Ulaby and Dobson, 1989). Hence, σ^0 (in dB) is calculated as shown in Equation 4.1.

$$\sigma^{0}{}_{j} = 10 \log_{10} \left[DN_{j}{}^{2} \right] \cdot \kappa \qquad \text{Equation 4.1}$$

where κ accounts for the calibration constant of the radar system and DN^2 is the digital number in intensity.

Previous to the conversion of DN to σ^0 different steps were adopted for RADARSAT and JERS-1. RADARSAT images acquired before November 1996 were processed using either a non-optimal or no antenna pattern calibration. To overcome this problem an algorithm was applied to all the images acquired before November 1996. The algorithm removes the original antenna pattern and applies a new corrected antenna pattern to the images (Wolf and Hawkins, 1997).

Following this operation, the images were converted from 16 bit to the original 32 bit format according to a look up table. For RADARSAT, the processor's internal operations were carried out in floating point format (32 bit) and later converted to an integer format (16 bit) to be stored on the output media. This conversion requires a look up table (LUT) scaling (gain and offset). To recover the original σ° values, the LUT scaling needs to be removed. The gain and offset of the LUT are stored in the radiometric data record of the original file. The variation in the calibration constant K (Equation 4.1) has already been computed in the DN values of the image. Therefore, for RADARSAT, the σ° was calculated as follows (Shepard, 1997):

$$\sigma^{o}{}_{j} = 10 \ \log_{10} \left[\left(DN_{j}^{2} + A_{o} \right) / A_{gj} \right] + 10 \ \log_{10} \sin \theta j \qquad \text{Equation 4.2}$$

where σ^{o}_{j} is the radar calibrated backscattering (in dB) retrieved from the corresponding digital number (DN^2), A_{gj} is the scaling gain value for *jth* pixel, A_{of} is the fixed offset, and θ_j is the incidence angle along the range direction taking into account the ellipsoid of the earth. Correction for the ellipsoid of the earth is adequate for flat areas (Freeman, 1992).

For JERS-1 (product level 2.1), the images were already calibrated for the antenna pattern and the images were not submitted to a LUT scaling process. Accordingly, DN was converted through the following expression (Shimada, 1996);

$$\sigma^{o}{}_{j} = 10 \ \log_{10} \left[DN_{j}^{2} \right] \cdot \kappa \qquad \text{Equation 4.3}$$

K assumes a value -68.2 for data processed after November 1, 1996. Note that $\sin\theta$ is not part of the equation; JERS-1 images are already corrected for the ellipsoid of the earth (Kellndorfer et al., 1996).

After the data set was corrected in terms of radiometric calibration, a test of the radiometric stability of the systems along range (incidence angle) and time was carried out. The study area was divided into a grid of 1' 30" by 1' 30" degree block. Three samples were selected of each block along the row of the grid (range) from west to east of the far North section of the images. According to the thematic maps of the study area (1:100,000 scale), the far North part of the images has the most continuous areas of upland forest. For this study area upland forest is considered the most stable target in terms of backscattering. Generally, we expect that homogeneous stable targets, for instance upland forest, yield an approximately constant σ^0 with time for stable radiometrically calibrated SAR systems (Shimada, 1998; Hawkins and Srivastava, 1999); slight differences both multi-temporal and within the image are acceptable due to environmental changes (e.g. humidity) and characteristics of the terrain/target (e.g. elevation).

Figure 4.1 shows the multi-temporal variation of σ^0 over the range of acquisition (various incident angles) for upland forest. Both RADARSAT S6 and JERS-1 showed radiometric stability, temporally and within the image. The differences within the images are associated with variations in the topography of the terrain. For instance, at point 11 (range) the terrain is mountainous when compared with to other regions along the range of the images. The small differences in the average backscattering between images may be associated with the different environmental conditions at the time of acquisition of the images. For instance, for RADARSAT S6, the lowest backscattering values occurred in November, when the precipitation and the relative humidity were the lowest (70%), and the temperature was the highest (approximately 30°C). Dry conditions favor lower backscattering values. For a given surface, if the roughness remains constant the σ^0 increases when the moisture content of the material increases (higher dielectric constant) (Dobson et al., 1996). The same pattern is observed for JERS-1, i.e. the image acquired in December (dry month) showed lower backscaterring values than the images acquired in wet months (March, May and August).

For RADARSAT S1 images, the lowest backscattering values occurred in June 1999, a drier month compared to May 1996 according to the mean precipitation graphic. However, the daily precipitation analysis showed similar dry conditions (no rain for approximately 7 days) for the days previous to the image acquisition. Furthermore, the analysis of the GOES images (Appendix III) acquired on the same morning of the RADARSAT S1 images did not show any significant difference in terms of atmospheric circulation. Note that at this wavelength (5.6cm) the total attenuation of the microwave radiation by the atmosphere is very low; however, during tropical storms some interference on the backscattering values may occur (Ulaby et al., 1981). Therefore, the analysis of all the available data could not explain the differences between the RADARSAT S1 images acquired in May and June. For RADARSAT S1, the system was not temporally stable. Also, for the image acquired in June 1999, the lower σ^0 values at near range compared with the values at far range suggested that the antenna pattern was not properly calibrated. Therefore, the system was not stable even within the image. The image acquired in May 1996 showed high stability along range. We can speculate that the image acquired in June 1999 was not properly, relatively and absolutely calibrated.

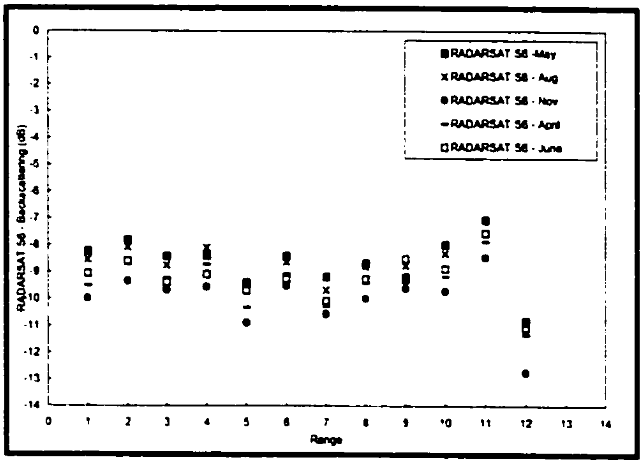

a. RADARSAT S6 – upland forest

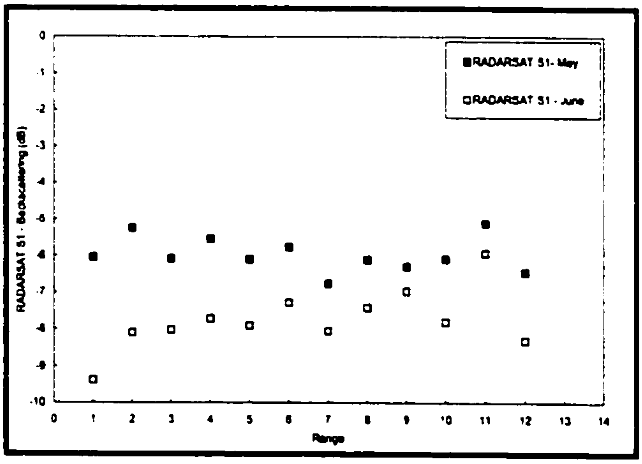

b. RADARSAT S1 – upland forest

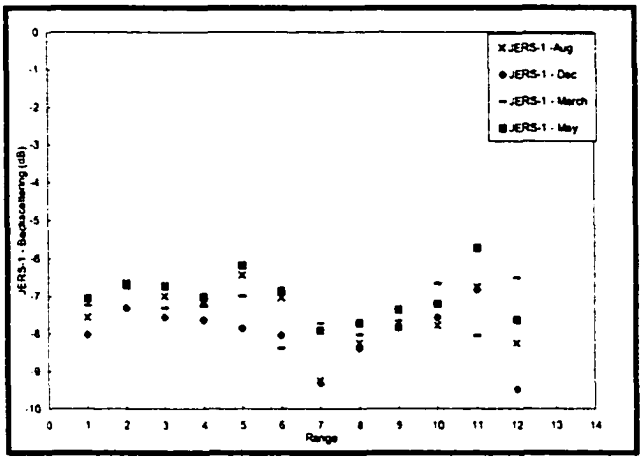

c. JERS-1 – upland forest

Figure 4.1. Multi-temporal variation of backscattering of forest in the range direction. (a) RADARSAT S6; (b) RADARSAT S1; (c) JERS-1.

4.1.2. Geometric correction

Precise geometric correction is an important step in integrating multi-sensor and multi-temporal SAR. The SAR images were geometrically corrected by using an ortho-rectification procedure (Toutin, 1995). The ortho-rectification integrates the complete viewing geometry, which includes the position and velocity of the platform, the parameters of the sensor, the characteristics of the earth, and the cartographic projection. Unlike polynomial methods, this method is not strongly affected by the number of GCPs (Ground Control Points) because it respects the complete geometry of viewing. Previous studies in areas of low relief (Toutin, 1995) have shown an error of precision 2 to 3 times greater for polynomial transformation when compared with Toutin's ortho-rectification method. The key processing steps of the geometric correction were as follows:

(i) Collecting the GCPs

In the first instance, corresponding GCPs were collected from the first image and maps. The following thematic maps (1:100,000 scale - the best scale of maps available for the study area) were used to collect GCPs (X, Y, and Z). The cartographic parameters were:

Projection – UTM
Ellipsoid – New International 1967
Row UTM – M
Zone UTM – 21

(ii) Digital Elevation Model (DEM) generation

Contours from 1:100,000 scaled topographic maps were manually digitized and a raster DEM was produced. The vector contours were converted to raster data (spatially continuous format) according to a Delaunay triangulation algorithm (Bonham-Carter, 1994). The raster data were subsequently interpolated to a 12.5m pixel spacing.

(iii) Integration of GCPs, DEM, and satellite parameters

The satellite parameters (attitude) were extracted from the original RADARSAT and JERS-1 data. The orthorectification algorithms integrated the satellite parameters, the GCPs, and the DTM and generated a geometric correction model. In order to reduce the errors of the geometric model, the GCP errors (X, Y) were kept lower than 2 times the root mean square (RMS) on both X and Y directions. Check points (CP) were selected in order to verify the quality of the restitution. The accuracy of the model and the accuracy of the restitution were verified throughout the GCP-RMS and CP-RMS, respectively (Toutin et al., 1992). Table 4.1 presents the results of the restitution.

Table 4.1. Final results of the geometric correction

Images	Number of GCP	Number of CP	GCP RMS (m)	CP RMS (m)
RADARSATS6 May	25	10	32.9	60.3
RADARSATS1 May	26	8	12.6	19.9
JERS May	41	15	11.2	18.3
RADARSATS6 Aug.	46	17	15.6	20.9
JERS Aug.	18	7	20.7	16.3
RADARSATS6 Nov.	16	6	12.4	18.6
JERSdec	20	8	13.4	18.1
RADARSATS6 April	18	7	4.7	13.5
JERS March	22	7	4.3	17.6
RADARSATS6 June	18	8	8.1	17.1
RADARSATS1 June	23	7	9.5	17.4

In summary, the accuracy of the models (GCPs RMS) was on average 14 meters and the accuracy of the restitution (CP RMS) was on average 21 meters. The accuracy of the restitution is indeed the important value in the evaluation of the geometric correction because it was estimated based on control points not used to build the model. The final accuracy of the restitution is considered adequate for the purposes of this research; it is less than two pixels spacing and less than the pixel resolution of both RADARSAT and JERS-1.

(iv) Resampling

Resampling consists of estimating the sample values (pixel values) for the geo-corrected image by interpolating between the values of the original image (Richards, 1986). Interpolation can change the statistics of the images, therefore compromising the backscattering value of the targets. Better preservation of the statistics of the images is achieved with the cubic convolution algorithm when compared with the nearest neighbor or bilinear methods (Shlien, 1979). For SAR images, Quegan (1990) shows that in obtaining a minimum difference between the variance of both the original and the interpolated image at least 16-points (pixels) of the original image must be used in the interpolation. A cubic-convolution (16-points) resampling algorithm was used to assign the pixel values for the new corrected image.

In summary, an ortho-correction procedure and cubic convolution algorithm were applied to the satellite images yielding a mean accuracy of the restitution of 21 m (average of all images). The calibrated and geometrically corrected SAR images were subsequently submitted to three distinct procedures, namely: (i) minimize the speckle effect so that the images could subsequently be classified; (ii) evaluate the potential of using texture images in the classification; and (iii) recover normalized backscattering coefficients from intensity images of known targets.

4.1.3. Speckle

Oliver and Quegan (1997) describe in a very simple manner the origin of the speckle in SAR images. When electromagnetic radiation is scattered from the ground, the physical properties of the ground modify both the phase and amplitude of the radiation. A SAR system records both the phase (related to the distance between the scatter and the radar) and amplitude backscattered from the ground. From this set of information the processor forms an image. When we look at SAR images the "salt-and-pepper" texture or the grainy appearance is apparent. Why does this happen? As the radiation reaches a resolution cell on the ground it interacts with all the scatters within the resolution cell. Each of the scatters cause a change in the amplitude and phase of the radiation within the resolution cell, and the combination (constructive and destructive) of these changes is backscattered towards the radar antenna as a single signal. This happens because the resolution of the sensor is not sufficient to resolve individual scatters within the resolution cell. The phase difference between the scatters is the source of the noiselike texture or speckle of the SAR images. Hence, speckle is not a noise; in fact, it is the natural spatial variability of the targets on the ground. However, the speckle degrades the radiometric information of the image because for similar targets the backscattared signal might be different due to the differences between scatters within a resolution cell. Further, classification with the presence of speckle is highly ineffective (Oliver and Quegan, 1998).

There are several ways of reducing the speckle effect of the images. One way is to increase the number of looks of the image, which is equivalent to trading off spatial resolution for improving radiometric resolution (Ulaby et al., 1986). An example of this trade off is RADARSAT fine mode image and RADARSAT standard mode image. The first is a 1 look and 8 meters resolution image and the second is a 4 looks and 24 meters resolution image. Hence, as the number of looks increase, the spatial resolution degrades, but the radiometric quality of the image improves. A second method of minimizing the speckle is by increasing the number of independent samples through spatial filtering. This is equivalent to applying either a simple low pass filter (for instance, averaging) or an adaptive filter over the image. The most common adaptive filters for minimizing the speckle of SAR images are Lee, Frost, and Gamma filters (Lopes et al., 1990, Shi and Fung, 1994, Oliver and Quegan, 1998).

Several tests were performed applying Enhanced Frost and Gamma filters with one, two, and three interactions for minimizing the speckle (Oliver and Quegan, 1998). The Enhanced Frost filter acts differently depending on the local coefficient of variation, i.e. for homogeneous areas it reduces the speckle by applying a low pass filter; for heterogeneous areas, it reduces the speckle while preserving the texture; and for isolated point targets, it preserves the value. The Gamma filter combines the characteristics of the Frost filter with the prior knowledge of the probability density function of the image (Shi and Fung, 1994). The filter assumes that the image has a Gamma distribution and therefore it only changes the values of those pixels that lie within a certain range of the central pixel value of the filtering window.

Quantitative and visual analyses of the filtered images were performed for the purposes of evaluating the filters. The criteria to evaluate the filtered images were (1) mean backscattering preservation, (2) increasing in the equivalent number of looks - ENL (the same as decreasing the local variance), (3) discriminating different textured areas (the same as increasing the spread of the coefficient of variance-CV), and (4) a visual analysis of edge preservation. The first three criteria were suggested by Lopes et al., (1990) as a proper methodology for evaluating filtered images. For both filters, a 5 by 5 window was chosen after numerous visual tests for evaluation of edge preservation, such as narrow water channels.

Several samples of a homogeneous target (water) were selected and their backscattering coefficients calculated for the original and filtered images. Figure 4.2

shows the difference between the backscattering of the original image and the filtered images (criteria 1). The result suggested that the backscattering information were preserved for all the filters, except for one sample that shows a difference of –0.2 dB for all the filters, and for three interaction of Frost filter, a second sample present a 0.2 dB difference.

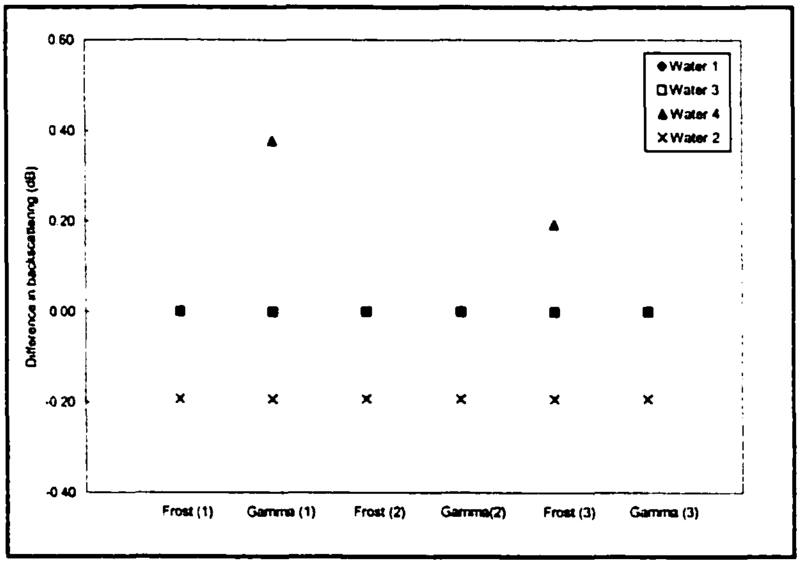

Figure 4.2. Differences between the backscattering coefficients of the original image and the filtered images for different samples of water. A 5 x 5 window was selected for the filters. Numbers between brackets represent the number interactions, e.g. (2) means that the filter runs over the image 2 times.

Figure 4.3 shows that the ENL of homogeneous areas (water) is the highest for 3 applications of Enhanced Frost and Gamma filters, i.e. the local variance was decreased (criteria 2). The equivalent number of looks (ENL) for the SAR images is given as $ENL = 1 \div CV^2$ (Oliver and Quegan, 1998). The analyses of the CV of different textured areas (criterion 3) did not suggest any significant difference ($p<0.05$) between the spread of CV of the original image and the filtered images (Figure 4.4). The filtered images presented lower CV when compared to the original image due to the increased

ENL. Hence, the last test suggests that regardless of the filter, the textures of the different areas are preserved. Indeed, the test showed that the texture of the ground cover could not be separated by the coefficient of variation. Texture is the focus of the following section.

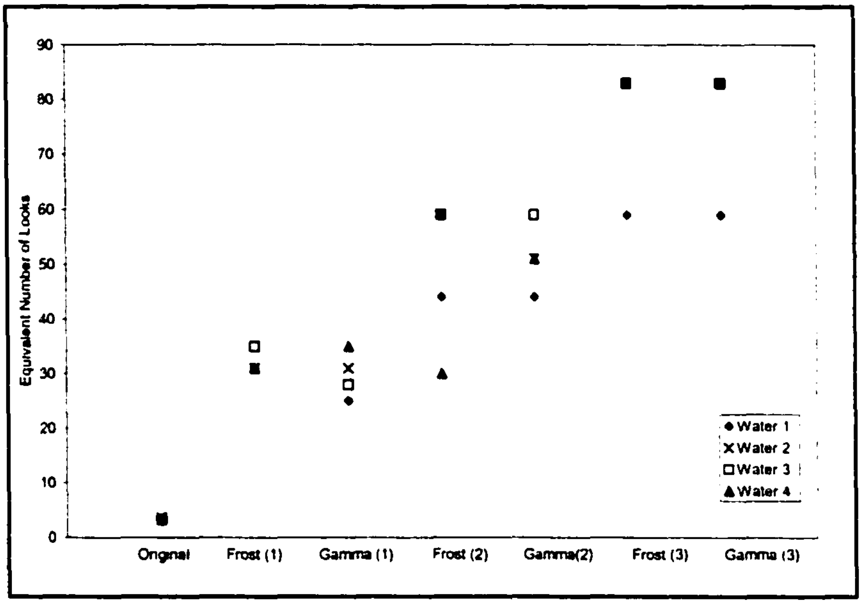

Figure 4.3. Variation of the equivalent number of looks according to the speckle filter

Overall, three times interaction of the gamma filter showed the best compromise in terms of preservation of the statistics of the image and the definition of structures such as water channels and edges. The application of three times the Gamma filter resulted in (i) the highest equivalent number of looks (i.e. the lowest coefficient of variance), (ii) the minimum difference between original mean values and filtered values (differences lower than 0.2 dB), (iii) visually, the highest preservation of edges, and (iv) the analysis of different targets showed a decrease in the coefficient of variance from 0.58 (average) for the original images to 0.15 (average) for the filtered images, i.e. reduction of variance within targets. The results of the enhanced Frost and Gamma filters are illustrated in Figure 4.5.

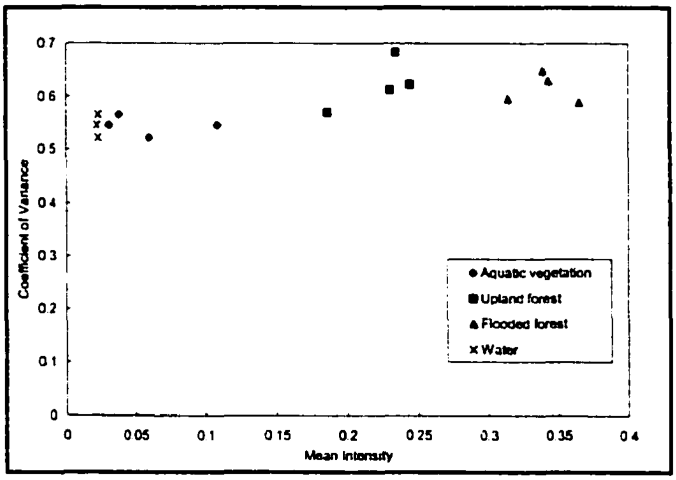

(a). Original image

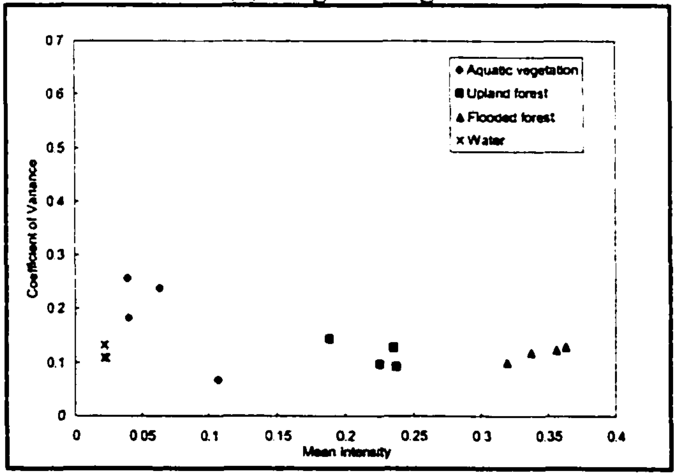

(b). Enhanced Frost filter

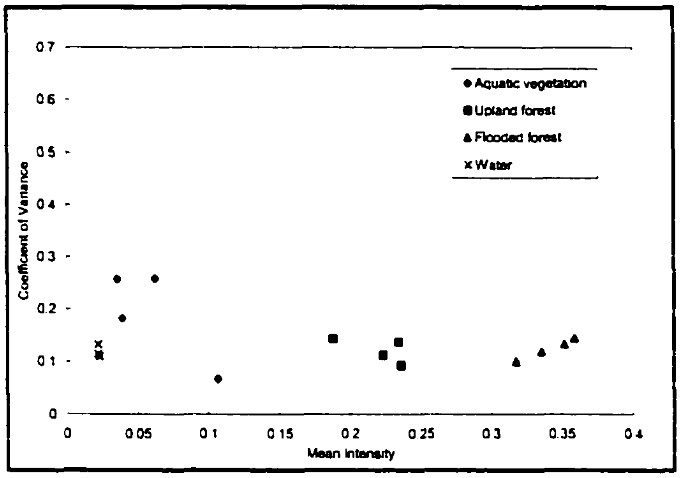

(c) Gamma filter

Figure 4.5. Coefficient of variance of different ground cover in intensity images for: (a) original image; (b) Enhanced Frost filter (5 x 5 window), three interactions; (c) Gamma filter (5 x 5 window), three interactions.

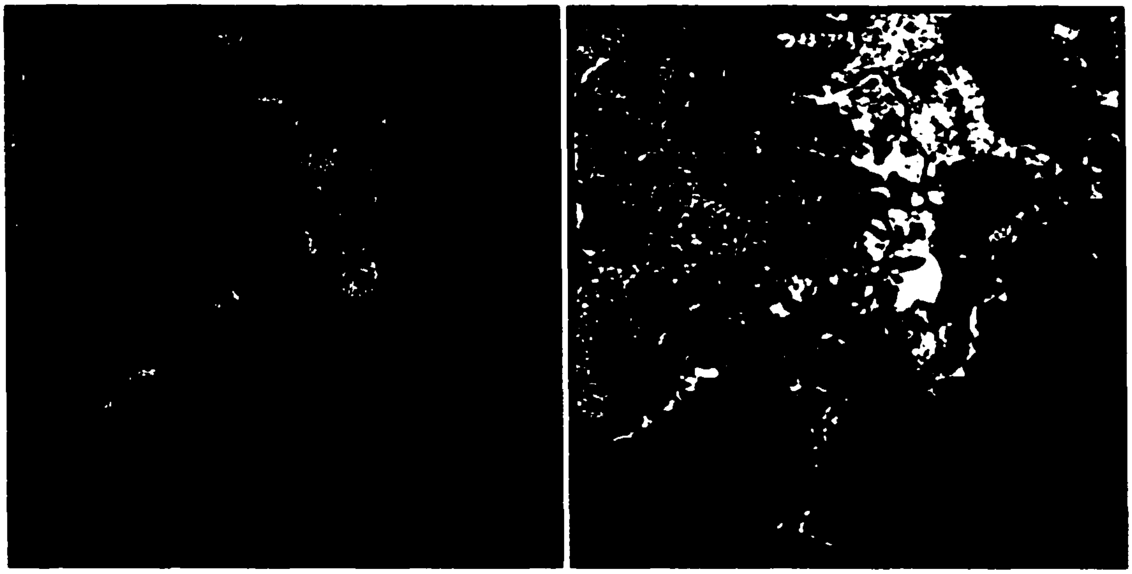

(a) original JERS-1 image

(b) Enhanced Frost filter

(c) Gamma filter

Figure 4.5. (a) Original JERS-1 image, 3 looks; (b) Despeckled version of (a) after 3 interactions of an enhanced Frost filter, 5 x 5 window; (c) Despeckled version of (a) after 3 interactions of a Gamma filter, 5 x 5 window.

4.1.4. Texture images

As previously mentioned, the intrinsic texture of the image is a component of SAR images. Texture represents the natural spatial variability of neighboring pixels that represent the same target within the image (Laur et al., 1987). Several authors (Ulaby et al., 1986, Laur et al., 1987, Anys and Dong-Chen, 1995, Oliver and Quegan, 1998, Luckman et al., 1997) have shown that texture is an important component of SAR image interpretation. For example, two distinct vegetated areas may show similar backscattering coefficients at short wavelengths (C-band). However, an area with very uniform canopies may present little backscattering variation (homogeneous areas), and an area with short and tall trees may present some backscattering variation (heterogeneous area). An analysis of these two vegetated areas may show some different texture measurements that will facilitate the separability between them (Luckman et al., 1997, study conducted in tropical forest), even though the backscattering coefficients might be very similar. Texture measures were generated and their contribution to the classification was evaluated.

The most common methods of generating texture SAR images are statistical ones. Some of these methods generate texture based on first-order-statistics, for instance, the mean measure (Ulaby et al., 1986), and semivariance analysis (Amaral et al., 1997). Other methods are based on second order statistics represented by standard deviation and the coefficient of variance measures and the co-occurrence matrix of the digital numbers (Laur et al., 1987, Luckman et al., 1997). The co-occurrence matrix is an estimate of the frequency that two digital numbers of neighboring pixels occur within a matrix, given a certain inter-pixel distance and orientation (Ulaby et al., 1986).

Given all the available statistics that can quantify different aspects of SAR image texture, the following three statistics were selected: the standard deviation, and the co-occurrence measures, homogeneity and contrast. The extraction of the standard deviation measure requires information of the size of the window. The co-occurrence measures require information of the size of the window, the distance between pixels, and the moving direction of the window.

The specification of the window size is crucial. For instance, in the case of a very large window the information of two distinct targets may overlap. The choice of the optimal window size was based on both the variation of the coefficient of variance of the contrast measure according to the window size (Anys and Dong-Chen, 1995) and the visual observation of the transitional boundaries between different ground cover. Figure 4.6 shows the results of the variation of the CV and window size for four different ground cover of the original image. The CV values declined rapidly from a window of 3 by 3 towards a window of 5 by 5 pixels, and started to stabilize at a window of 7 by 7. At this window size, the ground cover showed low variability (low CV), which signifies meaningful spatial information, in this case the contrast between ground cover, might be captured. As to a 3 by 3 window, the CV value is dependent on the variability within the same ground cover, and we are not interested in this. A visual analysis suggested that with windows larger than 5 by 5 the transitional boundaries between adjacent areas would be fuzzy and this would result in classification errors. A window size of 5 by 5 was chosen as a trade-off between the ability of capturing spatial information and the preservation of adjacent boundaries.

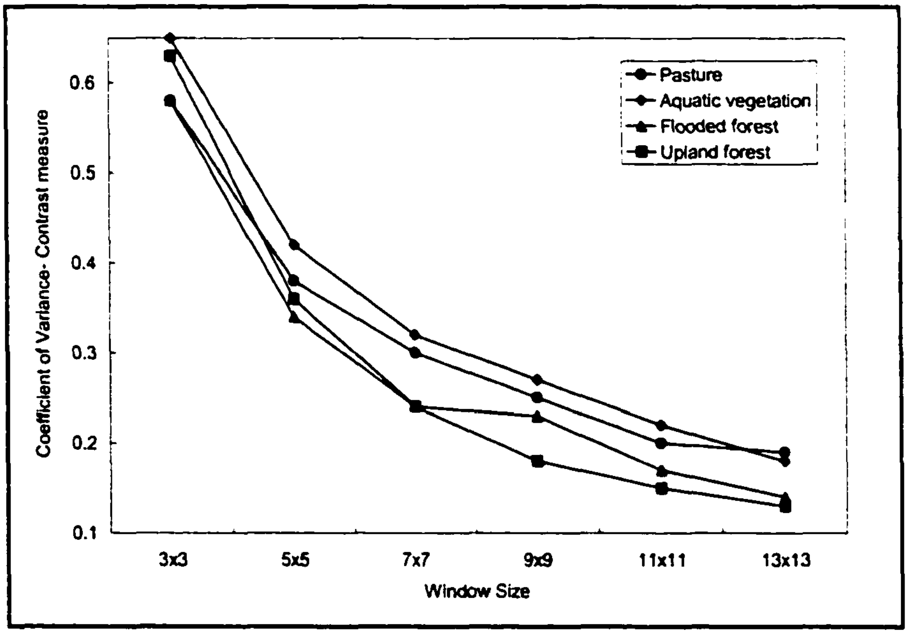

Figure 4.6. Variation of the coefficient of variance of different targets according to the window size

The selection of the proper distance between pixels, i.e. "the jump of the window", is a difficult task and it may be defined based on the repetitive visual analysis of the scale of the texture on the image associated to the scale of the features on the ground (Luckman et al., 1997). For specific SAR images it is expected a large range of variation of the texture and some times no variation in texture. The visual analysis of the images showed no obvious trend in terms of the texture scale. Consequently, a generic distance of one pixel was selected. The same approach was adopted for choosing a preferential moving direction of the window. A visual analysis suggested that there is no preferential direction (isotropic) for the variability of the features on the ground.

The three selected statistics measures were generated for the RADARSAT S6 and S1, and JERS-1 images acquired in May. The simple first-order statistics measure, standard deviation, visually, showed the best result in terms of discriminating between different targets. For the homogeneous measure, high digital numbers indicate homogeneity areas in terms of variability of backscattering values. This was apparent in areas where the predominant target was water. For contrast measure, the opposite was observed, i.e. high digital values are found in regions where the local variation is high. For RADARSAT S6, S1, and JERS-1, the contrast images were very similar to the standard deviation images (correlation coefficients of 0.94, 0.95, and 0.96, respectively, n=32); hence, due to the redundancy of information, the contrast images were not used for the final evaluation of the texture measure.

Quantitative analyses were carried out for the purposes of evaluating the efficiency of the texture measures in terms of discriminating among targets. Samples of five different ground cover were extracted from the texture and the original images (despeckled according to section 4.1.3) and a distance function between the ground cover was determined. The Jeffries-Matusita distance, or Bhattacharyya distance (*B*), was used to define the distance between the classes for each of the texture and original images. The

Bhattacharyya distance is a measure of the average distance between the two class probability density functions. The *B* distance varies in a range of 0 to 2; with 0 to 1 – poor, 1 to 1.9 – fair, and 1.9 to 2 – good separability (Richards, 1986).

The analysis of separability (*B* distance) for each image suggested that the filtered backscattering images (tonal information) generally exhibited the best results in terms of separability between the classes; average *B* equals to 0.95, 1, and 1.6, for RADARSAT S6, S1, and JERS-1, respectively. The standard deviation images showed average *B* equals to 0.53, 0.58, and 1.2, for RADARSAT S6, S1, and JERS-1, respectively. For RADARSAT S6, S1, and JERS-1, the homogeneity measure yielded the least separability between classes, 0.26, 0.26, and 0.9, respectively. The scatterplots of the backscatter means from the filtered images against the mean texture for the same area corroborates these results (Figure 4.7). Note that in any case the mean intensity (filtered original images) gave the larger spread of values among ground cover. The standard deviation measure suggested a very similar behavior, however no improvement of separability was detected when compared to the mean intensity measure.

Contrary to other results (Ulaby et al., 1986, Luckman et al., 1997), the filtered backscattering images exhibited the best measure to discriminate between the ground cover being studied. Luckman et al. (1997) showed that the coefficient of variance (one look image) is the most suitable measure to discriminate between mature forest and other classes of cover in the Amazon region. For the specific data of this study, the CV, which characterizes the inhomogeneity of a population, was consistent for all of the classes (0.56±0.05, 0.57±0.07, 0.59± 0.07, for RADARSAT S6, S1, and JERS-1). The local heterogeneity on the ground cover occur on a much smaller scale than the spatial resolution detectable by both RADARSAT and JERS-1 (approximately 27 m); hence, it was not feasible to detect texture variations. Figure 4.8 illustrates the texture measures homogeneity and standard deviation produced from a JERS-1 image. Note that no additional discrimination between ground cover if foreseen when compared with the filtered image (Figure 4.5c); this corroborates the analysis of the scatterplots (Figure 4.7). From these results, the texture measures were far from offering the highest separability between classes, consequently, they were not expected to improve the classification results of the images. Therefore, the texture images were not used on the classification procedure.

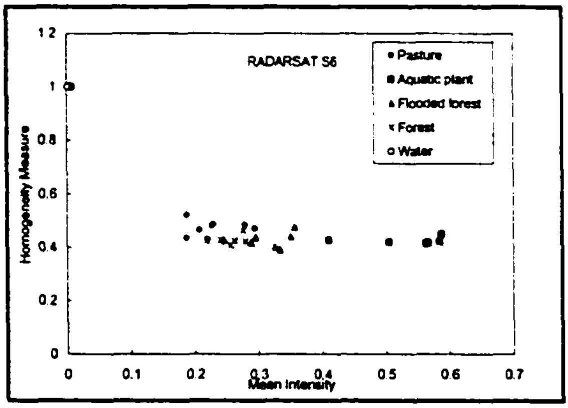

(a). RADARSAT S6, Homogeneity versus mean intensity

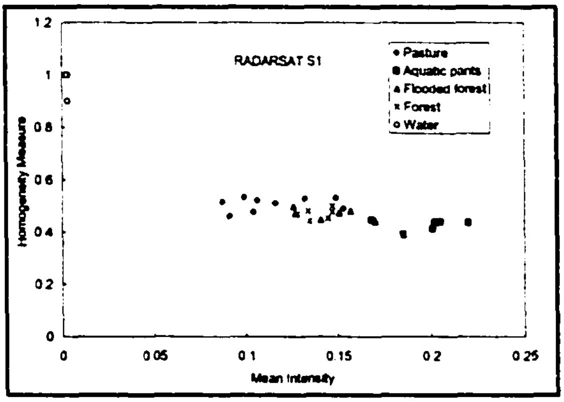

(b). RADARSAT S1, Homogeneity versus mean intensity

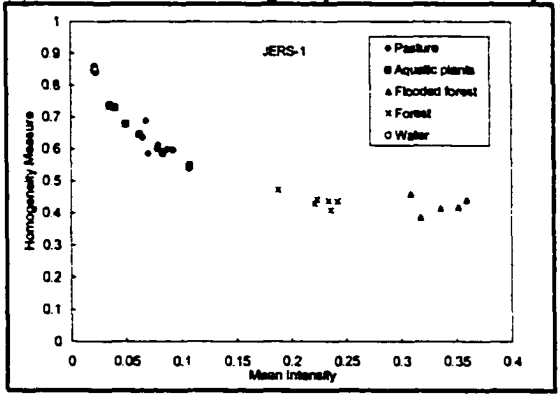

(c). JERS-1, Homogeneity versus mean intensity

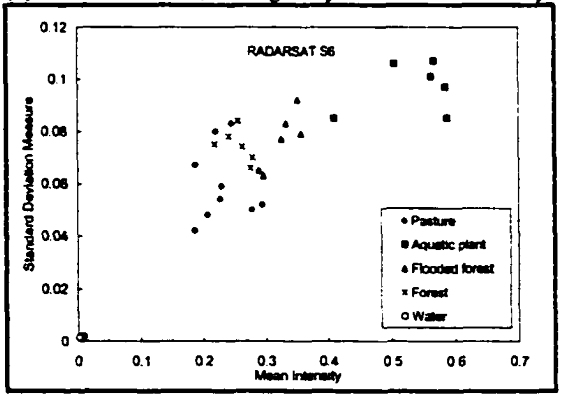

(d). RADARSAT S6, Standard deviation versus mean intensity

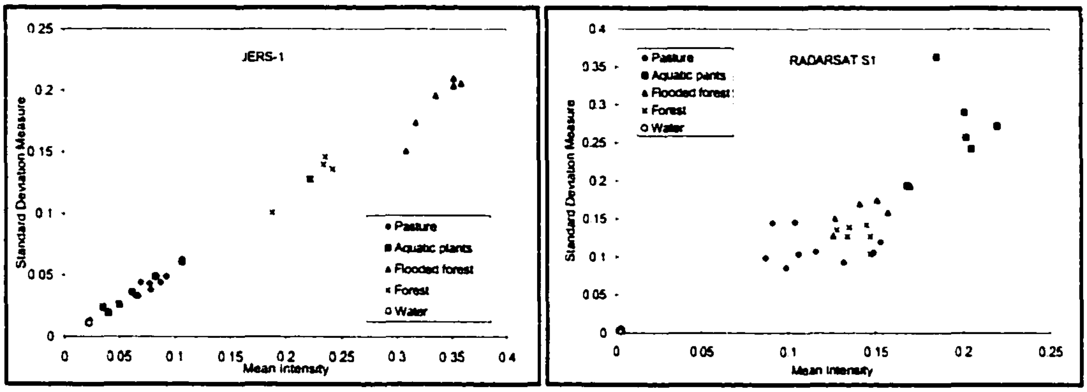

(e). RADARSAT S1, Standard deviation versus mean intensity (f) JERS-1, Standard deviation versus mean intensity

Figure 4.7. Scatterplots of texture measures of different ground cover; all values are in intensity.

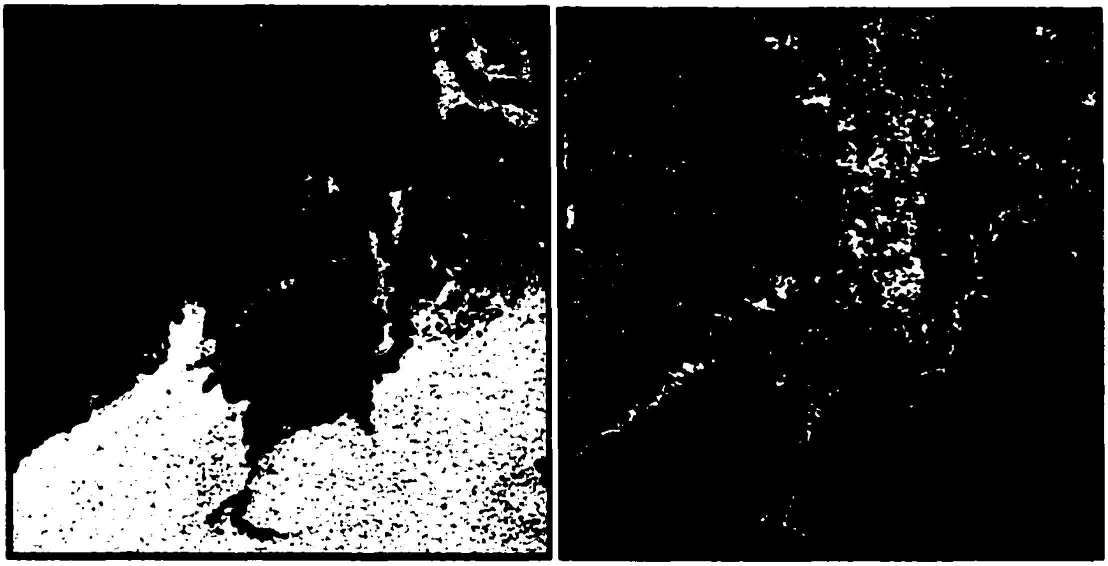

Figure 4.8. Texture measure for JERS-1 image. (a) homogeneity image, 5 by 5 window; (b) standard deviation image, 5 by 5 window.

5. BACKSCATTERING COEFFICIENT FROM DIFFERENT GROUND COVER

The previous chapter described how SAR satellite data was processed to (i) analyze the backscattering coefficients in relation to different ground cover, and (ii) to classify the seasonal area occupied by the aquatic vegetation. Backscattering coefficients were extracted from radiometrically and geometrically calibrated SAR images and evaluated for different ground cover. The desired ground cover for global biogeochemical studies are water, wetlands, bare soils, agriculture, grassland, shrubland, savanna, deciduous and coniferous forest, and urban areas (Dobson et al., 1996). From these, water, aquatic vegetation, flooded forest, upland forest, savanna, and pastureland were analyzed according to their seasonal backscattering coefficients. A detailed analysis of the relationship between the biophysical properties of aquatic vegetation and backscattering coefficients is presented.

5.1. Estimates of Backscattering Coefficients

For estimating σ^0 from intensity image pixels values are averaged so that the effects of the radiometric resolution errors (speckle) are minimized, and the confidence of the estimated σ^0 determined (Oliver and Quegan, 1998). Laur et al., (1996) calculated the probability of an estimated intensity σ^0 (average of N pixels) of a homogeneous area lying between error bounds and according to a certain level of confidence. This probability is calculated based on the assumption of normalized gamma distribution of the data (valid for large number of pixels), which is a function of the ENL of the intensity image (Oliver and Quegan, 1998).

An average CV of 0.58 of homogeneous target, in this case water (number of pixels per sample was higher than 350), was calculated for RADARSAT S6 and S1, and JERS-1, yielding an average ENL equal to 3. Therefore, knowing the ENL, Laur et al., (1996) calculated that approximately a minimum number of 100 averaged pixels are required to yield a 95% confidence, with an error boundary of the estimated σ^0 at ±1dB. The 1dB error boundary was selected because it corresponds roughly to the relative calibration accuracy of RADARSAT (Hawkins and Srivastava, 1999) and JERS-1 (Shimada, 1998). Table 5.1 presents the multitemporal mean, lower, and upper bound of backscattering coefficients of aquatic plants, flooded forest, forest, pasture lands, and savanna. The detailed data set can be found in Appendix IV. The number of pixels (n) sampled for each sample was on average higher than the minimum number established at 95% confidence level, with the estimated σ^0 at 1dB error bound. The high average number of pixels per sample (215, 132, 666, 245, 159, for aquatic pants, flooded forest, forest, pastureland, and savanna, respectively) was only possible because the classes cover very large-homogeneous areas. Mean and standard deviation values of σ^0 for each sample were calculated assuming that the sample was normally distributed; this is a reasonable assumption since the speckle variation is, for large samples (number of pixels), insignificant compared with that due to the texture of the target (Ulaby et al., 1986). The 95% confidence interval for μ, the true mean of a population, is calculated as follows (Snedecor and Cochran, 1980):

$$P\left|\left(\sigma^{o} - z_c SD / \sqrt{n}\right) < \mu < \left(\sigma^{o} + z_c SD / \sqrt{n}\right)\right| = 0.95 \qquad \text{Equation 5.1}$$

where P is the probability at 95% of confidence, σ^0 is the estimated mean backscattering value in intensity for a sample of *n* pixels in size, SD is the standard deviation of σ^0, μ is the true value of σ^0, and z_c is the standard normal variant (equal to 1.96 for a 95% confidence interval). The final numbers of the mean σ^0, and lower and upper bounds of μ, were converted from intensity to dB (Yanasse, 1991) (Table 5.1).

5.2. Analysis of the within Image and Multi-temporal Dynamic Ranges of the Backscattering Coefficients

Table 5.1 lists the seasonal backscattering coefficients for aquatic vegetation, flooded-forest, upland forest, savanna, and pastureland. The analysis of the within image and multi-temporal dynamic ranges of the σ^0 showed that (i) generally, the within image dynamic ranges were higher for JERS-1 than for RADARSAT S6 (this statement is valid for the extreme periods of water level, i.e. high and low water periods, and we are not taking into account the σ^0 of water); and (ii) the multi-temporal analysis showed that JERS-1 has a higher dynamic range than both RADARSAT modes. The total multi-temporal dynamic ranges were approximately 10dB, 7dB and 7dB for JERS-1, RADARSAT S6, and RADARSAT S1, respectively. JERS-1 presented a minimum value (-14 dB) for aquatic plants during low water period and a maximum value (-4dB) for flooded forest during high water period. RADARSAT S6 presented minimum value (-14dB) for savanna at low water period and maximum value (-7dB) for aquatic vegetation and flooded forest during the other seasons. RADARSAT S1 showed minimum value (-

10dB) for savanna and maximum values (-3dB) for aquatic plants during high water period. The results for RADARSAT S1 could be biased due to the possibly incorrect calibration for the June 1999 image (section 4.1.2).

Table 5.1. Multitemporal mean, lower, and upper bound of backscattering coefficients (dB) at 95% confidence interval

Month	Ground cover	RADARSAT S6	lower	upper	RADARSAT S1	lower	upper	JERS-1	lower	upper
November/ December	Flooded forest n=41	-8.2	-9.0	-7.5				-7.4	-8.3	-6.6
	Forest n=41	-9.9	-10.1	-9.7				-8.0	-8.2	-7.8
	Pasture n=41	-12.0	-12.6	-11.5				-12.6	-13.3	-12.1
	Savanna n=33	-13.9	-14.4	-13.5				-11.0	-11.5	-10.5
	Aquatic plants n=11	-11.9	-12.4	-11.3				-13.6	-14.1	-13.4
March/April	Flooded forest	-6.9	-7.7	-6.3				-5.5	-6.3	-4.8
	Forest	-9.6	-9.9	-9.4				-7.4	-7.4	-7.1
	Pasture	-9.9	-10.5	-9.5				-10.8	-11.4	-10.1
	Savanna	-12.4	-12.9	-12.0				-9.6	-10.1	-9.2
	Aquatic plants n=16	-7.4	-7.8	-7.0				-10.5	-11.1	-10.1
May	Flooded forest	-6.6	-7.4	-6.0	-4.0	-4.8	-3.4	-4.4	-5.2	-3.7
	Forest	-8.6	-8.9	-8.4	-6.0	-6.2	-5.8	-6.8	-7.1	-6.6
	Pasture	-9.7	-10.2	-9.2	-6.3	-7.0	-5.8	-10.2	-10.9	-9.7
	Savanna	-11.8	-12.3	-11.4	-8.3	-8.6	-7.9	-9.5	-10.0	-9.1
	Aquatic plants n=12	-7.1	-7.5	-6.7	-3.3	-3.7	-3.0	-8.8	-9.2	-8.4
June	Flooded forest	-6.6	-7.4	-5.9	-4.5	-5.3	-3.9			
	Forest	-9.3	-9.5	-9.1	-7.6	-7.9	-7.3			
	Pasture	-9.7	-10.2	-9.2	-8.1	-8.4	-7.6			
	Savanna	-11.9	-12.4	-11.5	-10.1	-10.6	-9.7			
	Aquatic plants n=35	-6.9	-7.5	-6.3	-4.2	-4.4	-3.7			
August	Flooded forest	-6.9	-7.7	-6.3				-4.9	-5.8	-4.2
	Forest	-9.1	-9.4	-8.8				-7.4	-7.7	-7.2
	Pasture	-10.0	-10.6	-9.5				-11.8	-12.5	-11.2
	Savanna	-12.5	-13.3	-12.0				-10.2	-10.7	-9.7
	Aquatic plants n=15	-6.7	-7.0	-6.4				-9.0	-9.5	-8.5

n is the number of samples of each ground cover; the same masks were used to estimate the backscattering values monthly, with the exception of aquatic vegetation.

The statistical analysis of the data presented in Table 5.1 and Figure 5.1 showed that, generally, for RADARSAT S6, the mean σ^0 values of the ground cover did not change significantly ($p<0.05$) between seasons, except for November ($p<0.05$) when the σ^0 on average decreased by approximately 5dB, 1dB, 2dB, 2dB, and 1dB for aquatic plants, flooded forest, pasture, savanna, and forest, respectively. For JERS-1, likewise, the mean σ^0 values were only significantly different ($p<0.05$) for November when the σ^0 on average decreased by approximately 5dB, 3dB, 2.4dB, 1.5dB, and 1.2dB for aquatic plants, flooded forest, pasture, savanna, and forest, respectively. Note that for both RADARSAT and JERS-1, the highest σ^0 dynamic range was from the aquatic plants; and for JERS-1, flooded forest, i.e. biotopes that are highly subject to the water level variation.

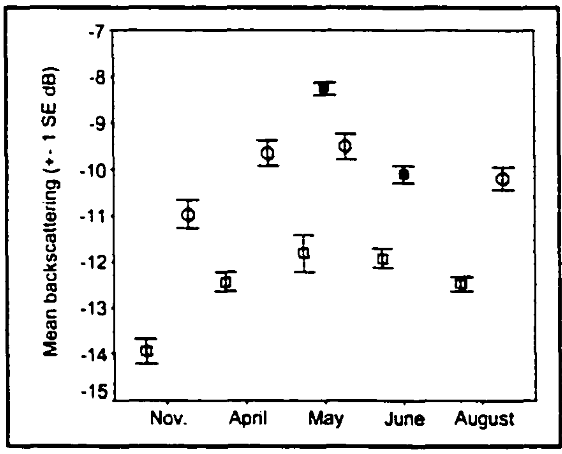

(a). Savanna

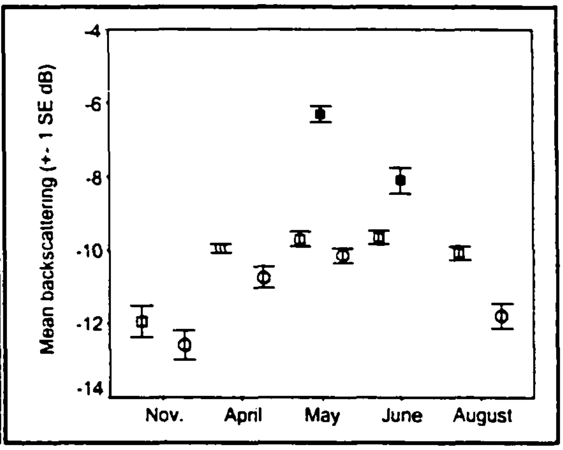

(b). Pasture

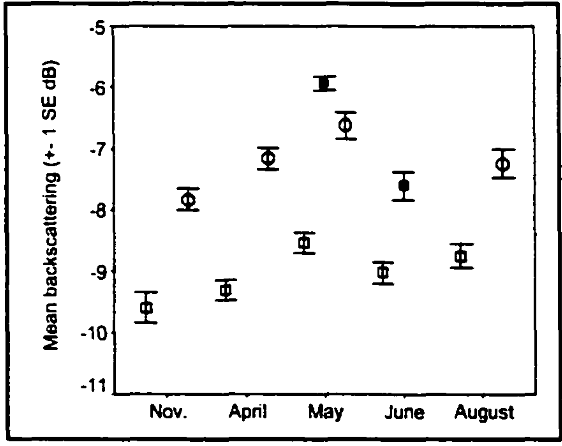

(c). Upland forest

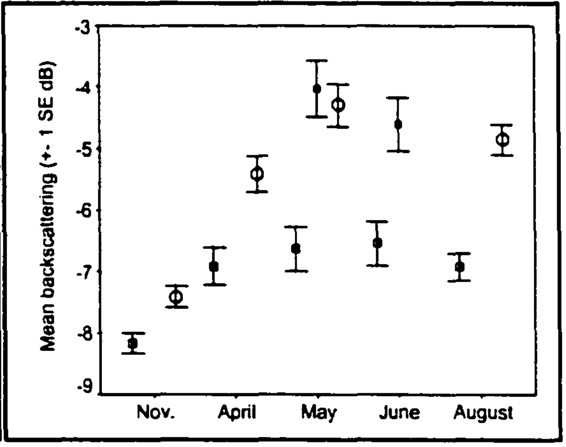

(d). Flooded forest

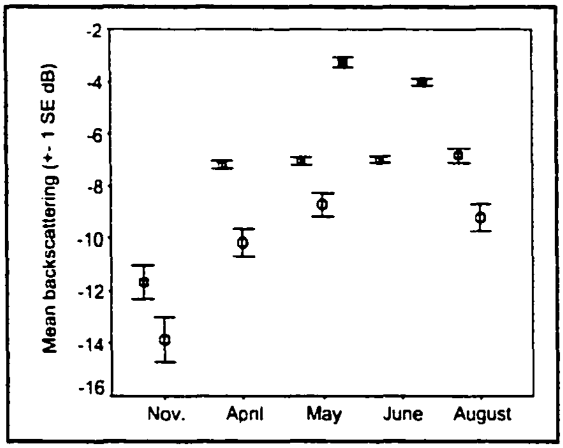

(e). Aquatic vegetation

Figure 5.1. Backscattering coefficients (dB) in the course of time for different ground cover. Open circle – JERS-1; open square – RADARSAT S6; filled square- RADARSAT S1.

For RADARSAT S1, the results showed a different scenario in terms of the multi-temporal variation of σ^0, even considering the limitations of the data set (data only for the high water period). The σ^0 was lower ($p<0.05$) by approximately 2dB for the surrounding floodplain biotones, and within the floodplain the difference was only 1dB (not significant at $p<0.05$); note that these differences in σ^0 were between images acquired in May and June (both high water periods). One possible explanation for this behavior could be the incorrect radiometric calibration on one of the S1 images. The radiometric stability test supported this consideration (section 4.1.2).

Hence, the results showed that when the floodplain was at its minimum water level the σ^0 values for both JERS-1 and RADARSAT S6 were the lowest; as the water level rose so did the σ^0 values, until they reached maximum. JERS-1 exhibited a greater dynamic range in response to the ground cover for the two extremes of water levels and also within image. This was mostly due to the greater penetration of the longer wavelength of L band and, accordingly, a greater sensitivity to the thickness of the vegetation cover when compared with C band. The following section explains in more detail the interactions between radiation and ground cover at each band. It is recognized that the following description lacks the support of radiative transfer models; however, the summary of the variation of backscattering from the different ground cover allowed a comparison of the results with model estimates and data of other regions of the world.

5.3 Backscattering Coefficients of Non-aquatic Vegetation Regions

Non-aquatic vegetation regions are specified as forest, pasture land, savanna, flooded forest, and water. These regions showed distinct backscattering values due to the different interaction of the medium (ground cover) with the microwave radiation. This interaction is a function of the characteristics of the medium, such as moisture content, geometric distribution and roughness, and the characteristics of the radiation, such as wavelength, incident angle and polarization (Ulaby et al., 1982). A combination of these characteristics defines the type of scattering mechanisms occurring between the radiation and the medium. The multi-temporal backscattering values (Table 5.1) of the different ground cover are a result of these scattering mechanisms, which are also dependent on the temporal behavior of the ground cover. Table 5.2 summarizes some of the main structural characteristics of the non-aquatic vegetation ground cover and the predominant scattering mechanisms.

In addition to these characteristics (Table 5.2) a combination of the dielectric constant (water content) of the different layers of the ground cover, and the ground surface (soil or water) generates the final backscaterring value. Radiation transfer models are the only procedure to resolve for each of these components (Dobson et al., 1996;

Wang et al., 1995). Hence the following discussion, as far as resolving for the contribution of each component to the total backscattering, is based exclusively on (i) the general characteristics of the ground cover, (ii) the recovered backscattering values from the SAR images, and (iii) the theoretical approach available in the literature.

In the study site, the most unvaried σ^o value was from water. The σ^o values were the lowest among the other ground cover for the different SAR data; -23 (±1dB), -23 (±5dB), and -16(±0.5dB), for RADARSAT S6, RADARSAT S1, and JERS-1, respectively. This was a result of specular reflection off the water opposite to the direction of the radar antenna. Generally, the lowest σ^o values were for RADARSAT S6 due its higher incidence angle (45°) when compared with RADARSAT S1 (25°) and JERS-1 (35°). We can expect that RADARSAT S6 images, regardless the season, provide the best discrimination between water and other ground cover.

The pastureland of the study area is predominantly covered by short grass-like vegetation, few random short non-woody shrubs, and bare soil. The grass-like vegetation is equivalent in size to the wavelength of C-band when compared with L-band. As a result, relatively higher trasmissivity of the radiation through this vegetation is expected at L band (Dobson et al., 1996) and therefore low backscattering values are observed (-12.6 and -10.2 dB, respectively for the driest (November) and wettest (May) periods, respectively). Conversely, C-band band radiation is expected to interact with the volume of the vegetation. However, at least for a 45° incidence angle, the observed backscattering values (-12.0 and -9.7 dB for the driest and wettest periods, respectively) suggested that the interaction was mostly the result of the roughness of ground surface. Note that for both C and L bands the lowest values occurred during the dry season when the levels of precipitation are much lower than for May. For a given surface, if the roughness remains constant, the σ^0 decreases when the moisture content of the surface decreases (Ulaby and Dobson, 1987).

A similar effect was evident for savanna areas where the vegetation (3 meters height) is sparse and the ground surface is composed of bare sandy soil and short grass; at during dry season, σ^0 were on average -14 and -11 dB for C (45°) and L bands, respectively. During the wet season, savanna areas showed values of -12 and -9.5 dB for C and L bands, respectively; the increased values are due to the higher moisture content of the surface during the wet season. In general, for both seasons, the low values of σ^0 suggested that both wavelengths interact with large patches of bare soil (surface scattering) than with the shrubs. Radiative transfer models are needed to better understand the interaction mechanisms. Figure 5.2 shows the ground view of a savanna region. Note the sandy soil covered by short grass and sparse shrubs.

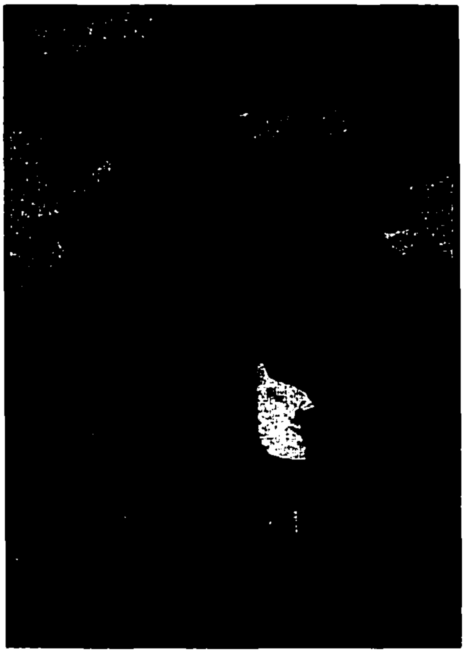

Figure 5.2. Savanna area showing the sparse short shrubs and grass cover.

The temporal variation of the backscattering values was the lowest for upland forest. The values were on average -8.6 to -6.8 dB for C and L bands, respectively, and the lowest values (less than 1dB difference) were for the dry season image (Figure 5.1c). The C band σ^0 was primarily a result of the interaction of the radiation with the top structures of the canopy (leaves). Volume scattering was the dominant mechanism. On the other hand, for the L band, the longer wavelength has deeper penetration into the canopy; consequently, the radiation interacts with the different scatter elements of the canopy (leaves and branches). Volume scattering is the dominant mechanism. Additionally, for areas less densely treed, some interaction between the canopy and the ground surface can also be expected. In this way, both volume scattering and surface scattering contribute to the total backscattering coefficient. Such an explanation may justify the differences between the estimated backscattering values and the values observed by other researchers.

Similar backscattering values were estimated for Amazonian forest (Hess at al., 1995; Valeriano, 1996; Luckman et al., 1997), and other evergreen broad-leaf forests of the world (Imhoff, 1995; Dobson et al., 1995). However, generally the σ^0 for the L band is lower than that for the C band. The upland forest in the study area is not a typical dense rain forest; it is mostly composed of secondary vegetation and a dense savanna (RADAMBRASIL, 1976). Therefore, it is hypothesized that the transmissivity of the radiation at L band wavelength through the less dense canopy of the trees is greater than at C band wavelength (Dobson et al., 1996). The radiation penetrates deeply and interacts with the trunk and ground surface; as a result, the total backscattering is a summation of volume-scattering interaction with the branches and double return (Ulaby, et al., 1982). As the ground surface gets rougher or moister the surface backscattering increases and the total backscattering increases. On the other hand, at a shorter wavelength (C band), the interaction is still mostly with the upper canopy scatters (leaves) regardless of the density of the forest. For dense tropical forest (Valeriano, 1996; Luckman et al., 1997), L band does not penetrate as deeply and is attenuated within the canopy; as a result a lower signal is returned when compared with C band. The different structure of the forest may explain the results obtained in this study which differ with those of other authors; however, further analysis requires a more specific description of the local forest and unfortunately, these data are not available.

Forested areas that are seasonally flooded showed a large temporal σ^o variation. At low water period, the σ^o values were very similar to those observed from upland forest. At high water period, L band backscattering is higher than C band (the difference is approximately 2.2 dB). With an incidence angle of 35° (JERS-1), the long wavelength of L band interacts with the canopy elements and penetrates further into the tree canopy. As a result, additional interaction occurs between the trunk and the water underneath, and vice-versa. (Wang et al., 1995; Proisy et al., 2000). Double bounce is the dominant scattering mechanism. The total σ^o was on average -4.4 dB. At a 45° of incidence angle (RADARSAT S6), the short C-band wavelength interacts mostly with the canopy upper layer (Wang et al., 1995; Valeriano, 1996); the σ^o was on average -6.6 dB. Volume scattering is the dominant scattering mechanism.

At a steeper incidence angle, 25°, C band radiation (RADARSAT S1) interacts with the canopy elements and penetrates further into the canopy; consequently, interaction occurs between the trunk and the beneath water, and vice-versa. Similar to L band, the double-bounce mechanism is the dominant scattering mechanism. The total σ^0 was on average -4.3dB, which is very similar to the mean value observed for L-band. Figure 5.3 illustrates the dominant scattering mechanisms of C and L bands.

A comparison of the estimated backscattering values and the observed/modeled backscattering from other wetland forests around the world showed some differences. Lower backscattering values (average of -7.8dB) were reported from pine and cypress (excurrent) wetlands of Southwestern Florida at C-band (VV polarization and 20° of incidence angle -ERS-1) (Kasischke and Bourgeau-Chavez, 1997). The difference might be related to both the different structure of the vegetation and the polarization of ERS-1. Generally, decurrent trees (present in the study area) have larger number of large horizontal branches than excurrent trees. Furthermore, broad leaves are larger than needle leaves. The interaction of large horizontal elements of decurrent trees with the radiation enhances the HH return in relation to the VV return (Valeriano, 1996).

Model simulation (Proisy et al., 2000) has shown that the scattering mechanisms associated with the interaction of C (HH) and L (HH) bands, both at 35° incident angle, with mangrove forest were indeed similar to the mechanisms suggested by the results of this research with backscattering at C (45°) and L (35°). However, at least for L (HH), measured and simulated backscattering values of roughly -9 dB for mature mangrove forest were lower than our backscattering values (Proisy et al., 2000). Once more, understanding these differences is only possible with the acquisition of a more complete data set, and this is beyond the scope of this research.

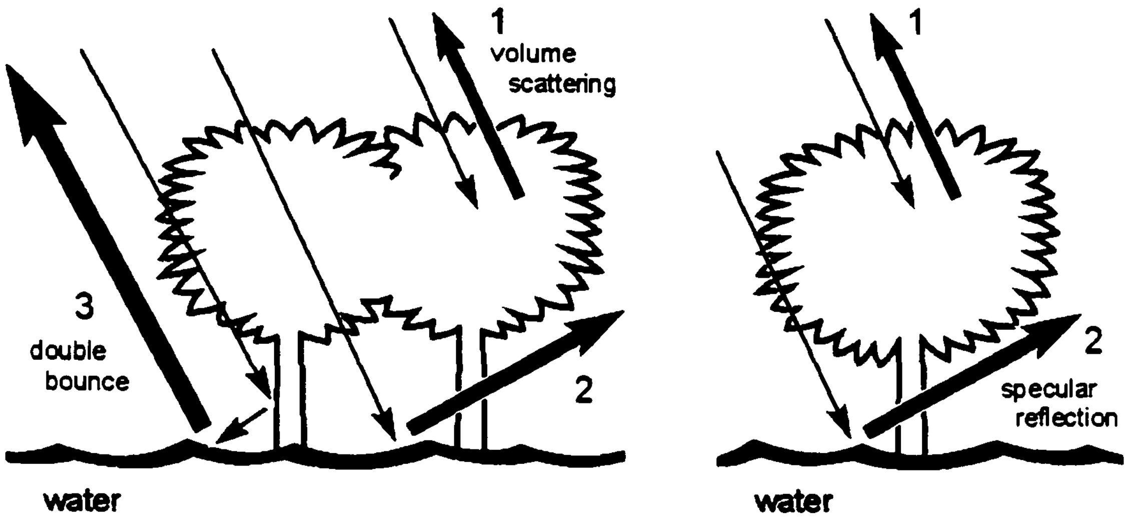

(a)L band interaction (b)C band interaction(45°incidence angle)
Figure 5.3. Schematic representation of the scattering mechanisms at C and L bands for flooded forest; the thickness of the returning arrows (1, 2, and 3) represents magnitude of scattered radiation.

During flooded conditions the σ^0 values for the different acquisition modes commonly change, according to the degree of defoliation of the flooded trees. For instance, *P. munguba* (30 m height above water) and *C. guianensis* (2 meters height above water) lose their leaves during this period. The σ^0 values increased to –5 and –3dB for C (45° of incidence angle) and L bands, respectively, due to less attenuation by the leaves, and as a consequence there was deeper penetration of the radiation and therefore pronounced double bounce effect between the tree trunk and water (Ulaby et al., 1982). Wang et al., (1995), showed similar results for simulated C and L band (HH polarization) backscattering from defoliated flooded trees of the Amazon (very low leaf area index). However, the total backscattering calculated (roughly -8dB) by the authors was relatively lower than the values observed from known flooded forested areas in this study site. Hess et al. (1995) showed estimated values from flooded Amazonian forest ranging from -6 to

-4dB at L band-HH, which are similar to our estimates. Figure 5.4 illustrates foliated and defoliated flooded forest.

(a) Foliated during the dry season

(b) Defoliated during the high water season

Figure 5.4. Foliated and defoliated *C. guianensis* during low and high water season.

M. arborescens is a tree-like semi-aquatic plant that colonizes areas where moisture is retained even during the low water period. The main structural characteristics of this species are as follows: form dense patches, 3 m height above water or 7m total height, cylindrical vertical trunk of 4 cm diameter, and a clump of approximately 4 broad leaves 50 cm long and 40 cm wide at an angle to the trunk of roughly 45 degrees. Figure 5.5 illustrates this type of vegetation. Overall, σ^0 values from this vegetation were as high as the values observed for defoliated flooded trees, possibly due to the same type of interaction with microwave radiation. The backscattering was on average -5.7, -2.4, and -4.8, at RADARSAT S6, RADARSAT S1, and JERS-1, respectively. At the low water period, the σ^0 from *M. arborescens* remained high due to the expected high moisture content of the areas colonized by this species. Backscattering values were on average -8 and -7dB at C and L bands, respectively.

Figure 5.5. Tree-like aquatic vegetation during the low water season.

The ground cover that exhibited the greatest temporal variation was aquatic vegetation. The following section discusses the effects of the biophysical characteristics of aquatic vegetation on SAR backscattering coefficients.

Table 5.2. General discription of some important vegetation found in the study site (adapted from Dobson et al., 1996)

	Ground cover						
	Non woody vegetation		Woody vegetation				
	Pasture land	Aquatic vegetation	Upland		Seasonally flooded		
Surface	Soil	water	Soil		Soil/water		
Growth form	Blade-like		Shrubs (savanna-sparse vegetation)	Decurrent (savanna dense and secondary forest)	Decurrent		Tree-like aquatic vegetation
Structural Characteristics							
Trunk	None		Many small trunks with random orientation	Cylindrical	Cylindrical		Cylindrical
Branches	Non-woody stalks or stems		Many small branches	Branches forked and randomly oriented	Branches forked and randomly oriented		None
Foliage	Blade-like erectophile - short	Blade-like erectophile - tall	Broad leaves	Broad leaves	Broad leaves	Defoliated	Blade-like clump at top of trunk.
Scattering mechanism							
C-band (45°)	Volume scattering	Volume scattering	Surface-scattering (quasi-specular	Volume-scattering	Volume-scattering	Double-bounce	Double-bounce
C-band (25°)	Volume scattering	Volume and double bounce	Surface-scattering	Volume-scattering	Volume-scattering	Double-bounce)	Double-bounce
L-band (35°)	Surface scattering (quasi-specular)	Volume scattering and specular reflection	Surface-scattering (quasi-specular)	Surface and volume-scattering	Double-bounce	Double-bounce	Double-bounce
Measured backscattering							
C-band (45°)	-10.5dB	-6.7dB	-12.5 dB	-9.1 dB	-6.8	-5	-5.7
C-band (25°)	-7.5 dB	-3.7dB	-9.2 dB	-6.5 dB	-4.3	-2.3	-2.4
L-band (35°)	-11.6 dB	-9.2dB	-10.1 dB	-6.5 dB	-4.9	-3	-4.8

5.4. Analysis of the Backscattering Coefficients from Aquatic Vegetation

The following analysis is based on the biophysical parameters of aquatic vegetation collected in the field and the backscattering coefficients extracted from the SAR images. This section presents (1) the statistical approach; (2) the analyses and model validation for estimating above water biomass of aquatic vegetation; and, (3) discusses the relationship between backscattering coefficients and aquatic vegetation properties.

5.4.1 Statistical method

The approach for the statistical analysis of the aquatic vegetation parameters and satellite data involved five main phases, namely (adapted from Neter et al., 1990):

(i) Data collection – sampling the backscattering coefficients;

(ii) Check on data quality and the relationship between SAR data and aquatic vegetation parameters;

(iii) Determine the possible statistical models for estimating above water biomass;

(iv) Model selection for estimating above water biomass; and

(v) Model validation for estimating above water biomass.

For each of these phases a series of statistical analyses were performed aimed at determining the best model to estimate above water biomass using SAR data as independent variables. The following section explains the adopted criteria for each phase of the statistical analysis.

(i) Data collection

The geographic coordinates (latitude and longitude) of each sample site were located on the georeferenced SAR images and masks defining homogeneous area in the images were determined for each site. The masks were, on average, larger than 100 pixels, which satisfied the assumption of the normality for each sample and ensured that the estimated backscattering values were between ±1dB of the true mean values ($p<0.05$)

(Laur et al., 1996). The definition of homogeneous areas was based primarily on the following data: (a) the visual description of the 100m surrounding the sample site (section 2.2.3), (b) the hand-held 35 mm photographs (North, South, East, and West) of the sample site, (c) the aerial photographs, 1:20,000 and 1:50,000 scales and the low altitude photo data, and (d) the evaluation of the variability of a set of sample sites spaced at a known distance.

The visual description of the 100 meters surrounding the sample site together with the hand-held 35-mm photographs, provided information on the dominant plant species, height, and distribution. The aerial photos were extremely useful in identifying possible flooded trees in the area surrounding the sample site. Finally, four sample sites distanced 200 m apart, and a fifth 900 m apart, were evaluated according to the dry biomass, height, and number of stems per m^2. Table 5.3 shows the parameters for the five sample sites. Biomass, height, and number of stems were very similar (low standard deviation) for the five sample sites spread within an area of approximately $0.2km^2$. This result corroborates the description of occurrence of large homogeneous stands of aquatic vegetation in the study area. Consequently, we can assume that the measured backscattering coefficients under the masks (more than 100 pixels) surrounding the sample site were representative of the measured biophysical properties of the site.

Table 5.3. Biophysical properties of the sample sites used on the evaluation of homogeneity of the area.

Sample site	Dominant species	Dry biomass (g/m^2)	Height (m)	Stem /m^2
# 30	H. amplexicaulis	303	0.9	116
#31	H. amplexicaulis	373	0.85	150
#32	H. amplexicaulis	238	0.85	108
#34	H. amplexicaulis	268	0.9	100
#35	H. amplexicaulis	295	0.9	92
Total mean (standard deviation)		295(50)	0.88(0.003)	113(22)

Appendix I presents the estimated backscattering values for each sample site for the entire data set. Table 5.4 summarizes the variables available for each field campaign used in this statistical analysis.

Table 5.4. Data set available for each field campaign.

Field campaign	Fresh-biomass	Dry-biomass	Height	% water	% canopy cover	Radarsat S6	JERS-1	Radarsat S1
May 1996	✓	✓	✓	✓	✓	✓	✓	✓
August, 1996	✓	✓	✓	✓	✓	✓	✓	
Nov., 1996	✓	✓	✓	✓	✓	✓	✓	
April, 1997	✓	✓	✓	✓	✓	✓	✓	
June, 1999	✓	✓	✓	✓	✓	✓	●	✓

✓- Represents collected data and ● represents data available from other period; this data set is only for above water properties.

Note in Table 5.4 that JERS-1 data were not acquired concomitant to the field campaign of June 1999 (section 2.3.2 gives some detail about the lack of acquisition of JERS-1 images in 1999). Based on some criteria we assumed that the backscattering coefficients of the JERS-1 image acquired in 1996 could be associated with the ground data collected in June 1999. The following observations were used to support this assumption:

(1) There was no significant difference between the water level of May 1996 (7.4m) and June 1999 (7.49m); since the water level is the main regulator of the life cycle of the aquatic vegetation, similar environmental conditions were assumed for both periods.

(2) There was no significant difference ($p<0.05$) in above water biomass and height of the aquatic vegetation for the two periods May 1996 and June 1999 (section 3.4). This corroborates the first observation, and therefore similar backscattering coefficients were expected for images acquired in May 1996 and June 1999.

(3) There was no significant difference ($p<0.05$) for the mean backscaterring values of RADARSAT S6 from aquatic plants for these two periods, which strengthens the second observation.

(4) A multi-temporal analysis of the backscattering values of JERS-1 from upland forest (temporally stable ground cover) showed that the differences between wet periods were less than 0.5dB (recall section 4.1.1, Figure 4.2c), which validated the radiometric stability of JERS-1 data. Based on these observations, we can assume that if the JERS-1 image were to be acquired in June 1999 it would be very similar to the JERS-1 image acquired in May 1996. This assumption allowed the establishment of relationships between backscattering coefficients estimated from the JERS-1 image acquired in May 1996 and the aquatic vegetation parameters collected in June 1999, making the statistical analysis more robust.

A "backscattering index" (σ^o_{index}) was also used in the statistical analysis. The σ^o_{index} was an adaptation of the approach suggested by Pope et al., (1994). According to the authors, the average of like-polarized (VV and HH) backscattering at C band reflects above water biomass of marsh vegetation. The theoretical approach behind the average like-polarized index is the increased attenuation of VV radiation by vertically oriented structures (grass-like herbaceous) compared with HH radiation. Thus, VV and HH polarization provide preferential information related to the canopy and the ground, respectively. This can be interpreted as higher backscattering values at VV than at HH polarization. However, for areas with a high density of plants, at C band, the canopy is the major attenuater of the radiation regardless of the polarization (Ulaby et al., 1986; Ferrazzoli et al., 1997), which can be interpreted as high backscaterring at both VV and HH polarization. In this sense, as the density or above water biomass of the vegetation increases so does the index (Pope et al., 1994).

Unfortunately, our data set was limited to only HH polarization; however, it was expected that average wavelength magnitude would follow the above-mentioned theoretical principle. For low biomass, C band (45° of incidence angle) contributes mostly to the σ^o_{index}; for high biomass, the contribution of L band (35° degrees of incidence angle) to the σ^o_{index} becomes significant resulting in a higher σ^o_{index}.. σ^o_{index} was obtained from the following equation:

$$\sigma^{o}{}_{index} = \frac{\sigma^{o}{}_{C} + \sigma^{o}{}_{L}}{2} \qquad \text{Equation 5.2}$$

where σ^o_C and σ^o_L are the backscattering coefficients at C band (RADARSAT S6) and L bands (JERS-1), respectively, in linear units. The values were subsequently converted to dB.

(ii) Check on data quality and analysis of the statistical relationship between variables–screening data

Once the data were properly organized in a spreadsheet (Appendix I), statistical measures such as mean, standard deviation, standard error of the mean, scatter plots, normality test, and the statistical relationship between variables (correlation matrix) were determined. Table 5.5 presents the results of both statistical measures and normality tests for each variable; Table 5.6 presents the linear correlation matrix between SAR data and aquatic vegetation parameters; the last table omits the duplicate terms.

According to Table 5.5 the variables $\sigma^o_{\text{RADARSAT S1}}$ and water content did not follow a normal distribution. The underlying assumption of normality of the data distribution is crucial for parametric statistical methods (Neter et al., 1990). In the event of a non-normal distributed variable in a regression model, such as the case of the variables $\sigma^o_{\text{RADARSAT S1}}$ and water content, the residual errors of the regression can not be presupposed as independent and normally distributed. Additionally, the correlation coefficients between $\sigma^o_{\text{RADARSAT S1}}$ and the aquatic vegetation parameters were not significant ($p>0.05$). The variable $\sigma^o_{\text{RADARSAT S1}}$ showed a positive significant correlation only with $\sigma^o_{\text{RADARSAT S6}}$ acquired at the same period; however, the lack of calibration of $\sigma^o_{\text{RADARSAT S1}}$ from June 1999 prevented a detailed analysis of the data set. The variable 'water content' and SAR variables were not significant ($p > 0.05$); regardless, a negative weak relationship was observed.

Table 5.5. Descriptive statistics and normality test

Variable	Number of samples	Mean	Standard error of the mean	Standard deviation	Significance of normality
Fresh weight (g/m^2)	83	2101	145	1363	$p<0.05$
Dry weight (g/m^2)	83	472	31	284	$p<0.05$
Log of dry weight	83	2.6	0.0037	0.33	$p<0.05$
Log of height	83				
Height (m)	83	0.86	0.0035	0.32	$p<0.05$
Water content (%)	83	76	0.83	7.5	n.s.
Canopy cover (%)	76	86	1.1	9.4	$p<0.05$
$\sigma^o_{\text{RADARSAT S6}}$	81	-7.3	0.16	1.4	$p<0.05$
$\sigma^o_{\text{JERS-1}}$	80	-9.5	0.24	2.2	$p<0.05$
σ^o_{index}	80	-8.2	0.17	1.5	$p<0.05$
$\sigma^o_{\text{RADARSAT S1}}$	45	-3.8	0.13	0.9	n.s.

n.s. stands for not significant; σ^o values are in dB.

Table 5.6. Linear correlation matrix between SAR data and aquatic vegetation parameters

Variables	$\sigma^o_{\text{RADARSAT S6}}$	$\sigma^o_{\text{JERS-1}}$	σ^o_{index}	$\sigma^o_{\text{RADARSAT S1}}$
Fresh weight (g/m^2)	0.470	0.535	0.573	0.167*
Dry weight (g/m^2)	0.554	0.636	0.672	0.098*
Log of dry weight	0.781	0.664	0.822	-0.011*
Height (m)	0.628	0.577	0.685	0.171*
Log of height	0.873	0.706	0.866	0.201*
Water content (%)	-0.204*	-0.123*	-0.178*	0.248*
Canopy cover (%)	0.302	0.420	0.396	-0.151*
$\sigma^o_{\text{RADARSAT S6}}$		0.576	0.902	0.580
$\sigma^o_{\text{JERS-1}}$			0.865	0.016*
σ^o_{index}				0.272*

* means that the correlation coefficients are not significant; the critical value at $p<0.05$ and $\nu = 1, 80$ (independent variable, degree of freedom) is 0.217, an for $\nu = 1, 44$ the critical value is 0.288.

Significant positive linear correlation coefficients ($p<0.05$) between SAR data and fresh biomass, dry biomass, height, and percentage of canopy cover of the aquatic vegetation were observed. Above water fresh and dry biomass variables were highly correlated ($r > 0.8$) and the relationships between SAR data and these variables were higher with dry biomass. Further, ecologically, the dry biomass is a standard parameter for the study of productivity; consequently, fresh biomass was considered a redundant variable in the statistical analysis. The variable "percentage of canopy cover" showed a weak positive relationship with the SAR data.

The relationships among the SAR data (except for $\sigma^{o}_{RADARSATS1}$) were positive and significant ($p<0.05$). Note the very high correlation between σ^{o}_{index} and $\sigma^{o}_{RADARSATS6}$ and σ^{o}_{JERS}; σ^{o}_{index} is the average value when σ^{o}_{RSATS6} and σ^{o}_{JERS} were combined; consequently, the relationship between these variables was always high. The analysis of these significant relationships is further developed in section 5.4.1.

(iii) Determine the possible statistical models for estimating above water biomass

The foregoing analysis was performed exclusively on the relationship between the SAR data (RADARSAT S6, JERS-1, and index) as independent variables and above water dry biomass as dependent variable. The analysis of the scatter plots between SAR data and dry biomass suggested that either a logarithmic regression function or a transformation of the dependent variables was the best fit for the regression analysis. A logarithmic transformation $Y_i' = \log_{10} Y_i$ was examined, where Y_i is above water dry biomass of the aquatic vegetation. Appendix I and Table 5.6 present the data for the transformed dependent variables and the new increased correlation coefficients with the SAR data, respectively. Figure 5.6 illustrates the scatter plots and the linear regression lines of the logarithmic transformed data (dependent variables) and the SAR data (independent variables). On the basis of this analysis it was decided to use the transformed data as the dependent variable for generating all possible linear regression models for estimating above water dry biomass.

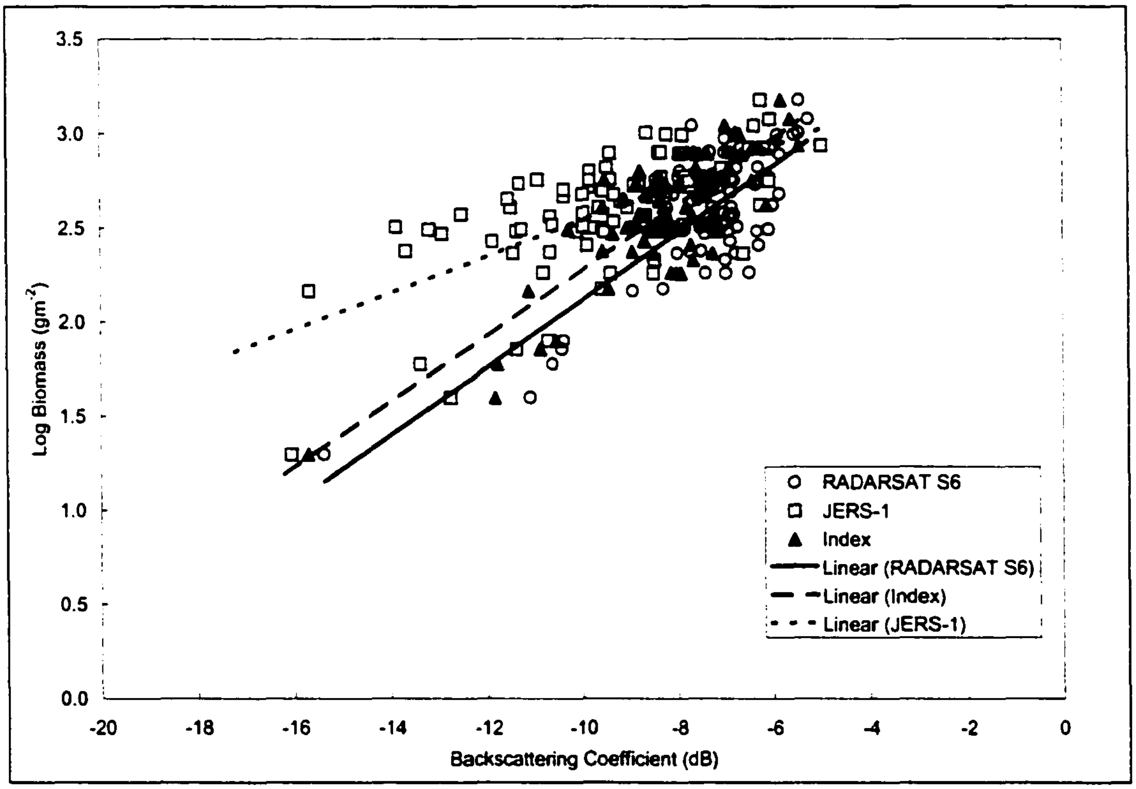

Figure 5.6. Variations of the log of above water dry biomass as a function of backscattering coefficient for RADATSAT S6, JERS-1, and the Index.

Linear regression equations were fitted to log of above water biomass (log biomass) versus SAR data. Further, a stepwise linear multiple regression was used to analyze the possibility of incorporating more than one independent variable in the linear regression model. The stepwise method has the following representation:

$$Y_i = B_o + B_1X_{i1} + \ldots B_nX_{in} + e_i \qquad \text{Equation 5.3}$$

where Y_i is the response in the ith case, X_{in} are the independent variables, B_n are the regression coefficients of the model and e_i is the error term. The stepwise procedure is an automatic search method in which the best subset of independent variables is selected according to some criteria. In the first step, this procedure calculates the F statistic and the correlation coefficient for each individual independent variable. The F statistic is defined by the relationship between the mean square of the regression (MSR) and the mean square of the residual (MSE). The procedure selects the independent variable with both the highest correlation coefficient and the highest F statistic at a 95% level of significance. In a second step, the procedure adds the variable with the second largest F statistic; a new F statistic called partial F, is calculated incorporating the second independent variable to the model. The partial F is tested at the 95% level of significance, and the final decision is made for either the inclusion or dropping of the second variable to the model. This procedure continues until all the independent variables are evaluated. An important consideration for the addition of any variable in the model is the test of multicollinearity between independent variables. Multicollinearity is when the independent variables are highly correlated; as a result of multicollinearity, the regression coefficients are unstable (Neter et al, 1990). Multicollinearity was expected between the σ^o_{index} and both $\sigma^o_{RADARSATS6}$ and σ^o_{JERS} due to the observed high coefficients of correlation (Table 5.6).

(v) Model selection

The linear regression models for each individual independent variable and the results of the stepwise procedure were evaluated according to the following statistical measures: (1) adjusted R^2, (2) MSE (mean square of the residual), (3) *F* statistic, (4) RMSE (root mean square error), (5) normal probability plot of the residuals, and (6) the standardized residual plot against the estimated values of biomass. Table 5.7 shows the regression models and the above statistic measures calculated using the entire data set. The RMSE is expressed in gm^{-2} of above water biomass.

Table 5.7. Regression models and statistic measures for estimating above water biomass – entire data set.

Model	Number of samples	R^2 adjusted	MSE	Statistic F	RMSE (gm^{-2})	Error
$Y = 3.898 + 0.179 * \sigma^o_{RSATS6}$	81	0.605	0.041	123.48	219	42%
$Y = 3.516 + 0.0976 * \sigma^o_{JERS}$	80	0.434	0.058	162.27	214	53%
$Y = 4.022 + 0.175 * \sigma^o_{index}$	80	0.671	0.034	61.498	206	34%

The analysis of the statistical measures suggested that the models best fitted for estimating biomass included the σ^o_{index} as independent variable. The multicollinearity between the SAR data prevented the inclusion of more than one independent variable in the model. According to the statistical evaluation, the model including σ^o_{index} showed the following characteristics:

(1) The highest adjusted R^2; adjusted R^2 takes into account both the number of samples and number of parameters in the model.

(2) The lowest MSE; MSE is an estimate of the variance of the regression and is given by:

$$MSE = \frac{\sum (Y_i - Y_{iest})^2}{\upsilon} \qquad \text{Equation 5.4}$$

where Y_i and Y_{iest} are the observed and estimated *i*th biomass case, respectively, and ν is the degree of freedom.

(3) The *F* statistic was not the highest; however, this was explained by the lower values of the mean square error of the residual and the mean square error of the regression compared with these values for the other models.

(4) The lowest RMSE and percentage of error of the estimate; RMSE is often used to assess the accuracy of a model against a set of independent observations and is defined as follows:

$$RMSE = \sqrt{\frac{\sum (Y_i - Y_{iest})^2}{N}} \qquad \text{Equation 5.5}$$

where N is the number of samples and Y_i and Y_{iest} are the observed and estimated values of biomass, respectively. In this analysis the observations were not independent since they were used to build the model; nevertheless, the RMSE was used as a measure of the mean difference between the observed and estimated biomass for the specific model. The percentage of error is the mean percentage of difference between the estimated and the observed above water biomass.

(5) The probability plot of the residuals (Figure 5.7) showed near-normal distribution of the residuals, which suggested the aptness of the linear model for estimating biomass.

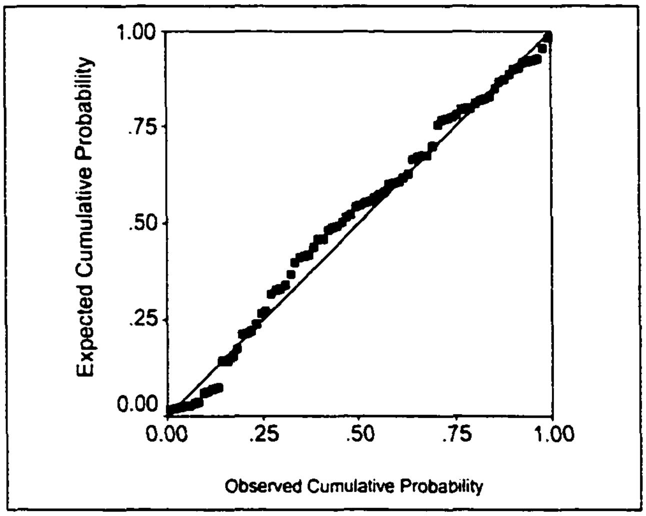

Figure 5.7. Normal probability plot for above water biomass and Index

(6) The plot of standardized residuals against the predicted value showed proper distribution of the residuals (Figure 5.8). The standardized residuals are very helpful in identifying outlying observations and are defined as follows:

$$e_i' = \frac{e_i}{\sqrt{MSE}} \qquad \text{Equation 5.6}$$

where e_i' is the standardized residual of the *i*th observation, e_i is the residual, and MSE is the mean square error of the residual. The analysis of the plot showed that the residuals were randomly departing from zero, i.e. there was no systematic trend for positive or negative values. Further, 100% of the standardized residual values were within ±2 interval of departure from zero, once more, showing the normality of the residual distribution and therefore the appropriateness of the linear model. The distribution of the residuals also suggested that there were no points lying beyond the scatter of the remaining residual by more than 3 standard deviations from zero; accordingly, no obvious outliers could be detected in the data set. A closer analysis of the plot suggested that there was a trend in underestimating small values of biomass, but the residuals were in general evenly distributed on both sides of the zero line.

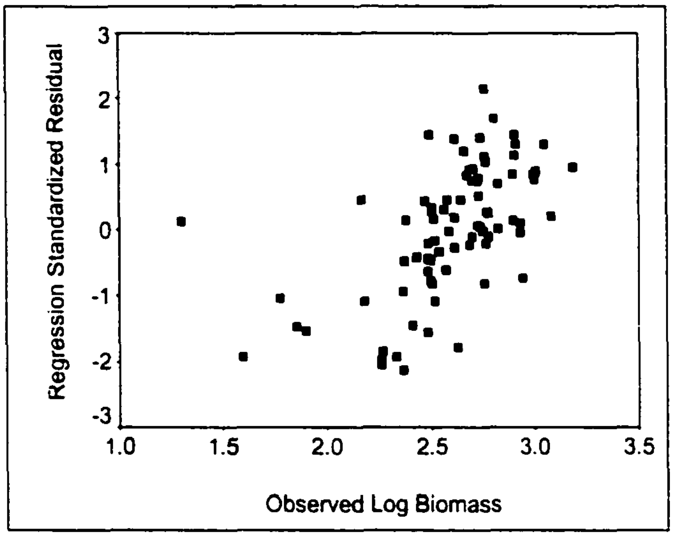

Figure 5.8. Residual plot of standardized residual and observed log biomass

In summary, the analysis of the statistical measures suggested that the model, including σ^{o}_{index}, was appropriate for estimating biomass; however, some problems were identified such as the potential of underestimating lower biomass values and the relative large RMSE and percentage of error. This is a reflection of both the adjusted R^2 values (0.67 or a correlation coefficient of approximately 0.82) and the saturation level for the σ^{o} coefficients (next section). The restricted data set does not allow further investigation for remedial action regarding these problems. The model including σ^{o}_{index} as an independent variable was selected for the final model validation.

(vi) Model validation

The statistical model was validated through the splitting of the entire data set into two sets: (1) the model-building set, which was used to develop the model, here called, the test-model, and (2) the validation set, which was used to evaluate the predictive capability of the test-model. The validation set was randomly chosen and comprised 25% of the entire data set. Table 5.8 presents the regression results for the test-model.

The test-model was evaluated according to the same statistical measures presented in the previous section. In addition, the statistic measure MSPR (mean square prediction error) was calculated. MSPR measures the predictive capability of the regression test-model through the prediction of the validation cases. The test-model is considered capable of prediction if the MSPR (validation set) value is close to the MSE value of the test-model. Both MSPR and MSE are estimators of the variance of the model, in this case for the validation data set and the test-model, respectively. MSPR is calculated as follows:

$$MSPR = \frac{\left(\sum (Y_i - Y_{iest})^2\right)}{n} \qquad \text{Equation 5.7}$$

where Y_i is the observed value in the *i*th validation sample, Y_{iest} is the estimated value for the *i*th validation estimated by the test-model, and *n* is the number of validation samples.

The evaluation of the statistic measures showed that the test-model had the same behavior as its parent data set (model built with the entire data set–Table 5.7). (1) The analysis of residual plots (Figure 5.9) showed the same pattern as the model with the entire data set, i.e. the test-model was appropriate for estimating biomass. (2) The estimated validation samples showed that the MSPR value was approximately similar the MSE values. (3) Further, for the model validation, RMSE was similar to the RMSE calculated for the parent model. RMSE was correctly calculated based on the prediction of the validation set through the test-model. Accordingly, the test-model, including σ^o_{index}

as independent variable, was considered valid, which suggested that the parent model is stable and suitable for estimating above water biomass. After the model had been validated, the entire data set was used for estimating the final model (parent model). The final model has already been presented in Table 5.7.

Table 5.8. Regression results based on model-building and validation data set for above water biomass and Index

Model-building set	Number of samples	R^2 adjusted	MSE	Statistic F	MSPR	RMSE (g/m^2)
$Y = 4.186 + 0.193 * \sigma^o_{index}$	60	0.636	0.031	104.27	0.046	236

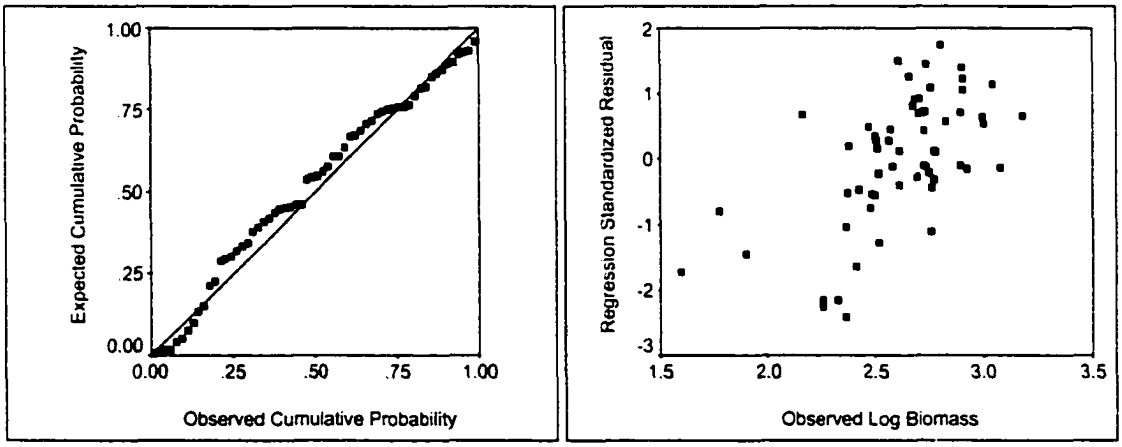

Figure 5.9. Residual plots for above water biomass versus Index – test-model. (a) Normal probability plot; (b) residual plot against observed log biomass

5.4.2. Relationships between SAR backscattering coefficients and aquatic vegetation parameters

5.4.2.1.Temporal variation of backscattering values and backscattering mechanisms

Table 5.9 shows the mean backscatering values from aquatic vegetation for the different periods of data acquisition. The mean σ^0 values did not change significantly ($p<0.05$) between seasons, except for November when the σ^0 on average decreaseed in approximately 5dB for both RADARSAT S6 and JERS-1. Figure 5.10 shows this temporal variation pattern of the σ^0 values and also the variability of the σ^0 values within each period. The differences among the values of biomass and height of the plants within each period introduce the variability of the backscattering values within the period. Hence, even though there was no significant difference ($p<0.05$) in either the mean above-water biomass or the height of the plants between periods (except November), there were still some differences within each period, and these differences clearly affected the backscattering values. This topic will be discussed in the following section.

Table 5.9. Temporal variation of backscattering coefficient, biomass, and height of aquatic vegetation (*H. amplexicaulis*)

Time	$\sigma^o_{RADARSATS6}$ (dB)	$\sigma^o_{RADARSATS1}$ (dB)	σ^o_{JERS-1} (dB)	Above-water Biomass (gm^{-2})	Above water Height (m)
November	-11.9(2.4)	-	-13.6(2.5)	92(101)	0.2(0.1)
April	-7.4(0.7)	-	-10.5(2.2)	279(93)	0.8(0.2)
May	-7.1(0.6)	-3.3(0.7)	-8.8(1.5)	489(281)	0.9(0.2)
June	-6.9(0.8)	-4(0.9)	-9(2.2)	611(285)	1(0.3)
August	-6.7(0.7)	-	-9(1.4)	541(206)	0.8(0.2)

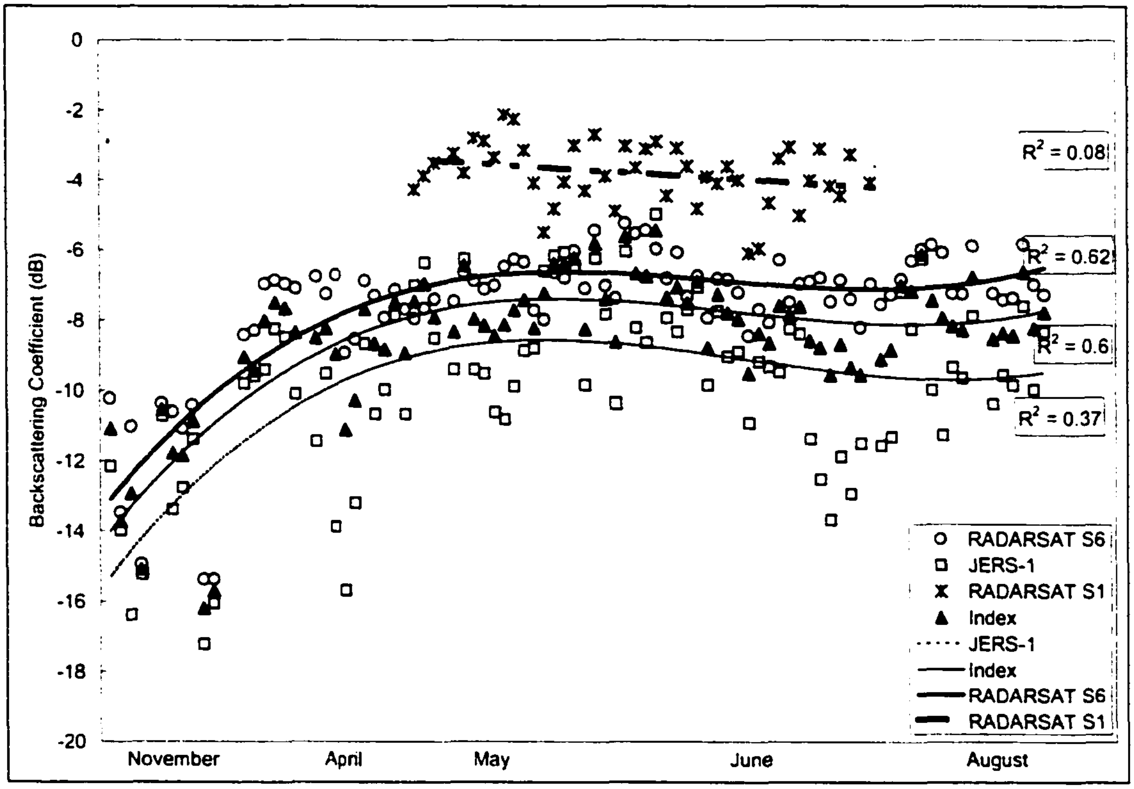

Figure 5.10. Temporal variation of the radar backscattering coefficients (dB)

The temporal variation pattern of backscattering values was representative of the growth cycle of the plants - as the plants started to grow with the rising water in November (lower σ^0), quickly developed a canopy (increase in σ^0) that did not change significantly throughout the year (saturation of σ^0), and collapsed by the end of the cycle (saturation of σ^0). The quick growth was a result of both stem growth and replacement of photosynthetic material (Piedade et al., 1991); hence, a constant above-water canopy was maintained during the growth and flowering periods. A schematic representation of both the growth cycle of the plants and the backscattering pattern is illustrated in Figure 5.11.

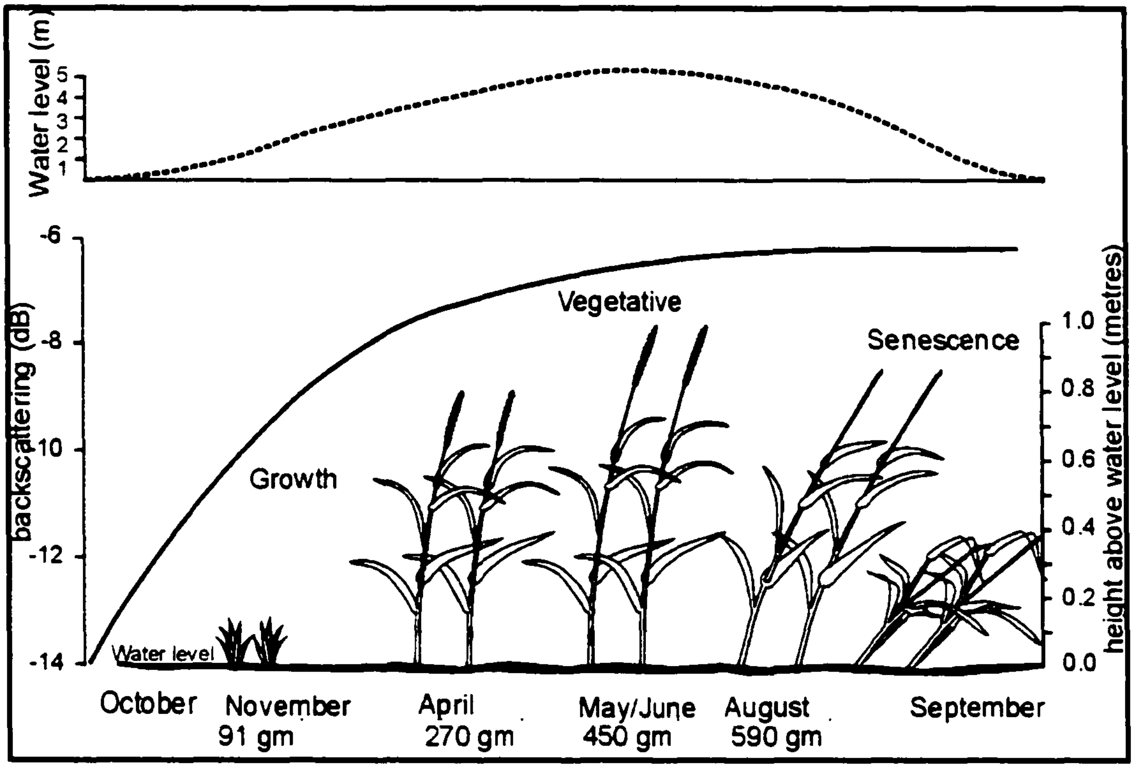

Figure 5.11. Schematic representation of the growth cycle and the temporal backscattering coefficient of RADARSAT S6. Values of above water biomass of the months are shown. The top diagram represents the water variation as a function of time. Note that the scales for water variation and height are not the same.

As the water rose, stands of *H. amplexicaulis*, the most common species in the study area, showed a density of approximately 111 stems m^{-2} (± 40, n=75 quadrats), five leaves of 25 cm long and 2 cm wide on average, stems of 0.85 m high and 0.4 cm of diameter, and a vertical span occupied by the canopy structures of approximately 40 cm (section 3.3). Given the above water architecture of this plant, different scattering mechanisms were expected due to the distinct interaction with the microwave radiation. At the high water stand, the most important scattering mechanisms were specular scattering, volume scattering, and double-bounce scattering. Figure 5.12 illustrates these mechanisms, which were a function of both the wavelength and the angle of incidence of the microwave radiation. The interaction of the canopy elements with radiation of 5.6 cm of wavelength at incident angle of 45° (RADARSAT S6) resulted in volume scattering mechanism. The total backscattering was on average –7dB. This type of interaction takes place within the volume of the medium which is composed of scatters with different dielectric constants, size and orientation, in this case the vegetation canopy. The radiation is scattered by the elements of the canopy in all directions, acting similar to a Lambertian surface. At a 45° incidence angle, the path of the radiation through the canopy is increased; thus, more attenuation (due to the scatter elements) and less penetration of the radiation occurs (Ulaby et al., 1982).

With an incident angle of 25° (steeper angle – RADARSAT S1), C band, HH radiation penetrated deeply into the canopy, interacting with the underlying water and vegetation (and vice-versa) and within the canopy. As a result, stronger backscattering was observed (-3dB) as a sign of dominant water/vegetation double reflection (double bounce). At a steep incident angle, a horizontal polarized wave propagating in the air (low dielectric constant) penetrates deeply into a canopy of elements oriented contrary to the wave plane; the radiation reaches the stem (high dielectric constant), bounces towards the water surface (higher dielectric constant), and bounces strongly in a specular direction towards the radar antenna. The opposite process is also valid. The combination of these interactions is summarized as double bounce mechanism and results in strong reflection from the surface (Ulaby et al., 1982). These two scattering mechanisms are the simplest way of explaining the different σ^0 of RADARSAT S6 and RADARSAT S1 from aquatic vegetation. The estimated σ^0 values for RADARSAT S6 were lower than σ^0 for RADARSAT S1.

Finally, with a wavelength of 30 cm and at 35° of incidence angle (JERS-1), a deeper penetration of the radiation within the canopy will occur and, accordingly, a double bounce mechanism was expected. Overall, the observed low values of σ^0 (-9dB) for JERS-1 did not suggest double-bounce mechanism. Instead both volume scattering (canopy) and specular scattering (off the water) were the most probable mechanisms (Figure 5.12). The signal was mostly scattered in the opposite direction of the radar antenna. At a radar wavelength of approximately 30 cm, the structures of the aquatic vegetation were mostly transparent to the radiation (specular reflection), except when dense canopies occurred (volume scattering). Among the aquatic vegetation, isolated high σ^0 values were observed at L-band, which were related to the areas of well developed-tall *E. polystachya* and *P. fasciculatum*, implying that some double-bounce may have occurred when the radiation was interacting with this species.

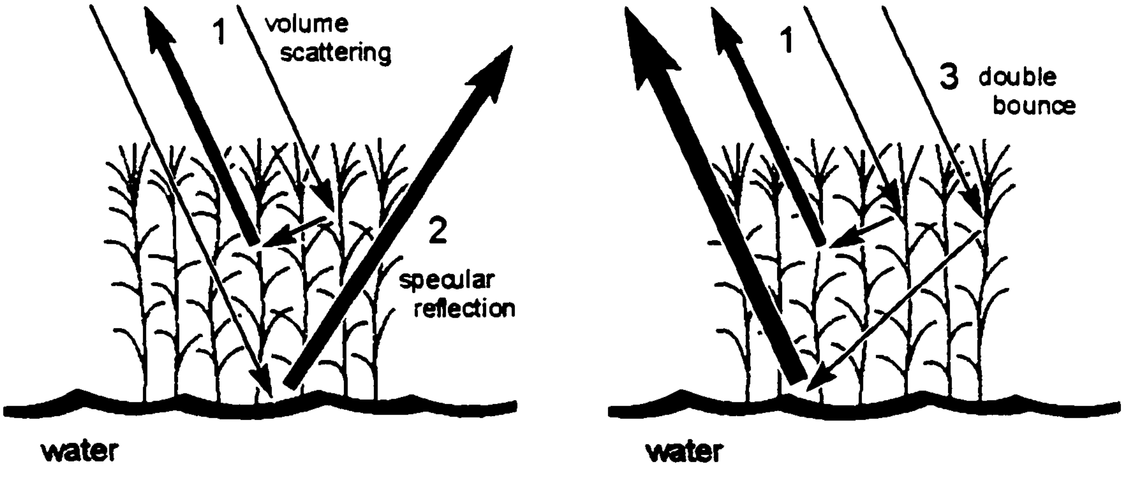

(a). L band (b). C band

Figure 5.12. Schematic representation of the scattering mechanisms at L bands (35°) - volume scattering and specular reflection, C (45°) – volume scattering; and C (25°) - double bounce. The thickness of the arrows represents the intensity of the scattered radiation.

A comparison of the backscattering coefficients of the Amazonian aquatic vegetation (this study) with previous studies of Amazonian aquatic vegetation (Hess et al., 1995, Novo et al., 1998), flooded rice fields (Kuroso et al., 1995, Le Toan et al., 1997, Ribbes and Le Toan, 1999, Rosenqvist, 1999), and other wetlands (Pope et al., 1997) suggest that major differences can be observed in terms of backscattering coefficients from grass-like aquatic vegetation. These differences are a result of the interaction of the microwave radiation (different characteristics) with the distinct architecture of the canopy and the distribution of the plants. For instance, σ^0 of C-VV, 23° (ERS-1) from well-developed flooded rice was approximately -7dB (Kurosu et al., 1995, Le Toan et al., 1997). ERS-1 differs from RADARSAT S1 only by the polarization. Vertically polarized radiation is strongly attenuated by vertically oriented canopies, while horizontally polarized radiation penetrates deeply into the canopy, unless the canopy is very dense (Holmes, 1992). This explains the lower σ^0 values for ERS-1 (-7dB) observed by Kuroso et al., (1995) and Le Toan et al., (1997) when compared with RADARSAT S1 (-3dB), this study.

On the other hand, if the characteristics of the radiation are kept constant and the distribution and density of the plants is different, distinct results are observed. The data published by Ribbes and Le Toan (1999) for flooded rice crops and RADARSAT S1 were compared with the results from RADARSAT S1 from this research. Ribbes and Le Toan reported σ^0 values from well-developed rice of approximately -6dB for RADARSAT S1; this is 3dB lower than the σ^0 values of our results for the same sensor. The slight structural differences between the rice plants and the Amazonian aquatic vegetation could be the cause of this discrepancy. Le Toan et al., (1997) describe the rice plants as bunches of 10 stems and 20 bunches m^{-2}. The Amazonian plants do not form bunches, the density varies from 27 to 111 stems per m^{-2} for *E. polystachya* and *H. amplexicaulis*, respectively, and there is neither preferential field orientation nor distribution of the plants. Conceivably, at the scale of the resolution of RADARSAT S1 data compared with the distribution of the plants, Ribbes and Le Toan were observing a combination of specular scattering off the water and volume-scattering from the canopy; as a consequence, lower σ^0 values were obtained when compared with our results for the more dense plants of the Amazon. Rosenqvist (1999) has already reported that plant spacing and field orientation of flooded rice crops can cause differences as great as 20dB at L band.

Conversely, Pope et al., (1997), reported a σ^0 value at C band (HH polarization and 25° of incidence angle – similar to RADARSAT S1) of approximately 0dB from mangrove tall-vegetation (*Cladium*). The same author reported values of σ^0 of -4.5 dB at L (HH polarization and 25° of incidence angle – almost the same configuration as JERS-1) from the same vegetation. The higher σ^0 values may be related to the lower canopy cover (58%) of *Cladium* and the tall structure (2 m height) of these plants compared with the Amazonian aquatic vegetation (86% m^{-2} of canopy cover and 1 m height), which showed σ^0 values of -3 and -9 dB, for C (RADARSAT S1) and L bands, respectively. Possibly, lower canopy cover of tall plants allows deeper penetration of the radiation and consequently double-bounce mechanism.

Similar to our results are the data reported by Hess et al., (1995) and Novo et al. (1998) for aquatic vegetation from different areas of the Amazon floodplain. Hess et al., (1995) reported σ^0 values of roughly -4dB and -10 dB for C and L bands (HH polarization and 33° of incidence angle), respectively. Novo et al., 1998, also reported similar magnitude of σ^o values (-4.5dB) for RADARSAT S1, and -6.5dB for RADARSAT S5 (39° of incidence angle), approximately the same configuration of RADARSAT S6. Further speculation regarding the differences and similarities of σ^o responses between naturally-occurring aquatic vegetation and irrigated rice crops are only possible with a more in-depth investigation of the ecosystems and radiative transfer models. Nonetheless, it is evident that the structures of the canopy, the distribution of the plants and the characteristics of the microwave radiation define the scattering mechanisms and the magnitude of the σ^o values.

5.4.2.2. Effect of the biophysical properties of aquatic vegetation on SAR σ^o

The correlation coefficients between SAR backscattering and aquatic vegetation biophysical properties were significant at the 95% level of significance, except for $\sigma^o_{RADARSATS1}$ (Table). The limited data set for RADARSAT S1 (only acquired at high water periods) constrained this analysis, hence no further conclusions can be drawn. Furthermore, RADASAT S1 data acquired in June 1999 is believed to be improperly radiometrically calibrated. Despite the lack of radiometric calibration of $\sigma^o_{RADARSATS1}$, a significant correlation was observed between $\sigma^o_{RADARSATS1}$ and $\sigma^o_{RADARSATS6}$ acquired in the same period. The scatter plot (Figure 5.13) shows that on average the $\sigma^o_{RARARSATS1}$ values were 3dB higher than $\sigma^o_{RADARSATS6}$ values. The enhanced $\sigma^o_{RADARSATS1}$ was a result of the double-scattering mechanisms as previously explained.

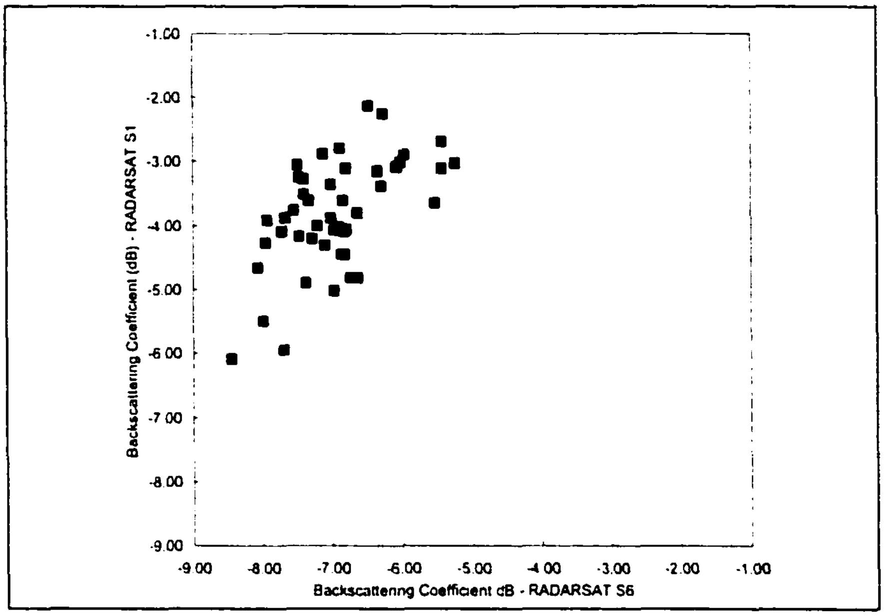

Figure 5.13. Backscattering coefficients from RADARSAT S6 versus RADARSAT S1 for the high water season (May and June)

Positive significant linear correlation coefficients ($p<0.05$) between $\sigma^{0}_{RADARSATS6}$, σ^{0}_{JERS}, σ^{0}_{index} and percentage of canopy cover, height, and dry biomass of the aquatic vegetation were observed. The correlation coefficients between SAR data and percentage of water content in the plants were not significant. However, $\sigma^{0}_{RADARSATS6}$ and σ^{0}_{JERS} were lower for higher values of water content (negative correlation); this might be due to the adsorption of microwave radiation by moist plants. A similar phenomenon was previously observed with wetland vegetation (Pope et al., 1994), aquatic vegetation of Amazonian reservoirs (Novo et al., 1998), as well as with flooded rice crop at the end of the growth period when a decrease of leaf and stem moisture content occurred (Kuroso, et al., 1995).

The positive correlation between SAR data and percentage of canopy cover, dry biomass, and height of aquatic vegetation suggestes that as the above water canopy increased (higher biomass, height, and canopy cover) so did the backscattered radiation at both C (45°) and L bands. Specifically for canopy cover, the correlations were very weak, however, they still indicated that an increase in either the number and the size of the scatter elements of the plants (leaves and stem) or the randomized distribution of these scatters may cause an increase in the backscattered radiation at both C and L bands. A closer analysis of number of stems against canopy cover suggests that, for instance, for a given 90% of canopy cover, the number of stems vary from 20 to 90 per $0.25m^2$. In addition, for the same 90% of canopy cover, variations of approximately $1000gm^{-2}$ of above water biomass and 1m of above water height were observed. Hence, canopy cover is indeed affected mostly by the randomized distribution of the canopy elements than the number of stems, biomass, and height of the plants. Consequently, canopy cover could not be used as an indicator of density of the scatter elements of the aquatic vegetation. Canopy gap fraction, which is the inverse of canopy density, was found to be an important parameter for monitoring structural elements of the canopy of tropical forests through multi-polarized C band (Valeriano, 1996). The higher result for forest was probably due to the better relation between the resolution of the SAR data and the scale of acquisition of canopy GAP fraction. Our data showed a large variability in the relationship between both C and L bands and canopy cover (Figure 5.14), implying that further analysis was not possible, at least on the scale that this data were acquired.

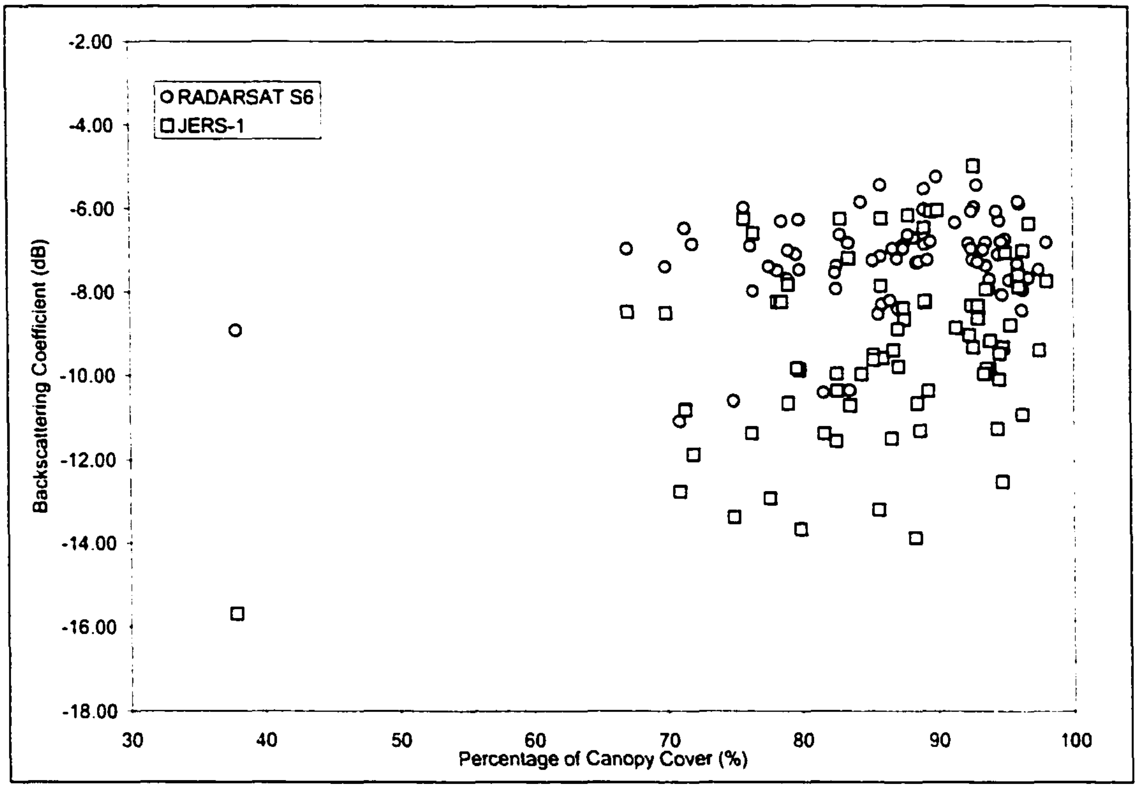

Figure 5.14. Variation of backscattering coefficients with percentage of canopy cover at C (RADARSAT S6) and L bands (JERS-1)

The graphics illustrating the relationship between C band, L band, and the Index with above water height, and biomass of the plants suggests that logarithmic regression functions would better fit the data. Figure 5.15 and Figure 5.16 show the logarithmic regressions and the R^2 between the SAR data and above water biomass and height, respectively. The same R^2 values were encountered when we applied logarithmic transformations of the variable height and biomass so that a linear regression function could be adjusted to the data instead. For the purposes of visualization, the following analysis will focus on the logarithmic regressions (Figure 5.15 and Figure 5.16).

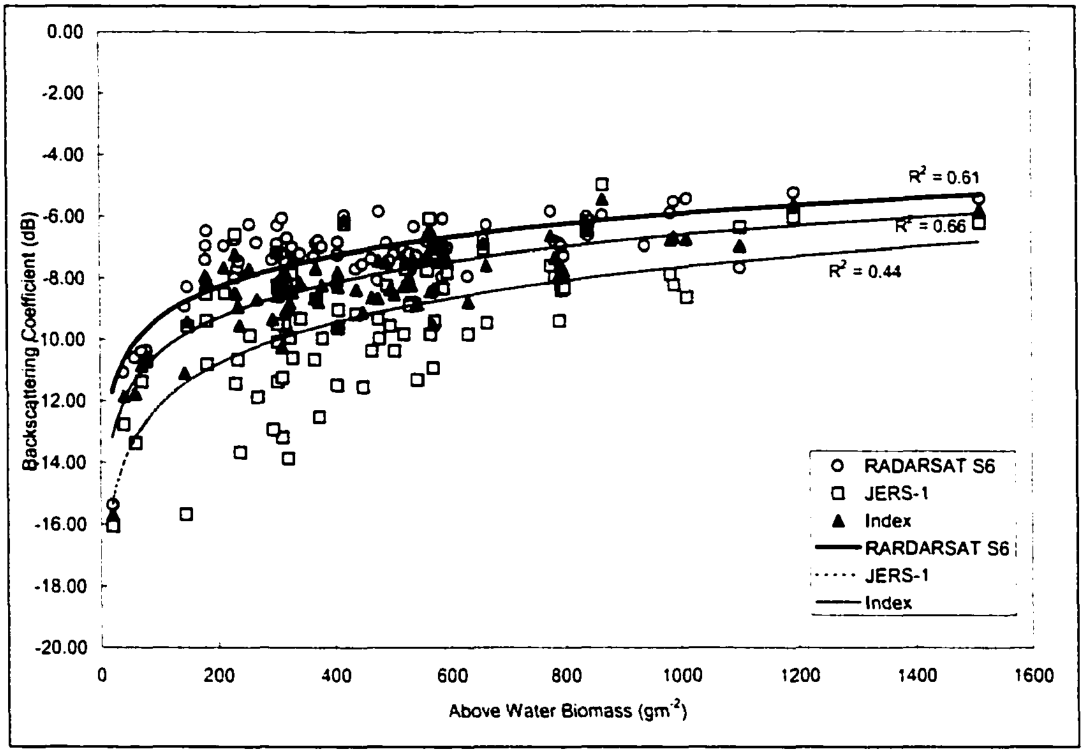

Figure 5.15. Variation of backscattering coefficient (dB) with above water biomass

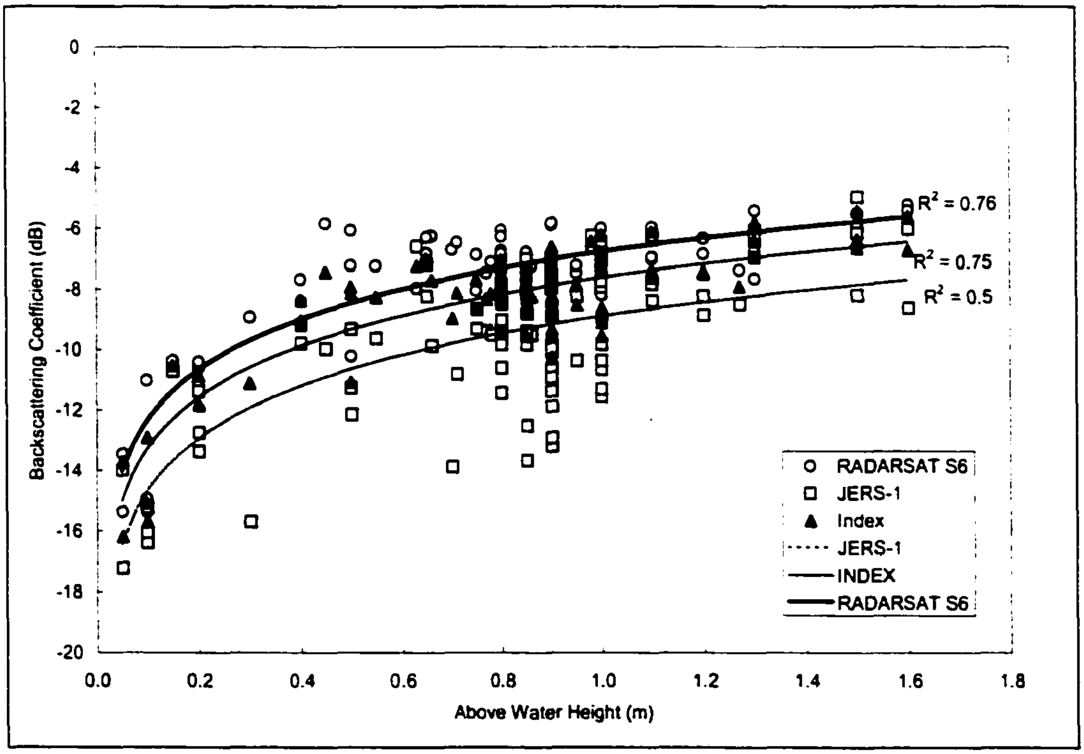

Figure 5.16. Variation of backscattering coefficient (dB) with above water height

The log curves showed a general trend of increasing σ^0 values with increasing height. However, the dispersion of σ^0 for a given biomass and height prevented higher R^2 values. A similar trend of backscattering was traced for biomass of *juncus* marsh and rice plants through the use of radiative transfer models (Dobson et al., 1996; Le Toan et al., 1997); the differences are only related to the magnitude of the backscattering values. For instance, the modeled σ^0 values presented by Dobson et al., (1996), for JERS-1 from *juncus* are in general lower than the values observed in this study for the same dry biomass. The modeled σ^0 values calculated by Le Toan et al., (1997) for ERS-1 from rice plants are closer to the values observed in this study for similar dry biomass. These results encourage the future use of radiative transfer models to better understand the scattering mechanism from the Amazonian aquatic vegetation.

The logarithmic regression curves of SAR data (RADARSAT S6, JERS-1 and Index) versus above water biomass showed three major regions. (1) A region of rapid increase in the backscattering values when the slope of the regression is high. (2) A region of moderate increase in backscattering values when the change in the slope of the regression is small reaching the saturation point. (3) A region of very subtle changes in backscattering values as the slope of the curve passed the saturation point. Despite some differences such as the boundaries between regions, the curves were alike in shape.

In the region of rapid increase in backscattering values, the difference in size and density of the scatter (stem and leaves) relative to the wavelength of the incident radiation were very important in defining the contribution of surface scattering (water) and canopy scattering to the total σ^0 value. In areas with biomass levels lower than $100 gm^{-2}$ and height lower than 0.2 m, the L band transmissivity through the canopy is high due to the small size and density of the scatter elements relative to the wavelength of the radiation (25cm). Therefore, backscattering from the water dominates, with a minor contribution from the canopy. This area can be considered slightly smooth and the backscattering values vary from -16 to -12 dB. On the other hand, at the same range of biomass and height, the C band σ^o showed a stronger canopy component. The transmissivity through the canopy decreased due to the interaction of the elements of the canopy with the radiation; the backscattering values vary from -15 to -10.5dB. These initial rapid changes in σ^o values at both C and L bands decreased to roughly 1dB at a range between 100 and 200gm^{-2}. Hence, the magnitude of the shift of σ^o values until 200gm^{-2} of biomass was approximately similar at C and L bands; this point defined the first region of the curves.

The second region was defined by a moderate change in σ^o and ranged from 200gm^{-2} to the saturation point of each curve. The difference of where the σ^o approached the saturation point is very important for understanding the predictive capability of a model. The occurrence of a saturation point for biomass of vegetation when using satellites (optical and SAR) is the "Achilles heel" of biomass inventories worldwide (Imhoff, 1995; Luckman et al., 1997; Le Toan et al., 1997; Wulder, 1998; Ribbes and Le Toan, 1999).

A mathematical method was applied to determine from the regression curves the point at which the SAR backscattering approached saturation with respect to biomass and height. Using SAR data, a similar methodology was applied by Imhoff (1995) to define the biomass saturation point for different forests around the world using SAR data. First, a third order polynomial was fitted to the data set with the purpose to better follow the variability of the σ^0 values and therefore calculate the point where the slope of the regression line was at or near zero. The solution of the second derivative of the polynomial equation gave the first relative point of inflexion of the equation, i.e. the point where the curves first changed to a slope at or close to zero (the saturation point). Furthermore, the saturation point of the 95% confidence limit of each curve was calculated. The saturation point of the lower limit of each curve is presented in Table 5.10. Second, to increase the confidence of the calculated saturation points, it was decided that the final accepted saturation points were 25% lower than the points calculated by the second derivative, for both biomass and height (Table 5.10). The accepted points were 470, 660, and 620 gm^{-2}, at C band, L band, and the Index, respectively. The saturation points of height were 0.6, 0.7, and 0.7 m, at C band, L band, and the Index, respectively. Consequently, the range of the second region was defined as 200 to 470 (2dB variation) at C band, 200 to 660 (2.8 dB variation) at L band, and 200 to 620 (2.5 dB variation) at the Index.

At C band, the saturation point occurred before the saturation point at L band. This was a result of two factors (i) the relationship between size of the wavelength and size/density of the scatter elements of the canopy and (ii) the incident angle of the radiation. The shorter wavelength of C band (5.6cm) is highly attenuated by the leaves and stems of the plants. This, combined with the higher incident angle (45°) prevented higher transmissivity of the canopy, therefore the radiation was strongly attenuated in the upper canopy and less penetration occurred. The result was an earlier saturation point when compared with L band; it occurred at approximately 470gm^{-2} of biomass and 0.6 m height. Similar saturation points for both biomass (400gm^{-2}) and height (0.8m) were reported for flooded rice plants using ERS-1 data (C-VV, 23° of incidence angle) (Le Toan et al., 1997). However, Ribbes and Le Toan (1999), for the same plants, but different SAR data (RADARSAT, C-HH, 23° incidence angle), reported an earlier saturation point at 200 gm^{-2} for biomass and similar saturation point for height (0.6 m). The cause of this earlier saturation point for RADARSAT S1 is not well understood, and, indeed, was contrary to our expectations. As previously discussed, these differences might be associated with the pattern of the distribution of the rice plants compared with the random distribution of the Amazonian aquatic vegetation.

At L band, 35° of incident angle, the transmissivity of the canopy has a wider range due to the smaller size /density of the scatters relative to the wavelength. As the biomass increased the transmissivity of the radiation through the canopy decresed; consequently, the inclination of the curve decreased until it reached the point close to zero inclination. The saturation point occurred at 660 gm^{-2} of biomass and 0.7 m of above water height. However, at this point, the dispersion of both biomass and height was larger than at C band.

Table 5.10. Above water biomass and height saturation points

Data	Equation	Calculated saturation point	Accepted saturation point
Biomass x $\sigma^o_{RADARSATS6}$	$Y=9.58*10^{-9}x^3-2.36*10^{-5}x^2+0.018x-11.21$	630	470
Biomass x σ^o_{JERS-1}	$Y=2.09*10^{-9}x^3-7.54*10^{-6}x^2+0.011x-13.14$	890	660
Biomass x σ^o_{Index}	$Y=6.74*10^{-9}x^3-1.75*10^{-5}x^2+0.016x-11.98$	830	620
Height x $\sigma^o_{RADARSATS6}$	$Y=11.33x^3-32.35x^2+29.46x-15.63$	0.75	0.6
Height x $\sigma^o J_{ERS-1}$	$Y=6.63x^3-16.25x^2+18.75x-16.27$	0.89	0.7
Height x σ^o_{Index}	$Y=9.67x^3-27.23x^2+25.48x-15.91$	0.89	0.7

Biomass and height values are in gm^{-2} and m, respectively.

Finally, at the third region, the changes in σ^0 values were very subtle. The vegetation canopy was very dense relative to both wavelengths. Transmissivity of the canopy was neglegible at both C and L bands; as a result an increase in biomass showed little influence in the increase of σ^0. At the high biomass range the differences between the regression curves at C and L bands decreased to less than 1dB, which suggested that the canopy of the plants were affecting the two different wavelengths equally. The convergence of both curves towards a similar σ^0 is easily observed in the linear regression curves (Figure -log biomass versus σ^0).

In summary, the three regions of the curves were defined by the transmissivity of the canopy layer to the wavelength and incidence angle of the radiation. In the first region, higher transmissivity was observed at both C and L bands. The second region was characterized by a large difference between the transmissivity of the canopy layer at C and L bands. Accordingly, an earlier saturation point at 470 gm^{-2} and 0.6m of biomass and height, respectively, occurred at C band. At L band, higher transmissivity of the canopy allowed a later saturation point at 660 gm^{-2} and 0.7m of above water biomass and height, respectively. However, the dispersion of the points at L band was larger than at C band. At the third region, after the saturation point, the increase in the two-way transmissivity of the canopy had become insignificant, hence increments in volume scattering and double-bounce as biomass and height increased were negligible. Further investigation with radiative transfer models will be necessary to confirm the trend observed for each curve.

The final analysis suggests that the Index is indeed the best compromise between (1) an intermediate saturation point for biomass and height (Table 5.10), (2) lower variability of σ^0 within the second region (Figure 5.15 and Figure 5.16), (3) higher R^2 (Table), and (4) lower MSPR and RMSE for biomass estimates (Table 5.8).

Nevertheless, for both above water biomass and height, even though the correlation coefficients were significant, the capability of predicting the “property” past the saturation point could be jeopardized.

6. CLASSIFICATION

The understanding of the biogeochemical cycles in large spatial (e.g. regional and global) and temporal scales (e.g. seasonal) requires accurate maps and area estimates of actual land cover. The basic desired classes for such studies are water, wetlands, bare soils, agriculture, grassland, shrubland, savanna, deciduous and coniferous forest, and urban areas. These comprise a Level I classification (Dobson et al., 1996). Among these classes, water, grass land (pastureland), upland forest (primary and secondary), savanna, flooded forest, and aquatic vegetation classes are desirable for better understanding of the biogeochemistry of the Amazon Basin at a regional scale (Junk and Piedade, 1997; Forsberg et al., 2000; Mattews et al., 2000; Melack et al., 2000; Junk, 2000). Historically, upland areas have been mapped by LANDSAT images (INPE, 1999); the floodplain as a unit (flooded vegetation as one class) was partially mapped with LANDSAT, however, the images were not temporally consistent (Novo et al., 1997). A large scale mapping of classes within the floodplain is still lacking. Our goal is to extract the seasonal area of aquatic vegetation using multi-temporal/spectral SAR data, through a region-based classification technique. To do so, areas covered by aquatic vegetation were separated from water, flooded forest, upland forest, pastureland, and savanna areas.

Several different methods of classification are used to cluster data of remotely sensed images into pattern space. These methods are based on statistical decision theory built for optical and SAR images. Often, classification methods operate at a pixel level, in which each pixel of an image has a probability of belonging to a cluster (i.e. class) (Moik, 1980). Results of pixel level classification are very successful for optical images, mainly when the classifier is previously trained. However, pixel level classification is generally less efficient when applied to SAR images due to the large inter-pixel variability (speckle) present in the images (Oliver and Quegan, 1998). Attempting to overcome this problem, different techniques are applied to the image before the actual classification, such as filtering (Pope et al., 1994, Hess et al., 1995), texture extraction (Luckman et al., 1997), and segmentation procedures (Touzi et al., 1987, Lobo et al., 1996, Oliver and Quegan, 1998, Li. et al., 1999, Dong et al., 1999). The first two techniques are more often used as pre-classification steps because they are commonly available in commercial image processing software. Nonetheless, in the recent years, the use of segmentation procedures prior to classification have being reported as fundamental for the classification of SAR images (Lobo et al., 1996, Oliver and Quegan, 1998, Dong et al., 1999).

Segmentation is the decomposition of an image into several homogeneous regions, which have characteristics that are different from their surroundings (Dong et al., 1999). A homogeneous region can be characterized, for instance, by a texture measure (Oliver, 2000) or first and second order statistics (Li et al., 1999, Dong et al., 1999). Some segmentation procedures such as the one suggested by Dong et al., (1999), combine filtering, first and second order statistics, and texture measures to define homogeneous regions. Generally, segmentation algorithms are divided into three major groups: contour detection, watershed, and region growing. Contour, or edge detection, is defined as the difference between two contiguous pixels (Touzi et al., 1987). Watershed algorithms consider an image as a topographic surface in which valleys (regional minima) are flooded until crests are reached (boundaries between regions). The "flooded" area defines homogeneous regions (Li. et al., 1999). Region growing is an iterative process by which regions are merged starting from individual pixels, according to statistical measure and minimum region size, until every pixel is processed, resulting in spatially homogeneous regions (Li et al., 1999). In this research, a region growing method was used to create segmented images enabling a region-based classification instead of a pixel-based classification to be performed. The region growing algorithm is part of SPRING (Sistema de Processamento de Informações Georeferenciadas), developed by the National Institute of Space Research in Brazil.

Region growing algorithms consider two contiguous regions, *A* and *B*, to be different according to the following criteria (Bins et al., 1996):

(i) The first order statistics, the mean, defines that *A* and *B* are similar according to a threshold of similarity.

(ii) *A* and *B* are mutually close, i.e. *A* is spatially closer to *B* than to all other neighbors of A, and vice-versa.

(iii) If *A* and *B* satisfy the above criteria, *A* and *B* are joined as one region. Otherwise, the algorithm splits *A* and *B* into two regions and starts the aggregation-test for new neighbors.

(iv) After defining all similar regions in an image, the algorithm tests for the size of the regions (in terms of pixels) according to a minimum size threshold; it is a merging algorithm based on the minimum number of pixels allowed for each area according to a threshold.

(v) The algorithm creates closed lines (polygons) that represent each homogeneous region.

(vi) In the final step, the algorithm calculates the statistics of each new region (mean and variance) so that it can be used in the region-based classification.

The threshold of similarity consists of the minimum difference in observed digital numbers between two regions. Based on this threshold the algorithm makes the decision of either merging or keeping the two adjacent regions separate; if the difference between the mean of two regions is larger than the threshold, the regions are not merged. This threshold was defined according to the studentized value of the least significant difference (LSD) between two mean values. LSD is the studentized standard error of the difference between two means (Snedecor and Cochran, 1980). LSD is defined as follows.

$$LSD = Q_{0.05} * \sqrt{\frac{S^2}{n}} \qquad \text{Equation 6.1}$$

where $Q_{0.05}$ is the studentized amplitude at an accuracy of 95% given the degrees of freedom and the number of classes, S^2 is the standard error of the mean of the classes. According to the test, if the difference between the mean values of two regions is greater than the calculated LSD then the regions are considered different at 95% of confidence level; consequently, the two adjacent regions are not merged.

A minimum number of 50 pixels allowed in a region is decided based on the following criteria:

(i) Minimum number of pixels required so that the statistics of a region follow a normal distribution; this is related to the equivalent number of looks of the despeckled images (section 4.1.3). Due to the filtering process the final number of looks of the images was on average 50. Hence, a region created with a minimum number of pixels of 50 was sufficiently large to guarantee (90% of confidence) that the statistics of each final region are a good estimate of the true mean of the target, under the assumption of normality (Laur et al., 1996).

(ii) Avoid extreme over segmentation of the images.

6.1. Classification Procedure

Before applying the segmentation algorithm a series of steps was performed in the SAR despeckled data set aimed at facilitating the segmentation procedure (in terms of processing time) and having an accurate seasonal classification of aquatic vegetation areas. These steps were (i) the selection of the optimal combination of SAR image; (ii) the transformation of the image from 32 to 8 bit; (iii) masking water and upland areas, (iv) segmentation of the floodplain, and (v) classification of the aquatic vegetation areas.

6.1.1. Determination of the optimal combination of images

The Battacharrya distance (*B*), a separability measure, was calculated among the different ground cover for each image. The separability analysis was performed in the set of images acquired in May, which included RADARSAT S6, RADARADARSATS1, and JERS-1. The intention on doing a separability analysis was to evaluate the performance of single images for the segmentation/classification procedures. The *B* distance is defined as a measure of the average distance between the two class probability density functions, and varies from 0 to 1.0 (poor separability), 1.0 to 1.9 (fair separability), and 1.9 to 2.0 (good separability) (Richards, 1986).

Table 6.1 shows the separability distance between the classes (pasture land, aquatic vegetation, flooded forest, forest, and water) for RADARSATS6, RADARADARSATS1, and JERS-1, yielding overall separability of 1.4, 1.6, and 1.9, respectively. The separabilities among the classes in general were higher for JERS-1 than for both RADARSAT modes. However, for JERS-1, there was some confusion between pasture and aquatic vegetation, and upland forest and flooded-forest. A visual analysis of the individual images and the combination of images suggested that combined images would perform better in terms of separating the ground cover of interest. This was confirmed by the analysis of the scatter plots (Figure 6.1)

Table 6.1. Separability distance based on the SAR images

		JERS-1 overall class separability = 1.9		
	Pasture land	Aquatic vegetation	Flooded forest	Upland forest
Aquatic vegetation	1.38			
Flooded forest	2.0	2.0		
Upland forest	1.99	1.99	1.5	
Water	2.0	1.9	2.0	2.0
		RADARSAT S6 overall class separability = 1.4		
Aquatic vegetation	1.56			
Flooded forest	1.36	1.0		
Upland forest	0.79	1.0		
Water	2.0	2.0	2.0	
		RADARSATS1 overall class separability = 1.6		
Aquatic vegetation	1.9			
Flooded forest	1.09	1.5		
Upland forest	0.9	1.75	0.73	
Water	1.99	2.0	2.0	2.0

The scatter plots of the mean backscatter coefficients for the distinct ground cover at low and high water periods suggested that when the two RADARSAT images are used (Figure 6.1c), it was not possible to separate between ground cover classes, but when the JERS-1 image was used, in combination with a RADARSAT image (Figure 6.1a and Figure 6.1b), more ground cover could be separated.

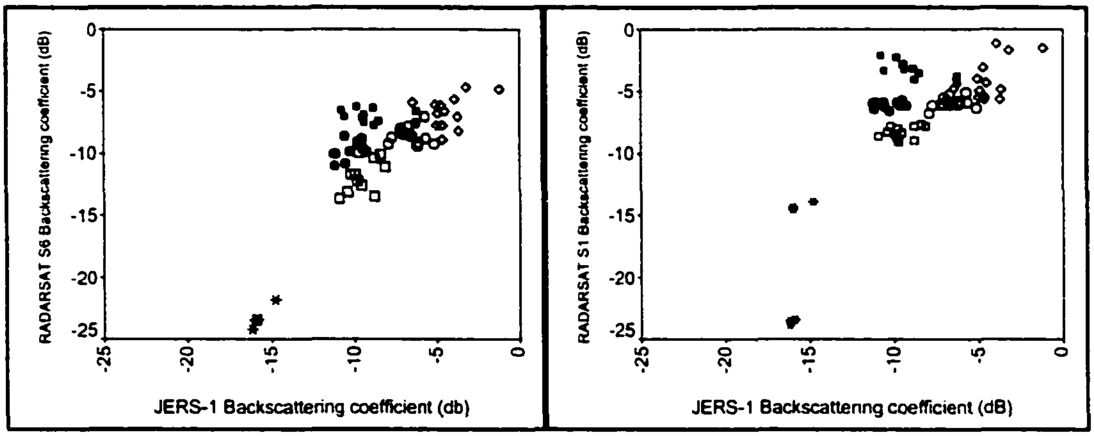

(a). RADARSAT S6 versus JERS-1, May (b). RADARSAT S1 versus JERS-1, May

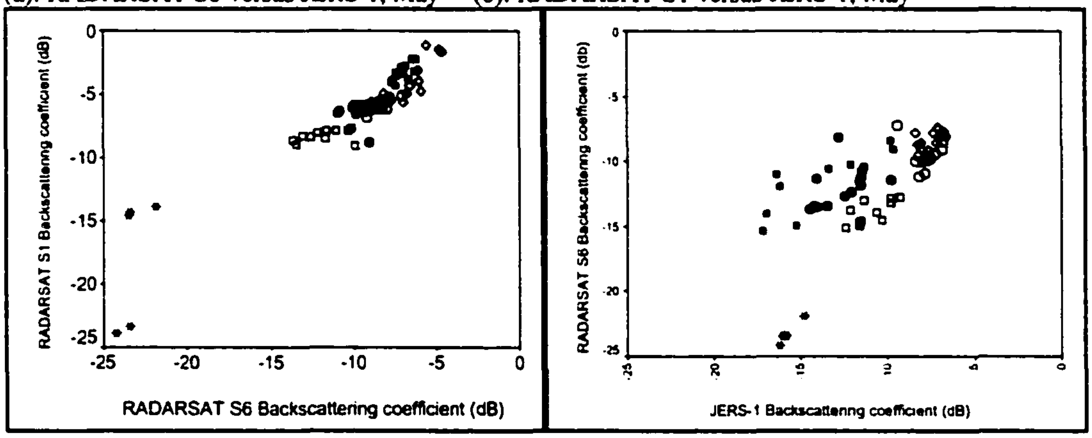

(c). RADARSAT S1 versus RADARSAT S6, May (d). RADARSAT S6 versus JERS-1, November

Figure 6.1. Scatter plots of the backscattering coefficient from RADARSAT versus JERS for high (May) and low (November) water seasons. Closed square-aquatic plant; open square-savanna; open circle-upland forest; open diamond-flooded forest; closed circle-pasture land; asterisk-water.

A sub-scene of approximately 19x19km was selected from the set of original images acquired in May. A classification was performed in each individual sub-scene of RADARSAT S6, RADARSAT S1, and JERS-1, and in the combined sub-scenes RADARSAT S6 and JERS-1, and RADARSAT S1 and JERS-1. The classified images were compared with the ground truth map (Figure 6.2a) that was generated from visual interpretation of the aerial photograph acquired in May. According to the comparison, the classification of RADARSAT alone yielded confusion among all the vegetated ground cover, and JERS-1 alone yielded confusion between flooded-forest and forest and pastureland and aquatic vegetation and, in addition, did not separate narrow water channels as well as RADARSAT. The multi-wavelength combination provided better classification of the ground cover. Figure 6.2 illustrates the poor performance of individual images and the improved classification when the different wavelengths were combined.

In summary, the analyses showed that a combination of different wavelengths would yield a better classification than either individual images or a combination of different incidence angles. The segmentation and classification procedures were performed in multi-wavelength combinations of RADARSAT S6 and JERS-1; RADARSAT S1 was not included due to the lack of data for most of the periods. However, according to the separability measure and the classification results, for separating aquatic vegetation from flooded forest, Radarsat S1 alone performs better than Radarsat S6 alone.

(a) Ground truth map (aerial photo interpretation) (b) JERS-1,May

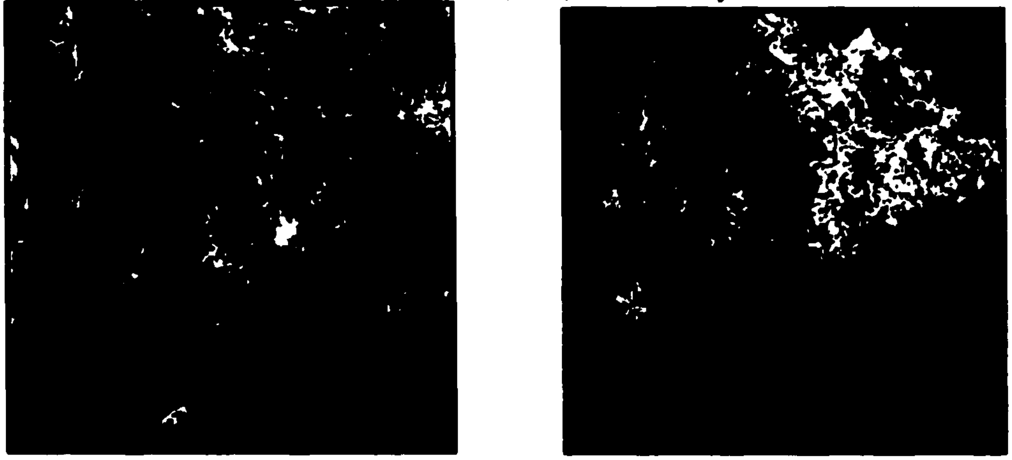

(c) RADARSAR S6, May (d) RADARSAT S1, May

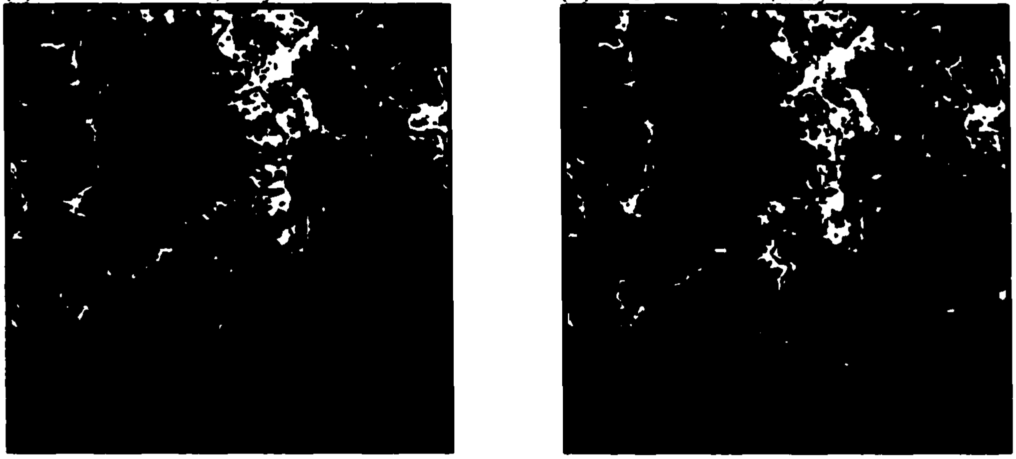

(e) JERS-1 + RADARSAT S6 (f) JERS-1 + RADARSAT S1

Figure 6.2. Classification results of a sub-scene of the SAR images acquired in May 1996. GREEN=forest; BLUE=water; ORANGE=pasture; YELLOW=flooded forest; CYAN=aquatic plants.

6.1.2. Transformation of the SAR images from 32 to 8 bit

For reason of data reduction (less computation time for processing) the images were reduced from 32 to 8 bit with a range of 0 to 255. The intensity values were converted from 32 to 8 bit according to the mean and 3 times the standard deviation of each image (use of most of the dynamic range of the 32 bits SAR images: 21dB). Consequently, each 8 bit digital number corresponds to roughly a 0.1dB step. Table 6.2 gives the 32 bits range for each SAR image.

Table 6.2. 32 bits dynamic range of the SAR images

Satellite data	32 bit range- linear units (dynamic range in dB units)
RADARSAT S6, November	0 – 0.228 (19)
JERS-1, December	0 – 0.313 (20)
RADARSAT S6, April	0 – 0.307 (20)
JERS-1, March	0 – 0.444 (21)
RADARSAT S6, May	0 – 0.359 (20)
RADARSAT S1, May	0 – 0.73 (24)
JERS-1, May	0 – 0.492 (22)
RADARSAT S6, June	0 – 0.341 (20)
RADARSAT S1, June	0 – 0.558 (22)
RADARSAT S6, Aug	0 – 0.353 (20)
JERS-1, Aug	0 –0.443 (21)

6.1.3. Water and upland masks

Since the focus of the classification is to accurately separate areas covered by aquatic vegetation, masks of water and upland areas were determined and subtracted from all the SAR images prior to the segmentation/classification. The final segmentation/classification was performed only within the vegetated areas of the floodplain. This was a requirement for decreasing the execution time (computer time) for the segmentation/classification procedures and to improve the accuracy of the final classifications. The following procedures were adopted to build each mask.

(i) Water mask

Water masks were determined from each RADARSATS6 images alone by determining thresholds corresponding to water. The thresholds were determined based on the histogram and the visual inspection of the 8 bit images (Table 6.3). Each water mask was subtracted from the images corresponding to the same period.

Table 6.3. Water thresholds for RADARSAT S6 images

RADARSAT S6 images (8 bit)	Water threshold (8 bit)
November	0-5
April	0-10
May	0 - 13
June	0 - 8
August	0 – 10

(ii) Upland mask

The process of building an upland mask required more than a simple threshold due to the different ground cover that correspond to upland. The selected set of images were segmented and classified separating upland from floodplain area. First, upland was defined as the area that was not flooded at the maximum water level, i.e. in May. The major ground cover within the upland area were pasture land, savanna, and forest; whatever was not upland, was either water or vegetated floodplain. A detailed visual inspection of the satellite images indicated that, in order to separate vegetated upland from vegetated floodplain areas, a combination of JERS-1 and RADARSAT S6 acquired in May (maximum water level) and JERS-1 acquired in December (minimum water level) offered the best contrast (Figure 6.3).

Figure 6.3. SAR false color composite. JERS-1, May: RED; JERS-1, December: GREEN; RADARSAT S6, May: BLUE

After defining the optimal composition of images for separating upland from floodplain, a similarity threshold was calculated and used as input for the segmentation procedure. The calculation of the similarity threshold was based on the least significant distance (LSD) between the mean values of flooded forest and forest at 95% confidence level. According to the scatter plots (Figure 6.1) flooded forest and upland forest are the ground cover most difficult to separate when RADARSAT and JERS are combined. The calculated LSD value was 30, which means that if the difference between the mean value of two regions was lower than 30 the regions were considered similar and therefore were merged. The minimum number of pixels per region was established as 50; the choice of the area size has been previously explained.

The segmented images (combination of RADARSAT S6, JERS-1 from May, and JERS-1 from December) were classified according to a region-based supervised Battacharya distance algorithm. The confusion matrix for the classification results is shown in Table 6.4, and the thematic classification map is presented in Figure 6.4. The applied procedures worked well to separate upland from floodplain areas with an overall accuracy of 94%. The greatest confusion was between savanna and water, and between aquatic vegetation and pastureland. The theoretical explanation of these errors is related to the interaction between the multi-wavelength radiation with the ground surfaces (section 5.3). Grass cover, such as pasture land and aquatic vegetation are nearly transparent at L band, and show volume scattering at C band; i.e. both ground cover showed similar scattering mechanisms at each wavelength. The confusion associated with water and savanna can be related to the low backscattering from both cover at C and L bands. A few misclassified areas such as aquatic vegetation and flooded forest within the upland area were visually identified in the thematic classification map. These misclassified areas were manually removed from the final upland mask.

In summary, based on the results of the seasonal threshold value for water mask and the classification of the upland area for the maximum water level, the entire data set was subtracted from both the water and upland masks. The resultant masked images were used to separate the seasonal area occupied by aquatic vegetation.

Table 6.4. Confusion matrix of Level I classification for separating upland from floodplain areas – test population

	True Class					
% Classified as	Water N=10 n=4	Flooded forest N=66 n=18	Aquatic vegetation N=44 n=20	Pasture land N=20 n=14	Upland forest N=39 n=12	Savanna N=7 n=7
Water	100	0	0	0	0	12.82
Flooded forest	0	100	6.81	0	0.15	0
Aquatic vegetation	0	0	92.9	9.24	0	0
Pasture land	0	0	0	90.76	0	0
Upland forest	0	0	0	0	99.85	0
Savanna	0	0	0	0	0	86.90

Overall accuracy = 94%; Accuracies are expressed in percentage. N represents the number of training regions and n represents the number of testing regions.

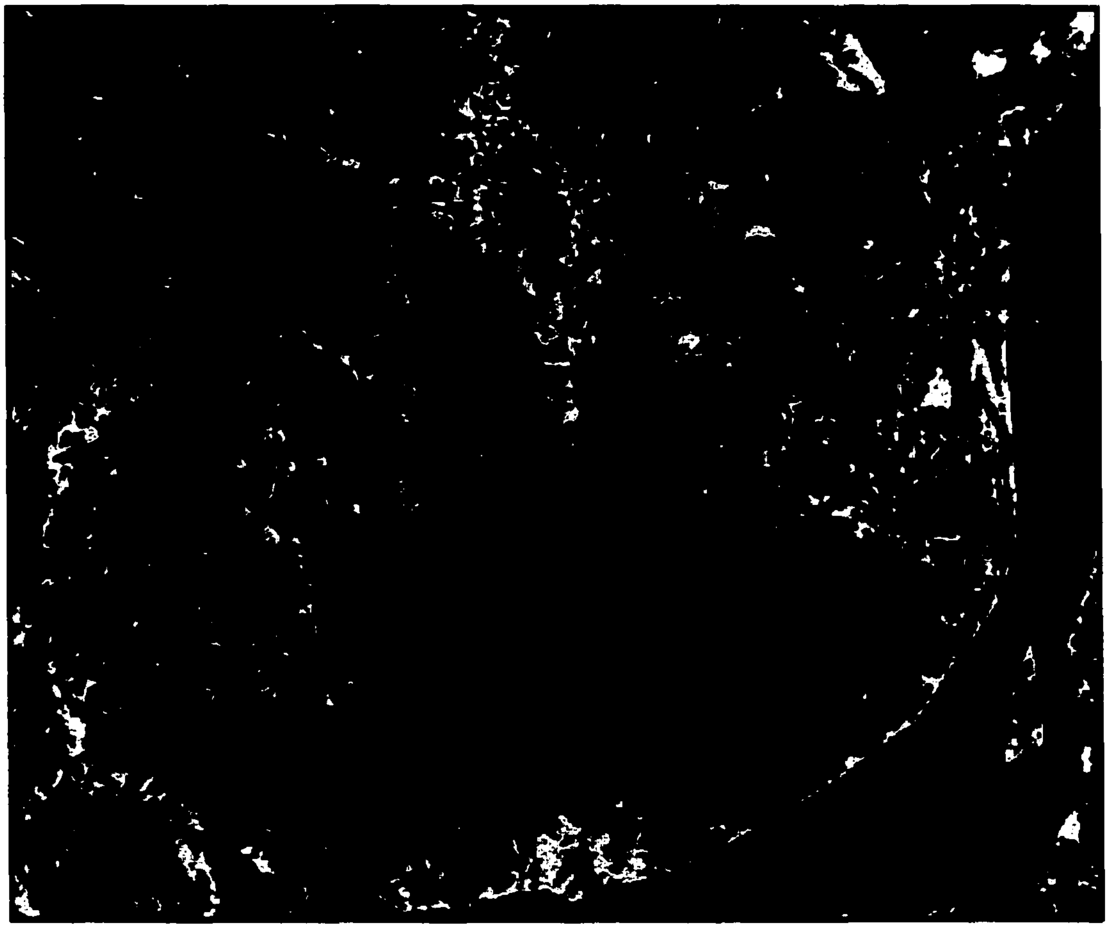

Figure 6.4. Classification of the upland area. GREEN=upland forest; BLUE=water; ORANGE=pasture; YELLOW=flooded forest; CYAN=aquatic plants; BROWN=savanna.

6.1.4. Classification of aquatic vegetation areas

After subtracting the water and upland mask, the final masked images were composed of four classes: aquatic vegetation, flooded forest, not flooded forest, and others (water and upland). The detail procedure for extracting the aquatic vegetation areas was as follows:

(i) Segmentation

The optimal set of images for the segmentation/classification was a combination of RADARSAT S6 and JERS-1 (section 6.1.1). First, the threshold of similarity (LSD) was calculated for each set of images acquired in the different periods. LSD was defined using the mean values of approximately 15 samples of aquatic vegetation and flooded-forest sampled in a stratified random system. The samples were chosen in areas where there were either field observations or aerial photographs. The definition of the threshold of similarity was critical for the success of the classification, since it defined the rule for merging regions; partially, it indicated the total number of regions in the image after the segmentation. Figure 6.5 is an enlargement of a small area of the image overlaid with the regions built by using different similarity thresholds of 20, 30 (LSD value), and 40, respectively, for the combination RADARSATS6 and JERS-1 acquired in May. Figure 6.5 illustrates that the larger the threshold, the fewer regions built, i.e. less detail was separated. Conversely, the lower the threshold, the more regions built; however, more regions is not synonymous with better results for the classification; in SAR images, it sometimes means oversegmentation due to the speckle (Dong et al., 1999). Therefore, if the threshold is very large it risks losing important regions, and if the threshold is very small the image is oversegmented. A visual inspection of several sectors of the segmented images generated by the different thresholds showed that, indeed, a threshold of 30 (the calculated LSD value) gave the better result in terms of defining regions.

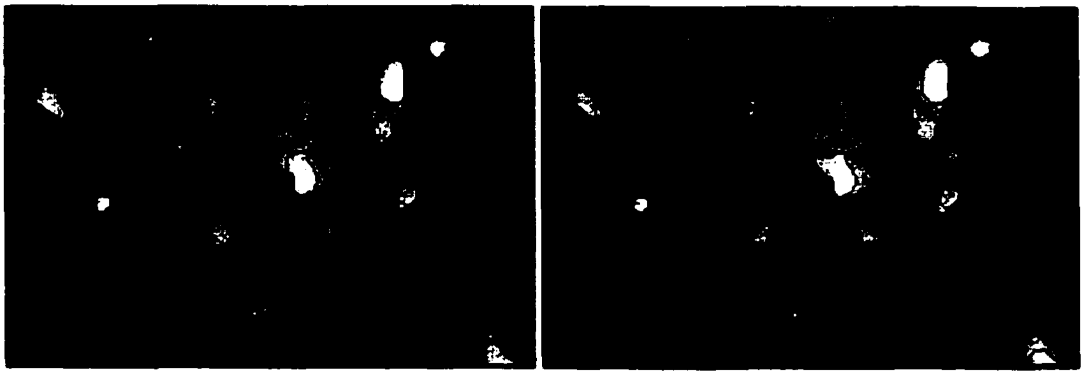

(a)Threshold of similarity equals to 20:more regions (b) Equals to 30 – intermediate number of regions

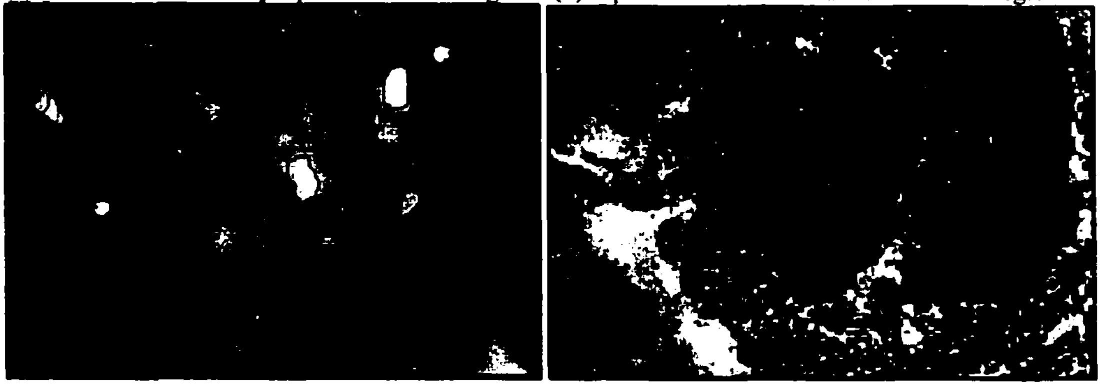

(c) Equals to 40 – less regions (d) Aerial photo of the same location

Figure 6.5. Segmentation results using the region-growing algorithm with different threshold values. JERS-1 image in the background. (a) Threshold of 20, (b) threshold of 30, (c) threshold of 40, and (d) aerial photo of the same location showing the different ground cover.

The final threshold of similarities (LSD) for each set of images is presented in Table 3.5. In addition, the threshold for the set RADARSAT S6 and RADARSAT S1 acquired in May is presented. The reason for processing a segmentation/classification of this set was to evaluate the use of multi-incidence angle instead of multi-wavelength. In all the cases, the minimum number of pixels per region (region size threshold) was 50 for all the sets.

Table 6.5. Calculated threshold of similarities for each pair of images

Period	Combined images	Threshold of similarity
May (high water)	RADARSATS6 and JERS-1	30
May (high water)	RADARSATS6 and RADARSATS1	25
June (high water)	RADARSATS6 and JERS-1*	30
August (falling water)	RADARSATS6 and JERS-1	25
November (low water)	RADARSATS6 and JERS-1	25
April (rising water)	RADARSATS6 and JERS-1	25

* JERS-1 image was indeed acquired in May 1996 (recall assumption made in section 5.4.1).

(ii) Classification

A supervised classification was performed for each pair of pre-segmented images according to the Battacharrya algorithm (Richards, 1986) with the objective of determining the seasonal area occupied by aquatic vegetation. This section describes the sample design and the analysis of the classification results.

(a) Classification scheme

The classification scheme was defined as a basic Level I classification (Dobson et al., 1996), which consisted of the seasonal separation of aquatic vegetation, flooded forest, and unflooded forest within the floodplain area; the upland (pasture land, forest, and savanna) and water classes were previously masked. Once more, these are the most important classes for seasonal studies of the biogeochemistry of the Amazon floodplain (Melack et al., 2000); the seasonal area of aquatic vegetation is needed for estimating net primary productivity as part of this study.

A more detailed classification was originally intended, a Level II, in which the aquatic vegetation classes would be further classified into three other sub-classes, namely, emergent grass-like aquatic vegetation, emergent short broad-leave aquatic vegetation (*Eichhornia* sp and *H. furcatus*), and emergent tall broad-leaf aquatic vegetation (*Montrichardia arborescens).* Nonetheless, the analysis of the field data (section 3.2) showed that the grass-like emergent aquatic vegetation comprised more than 85% of the sampled sites (dominated by *H. amplexicaulis*), which were assumed to be representative of the distribution of aquatic vegetation in the study area. The same distribution of grass-like aquatic vegetation is observed in other areas of the Amazon floodplain (Junk and Piedade, 1993; Junk and Piedade, 1997). Therefore, emergent broad-leaf aquatic vegetation was not considered as important at the scale of this research; a Level I classification was considered appropriate for our purposes.

(b) Sampling strategy

The training and test sample units were polygons (regions) generated by the segmentation. The samples were selected in a stratified random method. Only the regions with either available photograph coverage or field observation were used for selecting training and test samples. Aerial photographs, low altitude photographs, and field data were used for identifying training and testing sites; these sites guided the selection of training and test samples. Three different sets of training and test sites were selected according to the water level, namely (1) for high water images (data acquired in May and June), (2) for falling and rising water images (data acquired in August and April), and (3) for low water images (data acquired in November).

For high water periods, both field data and the 1:20,000 aerial photos acquired in May were used for determining the training and test sites of aquatic vegetation and flooded forest. The test sites of aquatic vegetation were the sites sampled during the field campaigns. For rising and falling water periods, both field data and the 1:15,000 aerial photograph acquired in March were used for selecting the training and test sites of aquatic vegetation, flooded forest, and unflooded forest. The water level at the period of the acquisition of aerial photograph was approximately the same as the water level of the images acquired in August and April. For the low water period, both field data and low altitude photograph acquired in November were used for selecting the training and test sites of aquatic vegetation, flooded forest, and unflooded forest. Digital files with the training and test sites of aquatic vegetation, flooded forest, and unflooded forest were created for each of the three major water level periods. These files were overlaid on the SAR images and the training and test regions selected.

Table 6.6 presents the number of training and test samples (regions) selected, based on the above mentioned procedure. Note that no samples of unflooded forest were selected for images acquired in May and June because of the complete flooding of the floodplain, i.e. all the forest areas within the floodplain were flooded. Furthermore, a smaller number of samples of unflooded forest were selected for images acquired in August and April, and samples of flooded forest for images acquired in November due to the scarcity of ground truth. Generally, the number of samples of both training and test sites were on average high: 82 and 58 for aquatic vegetation, respectively, 91 and 61 for flooded forest, respectively, and 31 and 15 for unflooded forest, respectively. The average high number of testing samples for each class allowed a site specific accuracy assessment of the classifications.

Table 6.6. Number of training and test regions

Classified images	Number of samples					
	Aquatic vegetation		Flooded forest		Unflooded forest	
	Training	Testing	Training	Testing	Training	Testing
RADARSATS6 + JERS, November	48	41	10	8	60	29
RADARSATS6 + JERS, April	57	49	100	67	20	8
RADARSATS6 + JERS, May	122	72	109	71	-	-
RADARSATS6 + JERS, June	76	54	120	64	-	-
RADARSATS6 + JERS, August	83	59	97	72	12	8
RADARSATS6 + RADARSATS1, May	103	75	111	84	-	-

The overall accuracy and the error matrix of each classification were computed. The overall accuracy (weighted by the area of the class) represents the accuracy of the entire classification. An 85% overall accuracy was established as a cutoff between acceptable and unacceptable results as suggested by Congalton and Green, (1999) and based on the classification accuracy compiled by Dobson et al., (1996). The accuracy results of the individual classes were also evaluated. The confusion matrices show these accuracy values together with the commission and omission errors. Matrices of confusion and overall accuracy for the classification results are shown in Table 6.7.

Table 6.7. Matrices of confusion for the classifications

	True class		
% Classified as	Aquatic vegetation	Flooded forest	Unflooded forest
	RADARSAT S6 + JERS-1, November – overall accuracy = 97.02%		
Aquatic vegetation	99.1	0	0.91
Flooded forest	0	58.9	41.
Unflooded forest	3.3	11.3	85.
	RADARSAT S6 + JERS-1, April – overall accuracy = 96.94%		
Aquatic vegetation	94.4	5.6	0
Flooded forest	0.9	97.8	1.2
Unflooded forest	0	2.9	97.1
	RADARSAT S6 + JERS-1, May – overall accuracy = 97.39%		
Aquatic vegetation	95.3	4.5	-
Flooded forest	0	100	-
Unflooded forest	-	-	-
	RADARSAT S6 + JERS-1, June – overall accuracy = 95.47%		
Aquatic vegetation	97.4	2.6	-
Flooded forest	0.6	99.36	-
Unflooded forest	-	-	-
	RADARSAT S6 + JERS-1, August – overall accuracy = 93.85%		
Aquatic vegetation	93.4	5.5	1.11
Flooded forest	4.6	95.5	0
Unflooded forest	0	8.1	91.9
	RADARSAT S6 + RADARADARSATS1, May – overall accuracy = 66.49%		
Aquatic vegetation	64.5	35.5	-
Flooded forest	30.9	69.1	-
Unflooded forest	-	-	-

Generally, the overall classification accuracy for the multi-wavelength, C and L bands combinations exceeded 95%, implying satisfactory results, except between flooded and unflooded forest in November. Aquatic vegetation areas were found to be accurately classified (>95%) at any season. Closer examination revealed that the small percentage of misclassification (4.5%) of aquatic vegetation as flooded forest occurred consistently in areas colonized by *P. fasciculatum* and *E. Polystachya*. In flooded periods (April, May, June, and August), these grass-like species have well-developed tall stems (diameter ~ 1.0 cm and height > 1.0 m), very long wide leaves, and are not as dense (number of stem ~ 25 m^{-2}) as *H. amplexicaulis* (~ 111 stems m^{-2}), which is the dominant species in the area. The combination of the architecture and the distribution of these plants promote double bounce mechanism at L band similar to that observed from flooded forest. At C-band, these species of aquatic vegetation and flooded forest also showed similar σ^0 values, but mostly due to volume scattering mechanism. This is related to the already discussed low transmissivity of the canopy of different types of vegetation at C band (45°). The source of confusion observed for the classified data was the similarity of the scattering mechanisms from the ground cover at each wavelength. The addition of a P band (> 30 cm of wavelength) image would probably solve this ambiguity, and as a consequence higher accuracy would be achieved. The interaction of P band radiation may result in two different mechanisms depending on the type of vegetation, namely (i) double-bounce – interaction of the radiation with flooded trees, and (ii) quasi-specular reflection – interaction of the radiation with all species of grass-like aquatic vegetation. It is unfortunate that, currently, P band is not operational on satellite platforms. Alternatively, C band multi-polarized images will be available in the near future from satellite platforms such as, ENVISAT (European satellite) and RADARSAT 2 (Canadian satellite). However, it is not expected that either C-VV or C-HV images will solve this misclassification due to the nature of the interaction of VV and HV polarization with the near vertical oriented canopy of the vegetation. At C band, radiation propagating in a vertical plane is strongly attenuated by the upper canopy of vertically oriented grass-like vegetation; the transmissivity of the canopy is very low (Ulaby et al., 1982; Ferrazzoli et al., 1997). Hess et al. (1995) also reported that airborne C-VV and C-HV (33° of incidence angle) could not discriminate between aquatic vegetation and flooded forest. Perhaps using C band multi-incidence angle and multi-polarization (RADARSAT 2) in conjunction with ALOS (L band Japanese satellite) will solve some of the ambiguities between flooded forest and aquatic vegetation; this is still unknown.

Flooded forest showed an average classification accuracy of 90%. Clearly, the different backscattering coefficients provided by C and L bands from the ground cover explain this accuracy (section 5.3 and 5.4.2), that is, different scattering mechanisms occur from the interaction of short and long wavelengths with the canopy of the vegetation. Aquatic vegetation areas were nearly transparent at L band, whereas flooded forest areas strongly attenuated the radiation. At C band, both flooded forest and aquatic vegetation attenuated the radiation in similar manner. In fact, the distinction between the classes is introduced primarily through JERS-1 backscattering differences. The main classification error was between unflooded forest and flooded forest, at low water period (November). At this period the water level was starting to rise; hence, the forested areas within the floodplain had three situations of ground surface: dry, moist, and nearly flooded. It is speculated that the source of misclassification was between moist and flooded surfaces, where both showed a weak double-bounce mechanism. Ground truth data are not available to justify this speculation.

Poor classification results were shown for the C band multi-incident angle combination, RADARSAT S6 (45°) and RADARSAT S1 (25°). These results suggested that the difference in the incidence angle of the radiation was a secondary effect on the discrimination of the ground cover. Other researchers have shown that multi-wavelength SAR combination improves the general classification of vegetated areas to values higher than 90% for forested areas (Pierce et al., 1994; Dobson et al., 1996; Bergan et al., 1998; and Kellndorfer et al., 1998), agriculture areas (Lobo et al., 1996), and wetlands (Hess et al., 1995). Further, multi-incidence angle, such as the case of only RADARSAT data, have been shown not to improve discrimination between grassland types (Hill et al., 2000).

The high ambiguity between classes resulting from the classification of RADARSAT S6 + RADARSAT S1 seems unresolvable using only multi-incidence angle combination. The short wavelength of C band was attenuated in the upper canopy of both aquatic vegetation and flooded forest regardless the incidence angle. As a result, the backscattering coefficients were very similar for both ground cover; slight differences in backscattering between ground cover were observed for RADARSATS1. The steeper incidence angle facilitates an additional penetration of the microwave energy into the aquatic vegetation canopy producing some double bounce mechanism (section 5.4.2). The overall accuracy of 66% was driven mainly by the contribution of RADARSAT S1.

The seasonal calculated area of aquatic vegetation, flooded forest, and unflooded forest are shown in Table 6.8. By November/December, the water level of the Amazon River, as measured in Óbidos, was already high in approximately 2.5 m. The dry regions of the floodplain were starting to flood, mostly the areas on the margins of the lake and areas nearest to the Amazon channel. In these areas, extent regions of aquatic vegetation at the beginning of the growth cycle were observed. Aquatic vegetation cover at the beginning of the growth cycle were also seen in very moist areas and in some dry areas close to the margin of the lakes. The total area covered by aquatic vegetation in November (342 km^2) was higher than in April (217 km^2). By April, the water level of the Amazon River was 4 m higher than in November, causing a 2 m increase in the water depth of the regions colonized by aquatic vegetation. The flood exterminated colonies of plants (established in November) that could not keep pace with the rapid change of the water level. This explains the higher area occupied by aquatic vegetation in November than in April. The maximum calculated area was in May (397 km^2), during high water. After May, the water started to recede with the consequence that some aquatic vegetation detached from the bottom and was carried away towards the Amazon River; the occupied area decreased to 296 km^2 (June) and 282 km^2 (August).

The area classified as flooded forest increased from November to May, and decreased again from June to August, clearly reflecting the annual water level variation. The length of the period under flooded conditions is important in order to define the characteristics of the flooded forest. This will be discussed later. The areas within the floodplain classified as forest (unflooded forest) decreased from November (333 km^2) to April (87 km^2) and May/June (0 km^2), and started to increase again by August (85 km^2), once again reflecting the water level variation. Large areas of floodplain forest were not flooded in November when the water level was 2.5 meters high. This area decreased considerably in April when the water level variation was 6 m; by high water, the areas of flooded forest were completely flooded. By August, when the water receded to the same level as April, the areas of flooded forest that were not flooded increased again to a value very similar to April.

Table 6.8. Total area (Km^2) per class

	Aquatic vegetation	Flooded forest	Unflooded forest	Upland*	Open water*
November	342	93	333	844	1045
April	217	156	87	844	1247
May	397	304	-	844	1112
June	296	290	-	844	1227
August	282	238	85.	844	1208
RADARSAT S6+RADARSAT S1, May	304	363	-	844	1112

* area of upland represents the upland mask; areas of open water represent the open water mask for each period.

The length of the inundation period is the primary force of the zonation in the *várzea* (Junk and Piedade, 1997; Worbes, 1997). The temporal thematic classification maps (Figure 6.6) in conjunction with the estimated areas of the ground cover within the floodplain (Table 6.8), gave some insights regarding the zonation in the study area. Four distinct areas of zonation were characterized based on the multi-temporal classification.

Two different ground cover were classified as under flooded conditions of at least 300 days yr^{-1}. The first area had aquatic vegetation continuously from when the water started to rise in November until August. The perennial aquatic vegetation tolerates flood condition for more than 300 days yr^{-1} as well as high rates of sedimentation; they are one of the pioneer species which fix their roots (Junk and Piedade 1997). In the study region, currently, *H. amplexicaulis* is the dominant first settler. In these areas, the sedimentation process is greatly increased, as well as the accumulation of organic material in different stages of decomposition, creating a propitious habitat for colonization by pioneer tree-like communities. *Montrichardia arborescens (aninga),* a tall tree-like aquatic plant, *Salix* sp.*(oierana)*, a shrub-like tree, and *Courupita guianenses (castanha de macaco)*, tolerate flood conditions of 300 days yr^{-1} (Junk and Piedade, 1997; Worbes, 1997). These pioneer tree-like communities comprised the second ground cover, which was flooded continuously from November to August.

Early and late secondary settlers colonized the areas of flooded forest that were flooded from April to August, i.e. approximately 150 days yr^{-1}. The most common species in the study area are *Cecropia latiloba (imbaúba)*, *Pseudobombax munguba (munguba)*, and *Astrocaryum jauari (jauari)*. Other species were seen, but the scientific names were not known. Unfortunately the temporal frequency in which the satellite images were acquired did not allow a separation of areas of early and secondary colonizers. It is not known when these areas started to become flooded due to the lack of image acquisition in January and February. Furthermore, it is not known when the flood receded from these areas due to the lack of images from September and October. It is only known that these areas were flooded from April to August, i.e. at least for 150 days yr^{-1}, and that they were not flooded in November, which suggests that the colonizers do not tolerate flood all year around.

Finally, climax forest colonizes areas that were flooded in May and June (possibly July, but the data was not available), totaling approximately 60 days yr^{-1}. These areas were not flooded from November to April, or in August. They were mostly seen in the northern areas of the classified maps. Very tall dense-wood species are dominant (Worbes, 1997).

The results achieved with the highly accurate multi-temporal classification of the study area allowed a very complex analysis of length of inundation, zonation, and estimates of the different habitats areas in the *várzea*. These results have major implications in the regard to estimates of primary productivity and carbon budget of the floodplain (Piedade et al., 1991; Melack and Forsberg, 2000), on understanding the vegetation's adaptations to flood conditions (Worbes, 1997; Junk and Piedade, 1997), on the evaluation of preferential habitats for fish (Junk et al., 1997), on estimates of methane emissions from the floodplain (Wassmann and Martius, 1997; Forsberg, 2000), and on the evaluation of human use of these areas (Junk, 1997). Specifically for this research, the spatial temporal area occupied by aquatic vegetation is an important component of the model for estimating net primary productivity. This is the focus of the next chapter.

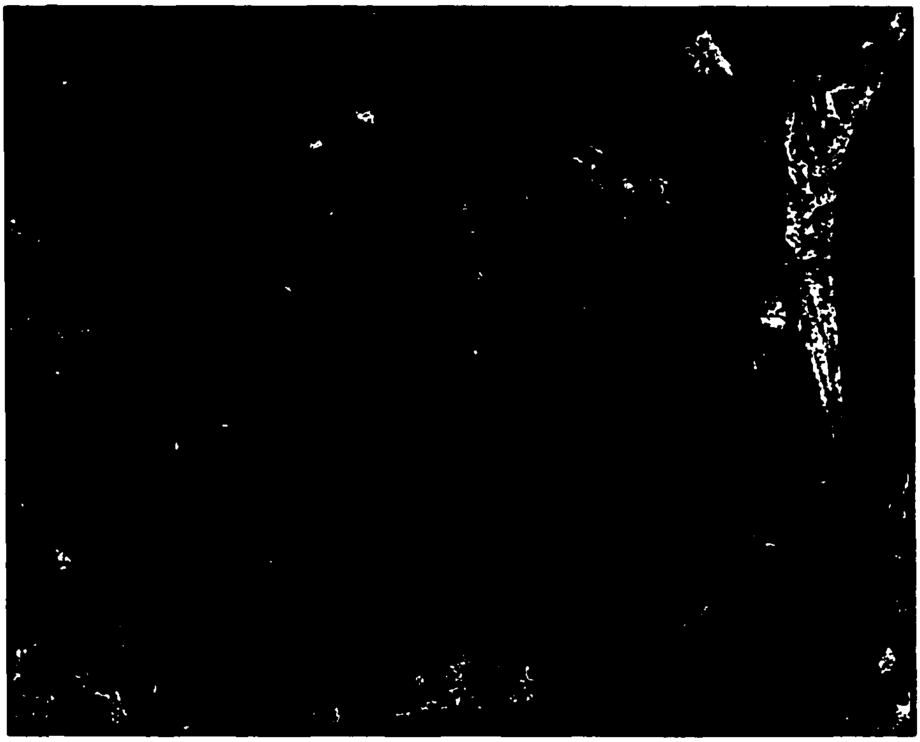

(a) November – low water

(b) April – rising water

(c). May – high water

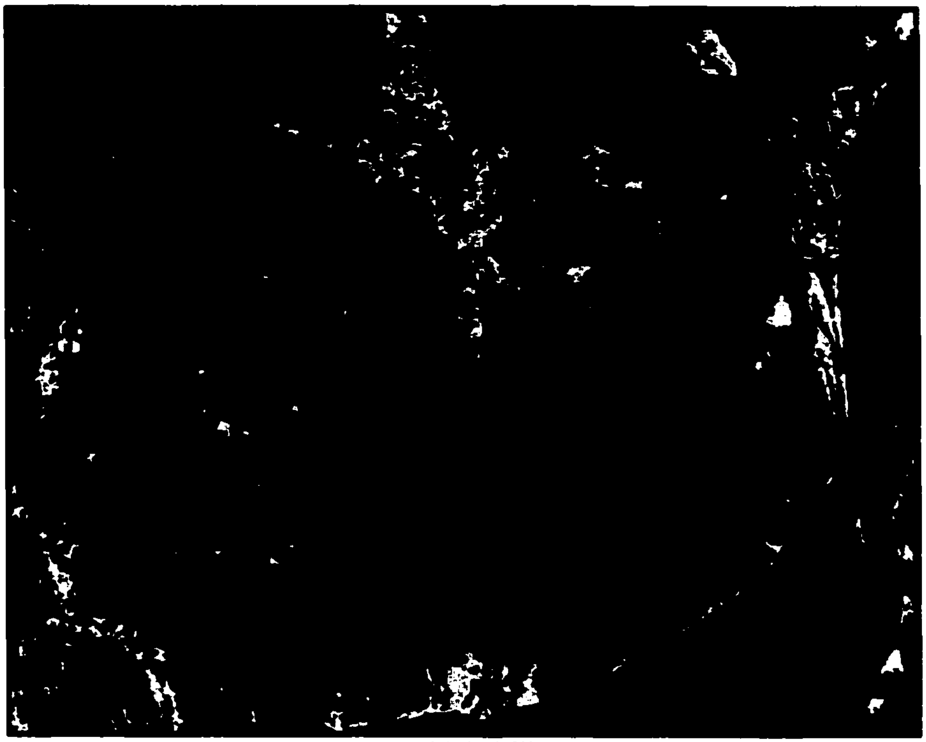

(d). June – high/falling water

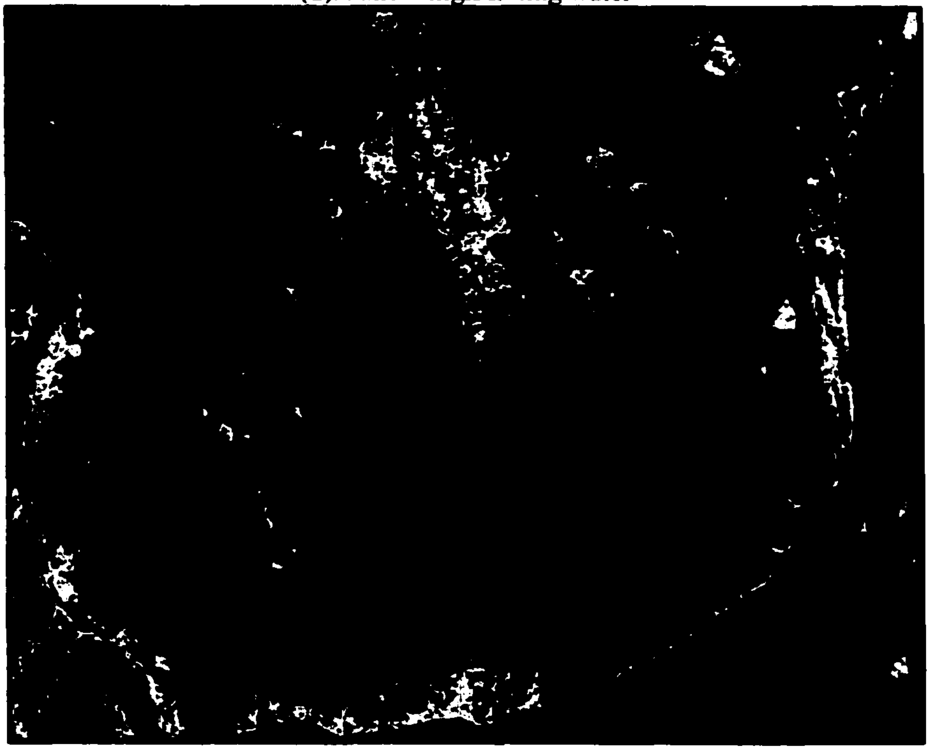

(e) – August, - falling water

Figure 6.6. Thematic classification maps. CYAN= aquatic vegetation; YELLOW= flooded forest; ORANGE= flooded forest not flooded; GREEN= upland; BLUE= water.

7. NET PRIMARY PRODUCTIVITY

Net primary productivity, the positive increment of plant biomass at a given period of time, after respiration loss has been subtracted, describes the removal of carbon from the atmosphere to the biosphere. The fate of the removed carbon is: (1) to be buried as organic carbon in the sediment, (2) to return to the atmosphere through respiration and degassing, and (3) to be transformed to bicarbonate through mineral weathering (Schlesinger, 1997). The Amazon floodplain produces approximately 113×10^{12} g of organic carbon annually, of which 62% is from herbaceous plants. Of the total organic carbon produced, a small component, 2.5%, is buried as organic carbon; 21% is respired back to the atmosphere; the remaining is exported to the water system (river to ocean). Currently, these are rough estimates (Melack and Forsberg, 2000). Part of the puzzle is to determine, on a regional scale, the total organic carbon produced by each ecosystem of the floodplain. To accomplish this requires knowledge of regional annual biomass production and the area of each ecosystem. This information is available on a local scale for various regions of the middle Amazon. As will be discussed, the combination of field and remotely sensing data will help provide this information on a large spatial and temporal scale.

The two previous chapters described the relationship between above water biomass and backscattering coefficient from aquatic vegetation and the estimated seasonal area occupied by aquatic vegetation. The estimates were combined for the purposes of calculating the seasonal total biomass and, therefore, net primary productivity of aquatic vegetation. The following section explains this procedure.

7.1. Estimates of Net Primary Productivity

Having established the accuracy of the statistical model for estimating biomass as well as the classified area of aquatic vegetation, the multi-temporal regional total biomass is presented in both a tabular form and as well as thematic maps. From these data, the NPP and carbon uptake were estimated through the following steps:

1. Overlay the classified area of aquatic vegetation on the backscattering images.
2. Apply the statistical algorithm to retrieve above water biomass as a function of backscattering coefficients on a pixel basis.

$$B_{a_i} = f\left(\sigma^o{}_{index\ i}\right) \qquad \text{Equation 7.1}$$

where B_{ai} is the above water biomass of the *i*th pixel calculated as $B_{a_i} = 4.022 + 0.175 \times \sigma^o{}_{index\ i}$; and $\sigma^o{}_{index\,i}$ was calculated as

$\sigma^o{}_{index\ i} = \dfrac{\sigma^o{}_{C_i} + \sigma^o{}_{L_i}}{2}$ in dB units.

3. Calculate the seasonal total biomass, B_T (above + submerged biomass), for each of the five images, as a function of the seasonal above water biomass (B_a) and the seasonal percentage of the submerged biomass to the total biomass estimated through field data.

$$B_{T_i} = f\left(B_{a_i}, \% B_{s_i}\right) \qquad \text{Equation 7.2}$$

where $\% B_{si}$ is the seasonal percentage of below water biomass to the total biomass, B_{Ti}. Figure 7.1 and Table 7.1 shows the seasonal B_{Ti} images and the main estimates of seasonal B_{Ti} (gm^{-2}), respectively. The total B_T is the $\sum_{i=1}^{n} B_{T_i}$, where i is the ith pixel of the image.

The mean error associated with B_T had three potential sources: (1) the classification, (2) the above water estimate from backscattering, and (3) the below water estimate based on field data. It is possible that other errors could be associated with B_T; for example, the error of above water biomass measured in the field. The field results were similar to other estimates from the Amazon floodplain (Junk, 1970; Piedade et al., 1991; Junk and Piedade, 1993; Junk and Piedade, 1997); therefore, the error associated with these measures was assumed to be minor. The first error, the classification accuracy, was also negligible due to the high accuracy of the classification (> 95%). In regard to the second error, the use of the statistical model to estimate above water biomass resulted in an average RMS error of 34%. This error presented a random distribution over the range of biomass. A slightly higher dispersion of the points was observed at high levels of biomass, which might be related to the saturation effect. However, this dispersion was difficult to evaluate due to a small sample size. The saturation point was previously determined to be 620gm^{-2} of above water biomass (item 5.4.2.2). Taking into account the seasonal differences of percentage of above water biomass to total biomass (Table 3.5), the above water biomass means (estimated from the satellite images) were below the saturation point. Mean above water biomass of 146, 338, 463, 478, and 584 gm^{-2} were estimated in November, April, May, June, and August, respectively. Therefore, the saturation effect of above water biomass did not inhibit the calculation of total biomass.

The variance of the below water biomass was estimated as 14% (section 3.4), and this comprised the third error. The uncertanties of the estimated B_T was a result of the combination of the second (34%) and third (14%) errors, with the percentage of above (20%) and below (80%) water biomass to B_T. The values of percentage of above and below water biomass were calculated according to the data of *H. amplexicaulis*, since this species was the most common in the study area. The final error of B_T was estimated as 18% (0.34 x 20 + 0.14 x 20); the same error was assumed for the calculated total NPP.

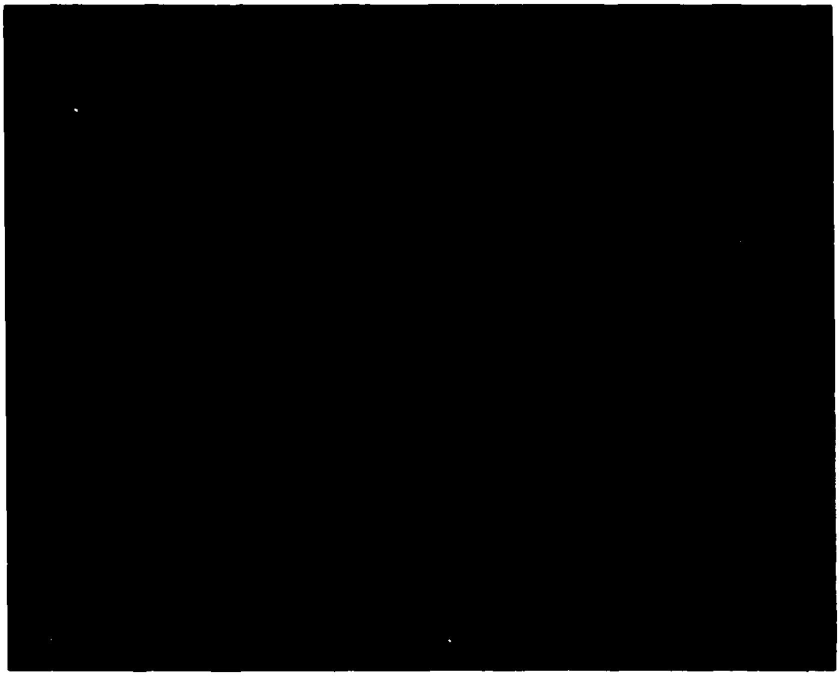

(a). November, low water

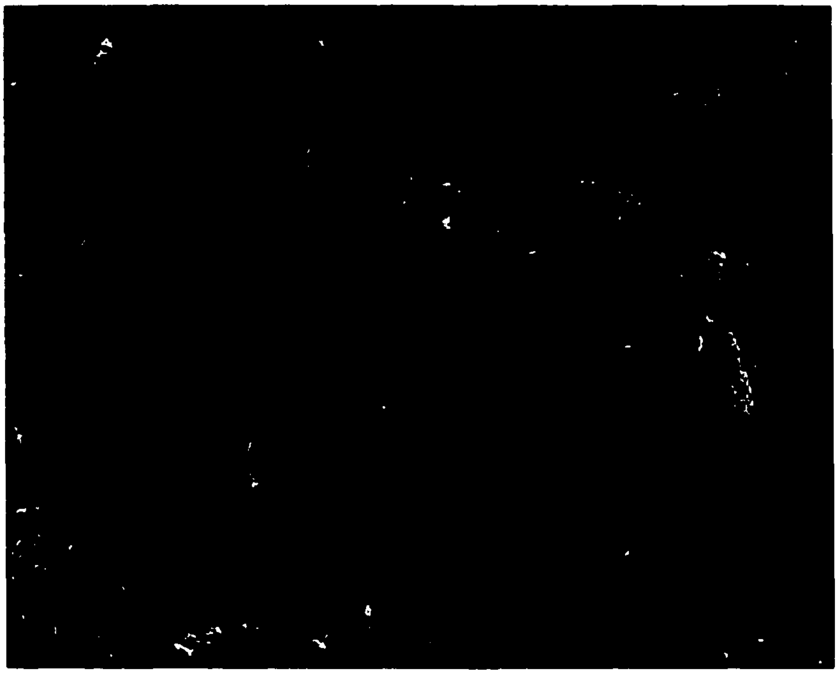

(b). April, rising water

(c). May, high water

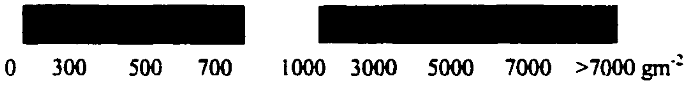

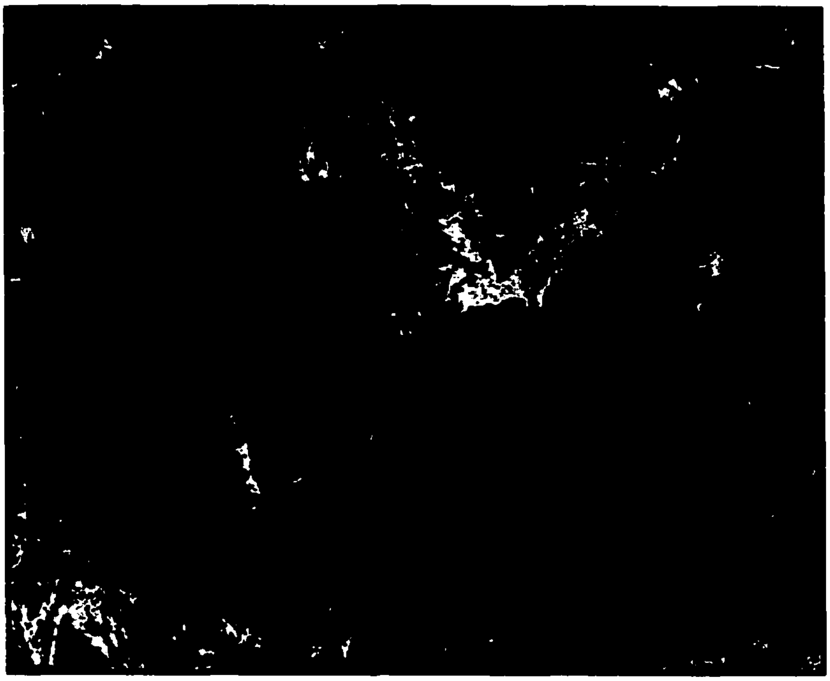

(d). June, high/falling water

(e). August, falling water

Figure 7.1. Seasonal spatial distribution of live total biomass of aquatic vegetation

0 300 500 700 1000 3000 5000 7000 >7000 gm^{-2}

Table 7.1. Comparison of mean and total biomass estimates through field and satellite data

	Mean Biomass (gm^{-2}) field	Mean Biomass (gm^{-2}) satellite	Total Biomass (g) Field + satellite [1]	Total Biomass (g) satellite
November	191(197)	303(225)	$0.65x10^{11}$	$1x10^{11}$
December	647*	1180(706)	$1.4x10^{11}$	$1.2x10^{11}$
January	1081*	1972(1179))	$2.3x10^{11}$	$2.1x10^{11}$
February	1493*	2722(1627)	$3.2x10^{11}$	$2.9x10^{11}$
March	1882*	3429(2050)	$4x10^{11}$	$3.6x10^{11}$
April	2255(314)	2820(1643)	$5x10^{11}$	$6.1x10^{11}$
May	2573(448)	3688(1676)	$10.2x10^{11}$	$14.5x10^{11}$
June	2934(674)	2386(1179)	$8.7x10^{11}$	$7.1x10^{11}$
July	3215*	2625(1296)	$9.5x10^{11}$	$7.1x10^{11}$
August	3489(210)	3389(1664)	$9.8x10^{11}$	$9.5x10^{11}$

Values between brackets are 1 standard deviation; * are estimated values (see next section); [1] are values estimated based on biomass measured in the field and area of aquatic vegetation measured with the satellite data.

4. The prefereble method of estimating annual NPP is to sum up monthly changes in live biomass plus litter (Junk and Piedade, 1993). According to Piedade et al. (1991), monthly estimates are especially important for studies of Amazonian aquatic vegetation because of the characteristics of the growth cyle of the vegetation. In the study area, the growing season extends from November to August (section 3.3). From September onwards the water level declines rapidly, and by October the floodplain becomes mostly dry. By September, the aquatic vegetation stands are in an advanced senescent stage (local community observation), which indicates that the growth season is finished.

The acquired data set refered to five months of the growing season: November, April, May, June, and August. As explained in the previous step, B_T was calculated for these months. For December, January, Feberuary, March, and July, B_T was estimated based on the rate of the increaes of total biomass between the months of acquired data, which showed a steady increase during the growth cycle. Steady growth is a common characteritic of the growth of Amazonian aquatic vegetation (Junk and Piedade, 1997). The growth rate was estimated through the relationship between the total biomass meassured in the field and time (R^2=0.99; n=5, p<0.01).

Having calculated the total biomass images for each of the ten months, monthly production was estimated. Production was equal to the increase of biomass and litter between two consecutive months; if biomass decreased or remained the same between two consecutives months, the production was only a function of litter (Junk and Piedade, 1993). This is stated as:

$$NPP_m = \left(B_{T_{t+1}} - B_{T_t}\right) + \left(L_{t+1} \times B_{T_{t+1}}\right) \quad \Delta B_T > 0 \qquad \text{Equation 7.3}$$

$$NPP_m = \left(L_{t+1} \times B_{T_{t+1}}\right) \quad \Delta B_T \leq 0 \qquad \text{Equation 7.4}$$

where NPP_m is the monthly productivity, B_{Tt+1} and B_{Tt} are the total biomass in months t+1 and t, respectively, L_{t+1} is litter produced during the interval, which is 25% of the B_{Tt+1} (Junk and Piedade, 1993), and ΔB_T is the increase in total biomass between two consecutive months. The annual NPP was calculated on a pixel basis through the summation of the monthly NPP_m, i.e. $NPP = \sum_{i=1}^{n} NPP_{m_i}$. Table 7.2 presents the mean annual NPP and the total NPP of the study area associated with an estimated 18% of uncertainty.

Table 7.2. Mean and total NPP estimated through satellite and field data

NPP			
Mean (gm^{-2})	Total (g yr^{-1})	Mean (gm^{-2})	Total (gyr^{-1})
satellite	satellite	field	field + satellite[1]
6350 (±1143)	$4.1\text{x}10^{12}(\pm 0.738\text{x}10^{12})$	8430	$5.4\text{x}10^{12}$

[1] value calculated based on the mean NNP (field data) and the area measure through the satellite images); values between brackets represent 18% of error.

5. The annual carbon uptake image was calculated as a function of the annual net primary productivity and the percentage of carbon content of the aquatic vegetation.

$$C_{uptake} = f(NPP\ ,\%\ C) \qquad \text{Equation 7.5}$$

The mean carbon content of *H. amplexicaulis* is 46% (±0.9, 1SD) of the dry matter, which is in agreement with general estimates of carbon content of vegetation elsewhere (Schelsinger, 1997). The total carbon uptake was $1.9\text{x}10^{12}$ g C yr^{-1} (±18%). Figure 7.2 illustrates the spatial distribution of the annual carbon uptake.

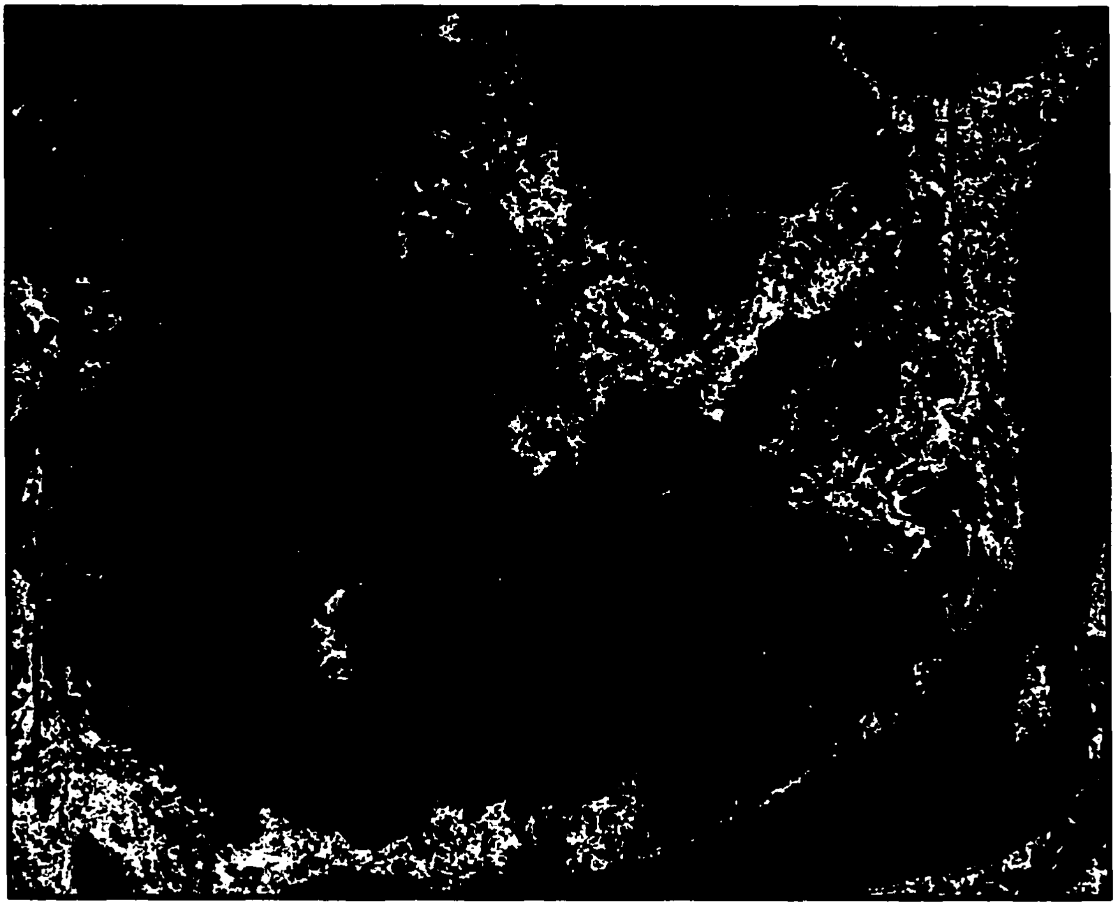

Figure 7.2. Spatial distribution of annual net carbon production of aquatic vegetation

0 900 2000 3000 3500 5000 >5000 g C m^{-2}

The satellite estimates of the total live biomass per month (Table 7.1) were statistically similar ($p<0.05$) to the values calculated through field measures, but they were generally higher than the field estimates. If an error of 18% (error of the total biomass estimate) is added to the satellite estimates, these differences are minimized. The difference between satellite and field estimates was also minimized when total biomass was expressed in terms of the total seasonal area occupied by the aquatic vegetation (Figure 7.3), which suggested that the satellite estimates have a positive skew distribution. After taking into account, both the monthly produced litter and the monthly produced biomass, the satellite estimate of mean total NPP was 6350g m^{-2} $yr^{-1}$and the total productivity for the entire area occupied by aquatic vegetation was $4.1x10^{12}$ g yr^{-1} (Table 7.2). The NPP estimate was a result of detailed spatial and temporal variability of aquatic vegetation from a large area. As yet, this is the first attempt to quantify net primary productivity of aquatic vegetation on such a scale.

The mean NPP value is within previous estimates for different species of aquatic vegetation of the central Amazon region (Table 7.3). The difference in productivity between the species is related to the requirements necessary to survive in the habitats that they colonize and the characteristics of the species. For instance, in a study conducted by Piedade et al. (1991), an environment subject to currents that reaches a maximum depth of 8m is described as an extremelly stressful environment for survival, and requires a fast-growing, strong species. *E. polystachya* colonizes this area. This species presents a high efficiency in converting intercepted solar radiation into dry biomass (2.3g/MJ) which is a characteristic of the highly productive C4 plants. Consequently, its thick stem grows approximately 1.1 m per month, keeping a live canopy above the water and resisting the currents. On the other hand, in a more protected area that reaches a maximum depth of 4 m, i.e. a less stressful environment, such as the case of this study area, *H. amplexicaulis* dominates. *H. amplexicaulis* is a smaller (thinner stems, smaller leaves, shorter, Table 3.2) C3 plant. Despite the smaller dimensions of *H. amplexicaulis* and the different photosynthetic pathway, its estimated productivity (gm^{-2}) is comparable to the value reported to *E. polystachya* (Table 7.3). This is partially due to the higher density of these plants (111 plants m^{-2}) compared with *E. polystachya* (30 plants m^{-2}). Furthermore, *H. amplexicaulis* might have the same adapatation as, for instance, *Juncus roemerianus*, which is a C3 plant from North America that increases its photosynthetic rate as light intensity increases to full sunlight, a behaviour similar to a C4 plant. Generally, C3 plants reach photosynthetic saturation at maximum ½ of full sunlight (Mitsch and Gosselink, 1993). This remains speculation for *H. amplexicaulis*, and experiments are still required to determine its photosynthetic saturation point. Therefore, in the Amazon, both C4 (Piedade et al., 1991) and C3 (this study) aquatic vegetation have, each in their own way, a strategy for achieving high productivity in their habitats.

Once more, a comparison between some NPP values reported in the literature (Table 7.3 and Wilen and Tiner, 1993), showed that Amazonian aquatic vegetation is among the wold's most productive wetland ecosystems. The high productivity of tidal salt and freshwater marshes is associated with the recycling of nutrients and toxins due to the effect of tides. The high productivity of the Amazonian aquatic vegetation is a survival mechanism (Piedade et al., 1991) allowed because of the nutrient rich environment (Weber, 1997) and the predictable monomodal flood pulse of the river-floodplain system (Junk et al., 1986).

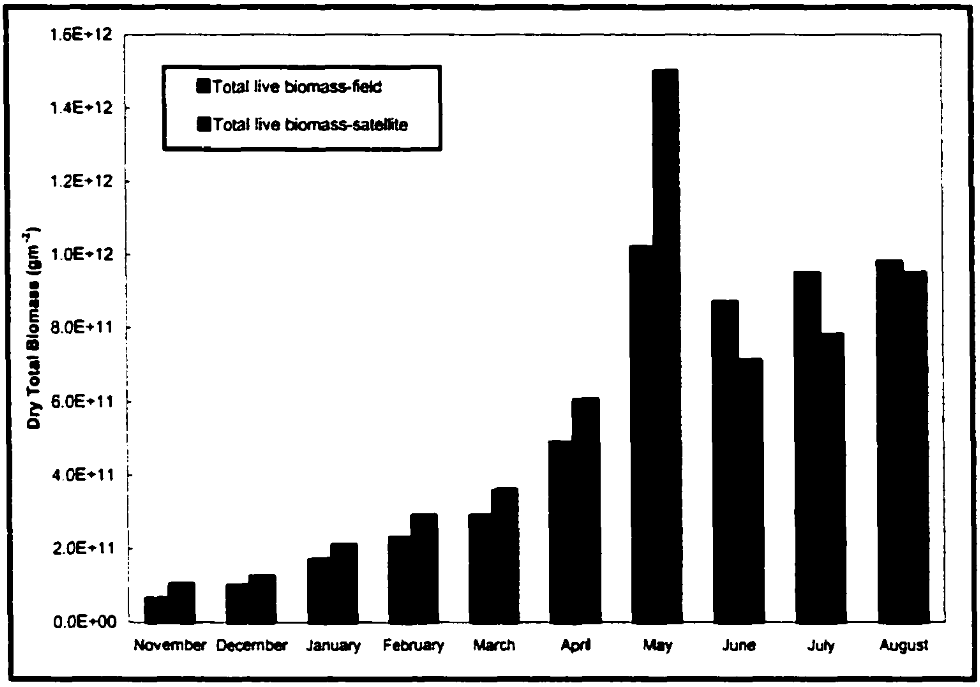

Figure 7.3. Total standing live biomass of aquatic vegetation

Table 7.3. Comparative estimates of NPP worldwide

Species	Location	Ecosystem	NPP (gm^{-2})	Period	Reference
H. amplexicaulis	Lower Amazon	Monomodal floodplain	6350	10 months	This study
E. polystachya	Central Amazon	Monomodal floodplain	9930	Annual	Piedade et al., 1991
P. repens	Central Amazon	Monomodal floodplain	3300	4 months	Junk and Piedade, 1993
H. amplexicaulis (sparse)	Central Amazon	Monomodal floodplain	1600	4 months	Junk and Piedade, 1993
O. perennis	Central Amazon	Monomodal floodplain	2700	4 months	Junk and Piedade, 1993
Spartina alterniflora	Alabama	Tidal salt marsh	8000	Annual	Compiled by Mitsch and Gosselink, 1993
Juncus roemerianus	Mississippi	Tidal salt marsh	10656	Annual	Compiled by Mitsch and Gosselink, 1993
Spartina alterniflora	Nova Scotia	Tidal salt marsh	1234	Annual	Compiled by Mitsch and Gosselink, 1993
Typha sp.	?	Tidal fresh water	1420	Annual	Compiled by Mitsch and Gosselink, 1993
Typha sp.	Wisconsin	Inland fresh water	3450	Annual	Compiled by Mitsch and Gosselink, 1993
Scirpus + Sparganium + Sagittaria and others	St. Lawrence River	Inland fresh water	1900	Annual	Hudon, 1997

The estimated NPP, 4.1×10^{12} g yr^{-1}, yielded a total carbon uptake of 1.9×10^{12} g C yr^{-1}. Spatially (Figure 7.2), the lower values of produced organic carbon (< 900 g C m^{-2}) were observed in regions that only developed in the beginning of hydrological cycle; values were generally higher (>5000 g C m^{-2}) in regions closer to the Amazon River where the influence of the nutrient rich water is higher. During the year and at the end of the growing cycle when the plants die, a continuous transfer of this carbon to the water takes place. However, this is not the total amount of carbon produced in the study area in a year. Aside from the aquatic vegetation, the main autochthonous primary producers are the flooded forest, phytoplankton, and periphyton. Using productivity data compiled by Melack and Forsberg, (2000) from different authors and our estimates of the area of the different habitats of the floodplain, we were able to estimate the total annual produced carbon for these groups. For flooded forest of the *várzea*, the total productivity is approximately 1150 g C $m^{-2}yr^{-1}$, which includes fine litter, dead wood, and root production (Melack and Forsberg, 2000, based on the data of Worbes, 1997). Taking into account the estimated maximum area of flooded forest, the total produced organic carbon was 0.35×10^{12}g C yr^{-1}.

Phytoplankton net primary productivity varies considerably due to the seasonallity of the floodplain, however a mean value of 195 g C m^{-2} yr^{-1} was considered a reasonable estimate (Melack and Frosberg, 2000). Applying this value to an area of maximum open water of 1143 km^2 produced a total net production of 0.22×10^{12} g C. For perithyton communities, the calculated productivity is approximately 100 g C m^{-2} yr^{-1}; the total net production was 0.03×10^{12} and 0.04×10^{12} g C for algae colonizing aquatic vegetation and flooded forest substrata, respectively. Consequently, the total combined autochthonous annual net primary productivity of the study area was $2.5x10^{12}$ g C, of which 75%, 14%, 8.8%, and 2.8% are from aquatic vegetation, flooded forest, phytoplankton, and perithyton, respectively. The total calculated production was approximately 2.2% of the total autochthonous net production of the Amazon floodplain estimated by Melack and Forsberg (2000). The percentages of each contributor to the total production in general agreed with their estimates; however, in our study area the estimated contribution of aquatic vegetation was slightly higher.

Part of the total produced organic carbon within the floodplain is respired due to the bacterial consumption of organic matter, part is buried in the lake sediment, but the majority is exported to the Amazon River .The percentages of total carbon losses are roughly estimated as 21%, 2.5%, and more than 70% for each of the end-members, respectively (Melack and Forsberg, 2000). Bacterial consumption of organic carbon releases high rates of CO_2 and CH_4 to the water and subsequently to the atmosphere. Generally, the Amazon waters are supersaturated in CO_2 and CH_4 compared to the atmosphere, and during falling water, when the aquatic vegetation starts to die, the rate of CO_2 evasion to the atmosphere doubles. The mean estimated emission (ebullition and evasion) of biogenic carbon (CO_2 and CH_4) from the floodplain to the atmosphere is approximately 1600 g C m^{-2} yr^{-1}(Richey et al., 1988) . The specific values of CH_4 emission rates show high variability for each habitat of the floodplain; however, it is generally agreed that the highest rates are from aquatic vegetation areas, on average ranging from 7.1 to 119 g C_{CH4} m^{-2} yr^{-1} (Bartlett et al., 1990; Devol et al., 1988; Wassmann and Martius, 1997). Assuming that emission rates of methane are related to the physio-chemical characteristics of the environment, the biomass production, the area of the habitat (Wasmann and Martius, 1997), and that the reported emission rates are valid approximations of the true emissions (Bartlett et al., 1990; Devol et al., 1988; Wassmann and Martius, 1997). The total annual methane emission from the aquatic vegetation of the study area was calculated as 0.037×10^{12} g C_{CH4} yr^{-1}, or approximately 0.6% of the total methane emission from the entire floodplain (Wassmann and Martius, 1997). In the Amazon floodplain, a common practice is the conversion of flooded forest to pasture land. If the existing flooded forest were to be replaced by aquatic vegetation, the methane emissions from the area would increase by approximately 50%. An extreme scenario would be the conversion of the entire flooded forest of the Amazon floodplain to pasture land; this would change the rough estimate of 6% contribution of methane emissions from the Amazon *várzea* (Wassmann and Martius, 1997) to the total wetland emissions worldwide (Bartlett and Harriss, 1993) into approximately 10%. Again, this is speculation; the test of its validity requires a more detailed knowledge of the organic carbon production, extent of floodplain habitats, and the understanding of the net fluxes of methane from the floodplain and upland regions.

The burial of organic carbon comprises the least loss of organic carbon in the floodplain. The quick and high rates of decomposition of the plant material (Howard-Williams and Junk, 1976), the physio-chemical characteristics of the water (Frosberg et al., 1988), and the sedimentation dynamic of the floodplain (Mertes et al., 1996) may prevent large rates of incorporation of the organic material into the sediment. Most of the organic carbon, more than 70% (Melack and Forsberg, 2000), is therefore exported to the river system. Analysis of suspended particulate organic material transported by the

Amazon River shows the predominance of upland soils in the fine fraction, and low and high components of C4 and C3 plant materials in the coarse fraction of the suspended sediment (Hedges et al., 1986). According to the authors, the C3 plant material is a combination of upland and flooded forest tissue; which are not distinguishable through the carbon isotope technique. Further, any contribution from C3 aquatic vegetation was camouflaged in the bulk particulate material; this could result in an underestimation of the contribution of the aquatic vegetation to the suspended organic load of the main stream.

Conceivably, the contribution of C3 aquatic vegetation, for instance, *H. amplexicaulis*, to the total load of exported material from the floodplain has been underestimated due to the assumption that C4 aquatic vegetation is dominant over the entire floodplain; this is not the case of this study area. The results clearly showed that the net organic carbon produced in an area dominated by *H. amplexicaulis* was high and therefore the contribution of this species to the carbon cycle of the Amazon region should be significant. Furthermore, the assumption that *E. polystachya*, a C4 plant, colonizes the entire floodplain could result in both overestimation of the net production of the floodplain and underestimation of the importance of aquatic vegetation to the exported carbon from the floodplain.

Large errors may result from the present methods of upscaling of field measures from a diverse ecosystem such as the Amazon floodplain to scales of global models. The global models for estimating net primary productivity are generally gridded either at a resolution of 0.5° latitude by 0.5° longitude, or coarser, and the productivity in equatorial regions ranges from 0 to 1500 g C m^{-2} yr^{-1} (Mellilo et al., 1993; Ruimy et al., 1994; Cao et al., 1996). At these spatial and carbon production scales, the productivity of a diverse and complex wetland such as the Amazon floodplain can undoubtedly be underestimated. For instance, at a 0.5° spatial resolution scale, which is approximately the total area of our study site (2°00'S/54 ° 00'W to 2°30'S/54 °30'W), the net productivity of the three main habitats (aquatic vegetation, flooded forest, and open water) would be averaged considering a normal distribution of the habitats (productivity and area). According to the results of this research, the annual net productivity of the floodplain has a bimodal frequency distribution with high frequency of low productivity (open water areas - phytoplankton), low frequency of intermediate productivity (flooded forest areas - flooded forest + perithyton), and intermediate frequency of high productivity (aquatic vegetation areas – aquatic vegetation + perithyton). Therefore, attempts to parameterize coarse scale models using data from the Amazon floodplain need to be non-linear. An interesting illustration of this problem is the net primary productivity calculated for natural wetlands worldwide by Cao et al. (1996) through a processed-based model at a resolution of 1° latitude by 1° longitude. The estimated mean net primary productivity for resolution cells (grid) within the Amazon floodplain is approximately 700 g C m^{-2} yr^{-1}; this is half of the mean net primary productivity estimated for the study area. The results show that the up scaling of ecosystem parameters from a heterogeneous region, such as the Amazon floodplain, towards a global model scale, requires complementary data on the scale of the variability of the ecosystem.

As well as the significant contribution of the results to the understanding of the regional carbon cycle, the methodology presented here can provide a set of tools that will help to understand ecological changes in the *várzea* as a result of human interference. The changes in the extent of flooded forest and aquatic vegetation areas due to human practices (cutting or burning) can potentially affect the fish population and the supply of nutrients to the *várzea* (Piedade et al., 1997). Aquatic vegetation is important as a direct, and indirect, source of food for fish. As a direct source, fish feed on the aquatic vegetation; as an indirect source, at the same time that zooplankton and other invertebrates feed on decomposing material of aquatic vegetation, they are an important food source for fish (Junk et al., 1997). However, the nutritionally rich fruits and seeds of the flooded forest are of greater importance, when available. The common burning of decomposing aquatic vegetation areas (dry season) for use as pastureland inevitably changes its role as a net source of nutrients for the *várzea* during low water (Piedade et al., 1997; Weber, 1997). The conversion of flooded forest and aquatic vegetation areas to pastureland can affect fish abundance, distribution, and food habits, and cause a disequilibrium in the nutrient budget of the floodplain.

8. SUMMARY AND CONCLUSIONS

8.1. Summary

The study area, located on the lower Amazon, describes the most common habitats of the Amazon floodplain where human impact is constantly increasing. This being so, it was an interesting site for evaluating the use of SAR satellites for estimating net primary productivity of aquatic vegetation through the hydrological cycle. The main feature of this floodplain is a large lake "Lago Grande de Monte Alegre", which is subject to water fluctuations of approximately 7 m between low and high water periods. To the north, a large area of flooded forest has been established; from the southwest to the southeast, the Amazon River runs towards the Atlantic Ocean; levees are present between the river and the large lake. The distribution of aquatic vegetation and flooded forest suggested a dynamic succession process in the area. *Hymenachene amplexicaulis* was the dominant aquatic vegetation, colonizing areas around the lake and levees; other species, such as *Paspalum repens* and *Echinochloa polystachya* also occurred.

Water levels are primarialy influenced by the Amazon and Tapajós Rivers. The combination of the hydrological cycle of these rivers promotes a predictable monomodal flooding cycle of the floodplain: the water level starts to rise in November, peaks in May/June, and quickly falls to a minimum level in October. The water cycle is the primary control of the growth pattern of the aquatic vegetation. The total biomass increased steadily from November to August ($p<0.05$) following the hydrological cycle. However, the above water canopy remained constant all year, with the exception of November; the biomass accumulates in the below water component. By November, new leaves and nodes were being formed. By April, a full canopy was developed and remained constant due to the high turnover rate of leaves. By August, the senescent stage began; the water content of the vegetation decreased, and the stems bent from an almost vertical orientation.

The seasonal consistency of the above water canopy resulted in seasonal similarities of the backscattering coefficients, except in November ($p<0.05$), for both C (RADARSAT S6) and L (JERS-1) bands. However, the spatial variability of the biophysical properties of the canopy distinctly affects the microwave radiation. The magnitude of radar backscattering generated by aquatic vegetation areas was a function of (i) the geometric properties of the vegetation and (ii) the underlying surface, in this case, water. Significant positive linear correlation ($p<0.05$) between backscattering coefficients or the derived index and above water fresh and dry biomass, height, and percentage of canopy cover were observed. Among the biophysical properties, the structure of the vegetation was approximately the same regardless the biomass; consequently, backscattering was mostly sensitive to the vegetation biomass, which in turn was dependent on the height and density of the plants. The parameter above water height showed extremely low variability, approximately 1m for most of the growing cycle. The 1 m height difference was only observed between the beginning of the growth (November) and the maximum height reached in May/June. The percentage of canopy cover, as measured, was not representative of either the occurrence of gaps in the stands or the variability of biomass of the stands. Generally, the combination of very dense stands (111 plants m^{-2}) with the orientation of stems and leaves resulted in the high percentage of canopy cover all year round, except for November. Correlation between

RADARSAT S1 and the biophysical properties was not significant ($p>0.05$); the restricted data set of RADARSAT S1 contributed to the low correlation coefficients.

The logarithmic relationship between backscattering coefficients and biomass suggested three levels of transmissivity of the radiation through the canopy related to the biomass of the plants. Low biomass (0 to 200 gm^{-2}) caused specular reflection for both C and L bands, and some canopy volume scattering for C band. As the biomass increased, canopy volume scattering dominated for C band (lower transmissivity). A second level of transmissivity was defined by moderate changes in backscattering values at a range of biomass from 200 gm^{-2} to the σ^{o} saturation point, calculated as 470, 660, and 620 gm^{-2} (above water biomass) for C band, L band, and the index, respectively. The lower saturation point of RADARSAT S6 was a result of lower transmissivity of the radiation through the canopy because of the shallow incidence angle and short wavelength. As a result, the upper canopy strongly attenuated the radiation. After the saturation point reached for both C and L band, the high biomass equally dampened the transmissivity of the radiation. Consequently, the backscaterring coefficients approached the same value. The derived index combineed the capabilities of both C and L bands providing the best adjusted R^2 for $B_{a,} = 4.022 + 0.175 \times \sigma^{o}_{index}$, ($R^2 = 0.67$), an intermediate saturation point for estimating above water biomass of aquatic vegetation (620 gm^{-2}), and the lowest root mean square error (34%). These results encourage the future development of radiative transfer models to confirm the important scattering mechanism attributable to the interaction of C and L bands with aquatic vegetation.

The analysis of the interaction of the backscattering coefficients with the ground cover of the floodplain and surrounding areas indicated that at periods of minimum water level the backscattering coefficients in both C and L bands were the lowest; as the water level rose so did the backscattering coefficients. JERS-1 exhibited a larger dynamic range of backscattering in response to the ground cover for the two extreme periods of water level (10dB) and within the image (6dB) compared with RADARSAT S6. A conclusion to be drawn from this is that the longer L band wavelength was more sensitive to the thickness and size of the scatter elements of the vegetation compared with the C band shorter wavelength. The different seasonal scattering mechanisms allowed the production of seasonal thematic maps of the floodplain.

The classification of the floodplain through a polygon-based approach resulted in high accuracy of the seasonal thematic maps of the floodplain for Level I classes (water, upland forest, floodplain forest – flooded and unflooded, and aquatic vegetation). Prior to the classification, the SAR images were submitted to a series of processing and analysis. First, the data set was radiometrically and geometrically rectified. Second, a detailed analysis of the adaptive speckle filters and enhanced Frost and Gamma filters with several interactions was performed. A quantitative analysis showed that three interactions of the gamma filter (i) adequately homogenized similar ground cover by decreasing the coefficient of variance in 25% of the original image, (ii) preserved the mean value of the ground cover, and (iii) visually, resulted in the best preservation of edges. Thereupon, texture measures of the original images were evaluated for integration into in the classification. A quantitative analysis did not show any improvement in the use of texture measures for separating ground cover when compared with the filtered images. The local heterogeneity of the ground cover occurred at a much finer scale than the spatial resolution detectable by RADARSAT and JERS-1. After completion of the rectification and improvement of the data quality, a segmentation and polygon-based supervised classification was applied to the SAR data set.

Quantitative and qualitative analysis suggested that a multi-wavelength classification performed better than individual wavelength or multi-incidence angle classification. The segmentation of the sets of RADARSAT S6/JERS-1 images used a region-growing algorithm, which depended on the thresholds of similarity and area. The statistical measure of the least significant distance (LSD) between the ground cover consistently defined the thresholds of similarity at a 95% level of significance. The minimum number of pixels required to have a polygon that was a good estimate of the mean of the ground cover defined the threshold of area. The supervised classifications of the pre-segmented RADARSAT S6/JERS-1 images yielded overall accuracy higher than 95% for any period. It is believed that the addition of P band data will solve some of the ambiguities for Level II classification, for instance, between well developed tall aquatic vegetation and flooded forest, or forest over moist and nearly flooded surfaces. Based on scattering mechanism theory, it is not expected that the upcoming C band multi-polarization satellites, RADARSAT 2 and ENVISAT, will solve these residual errors of the classification. Although the supervised classification of the floodplain produced highly accurate maps, the selection of training and testing polygons for the classification was laborious and time-consuming. A better approach for large-scale mapping would be the use of a polygon-based decision tree classifier trained through a seasonal library, with signatures from ground cover of the Amazon.

The results achieved with the multi-temporal classification yielded an estimate of the length of inundation of different regions of the floodplain. Regions under flooded conditions for at least 300 days yr^{-1} were colonized predominantly by the aquatic vegetation, *H. amplexicaulis*, the tree-like aquatic plant *Montrichardia arborescens*, and some shrub-like trees. Secondary settlers such as *Cecropia latiloba*, *Pseudobombax munguba*, and *Astrycaryum jauari*, which are all well-developed flooded forest, colonized regions under flooded conditions of approximately 150 days yr^{-1}. Climax forest colonized regions under flooded conditions of approximately 60 days yr^{-1}. The zonation according to the length of the flooding is a result of the different adaptations of the vegetation for tolerating flood stress. On the Amazon floodplain, the zonation status of a region can give some insight in regard to the annual autochthonous carbon production. Generally, the organic carbon production decreases according to the extent of the area of aquatic vegetation, flooded forest, and open water (in this order).

The combination of the seasonally flooded area and the statistical algorithm, which estimated above water biomass through backscattering of C and L bands, allowed the calculation of the seasonal total biomass. This represents the first attempt to develop a method using SAR and field data for estimating spatial and temporal variations in biomass of aquatic vegetation from a natural floodplain. Following the hydrological cycle, the total estimated biomass of the area increased steadily. By November, the new generation of aquatic vegetation started to develop; total biomass in the areas was 0.1×10^{12} g, new leaves and nodes formed as rapidly as the water rose, keeping the well-developed photosynthetic canopy above the water. The steady growth of vegetation yielded a total estimated biomass of 1.5×10^{12} g in an area of 395 km^2 in May. From May onwards, the water started to recede, the plants detached from the sediment and were carried towards the Amazon River. Consequently, by August, both the area and total biomass decreased to 281km^2 and 5x10^{11} g, respectively. Any estimate of total biomass had a margin of error of at least 18%. After correction for seasonal biomass loss, the total net primary productivity was 6350gm^{-2} or 4.1x10^{12} g for the entire area. Figure 8.1 summarizes total live biomass and NPP through the hydrological cycle of the study area.

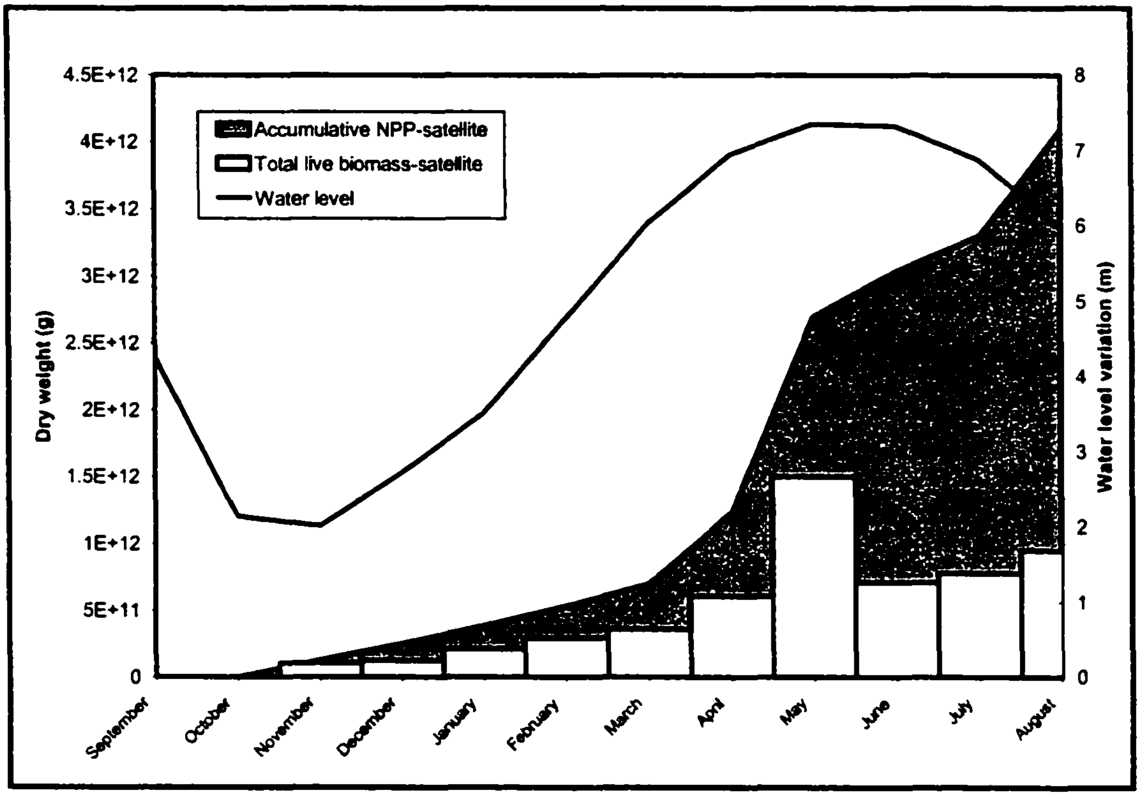

Figure 8.1. Total biomass and net primary productivity for the study area.

The estimated NPP of the aquatic vegetation yielded a total carbon uptake for the study area of 1.9x10^{12} g C yr^{-1}. Calculations based on the estimated area of each habitat of the floodplain and the productivity data suggested in the literature, produced a net carbon productivity from flooded forest, phytoplankton, and periphyton of 0.35x10^{12}g C yr^{-1}, 0.22x10^{12} g C yr^{-1}, 0.07x10^{12} g C yr^{-1}, respectively. The total combined autochthonous annual net carbon productivity of the study area was 2.5x10^{12} g C, of which 75%, 14%, 8.8%, and 2.8% are from aquatic vegetation, flooded forest, phytoplankton, and perithyton, respectively. Therefore, the aquatic plants are the most important autochthonous producers in the study area. During the year and at the end of the growing cycle when the plants decompose, a continuous transfer of this carbon to the water takes place.

8.2. Conclusions

The large data set compiled in the present study allowed (1) the seasonal characterization of an area of the lower Amazon floodplain, (2) the understanding and processing of the relatively new technology of SAR satellite data, (3) the understanding of the interaction of multi wavelength SAR data with the floodplain and surrounding area of the Amazon, (4) the development of a method to estimate net primary productivity of aquatic vegetation using backscattering coefficient and mapped area derived from multi-wavelength SAR data, and (5) the understanding of the role of aquatic vegetation in the carbon cycle of the study region.

The temporal analysis of the satellite data showed that the dynamic range of σ^o for RADARSAT S6 and JERS-1 from aquatic vegetation was approximately 5dB. However, the significant difference was only observed between low water season when plants were small and emerging and the other seasons when canopies were fully developed. During the growth and flowering periods, the dominant scattering mechanisms were different for C and L bands. For C band (45° of incidence angle), the main mechanism was volume scattering and for L band (35° of incidence angle), volume scattering and specular reflection are the dominant mechanisms, but for some species, double bounce may occur.

The spatial variability of the canopy's biophysical properties was detectable with microwave radiation. C and L band backscattering coefficients and the derived index (average of C and L band) significantly correlates with above water dry biomass. The derived index combines the capabilities of both C and L bands providing the best correlation (R^2 =0.67) and an intermediate saturation point (620 gm^{-2}) for estimating above water biomass of aquatic vegetation.

The analysis of the backscattering coefficients from different ground cover of the floodplain and the surrounding upland regions showed that together RADARSAT S6 and JERS-1 effectively mapped the areas colonized by aquatic vegetation. A region based classification, used for the first time for a multi-temporal mapping a large area of the Amazon floodplain, yielded accuracy higher than 94% for classifying vegetated areas within the floodplain. The multi-temporal classified data allowed the estimation of the length of inundation for different regions of study area. The spatial distribution of the inundation associated with the vegetation living in different flooding regimes constitutes a key insight for understanding regional zonation and planning future mapping missions and use of the floodplain.

The combination of the seasonal mapped area of aquatic vegetation with the statistical SAR-algorithm for estimating above water biomass and the percentage of below water biomass yielded a total annual NPP of 4.1×10^{12} g of dry weight (± 18%) or 1.9×10^{12} g C yr^{-1} (±18%). Despite the smaller dimensions and the C3 photosynthetic pathway of *Hymenachene amplexicaulis*, its estimated productivity was comparable to the value reported for the most productive aquatic vegetation of the Amazon floodplain, and other aquatic plants colonizing wetlands worldwide.

The results of this research were generated by estimates based on measures of a small area within the context of the Amazon floodplain. Validation with more data at a regional scale will possibly allow the use of the proposed method on the entire floodplain. Further improvement of this method depends on (i) a better understanding of the interaction of microwave radiation with aquatic vegetation, (ii) developing a model for estimating the seasonal depth of the areas colonized by aquatic vegetation in order to improve the accuracy of below water biomass estimates, and (iii) increasing the temporal frequency of acquisition of satellite and field data in order to improve the accuracy of the total biomass estimates.

REFERENCES

Amaral, S.; Shimabukuru, Y.E.; Ahern, F.J.; Lévesque, J. (1997). Pre-processing and semivariogram analysis of Radarsat fine mode images for forest applications: Tapajós national forest, Brazilian Amazon. In: *RADARSAT for Amazonia: results of ProRADAR Investigations*. 1-14.

Anys, H.; He, D.C. (1995). *IEEE Transaction of Geoscience and Remote Sensing*. 33(5):1170-1181.

Aselmann, I.; Crutzen, P.J. (1989). Global distribution of natural freshwater wetlands and rice paddies; their net primary productivity, seasonality, and possible methane emissions. *Journal of Atmospheric Chemistry*. 8:307-358.

Augusteijn, M.F., and Warrender, C.E. (1998), Wetland classification using optical and radar data and neural network classification. *International Journal of Remote Sensing*. 19(8):1545-1560.

Barbosa R.I.; Fearnside, P.M. (1996). Pasture burning in Amazonia: dynamics of residual biomass and the storage and release of aboveground carbon. *Journal of Geophysical Research*. 101 (D20):25,847-25,857.

Barbour, M.G., Burk, J.H., Pitts, W.D. (1987). *Terrestrial Plants Ecology*. The Benjamin/Cummings Publishing Company, Inc. California. 634p.

Bartlett, K.B.; Crill, P.M.; Sebacher, D.I.; Harriss, R.C.; Wilson, J.O.; Melack, J.M. (1988). Methane flux from the central Amazonian floodplain. *Journal of Geophysical Research*. 93(D2):1571-1582.

Bartlett, K.B.; P.M Crill.; J.A. Bonassi; J.W. Richey; R.C. Harris. (1990). Methane flux form the Amazon river floodplain: emissions during rising water. *Journal of Geophysical Research*. 95(10):16773-16788.

Bartlett, K. B.; Harriss, C. (1993). Review and assessment of methane from wetlands. *Chemosphere*. 26(1-4):261-320.

Bergen, K.M.; Dobson, M.C.; Pierce, L.E.; Ulaby, T. (1998). Characterizing carbon in a northern forest by using SIR-C/X-SAR imagery. *Remote Sensing of Environment*. 63:24-39.

Bernard, J.M.; Gorham, E. (1978). Life history aspects of primary production in sedge wetlands. In: *Freshwater Wetlands: Ecological processes and management potential*. Academic Press, Inc., London. 39-51.

Bins, L.S.; Fonseca, L.M.G.; Eethal, G.J.; Mitsuo, F. (1996). Satellite imagery segmentation: a region growing approach. *Proceedings. CD.* In: Simpósio Brasileiro de Sensoriamento Remoto. Salvador, Bahia, Brasil.

Brock, T.C.M.; Arts, G.H.P.; Goossens, I.L.M.; Rutenfrans, A.H.M. (1983). Structure and annual biomass production of *Ninphoides peltata* (Gmel.)). Kuntze (Menyanthaceae). *Aquatic Botany*. 17:167-188.

Brown, I.F.; Martinelli, L.A.; Thomas, W.W.; Moreira, M.Z.; Ferreira, C.A.; Victoria, R.A. (1995). Uncertainty in the biomass of Amazonian forests: an example from Rondônia, Brazil. *Forest Ecology and Management*. 75:175-189.

Camarão, A.P., Marques, J.R.F., Serra, E.A.S., and Ferreira, W.A. (1998*). Avaliação de pastagens nativas de várzeas do médio Amazonas*. 181, EMBRAPA, Brazil.

Camarão, A.P.; Marques, J.R.F. (1995*) Gramíneas nativas de terra inundável do trópico úmido Brasileiro*. Belém, EMBRAPA-CPATU. 62p.

Camargo, A.F.M.; Esteves, F. (1994). Biomass and productivity of aquatic macrophytes in Brazilian lacustrine ecosystems. In: *Limnology in Brazil*. 137-149.

Cao, M; Marshall, S.; Gregson, K. (1996). Global carbon exchange and methane emissions from natural wetlands: application of a process-based model. *Journal of Geophysical Research*. 101(D9):14,399-14,1414.

Caputo, M.V. (1991). Solimões megashear: interplate tectonics in northwestern Brazil. *Geology*. 3:246-249.

Cochran, W.G. (1963). *Sampling Techniques*. John Wiley & Sons. New York.

Colquhoun, D. (1971). *Lecture on Biostatistics*. Clarendon Press. Oxford. 425p.

Congalton, R.G.; Green, K. (1999). *Assessing the Accuracy of Remotely Sensed Data: principles and Practices*. CRC Press, Inc. Florida. 137p.

Costa, M.P.F.; Novo, E.M.L.M.; Ahern, F.; Mitsuo II,F.; Mantovani, J.E.; Ballester, M.V.; Pietsch, R.W. (1998). The Amazon floodplain through radar eyes: Lago Grande de Monte Alegre case study. *Canadian Journal of Remote Sensing*. 24(4):339-349.

Devol, A.H.; J.E Richey ; W.A Clarck ; S.L King ; L.A Martinelli. (1988). Methane emissions to the troposphere from the Amazon floodplain. *Journal of Geophysical Research*. 93:1583-1598

Dobson, M.C.; Pierce, L.E.; Ulaby, F.T. (1996). Knowledge-based land-cover classification using ERS-1/JERS-1 SAR composites. *IEEE Transaction of Geoscience and Remote Sensing*. 34(1):83-99.

Dobson, M.C.; Ulaby, F.T.; Pierce, L.E.; Sharik, T.L.; Bergen, K.M. (1995). Estimation of forest biophysical characteristics in northern Michigan with SIR-C/X-SAR. *IEEE Transaction of Geoscience and Remote Sensing*. 33(4):877-895.

Dong, Y., Forester, B.C., and Milne, A.K. (1999). Segmentation of radar imagery using the Gaussian Markov random field model. *International Journal of Remote Sensing*. 20(8), 1617-1639.

Downing, J.A.; Anderson, M.R. (1985). Estimating the standing biomass of aquatic macrophytes. *Canadian Journal of Fisheries and Aquatic Science*. 42:1860-1869.

Fearnside, P.; Ferraz, J. A. (1995). A conservation gap analysis of Brazil's Amazonian vegetation. *Conservation Biology*. 9(5):1134-1147.

Fearnside, P.M. (1991). Greenhouse gas contribution from deforestation in Brazilian Amazonia. In : *Global Biomass Burning: Atmospheric, Climatic, and Biospheric Implications*, edited by J.S Levine, pp 92-105, MIT Press, Cambridge, Mass.

Fearnside, P.M. (1996). Amazonian deforestation and global warming: carbon stocks in vegetation replacing Brazil's Amazon forest. *Forest Ecology and Management*. 80: 21-34.

Fearnside, P.M.; Leal, N.; Fernandes, F.M. (1993). Rainforest burning and the global carbon budget: biomass, combustion efficiency, and charcoal formation in the Brazilian Amazon. *Journal of Geophysical Research*. 98 (D9): 16,733-16,743.

Ferrazzoli, P; Paloscia, S.; Pampaloni, P.; Schiavon, G. Sigismondi, S.; Solamini, D. (1997). The potential of multifrequency polarimetric SAR in assessing agriculture and arboreous biomass. *IEEE Transaction of Geoscience and Remote Sensing*. 35(1):5-15.

Field, C.B.; Randerson, J.T.; Malstrom, C.M. (1995). Global net primary production: combining ecology and remote sensing. *Remote Sensing of Environment*. 51(1):74-88.

Ford, J.P.; Casey, D.J. 1988. Shuttle radar mapping with diverse incidence angles in the rainforest of Borneo. *International Journal of Remote Sensing*. 9(5):927-943.

Forsberg, B.R.; Devol, A.H.; Richey, J.E.; Martinelli, L.A.; Santos, H. (1988). Factors controlling nutrient concentrations in Amazon floodplain lakes. *Limnology and Oceanography*. 33(1):41-56.

Forsberg, B.R.; Rosenqvist, A.; Pimentel, T.P.; Richey, J.E. (2000). Modeling of flooding patterns and methane emissions in the Jau River floodplain (Central Amazon) using JERS-1 imagery. *Resume*. In: Wetlands 2000. Quebec. p.131.

Francin, R.C.; Van Dyne, G.M.; Williams, B.K. (1979). An evaluation of weight estimation double sampling as a method of botanical analysis. *Journal of Environmental Management*. 8:55-72.

Frazer, G.W.; Canham, C.D. (1999). *Gap Light Analyzer*. CD.

Freeman A. (1992). SAR calibration: an overview. *IEEE Transaction of Geoscience and Remote Sensing.* 30(6):1107-1121.

Furch, K.; Junk, J.W. (1997). Physicochemical Conditions in Floodplains. In: *The Central Amazon Flooodplain.* Junk (Ed.), Springer-Verlag, Berlin. 525p.

Giroux, J.F.; Bédard, J. (1897). Factors influencing aboveground production of *Scirpus* marshes in the St. Lawrence estuary, Québec, Canada. *Aquatic Botany.* 29:195-204.

Glackin, D.L. (1998). International space-based remote sensing overview: 1980-2007. *Canadian Journal of Remote sensing.* 24(3):307-314.

Glooschenko, W.A.; Tarnocai, C.; Zoltai, S.; Glooschenko, V. (1993). Wetlands in Canada and Greenland. In: *Wetlands of the World I: Inventory, Ecology and Management.* Kluwer Academic Publisher, Dordrecht, Netherlands. pp 415-514.

Goulding, M. (1993). Flooded forest of the Amazon. *Scientific American.* 112-120.

Goulding, M.; Smith, N.J.H.; Mahar, D.J. (1995). *Floods of Fortune: Ecology and Economy along the Amazon.* Columbia University Press, New York. 193p.

Hawkin, R.K.; Srivastava, S.K. (1999). *The radiometric calibration budget of RADARSAT-1.* ESA/ESRIN.

Hedges, J.I.; Clark, W.A.; Quay, P.D.; Richey E.J.; Devol, A.H.; Santos, U.M. (1986). Composition and fluxes of particulate organic material in the Amazon River. *Limnology and Oceanography.* 31(4):717-738.

Hess, L.L.; Melack ,J.M.; Simonett, D.S. (1990). Radar detection of flooding beneath the forest canopy: a review. *International Journal of Remote Sensing.* 11(7):1313-1325

Hess, L.L.; Melack,J.M.; Filoso, S.; Wang, Y. (1995). Delineation of inundated area and vegetation along the Amazon Floodplain with SIR-C synthetic aperture radar. *IEEE Transaction on Geoscience and Remote Sensing.* 33(4):896-903.

Holmes, M.G. (1992). Monitoring vegetation in the future: radar. *Botanical Journal of Linnean Society.* 108(2):93-109.

Houghton, R.A.; Skole, D.L.; Nobre, C.A.; Hackler, J.L.; Lawrence, K.T.; Chomentowski, W.H. (2000). Annual fluxes of carbon from deforestation and regrowth in the Brazilian Amazon. *Nature.* 403:301-304.

Howard-Williams, C.; Junk., W.J. (1976). The decomposition of aquatic macrophytes in the floating meadows of a central Amazonian Várzea lake. *Biogeographic.* 7:115-123.

Hudon, C. (1997). Impact of water level fluctuations on St. Lawrence River aquatic vegetation. *Canadian Journal Fish and Aquatic Science.* 54:2853-2865.

Imhoff, L.L. (1995). Radar backscatter and biomass saturation: ramifications for global biomass inventory. *IEEE Transaction of Geoscience and Remote Sensing.* 33(2):511-518.

Iron, G.; Junk, W.J.; Mello, J.A.S.N. (1997). The large central Amazonian river floodplains near Manaus: geological, climatological, hydrological, and geomorphological aspects. In: *The Central Amazon Floodplain.* Ed. Junk, W.J. Springer. Germany. Part II.

Jollineau, M.Y.; Howarth, P.J. (2000). Mapping and monitoring wetland ecosystems using high resolution CASI imagery. In: 22nd Annual Canadian Remote Sensing Symposium. *Proceedings.* 241.

Junk, W. J. (1970). Investigations on the ecology and production-biology of the floating meadows (Paspalo-Echinochloetum) on the middle Amazon. *Amazoni*ana. 2(4):449-495.

Junk W.J.; Howard-Willians, C. (1984). Ecology of aquatic macrophytes in Amazonia - In: *The Amazon: Limnology and Landscape Ecology of a Mighty Tropical River and its Basin.* - 269-293, Dr. W.Junk Publishers, Dordrecht, Boston, Lancaster.

Junk, W.J. (1984). Ecology of the várzea, floodplain of Amazonian white-water rivers. In: *The Amazon: Limnology and Landscape Ecology of a Mighty Tropical River and its Basin*, Dr. W.Junk Publishers, Dordrecht, Boston, Lancaster. 215-243.

Junk, W.J. (1985). The Amazon floodplain - a sink or source of organic carbon? In: Degin, E.T., Kempe, S and Herrera, R. (Editors*). Transport of carbon in the major World Rivers.* Part 3. Mitteilungendr Geologisches- Paleontologisches Institut Universitat Hamburg, SCOPE/UNEP. Sonderbd. 58: 267-283.

Junk, W.J.; Bayley, P.B.; Sparks, R.E. (1989). The flood pulse concept in river-floodplain system. In: D.P. Dodge (ed.). *Proceedings of the International Large River Symposium.* Can Spec. Publ. Fish. Aquat. Sci. 106. 110-127.

Junk, W.J.; Piedade, M.T. (1993). Biomass and primary productivity of herbaceous plant communities in the Amazon floodplain. *Hydrobiology.* 263:155-162.

Junk, W.J.; Piedade, M.T. (1994). Species diversity and distribution of herbaceous plants in the floodplain of the middle Amazon. *Verh. Internat. Verein. Limnol.* 25:1862-1865.

Junk, W.J. (1997). General aspects of floodplain ecology with special reference to Amazonian floodplains. In *The Central Amazon Floodplain: Ecology of a Pulsing System*, edited by W.J. Junk (Berlin: Springer), pp. 3-17.

Junk, W.J. and Piedade, M.T. (1997). Plant life in the floodplain with special reference to herbaceous plants. In *The Central Amazon Floodplain: Ecology of a Pulsing System*, edited by W.J. Junk (Berlin: Springer), pp. 147-181.

Junk, W.J.; Robertson, B.A. (1997). Aquatic Invertebrates. In: *The Central Amazon Floodplain*. Junk (Ed.), Springer-Verlag, Berlin. 279-296.

Junk, W.J.; Soares, M.G.M.; Saint-Paul, U. (1997). The fish. In: *The Central Amazon Floodplain*. Junk (Ed.), Springer-Verlag, Berlin. 385-405.

Junk, W.J. (2000). Status of knowledge, ongoing research, and research needs in Amazonian floodplain. *Resume*. In: Wetlands 2000. Quebec. p.318.

Kasischke, E.S.; Bourgeou-Chavez, L.L. (1997). Monitoring south Florida wetlands using ERS-1 SAR imagery. *Photogrammetric Engineering and Remote Sensing*. 63(3):281-291.

Kasischke, E.S.; Melack, J.M.; Dobson, M.C. (1997). The use of imaging radars for ecological applications – a review. *Remote Sensing of Environment*. 59:141-156.

Kellndorfer, J.M.; Dobson, M.C.; Ulaby, F.T. (1996). Geocoding for classification of ERS/JERS-1 SAR composites. *IEEE Transaction of Geoscience and Remote Sensing*. 2335-2337.

Kellndorfer, J.M. and Pierce, L.L. (1998). Towards consistent regional-to-global-scale vegetation characterization using orbital SAR systems. *IEEE Transaction on Geoscience and Remote Sensing*. 36(5):1396-1411.

Klinge, H. (1967). Podzol soils: a source of black water rivers in Amazonia. *Simpósio sobre a Biota Amazônica*. 3:117-125.

Konhauser, K.O.; Fyfe, W.S.; Kronberg, B.I. (1994). Multi-element chemistry of some Amazonian waters and soils. *Chemical Geology*. 111:155-175.

Kuruso, T.; Fujita, M.; Chiba, K. (1995). Monitoring of rice crop growth from space using the ERS-1 C-band SAR. *IEEE Transaction of Geoscience and Remote Sensing*. 33(4):1092-1096.

La Cruz, A.A. (1978). Primary production processes: summary and recommendations. In: *Freshwater Wetlands: Ecological processes and management potential*. Academic Press, Inc., London. 79-86.

Laur, H., Bally, P., Meadows, P., Sanchez, J., Schaettler, B., and Lopinto, E. (1996). *Derivation of the backscattering coefficient* σ^0 *in ERS.SAR.PRI products*. ESA/ESRIN, Issue 2, Rev. 2.

Laur, H.; Le Toan, T.; Lopes, A. (1987). Textural segmentation of SAR images using first order statistics parameters. In: IGARSS'87. *Proceedings*. 1463-1468.

Le Toan, T.; Ribbes, F.; Wang, L.; Floury, N.; Ding, K.; Kong, J.A.; Fujita, M. (1997). *IEEE Transaction of Geoscience and Remote Sensing*. 35(1):41:55.

Li, W.; Bénié, G.B.; He, D.C.; Wang, S.; Ziou, D.; Gwyn, Q.H.J. (1999). Watershed-based hierarchical SAR image segmentation. *International Journal of Remote Sensing*. 20(17):3377-3390.

Lieffers, V.J. (1983). Growth of *Typha latifolia* in boreal forest habitats, as measured by double sampling. *Aquatic Botany*. 15:335-348.

Lobo, A.; Chic, O.; Casterad, A. (1996). Classification of Mediterranean crops with multisensor data: per-pixel versus per-object statistics and image segmentation. *International Journal of Remote Sensing*. 17(12):2385-2400.

Lopes, A.; Touzi, R.; Nezry, E. (1990). Adaptive speckle filters and scene heterogeneity. *IEEE Transaction of Geoscience and Remote Sensing*. 28(6):992-1000.

Luciano, S.C. (1997). *Macrófitas aquaticas na Ilha do Ituqui (uma região de várzea do Baixo Amazonas/Santarém-PA) e suas relações com recursos icticos e atividades de pesca*. Projeto Várzea WWF/IPAM/UFPA, Brazil.

Luckman, A., Baker, J., Kuplich, T.M., Yanasse, C.C.F., and Frery, C. (1997). A study of the relationship between radar backscatter and regenerating tropical forest biomass for spaceborne SAR instruments. *Remote Sensing of Environment*. 60, 1-13.

Martinelli L.A.; Victoria, R.L.; Forsberg, B.B.; Richey, J.E. (1994). Isotopic composition of majors carbon reservoirs in the Amazon floodplain. *International Journal of Ecology and Environment Sciences*. 20:31-46.

Martinelli, L.A.; Victoria, R.L.; Dematte, J.L.; Richey, J.E.; Devol, A.H. (1993). Chemical and mineralogical composition of Amazon River floodplain sediments, Brazil. *Applied Geochemistry*. 8:391-402.

Matthews , E. and Fung, I. (1987). Methane emissions from natural wetlands: global distribution, area, and environmental characteristics of sources. *Global Biogeochemical Cycles*. 1:61-86.

Matthews, E.; Walter, E.B.; Gauci, V. (2000). Wetlands and the global methane cycle: current role and future outlook. *Resume*. In: Wetlands 2000. Quebec. p.236.

Melack, J.M.; Fisher, T.R. (1990). Comparative limnology of tropical floodplain lakes with an emphasis on the central Amazon. *Acta Limnologica Brasiliensia*. 3:1-48.

Melack, J. Hess, L.L.; Mertes, L.; Novo, E.M. (2000). Regional estimates of methane emission derived from remote sensing and filed measurements for the central Amazon. *Resume*. In: Wetlands 2000. Quebec. p.392.

Melack, J.M.; Forsberg, B.R. (2000). Biogeochemistry of Amazon floodplain lakes and associated wetlnads. In: *The Biogeochemistry of the Amazon Basin*. M.E. McClain, R.L. Victoria, J.E. Richey (eds.). Oxford University Press.

Melillo, J.M.; McGuire, A.D.; Kicklighter, D.W.; Moore, B.; Vorosmarty, C.J.; Schloss, A.L. (1993). Global climate change and terrestrial net primary production. *Nature*. 363:234-240.

Mertes, L.A.K. (1994). Rates of floodplain sedimentation on the central Amazon River. *Geology*. 22:171-174.

Mertes, L.A.K.; Daniel, D.L.; Melack, J.M.; Nelson, B.; Martinelli, A.; Forsberg, B.R. (1995). Spatial patterns of hydrology, geomorphology, and vegetation on the floodplain of the Amazon River in Brazil from a remote sensing perspective. *Geomorphology*. 13: 215-232.

Mertes, L.A.K.; Dunne, T.; Martinelli, L.A. (1996). Channel-floodplain geomorphology along the Solimões-Amazon River, Brazil. *Geological Society of America Bulletin*. 108(9):1089-1107.

Mitsch, J.W. and Goselink, J.G. (1993). *Wetlands*. 2nd edn. New York: Van Nostrand Reinhold.

Moik, J.G. (1980). *Digital Processing of Remotely Sensed Images*. Washington, DC. NASA.

Molion, L.C.B. (1991). The Amazônia and the global climate. *Boletim IG-USP*. 8:15-23.

Nepstad, D.C; Carvalho, C.R.; Davidson, E.A.; Jipp, P.H.; Lefebvre, P.A.; Negreiros, G.H.; Silva, E.D.; Stone, T.A.; Trumbore, S.E.; Vieira, S. (1994). The role of deep roots in the hydrological and carbon cycles of Amazonian forests and pastures. *Nature*. 372: 666-669.

Neter, J.; Wasserman, W.; Kutner, M.H. (1990). Applied Linear Statistical Models. IRWIN. U.S. 1181p.

Novo, E.M.L.M.; Leite, F.A.; Avila, J.; Ballester, V.; Melack, J.M. (1997). Assessment of Amazon floodplain habitats using TM/Landsat data. *Ciência e Cultura*. 49(4):280-284.

Novo, E.M.L.N.; Costa, M.P.F.; Mantovani, J.E. (1998). RADARSAT exploratory survey on macrophyte biophysical parameters in tropical reservoirs. *Canadian Journal of Remote Sensing*. 24(4):367-375.

Oliver, C. and Quegan, S. (1998). *Understanding Synthetic Aperture Radar Images.* 1st edn (Artech House, Inc. MA). 478p.

Piedade, M.T.F.; Junk, W.J.; Long, S.P. (1991). The productivity of the C4 grass *Echinochloa polystachya* on the Amazon floodplain. *Ecology.* 72(4):1456-1463.

Piedade, M.T.F.; Junk, W.J.; Mello, J.A.N. (1992). A floodplain grassland on the central Amazon. In: *Primary Productivity of Grass Ecosystems of the Tropics and Subtropics.* B.J.Jones and M.J. Roberts (eds.). Chapman & Hall/UNEP. 127-158.

Piedade, M.T.F.; Long, S.P.; Junk, W.J. (1994). Leaf and canopy photosynthetic CO2 uptake of a stand of *Echinochloa polystachya* on the central Amazon floodplain. Oecology. 97:193-201.

Pielou, E.C. (1981). Rapid estimation of the standing crop of intertidal fucoids on an exposed shore. *Journal of Environmental Management.* 13:85-98.

Pierce, L.E.; Ulaby, F.T.; Sarandi, K.; Dobson, M.C. (1994). Knowledge-based classification of polarimetric SAR images. *IEEE Transaction on Geoscience and Remote Sensing.* 32(5):1081-1086.

Pompêo, M.L.M.; Henry, R. (1998). Decomposition of macrophyte *Ecinochloa polystachya* (H.B.K.) Hotchcock, in a Brazilian reservoir (Paranapanena river mouth zone). *Verh. Internat. Verein, Limnol.* 26:1871-1875.

Pope, K.O.; Rey-Benayas, J.M.; Paris, J.F. (1994). Radar remote sensing of forest and wetland ecosystems in the Central American tropics. *Remote Sensing of Environment.* 48:205-219.

Pope, K.O.; Rejmankova, E.; Paris, J.F.; Woodruff, R. (1997). Detecting seasonal flooding cycles in marshes of the Yucatan Peninsula with SIR-C polarimetric radar imagery. *Remote Sensing of Environment.* 59:157-166.

Potter, C.S.; Randerson, J.T.; Field, C.B.; Matsaon, P.A.; Vitousek, P.M.; Mooney, H.A.; Klooster, S.A. (1993). Terrestrial ecosystem production: a process model based on global satellite and surface data. *Global Biogeochemical Cycles.* 7(4):811-841.

Proisy, C.; Mougin, E.; Fromard, F.; Karan, M.A. (2000). Interpretation of polarimetric radar signatures of mangrove forest. *Remote Sensing of Environment.* 71:56-66.

Quegan, S. (1990). Interpolation and sampling in SAR images. *IEEE Transaction of Geoscience and Remote Sensing.* 28(4):641-646.

RADANBRASIL. (1976). Folha SA.21-Santarém. *Levantamento de Recursos Naturais.* Vol.10. Rio de Janeiro, Brasil.

Raney, R.K.; Freeman, T.; Hawkins, R.W.; Bamler, R. (1994). A plea for radar brightness. *Proceedings of the International Geoscience and Remote Sensing Symposium* ,IGARSS`94, Pasadena, California, 8-12 Aug., 1994, pp.1090-1092.

Ribbes, F. and Le Toan, T. (1999). Rice field mapping and monitoring with RADARSAT data. *International Journal of Remote Sensing.* 20(4), 745-765.

Richards, J.A. (1986). *Remote Sensing Digital Analysis*, 1st edn. Springer-Verlag. 281p.

Richards, J.A.; Woodgate, P.W.; Skidmore, A.K. (1987). An explanation of enhanced radar backscattering from flooded forest. *International Journal of Remote Sensing.* 8(7):1093-1100.

Richey, J.E,; Martes, L.A.K.; Dunne, T.; Victoria, R.; Forsberg, B.R.; Tancredi, A.C.N.S.; Oliveira, E. (1989). Sources and routing of the Amazon River flood wave. *Global Biogeochemical Cycles.* 3(3):191-204.

Richey, J.E.; Devol, A.H., Wofsy, S.C.; Victoria, R.; Ribeiro, M.N.G. (1988). Biogenic gases and the oxidation and reduction of carbon in the Amazon floodplain and floodplain water. *Limnology and Oceanography.* 33(4):551-561.

Richey, J.E.; Meade, R.H.; Slati, E.; Devol, A.H.; Nordin, C.F.; Santos, U. (1986). Water discharge and seuspended sediment concentrations in the Amazon River:1982-1984. *Water Resources Researcher.* 22(5):756-764.

Rosenqvist, A. (1999). Temporal and spatial characteristics of irrigated rice in JERS-1 L-band SAR data. *International Journal of Remote Sensing.* 20(8), 1567-1587.

Ruimy, A.; Saugier, B.; Dedieu, G. (1994). Methodology for the estimation of terrestrial net primary production from remotely sensed data. *Journal of Geophysical Research.* 99(D3):5263-5283.

Schlesinger, W.H. (1997). *Biogeochemistry: an analysis of global change.* Academic Press, Inc. San Diego California. 443p.

Schobbenhaus, C.; Campos, D.A. (1984). *Geologia do Brasil.* Brasilia, Brasil.

Sellers, P.J., et al. (1997). BOREAS in 1997: experiment overview, scientific results, and future directions. *Journal of Geophysical Research.* 102(D24):28,731-28,769.

Sellers, P.J.; Meeson, B.W.; Hall, F.G.; Asrar, G; Murphy, R.E.; Schiffer, R.A; Bretherton, F.P.; Dickinson, R.E.; Ellingson, R.G.; Field, C.B.; Huemmrich, K.F.; Justice, C.O.; Melack, J.M.; Roulet, N.T.; Schimel, D.S.; Try, P.D. (1995). Remote Sensing of the land surface for studies of global change: models-algorithms-experiments. *Remote Sensing of Environment.* 51(1):3-26.

Shepherd, N. (1997). Output scaling look up tables in RADARSAT CDPF products. In: *Proceedings of a Workshop on RADARSAT Data Quality*. Quebec, Canada.

Shi, Z.; Fung, K.B. (1994). A comparison of digital speckle filters. *Proceedings*. In: IGARSS'94.

Shimada, M. (1998). *User's guide to NASDA' SAR products*. Technical Report. NASDA.

Shimada, M. (1996). Radiometric and geometric calibration of JERS-1 SAR. *Advances in Space Research*. 17, 79-88.

Shlien, S. (1979). Geometric correction, registration, and resampling of Landsat imagery. *Canadian Journal of Remote Sensing*. 5(1):74-89.

Singh, J.S.; Lauenroth, W.K.; Steihorst, R.K. (1975). Review and assessment of various techniques for estimating net aerial primary production in grasslands from harvest data. *The Botanical Review*. 2(2):181-232.

Sippel, S.J.; S.K. Hamilton; J. M. Melack. (1992). Inundation area and morphometry of lakes on the Amazon River floodplain, Brazil. *Arch. Hydrobiology*. 123:385-400.

Snedecor, G.W.; Cochran, W.G. (1980). *Statistical Methods*. Iowa State University Press. 507p.

Soares, L.C. (1991). Hidrografia. In: *Geografia do Brasil: Região Norte*. IBGE. Rio de Janeiro, Brasil. 73-118.

Srivastava, S.K.; Lukowski, T.I.; Gray, R.B.; Shepard, N.W.; Banik, B.; Hawkins, R.K.; Cloutier, C. (1997). Calibration and image quality performance results of RADARSAT. *In Proceedings of a Workshop on RADARSAT Data Quality. Canada.*

Toutin, T.; Carbonneau, Y.; St-Laurent, L. (1992). An integrated method to rectify airborne radar imagery using DEM. *Photogrametric Engineering and Remote Sensing*. 58(4):417-422.

Toutin, T. (1995). Multisource data integration with an integrated and unified geometric modeling. In: Sensors and Environment Applications of Remote Sensing. *Proceedings*. Askne (ed.), Balkema, Rotterdan. pp:163-469.

Touzi, R.; Lopes, A.; Boudquet, P. (1987). A statistical and geometrical edge detector for SAR image segmentation. *Proceedings*. IGARSS'87. 1469-1474.

Townshend, J.; Justice, C.; Li., W.; Gurney, C.; McManus, J. (1991). Global land cover classification by remote sensing: present capabilities and future possibilities. *Remote Sensing of Environment*. 35:243-255.

Ulaby, F.T., Moore, R.K., Fung, A.K. (1981). *Microwave Remote Sensing: Microwave Remote Sensing Fundamentals and Radiometry.* Artech House. US. Volume I. 456p.

Ulaby, F.T., Moore, R.K., Fung, A.K. (1982). *Microwave Remote Sensing: Radar remote Sensing and Surface Scattering and Emission Theory.* Artech House. US. Volume II. 1064p.

Ulaby, F.T., Moore, R.K., Fung, A.K. (1986). *Microwave Remote Sensing, from Theory to Applications.* Artech House. US. Volume III. 2162p.

Ulaby, F.T.; Dobson, I. (1987). *Handbook of Radar Scattering Statistics for Terrain.* Artech House. US. 357p.

Valeriano, D.M. (1996). *Relationships between Tropical structure and Remotely sensed Synthetic Aperture Radar.* Ph.D. Thesis. University of California, Santa Barbara, U.S. 148p.

Van der Valk, A.G.; Davis, C.B. (1987). Primary production of prairie glacial marshes. In: *Freshwater Wetlands: Ecological processes and management potential.* Academic Press, Inc., London. 21-37.

Victoria, R. L., Martinelli, L.A.; Frosberg, B.R.; Richey, J.E.; Devol, A.H. (1989). Spatial and temporal variations in the chemistry of várzea sediments of the Amazon Basin. *Geology.Journal.* 19:45-52.

Walker, I. (1990). Ecologia e biologia dos igapós e igarapés. *Ciência Hoje.* 11(64):44-53.

Wang, Y.; Hess, L.L.; Filoso, S.; Melack, J. M. (1995). Understanding the radar backscattering from flooded and nonflooded Amazonian forests: results from canopy backscatter modeling. *Remote Sensing of Environment.* 54:324-332.

Wilen, B.O.; Tiner, R.W. (1993). Wetlands of the United States. In: *Wetlands of the World I: Inventory, Ecology and Management.* Kluwer Academic Publisher, Dordrecht, Netherlands. pp 515-636.

Worbes, M. (1997). *The forest ecosystem of the floodplains. In: The Central Amazon Flooodplain.* Junk (Ed.), Springer-Verlag, Berlin. 223-260

Wassmann, R.; Martius, C. (1997). Methane emissions from the Amazon floodplain. In: *The Central Amazon Flooodplain.* Junk (Ed.), Springer-Verlag, Berlin. 137-142.

Whigam, D.F.; Dykyjová, D.; Hejný, S. (1993). *Wetlands of the World I: Inventory, Ecology and Management.* Kluwer Academic Publishers. Netherlands. 768p.

Whittaker, R.H.; Marks, P.L. (1975). Methods of assessing terrestrial productivity. In: *Primary Productivity of the Biosphere*. Lieth, H.; Whittaker, R.H. (eds.) Springer-Verlag. New York Inc. U.S. pp 55-118.

Wolf, J. and Hawkins, R.W. (1997). Retro-active calibration of RADARSAT CEOS products. In *Proceedings of a Workshop on RADARSAT Data Quality*. Canada.

Wulder, M. (1998). Optical remote sensing techniques for the assessment of forest inventory and biophysical parameters. *Progress in Physical Geography*. 44(4):449-476.

Yanasse, C.C.F. (1991). *Statistical Analysis of synthetic aperture radar images and its applications to system analysis and change detection*. Ph.D. Thesis, University of Sheffield.

APPENDIX I

Data set

Sample order	Sample No.	Month sampled	Latitude	Longitude	Dominant species	Depth (m)
1	1	Nov-96	54 20 07	2 20 37	P. fasciculatum	0.2
2	2	Nov-96	54 24 06.67	2 21 30.39	grass	
3	3	Nov-96	54 24 4.73	2 21 29.74	grass	
4	4	Nov-96	54 26 28.45	2 21 22.66	grass	
5	6	Nov-96	54 05 59.05	2 01 36.48	grass	
6	8	Nov-96	54 8 49.92	2 7 13.7	grass	0.5
7	10	Nov-96	54 8 29 34	2 7 21.48	grass	0.2
8	11	Nov-96	54 08 59.9	2 7 51.29	grass	0.5
9	12	Nov-96	54 9 14.25	2 7 56.53	grass	0.1
10	13	Nov-96	54 11 08.06	2 08 00.49	grass	
11	15	Nov-96	54 17 07.4	2 13 08.01	grass	
12	17	Nov-96	54 14 29.0	2 13 31.9	grass	
13	18	Nov-96	54 14 17.1	2 13 19.6	grass	
14	19	Nov-96	54 27 39.85	2 18 46.46	grass	
15	1	Apr-97	2 21 24.42	54 20 15.58	P. repens	2.5
16	2	Apr-97	2 21 23.88	54 20 17.88	P. repens	2.5
17	3	Apr-97	2 21 52.74	54 25 24.3	E. polystachya	2.5
18	4	Apr-97	2 21 59.34	54 25 23.5	P. repens	2.5
19	5	Apr-97	2 22 27.6	54 25 10.02	P. repens	2.5
20	6	Apr-97	2 22 28.5	54 24 52.20	H. amplexicaulis	2.5
21	7	Apr-97	2 22 31.8	54 24 50.4	H. amplexicaulis	2.5
22	8	Apr-97	2 11 23.46	54 17 24	H. amplexicaulis	2.3
23	9	Apr-97	2 11 16.2	54 17 22.3	H. amplexicaulis	2.3
24	13	Apr-97	2 8 27.9	54 12 35.22	P. repens	2.2
25	14	Apr-97	2 8 34.14	54 12 32.10	P. repens	1.7
26	20	Apr-97	2 7 4.62	54 11 41.9	P. repens	2.6
27	21	Apr-97	2 6 1.26	54 8 18.24	H. amplexicaulis	2.6
28	22	Apr-97	2 5 50.64	54 8 14.4	P. repens	2.6
29	23	Apr-97	2 12 10.44	54 7 52.62	P. repens	3.4
30	24	Apr-97	2 12 16.86	54 7 52.68	P. repens	3.4
31	6	May-96	2 20 47.8	54 20 1.8	H. amplexicaulis	3
32	7	May-96	2 21 41.5	54 24 55.6	H. amplexicaulis	3
33	8	May-96	2 22 10.8	54 23 20.9	H. amplexicaulis	2.5
35	16	May-96	2 18 15.1	54 30 10.9	P. repens	2
36	22	May-96	2 8 11.8	54 22 48.3	P. repens	
37	24	May-96	2 11 38.548	54 17 3.974	H. amplexicaulis	2
38	25	May-96	2 10 34.23	54 17 38.27	H. amplexicaulis	3
39	26	May-96	2 11 27.9	54 16 39.6	H. amplexicaulis	3
40	27	May-96	2 8 33.4	54 11 22	H. amplexicaulis	3
41	28	May-96	2 8 24.9	54 11 15.7	P.repens	6
42	29	May-96	2 6 26.797	54 14 24.269	P. repens	3.5
43	36	May-96	2 7 22.6	54 9 22.3	P. repens	3.5
44	1	Jun-99	2 22 4.2	54 25 21.6	P. repens	3
45	2	Jun-99	2 22 10.7	54 25 15.9	H. amplexicaulis	3.5

Sample order	Sample No.	Month sampled	Latitude	Longitude	Dominant species	Depth (m)
46	3	Jun-99	2 22 23	54 24 25 5	H. amplexicaulis	3
47	4	Jun-99	2 23 00	54 24 35.2	P. fasciculatum	1.1
48	5	Jun-99	2 22 53.3	54 24 45.2	H. amplexicaulis	2.62
49	6	Jun-99	2 23 00.1	54 24 39.7	P. fasciculatum	1
50	7	Jun-99	2 23 1.4	54 25 13.8	H. amplexicaulis	3.25
51	8	Jun-99	2 23 1.1	54 26 5.2	P. repens	3.75
52	9	Jun-99	2 21 46.4	54 25 18.7	H. amplexicaulis	4
53	10	Jun-99	2 21 29.4	54 20 21.7	E. polystachya	3.85
54	11	Jun-99	2 21 31.0	54 20 07.7	E. polystachya	3.5
55	12	Jun-99	2 21 59.4	54 19 57	E. polystachya	3.5
56	13	Jun-99	2 21 07.0	54 20 20.5	H. amplexicaulis	3.5
57	14	Jun-99	2 11 39.8	54 08 21.6	H. amplexicaulis	3.25
58	15	Jun-99	2 11 55.6	54 08 19.2	H. amplexicaulis	3.75
59	16	Jun-99	2 12 0.1	54 8 31.4	H. amplexicaulis	4
60	17	Jun-99	2 8 19.1	54 11 27.8	H. amplexicaulis	4
61	18	Jun-99	2 8 16.8	54 11 27.3	H. amplexicaulis	3.9
62	19	Jun-99	2 7 46.2	54 11 6.9	H. amplexicaulis	4
63	20	Jun-99	2 7 21.1	54 10 53.2	H. amplexicaulis	4
64	21	Jun-99	2 05 56.6	54 14 45.4	H. amplexicaulis	3.6
65	22	Jun-99	2 06 18.4	54 14 37.7	P. repens	4.1
66	23	Jun-99	2 07 17.7	54 13 27.4	P. repens	3.85
67	24	Jun-99	2 07 19.3	54 13 26.3	mix	
68	28	Jun-99	2 06 29.7	54 10 51.4	H. amplexicaulis	3.6
69	29	Jun-99	2 06 51.6	54 10 27.1	H. amplexicaulis	4
70	30	Jun-99	2 09 12.4	54 14 17.8	H. amplexicaulis	2.8
71	31	Jun-99	2 09 39.1	54 14 7.3	H. amplexicaulis	2.6
72	32	Jun-99	2 09 45.7	54 14 7.0	H. amplexicaulis	2.85
73	34	Jun-99	2 09 45.4	54 14 35.1	H. amplexicaulis	2.85
74	35	Jun-99	2 09 52.3	54 14 37.4	H. amplexicaulis	3.1
75	36	Jun-99	2 10 49.3	54 17 28.5	H. amplexicaulis	3.1
76	37	Jun-99	2 10 51.8	54 17 19.5	H. amplexicaulis	4.25
77	38	Jun-99	2 10 59.3	54 17 15.4	H. amplexicaulis	4.1
78	39	Jun-99	2 10 52.2	54 17 16.0	H. amplexicaulis	3.85
79	1	Aug-96	54 20 8.3	2 20 56.1	H. amplexicaulis	2
80	2	Aug-96	54 25 19.7	2 21 44.6	P.repens	1.5
81	3	Aug-96	54 24 41	2 21 51	E. polystachya	1.5
82	4	Aug-96	54 26 59.4	2 21 21 5	H. amplexicaulis	
83	6	Aug-96	54 30 12.1	2 18 17.4	P. repens	1.5
84	7	Aug-96	54 30 13.3	2 18 18.4	H. amplexicaulis	1.5
85	8	Aug-96	54 17 31	2 11 49	H. amplexicaulis	2.2
86	9	Aug-96	54 17 21.2	2 11 45.3	H. amplexicaulis	2.2
87	10	Aug-96	54 17 36.5	2 10 39.8	H. amplexicaulis	2.2
88	11	Aug-96	54 17 25.7	2 10 41	H. amplexicaulis	2.2
89	12	Aug-96	54 17 10.3	2 10 45.1	H. amplexicaulis	2.2
90	13	Aug-96	54 17 2.7	2 11 5.5	H. amplexicaulis	2.2
91	16	Aug-96	54 11 54.3	2 9 18	H. amplexicaulis	1.5
92	17	Aug-96	54 11 40.7	2 8 53.3	H. amplexicaulis	1.5
93	18	Aug-96	54 8 59.4	2 6 43.1	H. amplexicaulis	2

Sample order	Phenology	No. leaves	Leaf length (cm)	Leaf width (cm)	Stem diameter(cm)
1					
2	growth				
3	growth				
4	growth				
5	growth				
6	growth				
7	growth				
8	growth				
9	growth				
10	growth				
11	growth				
12	growth				
13	growth				
14	growth				
15	flowering		70	3	0.75
16	no flower		14.5	0.4	2.5
17	flowering		61	3	0.95
18	flowering		53	4.25	2
19	flowering		46.5	2.5	0.7
20	flowering		22.5	2.15	0.35
21	flowering		34.5	2.26	0.52
22	flowering		22.5	2.1	0.45
23	flowering		31.5	2.75	0.6
24	flowering		24.25	2.2	0.7
25	no flower		54.5	1.45	0.85
26	flowering		33.5	1.45	0.75
27	flowering		36.2	2.25	0.7
28	flowering		23	1.25	0.85
29	flowering		54.5	2.15	1
30	flowering		0.52	2.25	0.85
31	flowering	6	35	3.5	0.5
32	flowering	8	46	3	0.7
33	flowering	6	52	1.9	0.6
35	flowering	8	26	1.5	0.6
36	flowering	6	32	1.5	
37	flowering	7	15.5	1.4	0.52
38	flowering	5	18	1.4	0.5
39	flowering	5	18	1.4	0.5
40	flowering	4	22	1.7	
41	flowering		14	1.4	0.5
42	flowering	7	22.5	1.7	0.4
43	flowering		23		
44	no flower	6	25	1.9	0.6
45	flowering	6	35	4.5	0.5

Sample order	Phenology	No. leaves	Leaf length (cm)	Leaf width (cm)	Stem diameter(cm)
46	flowering	5	35	4	0.5
47	no flower	10	30	2	0.5
48	flowering	5	45	3	0.55
49	drying	10	50	2	0.5
50	flowering	4	24	3	0.4
51	flowering	6	40	2	0.5
52	flowering	7	35	4	0.5
53	no flower	6	90	3.5	1.8
54	no flower	8	90	4	2
55	no flower	8	80	3	1.4
56	flowering	4	23	2	0.4
57	flowering	5	24	2	0.4
58	flowering	4	18	2	0.4
59	flowering	4	17	2	0.4
60	flowering	5	17	2	0.4
61	flowering	6	20	2	0.4
62	flowering	4	20	2	0.4
63	flowering	4	20	2	0.3
64	flowering	6	23	1	0.3
65	drying	5	10	0.4	0.3
66	flowering	6	23	1.5	0.2
67	flowering	4	13	0.5	0.1
68	flowering	5	20	2	0.3
69	flowering	5	20	2	0.4
70	flowering	4	18	1.8	0.3
71	flowering	4	15	1.5	0.3
72	flowering	4	15	1.5	0.3
73	flowering	4	15	1.5	0.3
74	flowering/drying	4	26	1.5	0.3
75	flowering/drying	4	20	1.5	0.8
76	flowering/drying	5	23	2	0.4
77	flowering/drying	4	20	2	0.3
78	flowering/drying	5	25	2	0.4
79	senescent		23	1.45	0.55
80	senescent		16	0.9	0.4
81	flowering		41	2.75	2.9
82	senescent		11.4	0.7	0.22
83	flowering/drying		13.2	1	0.5
84	senescent		11.5	1	0.35
85	senescent		13.7	0.8	0.3
86	senescent		14	1.5	0.4
87	senescent		21	2	0.5
88	senescent		17	1.75	
89	senescent		22.5	2	0.35
90	senescent		23	1.75	0.5
91	senescent		23.5	1.9	0.55
92	senes/flowering		22.5	2.5	0.3
93	flowering		23.5	2.2	0.55

Sample order	Stem inclination	Above height(m)	Below height (m)	Total height(m)	Above biomass(gm^{-2})
1			0.50		
2			0.05		
3			0.10		
4			0.10		
5			0.10		
6			0.15		79.2
7			0.20		59.4
8			0.20		39.6
9			0.20		71.3
10			0.05		
11			0.10		19.8
12			0.20		55.4
13			0.30		
14			0.40		316.8
15		0.8			149.6
16	25	0.8			181.4
17	15	1.2	3.55	4.75	491.2
18		0.8			212.6
19		0.9			303.2
20		0.8	2.73	3.53	185.6
21		0.8	2.73	3.53	231.2
22		0.86	2.48	3.34	314.6
23		0.7	2.48	3.18	319.4
24		0.3			145.2
25		0.9			310.0
26		0.75			368.6
27		0.9	2.85	3.75	365.0
28		0.9			323.0
29		0.8			327.4
30		1			235.4
31	10	0.85	3.40	4.25	586.8
32	20	1.3	4.30	5.60	1102.2
33	20	1.27	2.70	3.97	181.3
35	33	0.77			572.4
36	20	0.98			
37	15	0.85	3.40	4.25	790.7
38	10	0.78	3.40	4.18	302.8
39	10	0.8	3.40	4.20	327.7
40	22	0.71	3.40	4.11	182.7
41	10	0.66			255.9
42	10	1.2			539.4
43	26	0.85			533.9
44		0.63			231.3
45		1.5	4.00	5.50	840.7

Sample order	Stem inclination	Above height(m)	Below height (m)	Total height(m)	Above biomass(gm^{-2})
46		1.3	3.37	4.67	564.9
47		1	3.05	4.05	838.0
48		0.85	2.95	3.80	520.8
49		1.3	1.80	3.10	1511.4
50		1.1	3.55	4.65	595.9
51		1			464.9
52		1.6	4.64	6.24	1194.4
53		1.5	5.65	7.15	989.9
54		1.6	4.10	5.70	1012.0
55		1.5	5.70	7.20	866.0
56		1	4.00	5.00	783.5
57		0.8	3.68	4.48	587.9
58		0.9	4.32	5.22	524.9
59		1	4.64	5.64	658.4
60		1	4.50	5.50	630.7
61		1	4.60	5.60	561.3
62		0.8	4.50	5.30	407.2
63		0.9	4.92	5.82	530.7
64		0.9	4.13	5.03	569.3
65		0.4			438.5
66		0.75			475.9
67		0.8			663.5
68		0.95	3.95	4.90	317.2
69		1.1	4.64	5.74	794.4
70		0.9	2.93	3.83	302.9
71		0.85	2.87	3.72	372.7
72		0.85	3.51	4.36	238.3
73		0.9	3.19	4.09	268.1
74		0.9	3.28	4.18	294.5
75		1	3.49	4.49	404.9
76		1.3	4.92	6.22	939.7
77		1	4.82	5.82	449.5
78		1	4.33	5.33	543.6
79	15	0.65			572.3
80	30	0.65			303.2
81	10	1.1			418.8
82	37	0.45			477.7
83	45	0.5			310.6
84	37	0.5			341.4
85	45	0.55			407.0
86	10	0.9			984.0
87	40	0.8			781.2
88	30	0.95			504.0
89	45	0.8			496.6
90	30	0.8			565.3
91	20	0.9			776.6
92	20	0.9			378.9
93	30	0.85			799.3

Sample order	Log above biomass	Below biomass (gm^{-2})	Total biomass (gm^{-2})	% Water	% Canopy cover
1					
2					
3					
4					
5					
6	1.90	87.5	166.7	80	84
7	1.77	65.7	125.1	80	75
8	1.60	43.8	83.4	80	71
9	1.85	78.8	150.1	80	82
10					
11	1.30	21.9	41.7	80	
12	1.74	61.2	116.6	80	
13					
14	2.50	350.1	666.9	80	87
15	2.17	197.3	346.9	90	86
16	2.26	101.6	283.0	88	87
17	2.69	1958.8	2450.0	83	89
18	2.33	137.3	349.9	88	67
19	2.48	445.8	749.0	80	95
20	2.27	1840.7	2026.3	82	81
21	2.36	1592.6	1823.8	79	
22	2.50	2103.5	2418.1	83	85
23	2.50	2283.8	2603.2	88	88
24	2.16	150.3	295.5	85	38
25	2.49	448.1	758.1	92	86
26	2.57	224.8	593.4	88	88
27	2.56	2037.6	2402.6	85	89
28	2.51	310.7	633.7	87	83
29	2.52	539.9	867.3	87	86
30	2.37	281.5	516.9	87	79
31	2.77	2172.8	2759.6	77	96
32	3.04	2522.2	3624.4	84	97
33	2.26	2373.0	2554.3	81	70
35	2.76	167.5	739.9	76	97
36		167.5	492.1	83	83
37	2.90	3211.7	4002.4	76	
38	2.48	1798.0	2100.8	78	
39	2.52	1799.3	2127.0	78	
40	2.26	2235.8	2418.5	82	71
41	2.41	138.9	394.8	80	80
42	2.73	115.4	654.8	82	91
43	2.73	138.9	672.8	80	95
44	2.36	233.7	233.7	80	76
45	2.92	1823.0	2663.7	75	88

Sample order	Log above biomass	Below biomass (gm^{-2})	Total biomass (gm^{-2})	% Water	% Canopy cover
46	2.75	2235.2	2800.1	78	90
47	2.92	2394.9	2397.8	74	89
48	2.72	2872.9	3393.7	79	80
49	3.18	2104.6	2107.8	74	86
50	2.78	1881.5	2477.3	74	79
51	2.67	467.6	467.6	77	83
52	3.08	2611.1	3805.5	76	90
53	3.00	2682.8	3672.7	82	89
54	3.01	3635.8	4647.8	86	93
55	2.94	2357.2	3223.2	84	93
56	2.89	2535.5	3318.9	70	94
57	2.77	2447.8	3035.6	73	93
58	2.72	2364.7	2889.7	73	96
59	2.82	2356.0	3014.4	72	95
60	2.80	2338.3	2968.9	68	94
61	2.75	2875.9	3437.2	68	98
62	2.61	2609.3	3016.5	68	92
63	2.72	1922.7	2453.3	71	87
64	2.76	2262.0	2831.3	78	96
65	2.64	441.2	441.2	71	94
66	2.68	478.5	478.5	75	95
67	2.82			69	95
68	2.50	2152.1	2469.3	74	78
69	2.90	1792.0	2586.4	68	88
70	2.48	1874.4	2177.3	74	76
71	2.57	4087.4	4460.1	75	95
72	2.38	1679.3	1917.5	77	80
73	2.43	2913.1	3181.2	72	72
74	2.47	3451.3	3745.8	73	78
75	2.61	1834.6	2239.5	70	87
76	2.97	1454.7	2394.5	68	93
77	2.65	1505.3	1954.8	71	83
78	2.74	3568.2	4111.8	70	89
79	2.76	2888.8	3226.7	69	83
80	2.48	565.0	875.6	78	79
81	2.62	4252.6	4671.4	84	76
82	2.68	2919.2	3295.8	50	84
83	2.49	419.8	723.1	75	94
84	2.53	2908.5	3903.2	70	93
85	2.61	2893.9	3689.7	66	85
86	2.99	2893.5	3397.9	64	96
87		2897.1	3390.1	66	92
88	2.70	2908.2	3462.4	65	89
89	2.70	2887.3	3684.8	64	
90	2.75	2909.4	3266.2	63	94
91	2.89	2897.5	3708.7	62	96
92	2.58	2892.5	3469.8	68	93
93	2.90	2724.0	3370.2	74	93

Sample order	No.pixels	RADARSAT S6	RsatS6-IC-	RsatS6-IC+	JERS-1	JERS-IC-
1	117	-10.2	-10.9	-10.7	-12.1	-12.9
2	170	-13.5	-13.8	-15.1	-14.0	-14.5
3	133	-11.0	-11.6	-11.4	-16.4	-16.9
4	297	-14.9	-15.3	-16.5	-15.2	-15.6
5	211					
6	150	-10.4	-10.8	-11.8	-10.7	-11.2
7	154	-10.6	-11.1	-11.8	-13.4	-14.2
8	142	-11.1	-11.5	-12.5	-12.8	-13.3
9	230	-10.4	-10.7	-12.6	-11.4	-11.8
10	348	-15.4	-15.7	-17.0	-17.2	-17.5
11	97	-15.4	-15.8	-17.0	-16.1	-16.6
12						
13						
14	245	-8.4	-8.7	-10.4	-9.8	-10.3
15	56	-8.3	-8.9	-7.7	-9.6	-11.7
16	360	-7.0	-7.2	-6.7	-9.4	-9.7
17	226	-6.9	-7.2	-6.5	-8.2	-8.6
18	269	-7.0	-7.5	-6.5	-8.5	-8.5
19	385	-7.1	-7.3	-6.9	-10.1	-10.4
20	77					
21	184	-6.8	-7.1	-6.4	-11.4	-11.8
22	95	-7.3	-7.8	-6.8	-9.5	-10.2
23	150	-6.7	-7.1	-6.3	-13.9	-14.5
24	194	-8.9	-9.3	-8.5	-15.7	-16.1
25	56	-8.5	-9.4	-7.8	-13.2	-14.9
26	112	-6.9	-7.4	-6.4	-8.7	-9.1
27	243	-7.3	-7.6	-7.0	-10.7	-11.0
28	173	-7.9	-8.3	-7.6	-10.0	-10.4
29	138	-7.1	-7.5	-6.8	-7.9	-8.3
30	242	-7.7	-8.1	-7.3	-10.7	-11.1
31	126	-8.0	-8.4	-7.5	-7.0	-7.7
32	208	-7.7	-8.0	-7.4	-6.4	-6.8
33	136	-7.4	-7.8	-7.1	-8.5	-9.1
35	322	-7.5	-7.7	-7.2	-9.4	-9.8
36	178	-6.6	-7.2	-6.1	-6.3	-6.8
37	252	-6.9	-7.2	-6.6	-9.4	-9.8
38	146	-7.1	-7.5	-6.8	-9.5	-10.0
39	426	-7.0	-7.4	-6.6	-10.6	-10.9
40	249	-6.5	-6.7	-6.2	-10.8	-11.3
41	199	-6.3	-6.6	-5.9	-9.9	-10.3
42	150	-6.3	-6.8	-6.0	-8.9	-9.3
43	257	-7.7	-8.1	-7.3	-8.8	-9.2
44	243	-8.0	-8.4	-7.6	-6.6	-7.0
45	191	-6.6	-7.0	-6.3	-6.2	-6.5

Sample order	No.pixels	RADARSAT S6	RsatS6-IC-	RsatS6-IC+	JERS-1	JERS-IC-	JERS-IC+
46	378	-6.8	-7.0	-6.6	-6.1	-6.4	-5.8
47	122	-6.0	-6.5	-5.6	-6.5	-7.1	-5.9
48	272	-7.1	-7.4	-6.9	-9.8	-10.2	-9.5
49	116	-5.4	-6.0	-5.0	-6.2	-6.8	-5.7
50	288	-7.0	-7.3	-6.7	-7.8	-8.1	-7.5
51	270	-7.4	-7.6	-7.1	-10.4	-10.7	-10.1
52	95	-5.2	-5.7	-4.8	-6.0	-6.6	-5.5
53	221	-5.5	-5.8	-5.3	-8.2	-8.8	-7.7
54	282	-5.4	-5.7	-5.2	-8.6	-9.1	-8.2
55	319	-6.0	-6.2	-5.7	-5.0	-5.3	-4.6
56	258	-6.8	-7.1	-6.5	-7.9	-8.3	-7.6
57	220	-6.1	-6.4	-5.8	-8.3	-8.7	-8.0
58	169	-7.3	-7.8	-6.9	-7.7	-8.1	-7.3
59	74	-6.7	-7.4	-6.1	-7.1	-7.9	-6.3
60	232	-7.9	-8.3	-7.6	-9.8	-10.3	-9.4
61	217	-6.8	-7.1	-6.5	-7.7	-8.1	-7.4
62	223	-6.8	-7.2	-6.6	-9.0	-9.5	-8.6
63	237	-7.2	-7.5	-6.9	-8.9	-9.3	-8.6
64	368	-8.4	-8.7	-8.2	-10.9	-11.4	-10.5
65	359	-7.7	-7.9	-7.5	-9.2	-9.6	-8.8
66	213	-8.1	-8.4	-7.8	-9.3	-10.1	-8.7
67	89	-6.3	-6.8	-5.8	-9.5	-10.2	-8.8
68	214	-7.5	-13.1	-5.1	-8.2	-8.7	-7.9
69	264	-7.0	-7.3	-6.7	-8.4	-8.7	-8.1
70	163	-6.9	-7.3	-6.5	-11.4	-12.0	-10.8
71	191	-6.8	-7.2	-6.5	-12.5	-12.9	-12.2
72	208	-7.5	-7.8	-7.2	-13.7	-14.0	-13.3
73	212	-6.9	-7.3	-6.5	-11.9	-12.3	-11.5
74	161	-7.4	-7.8	-7.0	-12.9	-13.3	-12.6
75	163	-8.2	-8.5	-7.9	-11.5	-11.9	-11.1
76	136	-7.0	-7.4	-6.6			
77	97	-7.5	-8.0	-7.1	-11.5	-12.3	-10.9
78	137	-7.3	-7.8	-6.9	-11.3	-11.7	-10.9
79	182	-6.8	-7.2	-6.5	-7.2	-7.6	-6.8
80	112	-6.3	-6.9	-5.8	-8.2	-8.8	-7.6
81	182	-6.0	-6.3	-5.7	-6.3	-6.7	-5.8
82	130	-5.9	-6.2	-5.5	-10.0	-10.4	-9.5
83	99	-6.1	-6.4	-5.8	-11.2	-12.6	-9.9
84	170	-7.2	-7.7	-6.8	-9.3	-9.8	-8.9
85	147	-7.2	-7.6	-6.9	-9.6	-10.0	-9.2
86	172	-5.9	-6.3	-5.5	-7.9	-8.4	-7.4
87	168						
88	343	-7.2	-7.5	-7.0	-10.4	-10.8	-10.0
89	354	-7.4	-7.7	-7.2	-9.5	-10.0	-9.3
90	396	-7.4	-7.6	-7.2	-9.8	-10.2	-9.6
91	308	-5.8	-6.1	-5.6	-7.6	-7.8	-7.4
92	459	-7.0	-7.3	-6.7	-10.0	-10.5	-9.6
93	170	-7.3	-7.6	-7.0	-8.3	-8.7	-8.0

Sample order	RADARSAT S1	RsatS1-IC-	RsatS1-IC+	Index
1				-11.1
2				-13.7
3				-12.9
4				-15.1
5				
6				-10.5
7				-11.8
8				-11.8
9				-10.9
10				
11				-15.7
12				
13				
14				-9.0
15				-9.4
16				-9.4
17				-8.0
18				-7.5
19				-7.7
20				-8.3
21				
22				-8.5
23				-8.2
24				-9.0
25				-11.1
26				-10.3
27				-7.7
28				-8.7
29				-8.8
30				-7.5
31	-4.3	-4.8	-3.8	-7.5
32	-3.9	-4.5	-3.8	-7.0
33	-3.5	-3.9	-3.2	-7.9
35	-3.2	-3.5	-3.0	-8.3
36	-3.8	-4.4	-3.3	
37	-2.8	-3.1	-2.5	-8.0
38	-2.9	-3.2	-2.6	-8.2
39	-3.4	-3.6	-3.1	-8.4
40	-2.1	-2.4	-1.9	-8.1
41	-2.3	-2.5	-2.0	-7.7
42	-3.2	-3.6	-2.8	-7.4
43	-4.1	-4.4	-3.8	-8.2
44	-5.5	-5.9	-5.1	-7.2
45	-4.8	-5.2	-4.4	-6.4

IC- lower bound of the confidence interval
IC+ higher bound of the confidence interval
The backscattering coefficientes are in dB
Empty cells represent data not available

Sample order	RADARSAT S1	RsatS1-IC-	RsatS1-IC+	Index
46	-4.1	-4.3	-3.8	-6.4
47	-3.0	-3.4	-2.7	-6.2
48	-4.3	-4.6	-4.0	-8.3
49	-2.7	-3.1	-2.3	-5.8
50	-3.9	-4.1	-3.6	-7.4
51	-4.9	-5.2	-4.6	-8.6
52	-3.0	-3.5	-2.6	-5.6
53	-3.6	-4.0	-3.3	-6.7
54	-3.1	-3.4	-2.8	-6.7
55	-2.9	-3.2	-2.7	-5.4
56	-4.4	-4.8	-4.1	-7.3
57	-3.1	-3.4	-2.8	-7.1
58	-3.6	-4.1	-3.1	-7.5
59	-4.8	-5.4	-4.3	-6.9
60	-3.9	-4.3	-3.6	-8.8
61	-4.1	-4.4	-3.8	-7.3
62	-3.6	-3.9	-3.3	-7.8
63	-4.0	-4.4	-3.7	-8.0
64	-6.1	-6.3	-5.9	-9.5
65	-6.0	-6.2	-5.7	-8.4
66	-4.7	-5.0	-4.4	-8.6
67	-3.4	-3.8	-3.0	-7.6
68	-3.1	-3.4	-2.8	-7.9
69	-5.0	-5.3	-4.8	-7.6
70	-4.0	-4.4	-3.7	-8.6
71	-3.1	-3.5	-2.8	-8.8
72	-4.2	-4.5	-3.9	-9.5
73	-4.4	-4.8	-4.1	-8.7
74	-3.3	-3.6	-2.9	-9.3
75				-9.5
76	-4.1	-4.5	-3.6	
77	-3.8	-4.3	-3.3	-9.1
78	-4.2	-4.6	-3.8	-8.8
79				-7.0
80				-7.2
81				-6.1
82				-7.4
83				-7.9
84				-8.2
85				-8.3
86				-6.8
87				
88				-8.5
89				-8.4
90				-8.4
91				-6.6
92				-8.2
93				-7.8

APPENDIX II

Carbon data

Common species	% Carbon content
H. amplexicaulis	45.43
H. amplexicaulis	45.32
H. amplexicaulis	47.00
E. polystachya	43.41
E. polystachya	44.11
E. polystachya	44.22
P. repens	41.64
P. repens	42.79
P. repens	44.30
H. furcatus	47.93
H. furcatus	48.09
Oryza. sp	44.31
Oryza. sp	41.79
P. fasciculatum	45.33
P. fasciculatum	51.85
P. fasciculatum	44.65
Tripomonga	43.59
Tripomonga	44.08

% of carbon content of the most common species found in the study area.

Appendix III

GOES images

(a). 27.05.1996 – RADARSAT S6

(b). 30.05.1996 – RADARSAT S1

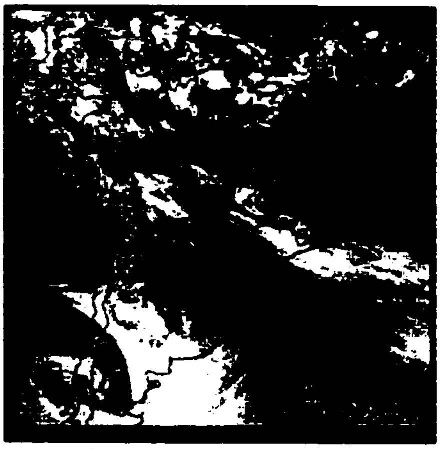

(c). 15.05.96 – JERS-1

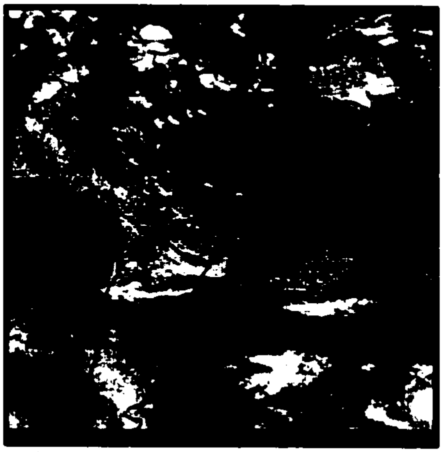

(d). 05.06.1999-RADARSAT S6

(e) 08.06.1999-RADARSAT S1

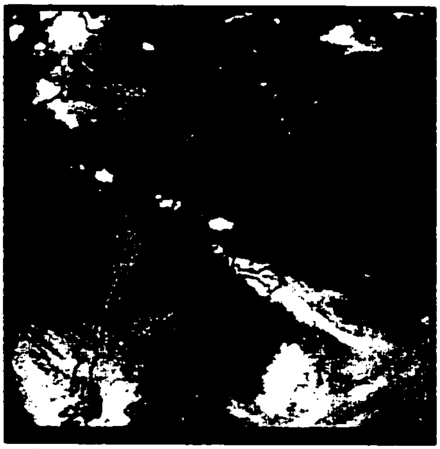

(f). 07.08.1996-RADARSAT S6

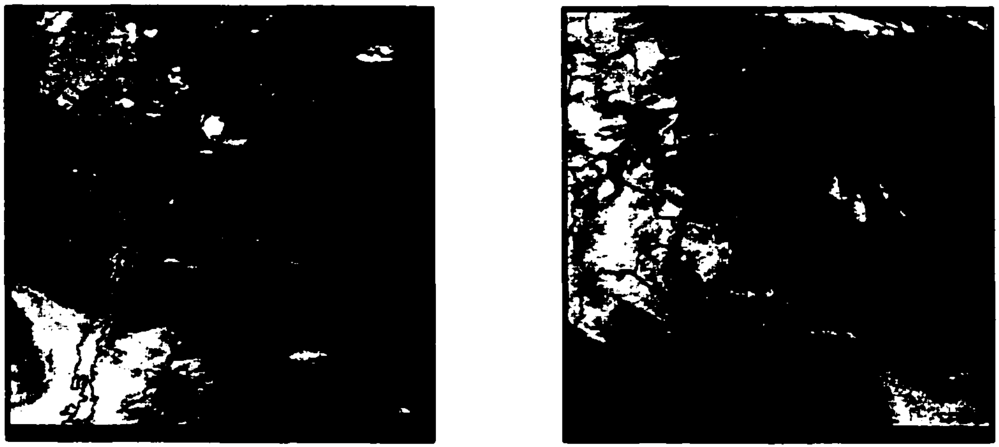

(g). 12.08.1996-JERS-1 (h). 11.11.96-RADARSAT S6

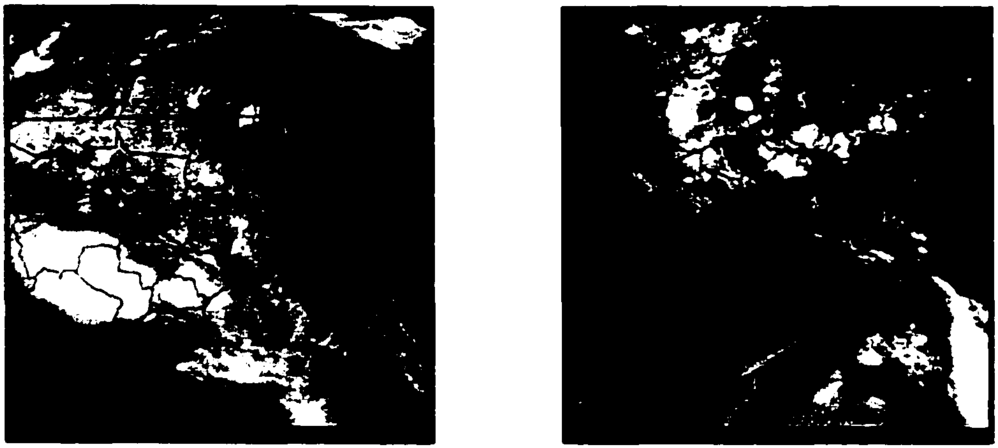

(i). 22.12.96-JERS1 (j). 05.04.1997-RADARSAT S6

(k). 20.03.1997-JERS-1

Infra-red channel of the meteorological satellite GOES-8, showing the constant cloud cover present at 9:00AM at the day of acquisition of RADARSAT and JERS-1 images. The dashed rectangle highlights the study area.

APPENDIX IV

a. Savanna

Sample no.	No. pixels	RsatS6nov	Cl-	Cl+	Jersdec	Cl-	Cl+
1	221	-16.2	-16.6	-15.8	-13.4	-13.8	-13.0
2	221	-13.5	-13.8	-13.2	-10.7	-11.1	-10.3
3	205	-15.2	-15.7	-14.8	-10.8	-11.4	-10.3
4	177	-15.4	-15.8	-15.0	-11.7	-12.1	-11.3
5	221	-15.5	-15.8	-15.3	-12.5	-12.9	-12.2
6	185	-12.9	-13.4	-12.5	-10.6	-11.0	-10.1
7	145	-14.0	-14.5	-13.5	-11.5	-12.0	-11.0
8	177	-13.0	-13.6	-12.5	-12.1	-12.6	-11.8
9	185	-12.1	-12.6	-11.6	-10.5	-10.9	-10.1
10	121	-14.2	-14.7	-13.7	-12.5	-13.3	-11.9
11	157	-13.7	-14.0	-13.3	-12.1	-12.7	-11.7
12	121	-13.4	-13.7	-13.0	-11.7	-12.3	-11.1
13	97	-16.0	-16.5	-15.6	-12.9	-13.5	-12.4
14	97	-13.3	-13.8	-12.8	-11.1	-11.7	-10.5
15	97	-14.8	-15.3	-14.4	-10.8	-11.5	-10.2
16	98	-12.8	-13.3	-12.2	-9.3	-9.8	-8.9
17	129	-12.9	-13.4	-12.5	-10.1	-10.6	-9.6
18	97	-12.8	-13.3	-12.4	-10.0	-10.6	-9.6
19	185	-12.8	-13.1	-12.4	-9.5	-9.9	-9.2
20	137	-12.1	-12.6	-11.7	-9.2	-9.9	-8.6
21	205	-13.3	-13.7	-12.9	-9.2	-9.7	-8.8
22	185	-15.7	-16.1	-15.3	-10.6	-11.1	-10.1
23	277	-13.3	-13.7	-12.9	-9.8	-10.2	-9.4
24	69	-14.7	-15.2	-14.2	-10.7	-11.3	-10.2
25	157	-15.7	-16.1	-15.3	-13.0	-13.5	-12.5
26	261	-13.8	-14.0	-13.5	-11.7	-12.0	-11.3
27	121	-15.9	-16.3	-15.4	-12.5	-13.0	-12.1
28	121	-13.2	-13.6	-12.8	-10.4	-10.8	-10.0
29	177	-13.6	-14.2	-13.0	-10.0	-10.6	-9.4
30	185	-14.9	-15.5	-14.5	-11.6	-12.1	-11.2
31	137	-13.5	-14.0	-13.0	-10.2	-10.9	-9.6
32	121	-12.9	-13.5	-12.4	-8.9	-9.5	-8.4
33	145	-13.0	-13.5	-12.6	-10.4	-11.0	-9.9

Sample no.	Jersmarch	Cl-	Cl+	RsatS6april	Cl-	Cl+
1	-12.1	-12.5	-11.7	-14.2	-14.6	-13.8
2	-8.3	-8.6	-7.9	-12.2	-12.6	-11.9
3	-10.0	-10.4	-9.6	-13.2	-13.6	-12.8
4	-10.7	-11.1	-10.3	-13.3	-13.7	-12.9
5	-10.4	-10.8	-10.0	-12.1	-12.5	-11.7
6	-9.5	-10.0	-9.1	-12.1	-12.5	-11.8
7	-10.5	-11.0	-10.0	-12.4	-13.0	-12.0
8	-10.7	-11.2	-10.2	-12.5	-12.9	-12.2
9	-9.0	-9.7	-8.4	-11.6	-12.0	-11.2
10	-10.5	-11.0	-10.0	-12.1	-12.6	-11.6
11	-10.1	-10.6	-9.7	-12.8	-13.3	-12.4
12	-10.0	-10.7	-9.3	-13.3	-13.7	-12.9
13	-10.7	-11.2	-10.1	-11.7	-12.2	-11.2
14	-9.4	-10.0	-8.9	-12.1	-12.5	-11.7
15	-9.5	-10.0	-9.0	-11.2	-11.8	-10.8
16	-7.9	-8.4	-7.3	-12.4	-13.0	-11.9
17	-7.8	-8.3	-7.4	-11.9	-12.3	-11.5
18	-8.7	-9.3	-8.2	-12.6	-13.1	-12.2
19	-9.0	-9.4	-8.6	-12.1	-12.5	-11.8
20	-8.9	-9.4	-8.5	-11.7	-12.3	-11.3
21	-8.4	-9.0	-8.0	-11.6	-12.1	-11.2
22	-10.1	-10.5	-9.7	-13.7	-14.0	-13.3
23	-8.1	-8.5	-7.8	-11.8	-12.1	-11.5
24	-9.7	-10.4	-9.1	-12.4	-12.9	-11.9
25	-12.4	-12.8	-12.0	-14.2	-14.7	-13.7
26	-9.5	-9.9	-9.2	-12.5	-12.8	-12.2
27	-11.6	-12.1	-11.2	-14.4	-14.9	-14.0
28	-10.0	-10.5	-9.6	-12.1	-12.6	-11.7
29	-9.5	-10.0	-9.0	-13.1	-13.5	-12.7
30	-10.1	-10.6	-9.7	-13.3	-13.7	-12.9
31	-9.0	-9.5	-8.5	-11.2	-11.7	-10.8
32	-7.5	-8.1	-6.9	-11.5	-12.0	-11.0
33	-9.0	-9.6	-8.5	-10.9	-11.4	-10.5

Sample no.	RsatS6may	CI-	CI+	RsatS1may	CI-	CI+	Jersmay	CI-	CI+
1	-14.7	-15.0	-14.4	-8.8	-9.1	-8.4	-12.4	-12.8	-12.1
2	-11.8	-12.2	-11.5	-7.7	-8.1	-7.5	-9.0	-9.4	-8.6
3	-12.8	-13.2	-12.3	-8.2	-8.6	-7.9	-9.7	-10.3	-9.2
4	-12.4	-12.8	-12.1	-9.3	-9.6	-9.0	-10.6	-10.9	-10.2
5	-12.2	-12.6	-11.9	-8.1	-8.4	-7.8	-10.5	-10.9	-10.1
6	-10.6	-11.0	-10.1	-7.9	-8.2	-7.6	-8.7	-9.2	-8.3
7	-10.0	-10.4	-9.7	-9.4	-9.7	-9.1	-10.2	-10.7	-9.8
8	-10.5	-10.8	-10.2	-9.1	-9.4	-8.8	-10.1	-10.5	-9.7
9	-9.2	-9.6	-8.9	-8.7	-9.1	-8.4	-8.9	-9.4	-8.5
10	-10.9	-11.3	-10.5	-7.4	-7.9	-7.0	-9.9	-10.4	-9.5
11	-11.7	-12.1	-11.4	-8.3	-8.6	-8.0	-9.8	-10.3	-9.4
12	-12.4	-13.0	-11.9	-7.9	-8.4	-7.5	-10.9	-11.6	-10.2
13	-13.6	-14.1	-13.1	-8.2	-8.7	-7.8	-10.0	-10.5	-9.5
14	-11.2	-12.0	-10.6	-8.2	-8.7	-7.8	-9.3	-9.8	-8.8
15	-13.0	-13.4	-12.6	-8.5	-9.1	-8.1	-9.3	-9.8	-8.8
16	-11.0	-11.5	-10.6	-7.7	-8.1	-7.3	-8.6	-9.2	-8.1
17	-9.2	-9.7	-8.7	-7.8	-8.2	-7.5	-9.5	-10.0	-9.1
18	-10.9	-11.3	-10.5	-8.0	-8.4	-7.6	-8.4	-8.9	-7.9
19	-11.1	-11.5	-10.8	-8.0	-8.3	-7.6	-8.1	-8.4	-7.8
20	-11.0	-11.5	-10.6	-7.0	-7.4	-6.6	-8.0	-8.4	-7.6
21	-11.1	-11.7	-10.5	-8.5	-8.9	-8.2	-8.3	-8.8	-7.8
22	-13.9	-14.3	-13.5	-9.0	-9.3	-8.7	-9.6	-10.0	-9.2
23	-11.8	-12.2	-11.5	-8.8	-9.1	-8.5	-8.2	-8.5	-7.8
24	-14.8	-15.4	-14.3	-9.2	-9.8	-8.7	-8.6	-9.2	-8.0
25	-13.6	-14.0	-13.2	-8.5	-8.9	-8.1	-12.1	-12.6	-11.7
26	-12.8	-13.1	-12.6	-7.8	-8.1	-7.5	-9.3	-9.7	-9.0
27	-14.6	-15.1	-14.1	-9.6	-10.1	-9.1	-11.2	-11.8	-10.8
28	-12.0	-12.5	-11.6	-7.2	-7.6	-6.9	-10.0	-10.5	-9.5
29	-11.8	-12.1	-11.5	-8.5	-8.9	-8.1	-9.3	-9.7	-8.9
30	-12.8	-13.2	-12.5	-8.4	-8.7	-8.1	-10.1	-10.5	-9.8
31	-10.2	-10.6	-9.8	-7.5	-7.9	-7.2	-8.5	-9.0	-8.1
32	-10.0	-10.6	-9.5	-7.3	-7.7	-6.9	-8.1	-8.8	-7.5
33	-10.2	-10.7	-9.8	-8.2	-8.6	-7.9	-8.6	-9.0	-8.2

Sample no.	RsatS6june	CI-	CI+	RsatS1june	CI-	CI+	RsatS6aug	CI-	CI+	Jersaug	CI-	CI+
1	-14.2	-14.5	-13.9	-12.0	-12.3	-11.7	-14.8	-15.2	-14.5	-12.4	-12.7	-12.0
2	-10.8	-11.1	-10.4	-9.8	-10.2	-9.5	-11.6	-12.0	-11.3	-9.3	-9.7	-8.9
3	-12.4	-12.8	-12.0	-10.5	-10.8	-10.2	-13.0	-24.6	-10.2	-10.8	-11.2	-10.4
4	-12.6	-13.0	-12.2	-11.1	-11.5	-10.7	-13.4	-13.8	-13.0	-10.6	-10.9	-10.2
5	-12.5	-12.8	-12.2	-9.9	-10.6	-9.3	-12.1	-12.5	-11.8	-11.3	-11.7	-10.9
6	-11.6	-12.0	-11.3	-9.6	-10.0	-9.2	-11.1	-11.6	-10.7	-10.0	-10.5	-9.6
7	-12.5	-12.9	-12.1	-9.7	-10.1	-9.4	-12.2	-12.6	-11.9	-10.7	-11.4	-10.1
8	-12.9	-13.3	-12.6	-11.1	-11.5	-10.7	-12.4	-12.8	-12.1	-10.8	-11.2	-10.4
9	-10.7	-11.1	-10.4	-8.9	-9.3	-8.6	-11.6	-12.0	-11.2	-9.6	-10.1	-9.2
10	-12.8	-13.2	-12.5	-9.6	-10.1	-9.1	-13.5	-14.1	-12.9	-11.5	-12.0	-11.1
11	-11.4	-11.8	-11.1	-10.1	-10.7	-9.7	-11.9	-12.4	-11.4	-10.5	-11.0	-10.1
12	-12.3	-12.7	-11.9	-9.7	-10.4	-9.1	-12.8	-13.2	-12.3	-11.4	-12.1	-10.8
13	-12.1	-12.6	-11.6	-10.8	-11.3	-10.4	-13.2	-13.7	-12.8	-11.3	-12.0	-10.7
14	-11.0	-11.7	-10.5	-8.0	-8.5	-7.6	-11.4	-11.9	-10.9	-9.2	-9.8	-8.7
15	-12.4	-12.8	-12.0	-10.1	-10.6	-9.7	-11.9	-12.4	-11.5	-9.7	-10.3	-9.1
16	-12.4	-13.0	-12.0	-10.3	-10.8	-9.8	-12.4	-12.9	-11.9	-9.1	-9.6	-8.7
17	-10.7	-11.2	-10.3	-10.6	-11.0	-10.2	-13.2	-13.7	-12.7	-10.2	-10.6	-9.8
18	-11.2	-11.7	-10.7	-10.2	-11.0	-9.6	-11.9	-12.4	-11.5	-9.2	-9.7	-8.7
19	-10.0	-10.4	-9.7	-9.0	-9.4	-8.6	-12.3	-12.6	-12.0	-9.7	-10.1	-9.3
20	-9.7	-10.2	-9.2	-7.8	-8.3	-7.4	-11.2	-11.7	-10.8	-8.2	-8.7	-7.7
21	-10.6	-11.0	-10.3	-9.7	-10.2	-9.2	-12.4	-12.8	-12.0	-9.1	-9.5	-8.8
22	-12.4	-12.8	-12.1	-11.5	-12.0	-11.2	-13.5	-13.8	-13.1	-9.7	-10.3	-9.3
23	-11.7	-12.0	-11.4	-9.5	-9.9	-9.2	-11.5	-11.8	-11.3	-9.1	-9.4	-8.8
24	-12.8	-13.4	-12.2	-12.2	-12.8	-11.7	-13.3	-14.0	-12.6	-11.7	-12.4	-11.0
25	-13.4	-13.8	-13.0	-10.5	-11.0	-10.1	-13.5	-13.9	-13.1	-12.1	-12.6	-11.8
26	-12.1	-12.4	-11.8	-10.2	-10.5	-9.9	-11.9	-12.2	-11.7	-10.0	-10.4	-9.7
27	-12.9	-13.4	-12.5	-11.1	-11.4	-10.7	-14.9	-15.5	-14.5	-12.2	-12.7	-11.8
28	-11.1	-11.6	-10.7	-9.7	-10.2	-9.2	-12.6	-13.1	-12.1	-10.2	-10.8	-9.8
29	-12.1	-12.6	-11.6	-10.4	-10.7	-10.0	-12.4	-12.8	-12.1	-10.2	-10.8	-9.7
30	-13.6	-14.0	-13.2	-10.5	-10.9	-10.2	-12.7	-13.1	-12.3	-9.9	-10.5	-9.4
31	-11.6	-12.0	-11.2	-11.0	-11.6	-10.6	-11.6	-12.1	-11.2	-9.1	-9.7	-8.5
32	-11.1	-11.6	-10.7	-8.8	-9.2	-8.4	-11.0	-11.5	-10.6	-8.4	-9.0	-7.9
33	-11.8	-12.4	-11.3	-9.5	-9.9	-9.1	-12.5	-13.0	-12.1	-9.1	-9.6	-8.6

Backscattering coefficing coefficients in dB

CI- represents the lower bound of the confidence interval

CI+ represents the higher bound of the confidence interval

b. Pasture

Sample no.	No. pixels	RsatS6nov	CI-	CI+	Jersdec	CI-	CI+
1	101	-10.7	-11.2	-10.3	-13.4	-14.0	-12.8
2	97	-11.2	-11.7	-10.8	-11.2	-11.9	-10.7
3	69	-12.5	-2.6	-2.5	-13.8	-14.4	-13.2
4	69	-13.3	-13.9	-12.8	-13.8	-14.3	-13.3
5	61	-15.5	-16.3	-14.8	-13.0	-13.7	-12.4
6	69	-11.8	-12.4	-11.3	-15.4	-15.9	-14.9
7	97	-9.7	-10.2	-9.2	-9.5	-10.2	-8.9
8	97	-14.0	-14.7	-13.4	-13.9	-14.4	-13.4
9	97	-11.8	-12.3	-11.3	-11.4	-12.0	-10.8
10	121	-10.5	-11.0	-10.0	-11.8	-12.3	-11.3
11	97	-11.5	-11.9	-11.1	-11.8	-12.4	-11.3
12	121	-10.2	-10.8	-9.7	-10.9	-11.7	-10.3
13	69	-11.1	-11.9	-10.4	-11.1	-11.8	-10.6
14	49	-11.1	-11.7	-10.6	-11.7	-12.5	-11.1
15	97	-14.9	-15.6	-14.4	-13.3	-14.7	-12.2
16	69	-15.4	-16.1	-14.8	-14.8	-15.8	-14.0
17	97	-12.9	-13.4	-12.5	-13.6	-14.1	-13.1
18	69	-12.7	-13.3	-12.2	-15.1	-15.7	-14.6
19	101	-10.9	-11.4	-10.4	-13.2	-13.7	-12.7
20	97	-10.9	-11.4	-10.5	-14.4	-14.9	-14.0
21	69	-12.2	-13.1	-11.5	-14.6	-15.1	-14.1
22	61	-10.8	-11.5	-10.2	-11.0	-11.8	-10.4
23	49	-13.1	-13.6	-12.6	-13.7	-14.2	-13.2
24	97	-10.6	-11.1	-10.2	-10.2	-10.7	-9.7
25	97	-13.3	-13.8	-12.8	-12.2	-12.7	-11.8
26	69	-14.2	-14.8	-13.6	-14.2	-14.7	-13.7
27	121	-12.8	-13.4	-12.4	-13.9	-14.8	-13.1
28	69	-9.2	-10.0	-8.6	-9.6	-10.4	-9.0
29	69	-11.3	-11.9	-10.7	-12.3	-12.9	-11.7
30	145	-13.1	-13.5	-12.8	-12.8	-13.4	-12.4
31	145	-9.6	-10.0	-9.2	-9.0	-9.5	-8.5
32	49	-12.4	-13.3	-11.7	-7.9	-10.1	-6.5
33	49	-12.2	-13.0	-11.6	-12.5	-13.9	-11.4
34	97	-14.0	-14.5	-13.5	-15.7	-16.1	-15.3
35	97	-12.6	-13.0	-12.2	-14.6	-15.0	-14.1
36	49	-13.8	-14.3	-13.3	-12.4	-13.0	-11.8
37	49	-12.1	-12.8	-11.4	-12.7	-13.4	-12.1
38	69	-11.1	-11.6	-10.6	-11.1	-11.8	-10.5
39	121	-14.3	-14.8	-13.9	-13.8	-14.3	-13.3
40	101	-13.6	-14.1	-13.1	-13.5	-13.9	-13.1
41	37	-13.1	-13.9	-12.4	-13.7	-14.5	-13.0

Sample no.	Jersmarch	Cl-	Cl+	RsatS6april	Cl-	Cl+
1	-8.9	-9.5	-8.3	-9.0	-9.5	-8.5
2	-8.5	-9.1	-8.0	-9.6	-10.1	-9.1
3	-9.0	-9.8	-8.4	-9.3	-9.9	-8.8
4	-10.2	-10.8	-9.6	-11.4	-11.9	-10.9
5	-11.7	-12.5	-11.1	-10.7	-11.2	-10.2
6	-10.0	-10.6	-9.4	-9.5	-10.0	-9.0
7	-8.1	-8.7	-7.5	-9.9	-10.4	-9.5
8	-11.0	-11.6	-10.5	-11.0	-11.4	-10.6
9	-10.6	-11.2	-10.0	-10.8	-11.2	-10.3
10	-10.9	-11.4	-10.5	-10.2	-10.7	-9.7
11	-10.7	-11.4	-10.1	-9.6	-10.0	-9.2
12	-8.2	-8.9	-7.7	-9.3	-9.8	-8.9
13	-10.6	-11.3	-10.0	-8.9	-9.4	-8.4
14	-9.4	-10.2	-8.8	-10.9	-11.6	-10.3
15	-12.1	-13.0	-11.5	-10.2	-10.6	-9.8
16	-10.9	-11.6	-10.4	-9.3	-9.8	-8.9
17	-10.5	-11.0	-10.0	-9.7	-10.3	-9.3
18	-11.9	-12.6	-11.2	-9.7	-10.1	-9.2
19	-11.8	-12.4	-11.3	-10.6	-11.0	-10.2
20	-12.2	-12.9	-11.7	-10.7	-11.3	-10.2
21	-12.0	-12.5	-11.5	-10.3	-10.8	-9.8
22	-10.5	-11.3	-9.8	-8.7	-9.3	-8.1
23	-10.7	-11.4	-10.0	-9.7	-10.3	-9.2
24	-9.7		-6.6	-9.5	-10.0	-9.0
25	-12.6	-13.1	-12.1	-10.7	-11.2	-10.2
26	-12.4	-13.0	-11.8	-9.8	-10.6	-9.2
27	-12.9	-13.4	-12.5	-10.7	-11.1	-10.3
28	-8.7	-9.4	-8.1	-9.5	-10.1	-9.1
29	-10.6	-11.4	-9.9	-11.6	-12.3	-11.0
30	-11.4	-11.9	-11.0	-8.3	-8.7	-7.9
31	-8.1	-8.5	-7.7	-9.2	-9.6	-8.7
32	-10.4	-11.3	-9.7	-10.8	-11.3	-10.3
33	-14.1	-14.7	-13.6	-11.4	-12.1	-10.8
34	-13.0	-13.6	-12.5	-9.2	-9.6	-8.8
35	-11.9	-12.5	-11.4	-8.4	-9.0	-8.0
36	-11.5	-12.3	-10.8	-11.0	-11.7	-10.4
37	-10.0	-10.6	-9.4	-9.7	-10.2	-9.3
38	-9.3	-9.9	-8.7	-10.5	-10.9	-10.1
39	-11.4	-11.9	-11.0	-8.9	-9.4	-8.5
40	-11.3	-11.9	-10.8	-10.0	-10.4	-9.5
41	-11.4	-12.4	-10.7	-9.2	-10.1	-8.6

Sample no.	RsatS6may	Cl-	Cl+	RsatS1may	Cl-	Cl+	Jersmay	Cl-	Cl+
1	-9.7	-10.1	-9.2	-5.3	-5.7	-4.8	-10.6	-11.2	-10.0
2	-8.8	-9.3	-8.4	-14.7	-21.8	-12.1	-8.9	-9.5	-8.3
3	-8.8	-9.3	-8.3	-6.4	-7.1	-5.8	-10.0	-10.6	-9.4
4	-14.2	-14.8	-13.7	-6.8	-7.3	-6.3	-10.3	-11.1	-9.6
5	-9.0	-9.8	-8.3	-5.5	-6.1	-5.0	-11.0	-11.8	-10.3
6	-9.4	-10.1	-8.8	-6.6	-7.0	-6.2	-10.5	-11.0	-10.0
7	-8.9	-9.4	-8.4	-6.0	-6.5	-5.6	-8.7	-9.2	-8.3
8	-9.0	-9.5	-8.5	-6.1	-6.7	-5.6	-11.8	-12.4	-11.3
9	-10.1	-10.7	-9.7	-5.5	-6.0	-5.0	-8.8	-9.3	-8.4
10	-9.9	-10.3	-9.4	-6.1	-6.6	-5.8	-9.7	-10.3	-9.2
11	-9.5	-10.0	-9.0	-6.2	-6.7	-5.8	-10.1	-10.6	-9.6
12	-8.5	-8.9	-8.1	-6.2	-6.6	-5.9	-9.0	-9.5	-8.5
13	-10.6	-11.2	-10.1	-5.6	-6.1	-5.1	-11.4	-12.2	-10.8
14	-10.9	-11.3	-10.5	-7.3	-8.0	-6.7	-9.7	-10.4	-9.2
15	-11.5	-12.0	-11.0	-6.4	-6.9	-5.9	-12.4	-13.1	-11.7
16	-9.5	-10.0	-9.1	-5.7	-6.1	-5.2	-10.6	-11.3	-10.0
17	-9.5	-10.1	-8.9	-6.3	-6.7	-5.9	-10.1	-10.8	-9.6
18	-10.6	-11.1	-10.1	-7.7	-8.5	-7.1	-10.0	-10.6	-9.5
19	-9.1	-9.6	-8.6	-6.4	-6.9	-6.0	-10.9	-11.4	-10.4
20	-11.7	-12.2	-11.3	-5.8	-6.2	-5.4	-11.7	-12.2	-11.2
21	-9.2	-9.9	-8.7	-5.5	-6.1	-4.9	-10.9	-11.4	-10.4
22	-9.5	-10.0	-9.0	-5.1	-5.7	-4.6	-9.0	-9.9	-8.3
23	-8.6	-9.2	-8.1	-5.4	-5.9	-4.9	-9.2	-10.0	-8.5
24	-8.3	-8.8	-7.9	-6.6	-7.1	-6.1	-10.3	-10.7	-9.9
25	-8.8	-9.2	-8.3	-6.2	-6.6	-5.8	-11.7	-12.3	-11.3
26	-9.2	-9.7	-8.8	-5.7	-6.2	-5.3	-9.6	-10.2	-9.1
27	-8.0	-8.4	-7.6	-5.9	-6.4	-5.4	-10.5	-11.1	-10.0
28	-9.3	-9.7	-8.9	-5.6	-6.1	-5.1	-9.6	-10.2	-9.0
29	-10.0	-10.6	-9.4	-6.3	-6.9	-5.9	-9.0	-9.8	-8.4
30	-9.6	-10.1	-9.2	-6.7	-7.0	-6.3	-9.8	-10.3	-9.4
31	-10.4	-10.8	-10.1	-5.6	-6.0	-5.3	-8.4	-8.9	-8.0
32	-9.1	-9.7	-8.5	-5.0	-5.9	-4.2	-9.5	-11.3	-8.2
33	-9.6	-10.2	-9.1	-7.0	-7.8	-6.4	-10.4	-11.4	-9.5
34	-10.7	-11.2	-10.3	-6.3	-6.7	-6.0	-12.9	-13.5	-12.4
35	-10.7	-11.1	-10.3	-5.3	-5.7	-4.9	-10.5	-11.0	-10.1
36		-9.6	-8.1	-6.5	-7.0	-6.0	-10.5	-11.2	-9.8
37	-9.8	-10.4	-9.2	-5.5	-6.0	-5.0	-9.7	-10.6	-9.1
38	-9.2	-9.8	-8.7	-5.7	-6.3	-5.2	-8.8	-9.5	-8.3
39	-10.6	-11.0	-10.1	-6.6	-7.0	-6.2	-9.7	-10.2	-9.3
40	-10.0	-10.7	-9.4	-7.2	-7.7	-6.7	-11.8	-12.5	-11.2
41	-9.2	-10.1	-8.5	-7.1	-7.9	-6.4	-12.1	-13.1	-11.2

Sample no.	RsatS6june	Cl-	Cl+	RsatS1june	Cl-	Cl+	RsatS6aug	Cl-	Cl+	Jersaug	Cl-	Cl+
1	-9.4	-10.0	-8.9	-7.6	-8.0	-7.3	-9.8	-10.4	-9.4	-12.5	-13.3	-11.8
2	-9.1	-9.6	-8.7	-7.2	-7.6	-6.8	-8.3	-8.9	-7.8	-9.6	-10.4	-9.0
3	-7.3	-7.8	-6.8	-6.1	-6.6	-5.7	-8.5	-9.0	-8.0	-11.8	-12.5	-11.2
4	-9.2	-9.7	-8.8	-7.2	-7.5	-6.9	-9.1	-9.6	-8.7	-13.5	-14.2	-12.9
5	-9.4	-10.0	-8.8	-19.3		-16.2	-10.2	-10.8	-9.7	-14.4	-15.2	-13.8
6	-10.3	-10.9	-9.8	-8.3	-8.9	-7.8	-9.1	-9.7	-8.6	-13.7	-14.2	-13.2
7	-8.4	-8.9	-7.9	-7.5	-8.0	-7.1	-9.5	-9.9	-9.2	-8.7	-9.2	-8.2
8	-10.1	-10.7	-9.6	-7.5	-8.2	-6.9	-10.0	-10.5	-9.5	-13.0	-13.5	-12.5
9	-8.0	-8.4	-7.6	-6.9	-7.4	-6.6	-11.2	-11.8	-10.7	-9.2	-9.9	-8.5
10	-8.6	-9.1	-8.2	-7.9	-8.3	-7.6	-10.0	-10.4	-9.6	-9.4	-10.1	-8.8
11	-9.7	-10.3	-9.3	-6.3	-6.8	-5.8	-9.0	-9.6	-8.5	-10.0	-10.5	-9.5
12	-8.6	-9.1	-8.1	-5.4	-5.8	-5.1	-8.8	-9.3	-8.3	-10.5	-11.1	-10.0
13	-9.8	-10.4	-9.3	-6.3	-7.0	-5.8	-9.9	-10.5	-9.3	-11.5	-12.1	-10.9
14	-8.3	-9.1	-7.6	-7.4	-8.1	-6.7	-8.4	-9.1	-7.9	-11.6	-12.4	-10.9
15	-12.9	-13.4	-12.5	-11.1	-11.6	-10.6	-10.9	-11.6	-10.2	-12.2	-13.6	-11.2
16	-9.5	-10.0	-9.0	-7.1	-7.6	-6.6	-11.3	-11.9	-10.8	-12.3	-12.9	-11.7
17	-9.9	-10.5	-9.4	-7.3	-8.0	-6.6	-11.0	-11.5	-10.6	-11.9	-12.4	-11.4
18	-8.4	-9.1	-7.9	-8.8	-9.3	-8.2	-11.5	-12.1	-10.9	-12.4	-13.1	-11.9
19	-8.9	-9.5	-8.4	-6.9	-7.4	-6.5	-10.2	-10.8	-9.7	-11.9	-12.4	-11.4
20	-9.6	-10.1	-9.2	-7.0	-7.6	-6.5	-11.5	-12.0	-11.0	-14.7	-15.3	-14.2
21	-10.8	-11.2	-10.3	-7.5	-8.1	-7.1	-10.2	-10.8	-9.7	-13.1	-13.8	-12.5
22	-10.3	-10.8	-9.8	-7.5	-8.0	-7.0	-8.6	-9.9	-7.7	-8.9	-10.0	-7.9
23	-11.0	-11.8	-10.4	-8.5	-9.0	-8.1	-10.5	-11.1	-9.9	-12.5	-13.4	-11.8
24	-9.7	-10.1	-9.3	-7.5	-8.0	-7.1	-10.3	-11.0	-9.8	-10.0	-10.6	-9.6
25	-10.0	-10.6	-9.4	-8.6	-9.1	-8.2	-10.4	-10.9	-9.9	-12.8	-13.4	-12.3
26	-11.7	-12.5	-11.0	-8.0	-8.8	-7.4	-11.4	-12.0	-10.8	-11.2	-11.9	-10.6
27	-9.9	-10.2	-9.5	-7.9	-8.4	-7.5	-9.7	-10.2	-9.4	-13.4	-13.9	-12.9
28	-8.2	-8.8	-7.7	-7.5	-8.2	-7.0	-9.4	-10.1	-8.9	-9.7	-10.2	-9.2
29	-8.9	-9.5	-8.4	-7.7	-8.4	-7.1	-9.7	-10.2	-9.2	-10.9	-11.7	-10.3
30	-10.2	-10.7	-9.7	-9.2	-9.6	-8.8	-9.9	-10.3	-9.6	-12.1	-12.6	-11.6
31	-9.2	-9.6	-8.8	-7.6	-8.0	-7.3	-9.3	-9.7	-9.0	-8.9	-9.5	-8.4
32	-9.0	-9.5	-8.5	-7.7	-8.3	-7.2	-11.4	-12.3	-10.6	-11.6	-12.5	-10.9
33	-10.9	-11.6	-10.3	-8.6	-9.2	-8.1	-10.9	-11.6	-10.4	-13.8	-14.4	-13.2
34	-10.8	-11.3	-10.4	-9.7	-10.1	-9.2	-10.8	-11.2	-10.3	-14.9	-15.4	-14.5
35	-9.6	-10.0	-9.2	-8.7	-9.2	-8.2	-10.8	-11.3	-10.3	-13.1	-13.6	-12.6
36	-10.2	-11.0	-9.5	-8.8	-9.4	-8.3	-10.2	-10.7	-9.7	-11.7	-12.4	-11.1
37	-9.8	-10.4	-9.3	-9.1	-9.9	-8.4	-8.4	-9.4	-7.6	-10.3	-11.3	-9.4
38	-9.9	-10.5	-9.4	-8.2	-8.7	-7.8	-11.0	-11.6	-10.4	-11.9	-12.4	-11.4
39	-10.2	-10.7	-9.8	-8.6	-9.0	-8.2	-9.5	-9.9	-9.2	-12.4	-12.9	-12.1
40	-10.9	-11.4	-10.4	-8.5	-9.2	-7.9	-11.6	-12.1	-11.2	-13.4	-13.9	-12.9
41	-10.6	-11.2	-10.0	-8.6	-9.5	-7.8	-9.7	-10.9	-8.8	-13.2	-14.1	-12.4

c. Forest

Sample no.	No. pixels	RsatS6nov	Cl-	Cl+	Jersdec	Cl-	Cl+
1	293	-10.3	-10.5	-10.0	-8.2	-8.5	-7.9
2	317	-10.2	-10.4	-9.9	-8.0	-8.3	-7.7
3	385	-9.6	-9.9	-9.3	-8.0	-8.3	-7.7
4	341	-9.4	-9.7	-9.2	-7.1	-7.5	-6.8
5	385	-9.2	-9.5	-9.0	-7.1	-7.4	-6.9
6	385	-9.4	-9.7	-9.2	-7.7	-8.0	-7.4
7	569	-9.3	-9.5	-9.0	-7.5	-7.7	-7.3
8	657	-9.9	-10.1	-9.7	-7.5	-7.7	-7.3
9	1005	-9.9	-10.1	-9.7	-7.7	-7.9	-7.5
10	1161	-9.4	-9.5	-9.2	-7.2	-7.4	-7.1
11	749	-9.7	-9.9	-9.6	-8.1	-8.3	-7.9
12	585	-9.5	-9.7	-9.3	-7.4	-7.6	-7.1
13	777	-9.3	-9.5	-9.1	-7.4	-7.6	-7.3
14	777	-9.8	-10.0	-9.7	-9.7	-10.1	-9.4
15	657	-10.5	-10.6	-10.3	-9.2	-9.4	-9.0
16	569	-10.0	-1.0	-1.0	-10.8	-11.1	-10.6
17	673	-10.2	-10.4	-10.0	-8.3	-8.5	-8.1
18	797	-9.9	-10.1	-9.7	-8.2	-8.4	-8.0
19	869	-10.0	-10.1	-9.8	-8.1	-8.3	-7.9
20	569	-10.2	-10.5	-10.0	-9.0	-9.2	-8.8
21	569	-9.4	-9.7	-9.0	-8.0	-8.3	-7.8
22	421	-9.7	-10.0	-9.5	-7.6	-7.9	-7.4
23	373	-9.8	-10.1	-9.5	-7.9	-8.1	-7.6
24	593	-10.2	-10.4	-10.0	-8.2	-8.5	-8.0
25	973	-9.5	-9.7	-9.4	-7.1	-7.3	-7.0
26	1005	-9.5	-9.7	-9.4	-7.4	-7.6	-7.3
27	757	-8.9	-9.1	-8.7	-6.8	-7.0	-6.6
28	657	-8.4	-8.6	-8.2	-7.0	-7.2	-6.8
29	673	-8.2	-8.3	-8.0	-6.7	-6.9	-6.5
30	593		-22.9	-22.5		-14.7	-14.4
31	673	-11.0	-11.2	-10.8	-7.9	-8.1	-7.7
32	837	-11.3	-11.5	-11.2	-8.5	-8.7	-8.3
33	457	-10.7	-10.9	-10.4	-7.8	-8.1	-7.6
34	505	-10.8	-11.0	-10.6	-7.9	-8.1	-7.6
35	489	-11.3	-11.5	-11.1	-7.9	-8.1	-7.7
36	585	-9.7	-9.9	-9.5	-7.7	-7.9	-7.5
37	593	-9.5	-9.8	-9.3	-7.7	-8.0	-7.5
38	421	-10.6	-10.9	-10.4	-7.9	-8.1	-7.6
39	657	-9.2	-9.3	-9.0	-6.9	-7.1	-6.7
40	421	-8.9	-9.2	-8.7	-6.7	-7.0	-6.5
41	593	-9.0	-9.2	-8.9	-7.1	-7.4	-6.9

Sample no.	Jersmarch	Cl-	Cl+	RsatS6april	Cl-	Cl+
1	-7.9	-8.2	-7.5	-9.4	-9.7	-9.1
2	-7.3	-7.6	-7.0	-9.5	-13.6	-7.5
3	-6.6	-6.9	-6.4	-9.6	-9.9	-9.4
4	-6.7	-7.0	-6.5	-8.3	-8.6	-8.0
5	-6.6	-6.9	-6.4	-9.4	-9.6	-9.1
6	-7.0	-7.2	-6.8	-8.6	-8.8	-8.3
7	-7.1	-7.4	-6.9	-8.9	-9.1	-8.7
8	-7.3	-7.5	-7.1	-9.2	-9.4	-9.0
9	-7.5	-7.7	-7.3	-9.6	-9.8	-9.4
10	-7.1	-7.2	-6.9	-8.3	-8.5	-8.2
11	-7.5	-7.7	-7.3	-9.2	-9.3	-9.0
12	-6.9	-7.2	-6.7	-9.1	-9.3	-8.9
13	-6.9	-7.1	-6.7	-9.0	-9.1	-8.8
14	-7.2	-7.4	-7.0	-9.1	-9.3	-9.0
15	-8.7	-8.9	-8.5	-10.7	-10.9	-10.5
16	-9.0	-9.2	-8.8	-10.4	-10.5	-10.2
17	-7.6	-7.8	-7.3	-9.9	-10.1	-9.7
18	-7.5	-7.7	-7.3	-9.1	-9.3	-8.9
19	-7.6	-7.8	-7.4	-9.0	-9.2	-8.9
20	-8.1	-8.3	-7.9	-10.3	-10.5	-10.1
21	-9.0	-9.2	-8.8	-8.9	-9.1	-8.7
22	-7.8	-8.0	-7.5	-9.7	-10.0	-9.5
23	-7.5	-7.8	-7.2	-9.7	-9.9	-9.5
24	-8.3	-8.6	-8.1	-9.3	-9.5	-9.1
25	-7.1	-7.3	-6.9	-9.1	-9.2	-8.9
26	-7.6	-7.8	-7.5	-9.2	-9.3	-9.0
27	-6.6	-6.8	-6.4	-8.3	-8.5	-8.1
28	-6.7	-7.0	-6.5	-7.9	-8.1	-7.7
29	-6.7	-6.9	-6.5	-7.4	-7.7	-7.3
30	-14.9	-15.2	-14.7	-22.2	-22.4	-22.0
31	-6.6	-6.8	-6.4	-9.4	-9.6	-9.2
32	-6.6	-6.7	-6.4	-10.0	-10.2	-9.8
33	-6.6	-6.9	-6.4	-10.2	-10.4	-10.0
34	-6.5	-6.8	-6.3	-10.6	-10.8	-10.4
35	-6.4	-6.6	-6.2	-10.2	-10.4	-10.0
36	-6.4	-6.6	-6.2	-9.5	-9.7	-9.3
37	-6.7	-7.0	-6.5	-9.7	-9.9	-9.5
38	-7.2	-7.5	-7.0	-9.5	-9.8	-9.2
39	-6.0	-6.2	-5.7	-9.1	-9.3	-8.9
40	-6.0	-6.3	-5.8	-9.2	-9.4	-9.0
41	-6.4	-6.6	-6.2	-9.4	-9.6	-9.2

Sample no.	RsatS6may	Cl-	Cl+	RsatS1may	Cl-	Cl+	Jersmay	Cl-	Cl+
1	-8.5	-8.8	-8.2	-6.8	-7.2	-6.5	-7.2	-7.5	-6.9
2	-8.1	-13.1	-5.8	-5.6	-5.8	-5.3	-7.1	-7.4	-6.8
3	-8.2	-8.4	-8.0	-5.8	-6.1	-5.5	-6.9	-7.2	-6.7
4	-8.2	-8.5	-8.0	-4.9	-5.2	-4.7	-6.7	-7.0	-6.4
5	-7.5	-7.8	-7.3	-5.1	-5.4	-4.9	-6.8	-7.1	-6.6
6	-7.8	-8.1	-7.5	-5.7	-6.0	-5.5	-6.7	-7.0	-6.4
7	-8.3	-8.5	-8.1	-5.9	-6.1	-5.7	-6.5	-6.7	-6.3
8	-8.6	-8.8	-8.4	-6.2	-6.4	-6.0	-7.1	-7.3	-6.9
9	-8.4	-8.5	-8.2	-6.1	-6.3	-6.0	-6.7	-6.9	-6.5
10	-8.1	-8.3	-8.0	-5.3	-5.5	-5.2	-6.7	-6.9	-6.6
11	-8.7	-8.9	-8.5	-5.8	-5.9	-5.6	-7.4	-7.5	-7.2
12	-8.5	-8.7	-8.3	-5.6	-5.8	-5.4	-6.9	-7.1	-6.7
13	-8.6	-8.8	-8.4	-6.0	-6.2	-5.9	-6.8	-7.0	-6.6
14	-8.2	-8.4	-8.0	-5.7	-5.9	-5.5	-6.9	-7.1	-6.7
15	-9.6	-9.8	-9.4	-7.1	-7.3	-7.0	-8.5	-8.8	-8.3
16	-9.2	-9.4	-9.0	-7.0	-7.2	-6.8	-8.1	-8.3	-7.8
17	-8.8	-9.1	-8.6	-6.2	-6.5	-6.0	-7.2	-7.4	-7.0
18	-8.5	-8.7	-8.3	-5.8	-6.0	-5.6	-7.5	-7.7	-7.3
19	-8.3	-8.5	-8.1	-5.9	-6.1	-5.7	-7.5	-7.7	-7.3
20	-9.4	-9.6	-9.2	-6.7	-6.9	-6.5	-8.2	-8.4	-8.0
21	-9.2	-9.4	-9.0	-6.1	-6.4	-5.9		-0.6	-0.5
22	-9.2	-9.5	-9.0	-5.9	-6.1	-5.7	-7.7	-7.9	-7.4
23	-9.2	-9.5	-9.0	-6.9	-7.1	-6.6	-7.2	-7.5	-7.0
24	-8.3	-8.5	-8.1	-6.3	-6.5	-6.1	-7.8	-8.0	-7.6
25	-7.7	-7.9	-7.6	-5.9	-6.1	-5.7	-6.8	-7.0	-6.7
26	-8.0	-8.1	-7.8	-6.1	-6.2	-5.9	-7.1	-7.2	-7.0
27	-7.3	-7.5	-7.1	-5.3	-5.5	-5.1	-5.9	-6.1	-5.7
28	-7.0	-7.2	-6.8	-4.9	-5.1	-4.7	-5.8	-6.0	-5.6
29	-6.9	-7.1	-6.7	-5.1	-5.3	-4.9	-5.5	-5.7	-5.3
30	-12.1	-12.1	-12.1	-8.0	-8.2	-7.8	-15.1	-17.6	-13.5
31	-9.0	-9.1	-8.8	-5.9	-6.1	-5.7	-6.1	-6.3	-5.9
32	-9.4	-9.5	-9.2	-5.8	-5.9	-5.6	-6.2	-6.4	-6.0
33	-9.5	-9.7	-9.3	-6.2	-6.4	-6.0	-6.2	-6.4	-5.9
34	-9.4	-9.6	-9.1	-6.3	-6.5	-6.1	-6.2	-6.5	-6.0
35	-9.4	-9.7	-9.2	-5.9	-6.0	-5.7	-6.2	-6.4	-5.9
36		-8.4	-8.0	-6.2	-6.4	-6.0	-6.9	-7.1	-6.7
37	-8.5	-8.8	-8.3	-5.7	-5.9	-5.5	-6.1	-6.4	-5.9
38	-9.1	-9.3	-8.9	-6.2	-6.4	-5.9	-6.6	-6.8	-6.3
39	-8.6	-8.8	-8.5	-6.4	-6.7	-6.2	-5.8	-6.0	-5.6
40	-9.1	-9.3	-8.9	-5.5	-5.8	-5.3	-5.2	-5.4	-4.9
41	-8.6	-8.8	-8.4	-5.8	-6.0	-5.6	-6.1	-6.3	-5.9

Sample no	RsatS6june	CI-	CI+	RsatS1june	CI-	CI+	RsatS6aug	CI-	CI+	Jersaug	CI-	CI+
1	-9.0	-9.2	-8.7	-9.4	-14.2	-7.2	-8.7	-9.0	-8.4	-7.2	-7.5	-6.8
2	-9.1	-9.3	-8.9	-9.3	-9.5	-9.0	-8.7	-9.0	-8.4	-8.0	-8.3	-7.7
3	-9.1	-9.4	-8.9	-9.5	-9.7	-9.2	-8.3	-8.6	-8.1	-7.6	-7.9	-7.4
4	-8.4	-8.7	-8.2	-7.8	-8.1	-7.6	-7.9	-8.2	-7.6	-7.1	-7.4	-6.9
5	-9.0	-9.3	-8.8	-8.5	-8.8	-8.3	-7.7	-8.0	-7.4	-6.0	-6.3	-5.8
6	-8.4	-8.6	-8.1	-8.0	-8.2	-7.7	-8.8	-9.1	-8.5	-6.8	-7.1	-6.6
7	-8.7	-9.0	-8.5	-7.6	-7.8	-7.4	-8.3	-8.5	-8.0	-7.1	-7.3	-6.9
8	-9.6	-9.8	-9.4	-8.3	-8.5	-8.1	-8.7	-8.9	-8.5	-7.0	-7.2	-6.8
9	-10.0	-10.1	-9.8	-8.2	-8.4	-8.1	-9.4	-12.4	-7.7	-6.9	-7.1	-6.7
10	-8.9	-9.0	-8.8	-7.6	-7.8	-7.4	-8.0	-8.2	-7.9	-6.7	-6.9	-6.6
11	-9.3	-9.5	-9.1	-7.9	-8.1	-7.6	-8.2	-8.4	-8.0	-7.6	-7.8	-7.4
12	-9.5	-9.7	-9.3	-7.4	-7.7	-7.2	-9.1	-9.3	-8.9	-7.0	-7.3	-6.8
13	-9.4	-9.8	-8.9	-7.2	-7.4	-7.0	-8.6	-8.8	-8.4	-6.8	-7.0	-6.6
14	-9.0	-9.1	-8.8	-7.2	-7.4	-7.1	-8.3	-8.5	-8.1	-7.3	-7.5	-7.1
15	-10.7	-10.9	-10.5	-8.5	-8.7	-8.3	-9.9	-10.1	-9.7	-9.7	-10.0	-9.5
16	-10.3	-10.5	-10.1	-8.4	-8.6	-8.2	-9.7	-9.9	-9.5	-10.0	-10.2	-9.7
17	-9.4	-9.6	-9.2	-7.4	-7.6	-7.2	-9.5	-9.7	-9.3	-8.3	-8.5	-8.1
18	-9.1	-9.3	-8.9	-7.2	-7.4	-7.0	-8.6	-8.8	-8.4	-7.7	-8.0	-7.5
19	-9.2	-9.3	-9.0	-7.2	-7.4	-7.0	-8.7	-8.9	-8.6	-8.1	-8.3	-7.9
20	-9.5	-9.8	-9.3	-7.9	-8.1	-7.7	-9.1	-9.3	-8.9	-9.0	-9.3	-8.8
21	-7.6	-7.8	-7.4	-5.9	-6.2	-5.6	-8.6	-8.8	-8.4	-8.0	-8.3	-7.8
22	-9.1	-9.4	-8.9	-7.3	-7.6	-7.1	-8.7	-8.9	-8.4	-8.1	-8.4	-7.9
23	-9.0	-9.3	-8.8	-8.0	-8.2	-7.7	-9.1	-9.3	-8.8	-7.4	-7.7	-7.2
24	-9.1	-9.3	-8.9	-7.9	-8.1	-7.7	-8.7	-8.9	-8.5	-8.4	-8.6	-8.1
25	-8.8	-9.0	-8.6	-7.9	-8.1	-7.8	-8.0	-8.2	-7.9	-7.4	-7.6	-7.3
26	-8.7	-8.9	-8.6	-7.6	-7.8	-7.4	-8.2	-8.4	-8.1	-7.6	-7.8	-7.5
27	-7.8	-8.0	-7.6	-6.3	-6.5	-6.1	-7.3	-7.5	-7.1	-6.8	-6.9	-6.6
28	-7.4	-7.6	-7.2	-5.7	-5.9	-5.5	-7.1	-7.3	-6.9	-6.9	-7.2	-6.7
29	-7.5	-7.7	-7.3	-5.9	-6.0	-5.7	-6.8	-7.0	-6.6	-6.6	-6.8	-6.4
30	-20.4	-20.6	-20.2	-8.2	-8.4	-7.9	-22.3	-22.5	-22.1	-15.1	-17.8	-13.4
31	-9.4	-9.5	-9.2	-8.3	-8.5	-8.1	-9.4	-9.5	-9.2	-6.7	-6.9	-6.6
32	-9.6	-9.8	-9.5	-8.5	-8.7	-8.4	-9.8	-10.0	-9.6	-6.9	-7.1	-6.7
33	-9.3	-9.5	-9.1	-7.6	-7.8	-7.4	-9.2	-9.5	-9.0	-6.7	-7.0	-6.5
34	-9.9	-10.1	-9.6	-7.8	-8.1	-7.6	-9.8	-10.1	-9.6	-6.1	-6.3	-5.9
35	-10.0	-10.2	-9.7	-8.4	-8.5	-8.2	-9.9	-10.1	-9.6	-6.5	-6.7	-6.2
36	-8.5	-8.7	-8.3	-6.9	-7.1	-6.7	-9.5	-9.7	-9.4	-6.8	-7.0	-6.6
37	-8.7	-8.9	-8.5	-7.1	-7.3	-6.9	-9.2	-9.4	-9.1	-6.5	-6.7	-6.3
38	-9.3	-9.6	-9.1	-7.0	-7.3	-6.8	-9.4	-9.7	-9.2	-7.0	-7.3	-6.7
39	-8.4	-8.5	-8.2	-6.5	-6.7	-6.3	-9.5	-9.7	-9.3	-5.8	-6.0	-5.6
40	-8.3	-8.5	-8.0	-5.7	-5.9	-5.5	-8.7	-8.9	-8.4	-5.4	-5.6	-5.1
41	-8.2	-8.4	-8.0	-6.5	-6.7	-6.3	-8.9	-9.1	-8.7	-6.5	-6.7	-6.3

d. Flooded forest

Sample no.	No. pixels	RsatS6nov	Cl-	Cl+	Jersdec	Cl-	Cl+
1	57	-10.1	-11.0	-9.4	-7.4	-8.4	-6.7
2	69	-9.2	-9.7	-8.7	-7.7	-8.4	-7.1
3	61	-8.2	-8.9	-7.5	-7.7	-8.4	-7.1
4	45	-9.4	-10.1	-8.8	-7.2	-8.0	-6.6
5	29	-9.7	-10.7	-8.8	-7.9	-8.7	-7.3
6	45	-8.2	-8.8	-7.6	-9.0	-9.8	-8.4
7	69	-8.2	-8.7	-7.8	-8.3	-8.8	-7.9
8	69	-7.4	-8.1	-6.9	-8.7	-9.3	-8.1
9	97	-7.7	-8.3	-7.2	-8.2	-8.8	-7.6
10	45	-7.4	-8.1	-6.9	-7.8	-8.6	-7.1
11	45	-8.9	-9.8	-8.2	-7.3	-8.3	-6.5
12	57	-7.0	-7.6	-6.4	-6.9	-7.7	-6.3
13	37	-8.7	-9.4	-8.1	-7.5	-8.3	-6.8
14	29	-6.4	-7.2	-5.8	-6.7	-7.9	-5.8
15	37	-8.0	-8.9	-7.3	-6.2	-6.9	-5.5
16	61	-8.5	-9.1	-8.0	-6.8	-7.5	-6.2
17	45	-7.2	-8.0	-6.6	-7.1	-8.0	-6.5
18	45	-8.1	-8.8	-7.4	-6.2	-7.4	-5.2
19	37	-9.1	-10.0	-8.4	-6.9	-8.0	-6.1
20	61	-7.0	-7.5	-6.6	-7.1	-7.8	-6.5
21	45	-8.0	-8.7	-7.4	-7.0	-7.6	-6.4
22	37	-8.6	-9.6	-7.8	-7.3	-8.1	-6.5
23	37	-8.5	-9.6	-7.6	-5.6	-7.1	-4.4
24	45	-8.6	-9.1	-8.1	-8.7	-9.4	-8.1
25	21	-7.3	-8.1	-6.5	-7.5	-8.8	-6.5
26	21	-7.1	-8.0	-6.3	-6.1	-7.0	-5.4
27	45	-8.1	-8.7	-7.5	-7.8	-8.8	-7.0
28	37	-6.9	-7.6	-6.4	-9.7	-10.7	-8.9
29	49	-9.5	-10.3	-8.9	-8.3	-8.9	-7.8
30	29	-9.1	-9.9	-8.4	-6.2	-7.2	-5.3
31	37	-8.2	-8.7	-7.7	-7.8	-8.7	-7.0
32	21	-9.0	-10.3	-8.0	-8.4	-9.5	-7.6
33	21	-9.1	-10.4	-8.1	-8.6	-9.7	-7.8
34	37	-9.5	-10.3	-8.9	-5.2	-6.3	-4.3
35	21	-6.3	-8.6	-4.9	-7.7	-9.2	-6.7
36	21	-8.3	-9.4	-7.4	-7.0	-8.0	-6.2
37	37	-7.8	-8.7	-7.0	-6.6	-7.9	-5.5
38	45	-6.2	-6.8	-5.6	-6.9	-7.7	-6.3
39	69	-8.5	-9.1	-8.0	-7.3	-8.0	-6.8
40	44	-7.5	-8.2	-6.9	-6.9	-7.8	-6.2

Sample no.	Jersmarch	Cl-	Cl+	RsatS6april	Cl-	Cl+
1	-6.4	-7.2	-5.7	-8.6	-9.3	-7.9
2	-6.1	-6.7	-5.5	-8.2	-8.7	-7.7
3	-5.1	-5.7	-4.6	-8.1	-8.7	-7.6
4	-4.6	-5.5	-3.9	-6.3	-7.3	-5.5
5	-6.1	-7.2	-5.3	-8.3	-9.3	-7.5
6	-5.4	-6.1	-4.8	-7.5	-8.1	-6.9
7	-5.4	-5.9	-4.8	-7.1	-7.7	-6.6
8	-5.7	-6.3	-5.2	-5.7	-6.2	-5.2
9	-5.2	-5.8	-4.7	-6.2	-6.7	-5.7
10	-7.7	-8.7	-6.9	-7.3	-8.1	-6.6
11	-7.1	-8.0	-6.3	-7.5	-8.1	-6.9
12	-7.1	-7.8	-6.5	-7.0	-7.5	-6.6
13	-4.2	-5.3	-3.2	-3.6	-4.3	-2.9
14	-3.1	-3.8	-2.5	-6.3	-7.3	-5.5
15	-3.7	-5.2	-2.6	-4.5	-5.2	-3.9
16	-8.2	-9.0	-7.5	-9.3	-10.0	-8.7
17	-7.2	-8.0	-6.6	-7.9	-8.7	-7.3
18	-6.3	-7.1	-5.6	-8.0	-8.6	-7.5
19	-4.0	-5.0	-3.3	-7.2	-7.8	-6.7
20	-3.1	-3.9	-2.4	-6.1	-6.8	-5.5
21	-4.8	-5.5	-4.3	-6.9	-7.7	-6.3
22	-4.6	-5.2	-4.0	-7.3	-8.1	-6.6
23	-4.7	-5.6	-3.9	-8.0	-8.7	-7.4
24	-5.9	-6.9	-5.1	-7.1	-7.9	-6.4
25	-5.7	-7.3	-4.6	-7.1	-8.3	-6.2
26	-4.5	-5.6	-3.7	-4.0	-4.6	-3.4
27	-6.9	-7.8	-6.2	-6.6	-7.4	-5.8
28	-6.3	-6.9	-5.8	-5.7	-6.5	-5.1
29	-4.6	-5.3	-4.0	-6.7	-7.5	-6.0
30	-6.0	-6.9	-5.3	-6.3	-7.2	-5.6
31	-4.5	-5.9	-3.5	-6.4	-7.1	-5.8
32	-6.0	-6.8	-5.2	-9.1	-10.2	-8.3
33	-4.2	-5.2	-3.4	-7.9	-9.0	-7.0
34	-3.6	-4.7	-2.6	-8.0	-8.9	-7.2
35	-6.0	-6.6	-5.4	-8.5	-9.5	-7.7
36	-3.9	-4.7	-3.1	-6.7	-7.8	-5.7
37	-7.2	-8.0	-6.5	-6.9	-7.6	-6.4
38	-6.5	-7.2	-5.9	-5.6	-6.2	-5.0
39	-5.1	-5.6	-4.5	-5.5	-6.2	-5.0
40	-6.3	-7.0	-5.6	-6.0	-6.7	-5.5

Sample no.	RsatS6may	CI-	CI+	RsatS1may	CI-	CI+	Jersmay	CI-	CI+
1	-8.4	-9.1	-7.9	-5.6	-6.4	-4.9	-4.6	-5.2	-4.0
2	-10.6	-12.2	-9.4	-5.5	-6.4	-4.8	-5.0	-5.7	-4.5
3	-7.7	-8.3	-7.2	-5.8	-6.5	-5.2	-4.4	-5.2	-3.7
4	-7.0	-7.5	-6.5	-4.2	-5.2	-3.4	-5.0	-5.9	-4.2
5	-7.4	-8.0	-6.8	-6.3	-7.2	-5.6	-5.7	-6.6	-4.9
6	-8.9	-9.5	-8.3	-5.8	-6.8	-5.1	-4.4	-5.4	-3.6
7	-6.1	-6.7	-5.7	-4.8	-5.4	-4.3	-7.1	-7.8	-6.5
8	-5.8	-6.3	-5.3	-4.8	-5.3	-4.4	-6.4	-7.1	-5.8
9	-5.9	-6.3	-5.5	-4.7	-5.3	-4.2	-5.9	-6.3	-5.6
10	-6.9	-7.8	-6.2	-3.2	-4.0	-2.6	-3.8	-4.6	-3.2
11	-6.4	-7.0	-5.8	-6.4	-7.2	-5.8	-6.5	-7.3	-5.8
12	-7.1	-7.7	-6.5	-5.1	-5.8	-4.6	-4.4	-5.1	-3.9
13	-4.1	-4.9	-3.4	-2.5	-3.2	-1.8	-3.4	-4.7	-2.5
14	-5.4	-6.6	-4.4	-1.0	-1.9	-0.2	-3.8	-4.6	-3.2
15	-4.6	-5.3	-4.0	-1.5	-2.4	-0.7	-2.3	-3.0	-1.7
16	-8.4	-9.0	-7.9	-5.7	-6.3	-5.2	-4.8	-5.4	-4.2
17	-7.0	-7.8	-6.4	-5.8	-6.5	-5.1	-5.4	-6.2	-4.7
18	-7.7	-8.6	-7.0	-4.8	-5.6	-4.1	-3.9	-5.1	-2.9
19	-5.3	-6.1	-4.7	-0.8	-1.3	-0.4	-1.3	-2.2	-0.5
20	-4.6	-5.1	-4.1	-1.7	-2.2	-1.2	-1.7	-2.5	-1.1
21	-4.5	-5.1	-4.0	-1.9	-2.6	-1.3	-0.5	-1.4	0.2
22	-7.0	-8.0	-6.3	-4.9	-5.7	-4.3	-3.9	-4.8	-3.1
23	-8.8	-9.3	-8.3	-4.9	-5.5	-4.3	-4.1	-4.7	-3.6
24	-8.9	-9.5	-8.4	-4.8	-5.4	-4.3	-3.1	-3.9	-2.4
25	-4.9	-6.2	-3.9	-2.9	-4.0	-2.0	-5.0	-6.0	-4.2
26	-8.0	-8.7	-7.4	-3.4	-4.4	-2.7	-3.5	-4.6	-2.6
27	-5.5	-6.2	-5.0	-3.0	-3.4	-2.7	-5.7	-6.5	-5.0
28	-5.6	-6.2	-5.1	-0.9	-1.7	-0.2	-3.9	-4.7	-3.2
29	-5.4	-6.1	-4.8	-0.5	-1.0	0.0	-2.9	-3.8	-2.2
30	-5.8	-6.6	-5.2	-2.1	-2.5	-1.6	-4.9	-5.8	-4.1
31	-6.6	-7.7	-5.7	-4.0	-4.6	-3.4	-4.2	-4.9	-3.5
32	-8.1	-8.8	-7.5	-6.0	-7.2	-5.1	-3.3	-4.4	-2.4
33	-6.3	-7.6	-5.4	-6.9	-7.8	-6.1	-3.8	-4.7	-3.1
34	-7.6	-8.9	-6.6	-5.8	-6.7	-5.1	-5.5	-6.5	-4.8
35	-6.2	-8.1	-4.9	-5.0	-5.9	-4.2	-4.5	-5.4	-3.8
36		-6.8	-5.2	-2.2	-3.4	-1.2	-3.6	-4.7	-2.7
37	-6.1	-6.7	-5.5	-3.9	-4.7	-3.3	-6.6	-7.8	-5.6
38	-6.3	-7.0	-5.7	-4.4	-5.3	-3.6	-4.7	-5.7	-3.9
39	-5.8	-6.3	-5.3	-3.4	-4.2	-2.8	-5.3	-6.0	-4.8
40	-6.0	-6.7	-5.5	-3.9	-4.8	-3.2	-5.5	-6.5	-4.8

Sample no.	RsatS6june	Cl-	Cl+	RsatS1june	Cl-	Cl+	RsatS6aug	Cl-	Cl+	Jersaug	Cl-	Cl+
1	-8.0	-8.6	-7.5	-7.7	-8.3	-7.2	-7.7	-8.4	-7.1	-4.7	-5.4	-4.2
2	-8.5	-9.2	-7.9	-4.8	-5.4	-4.3	-7.1	-7.8	-6.5	-5.0	-5.8	-4.3
3	-7.6	-8.3	-7.1	-5.7	-6.1	-5.3	-7.3	-7.8	-6.8	-5.2	-5.9	-4.6
4	-9.9	-10.6	-9.3	-7.0	-7.7	-6.5	-6.4	-7.2	-5.7	-3.7	-4.5	-3.0
5	-8.0	-9.0	-7.3	-7.1	-7.8	-6.5	-7.4	-8.3	-6.7	-5.3	-6.2	-4.6
6	-8.9	-9.5	-8.3	-5.2	-5.7	-4.7	-6.3	-7.1	-5.7	-4.8	-5.7	-4.1
7	-6.6	-7.1	-6.1	-5.1	-5.7	-4.5	-6.1	-6.6	-5.7	-5.8	-6.5	-5.3
8	-5.7	-6.2	-5.3	-5.2	-6.0	-4.6	-6.3	-7.0	-5.8	-5.0	-5.9	-4.3
9	-6.8	-7.3	-6.3	-5.9	-6.4	-5.5	-6.8	-7.3	-6.4	-5.9	-6.5	-5.4
10	-6.4	-7.1	-5.8	-4.2	-5.0	-3.5	-6.1	-6.7	-5.5	-4.6	-5.6	-3.8
11	-7.2	-8.0	-6.5	-5.5	-6.1	-5.0	-7.2	-7.9	-6.6	-6.0	-6.9	-5.3
12	-7.3	-7.7	-6.9	-5.0	-5.8	-4.4	-7.2	-7.9	-6.6	-5.8	-6.4	-5.2
13	-4.2	-4.8	-3.6	-2.7	-3.7	-1.9	-6.2	-7.1	-5.4	-3.4	-4.4	-2.5
14	-4.2	-4.8	-3.6	-2.0	-2.9	-1.3	-7.1	-8.2	-6.2	-5.0	-5.7	-4.4
15	-4.4	-5.1	-3.8	-2.1	-2.8	-1.5	-6.4	-7.2	-5.8	-3.3	-4.2	-2.5
16	-8.2	-8.8	-7.7	-7.0	-7.5	-6.6	-7.0	-7.5	-6.6	-5.8	-6.4	-5.3
17	-7.7	-8.6	-7.0	-5.2	-5.7	-4.7	-6.4	-7.2	-5.7	-6.3	-7.0	-5.6
18	-5.5	-6.2	-4.9	-6.1	-6.7	-5.6	-7.5	-8.4	-6.8	-4.7	-5.5	-4.1
19	-5.3	-6.0	-4.7	-2.3	-3.2	-1.6	-8.0	-9.1	-7.2	-2.8	-3.6	-2.0
20	-4.2	-5.1	-3.4	-2.8	-3.5	-2.2	-6.9	-7.7	-6.3	-2.3	-3.2	-1.5
21	-6.7	-7.7	-5.9	-2.1	-2.8	-1.6	-6.8	-7.5	-6.2	-4.1	-4.7	-3.6
22	-7.6	-8.3	-7.0	-6.6	-7.6	-5.9	-9.0	-9.7	-8.3	-4.1	-5.2	-3.2
23	-8.9	-10.0	-8.0	-6.5	-7.3	-5.8	-7.3	-8.1	-6.7	-3.5	-4.2	-2.8
24	-8.1	-8.9	-7.4	-6.9	-7.5	-6.4	-8.4	-9.0	-7.9	-6.4	-7.6	-5.5
25	-6.9	-8.1	-6.0	-3.4	-4.2	-2.8	-6.8	-7.8	-6.0	-5.2	-6.5	-4.3
26	-6.1	-6.7	-5.7	-5.3	-6.3	-4.4	-5.9	-6.7	-5.2	-5.5	-6.7	-4.6
27	-5.1	-5.9	-4.5	-5.2	-5.8	-4.7	-6.2	-6.9	-5.6	-6.0	-7.0	-5.2
28	-5.1	-6.2	-4.2	-2.2	-3.3	-1.4	-4.8	-5.6	-4.2	-4.4	-5.2	-3.7
29	-4.9	-5.7	-4.3	-2.3	-3.2	-1.6	-7.0	-7.6	-6.4	-4.3	-5.4	-3.5
30	-6.9	-7.7	-6.2	-3.1	-4.0	-2.3	-5.4	-6.1	-4.8	-3.9	-5.3	-2.8
31	-7.6	-8.2	-7.1	-4.4	-5.1	-3.9	-10.3	-11.2	-9.5	-4.5	-5.3	-3.9
32	-6.4	-7.6	-5.4	-4.8	-5.7	-4.1	-8.0	-8.8	-7.3	-4.9	-5.8	-4.1
33	-6.1	-7.5	-5.0	-6.0	-7.0	-5.2	-7.4	-8.0	-6.9	-4.8	-5.8	-4.0
34	-6.8	-7.9	-5.8	-3.7	-4.7	-2.8	-7.7	-8.7	-6.9	-5.8	-6.8	-5.0
35	-5.2	-6.8	-4.0	-5.4	-6.3	-4.6	-6.8	-7.6	-6.1	-3.9	-4.9	-3.1
36	-5.2	-6.7	-4.2	-2.2	-3.4	-1.3	-6.8	-7.9	-5.9	-3.2	-4.5	-2.3
37	-7.1	-8.1	-6.3	-2.0	-3.0	-1.2	-5.8	-6.4	-5.3	-6.6	-7.6	-5.8
38	-5.2	-6.2	-4.4	-4.3	-5.2	-3.5	-5.7	-6.6	-4.9	-7.2	-8.0	-6.5
39	-6.0	-6.6	-5.5	-2.8	-3.3	-2.3	-6.2	-6.8	-5.7	-5.6	-6.3	-4.9
40	-6.1	-7.0	-5.4	-3.0	-3.8	-2.3	-5.9	-6.6	-5.3	-6.4	-7.3	-5.7